UNIVERSITY OF SOUTHAMPTON

FACULTY OF PHYSICAL AND APPLIED SCIENCE

School of Electronics and Computer Science

Design of High Frequency Ultrasonic Array Transducers for Medical Imaging

by

Yichen Qian

Thesis for the degree of Doctor of Philosophy

Oct. 2011

UNIVERSITY OF SOUTHAMPTON

Abstract

FACULTY OF PHYSICAL AND APPLIED SCIENCE
School of Electronics and Computer Science

Doctor of Philosophy

DESIGN OF HIGH FREQUENCY ULTRASONIC ARRAY TRANSDUCERS FOR MEDICAL IMAGING

by Yichen Qian

Ultrasonic transducers have been widely used in the medical applications. High frequency array transducers have recently attracted many research interests, since it provides not only the electronic beamforming but also the very fine image resolution. The transducers are usually either annular or linear arrays. This study concentrates on the design of both types of array in high frequency applications.

The annular array is firstly investigated, and an optimized design of array geometry is developed including the kerfs influence which is usually neglected in the design of high frequency arrays. The improved imaging performance is found by this optimized design. More interestingly, the conventional annular array with element having the same surface area has a relatively large sidelobe closest to the main lobe. Two methods are applied to suppress the sidelobe. The method of using high-impedance single matching to enlarge the element bandwidth only shows very limited lobe suppression, however, a novel matching approach is found. Another method of changing the array geometry from equal area elements to equal width ones successfully suppressed the sidelobe. The imaging results suggest that the novel equal width array shows a good improvement.

The linear array is then analyzed. The kerfs influence again is found to be significant for the array especially for high frequency. It is essential to use a high attenuated kerfs material in the linear array design. More importantly, the limitation of current fabrication techniques forces the linear array to concede a high grating lobe in the imaging field if it operates in a relatively high frequency. A novel linear array is developed to suppress the grating lobe without using advanced fabrication techniques. The imaging results show that the novel linear array has a general reduction of -6dB for the lobe suppression. The novel design made the linear array operate in a very high frequency without strong grating lobe, and the array can be fabricated by current techniques.

Contents

Abstract i

Contents iii

List of Figures viii

List of Tables xiii

DECLARATION OF AUTHORSHIP xvi

Acknowledgements xvii

Definitions and Abbreviations xviii

Chapter 1 Introduction 1

1.1 Overview of Medical Ultrasound Imaging 1

1.2 Research Scale 4

1.3 Published Papers 5

1.4 Outline of Thesis 5

Chapter 2 Literature Review 7

2.1 Introduction 7

2.2 Transducer components 8

2.2.1 Piezoelectric Layer 8

2.2.2 Matching Layer 9

2.2.3 Backing Layer 10

2.3 Heart of the Transducer – Piezoelectric Layer 10

2.3.1 Piezoelectric Effect 10

2.3.2 Piezoelectric Equations 12

2.3.3 Vibration Modes 14

2.3.4 Waves produced by transducer element 18

2.3.5 Piezoelectric materials 19

2.4 Transducer Imaging 22

2.4.1 Imaging Principle 22
2.4.2 Imaging Properties 25
2.4.3 Focusing Techniques 28
2.5 Design of Transducers by Numerical Models 31
2.5.1 Classic 1-D models 31
2.5.2 Loss factors involved in 1-D model 34
2.5.3 Sensitivity and Bandwidth 35
2.5.4 Electrical and Mechanical Tuning 36
2.5.5 Model of Transducer Imaging 39
2.5.6 Directivity 41
2.6 Transducers Fabrication and Comparisons 44
2.6.1 Single-element Transducer 44
2.6.2 Linear array 45
2.6.3 Annular array 47
2.6.4 Comparisons 48
2.7 Summary 49
Chapter 3 High Frequency Annular Array 51
3.1 Introduction 51
3.2 Methodology 53
3.3 Optimized Design of Equal Area Annular Array Geometry 56
3.3.1 Conventional Design of Annular Element Geometry 57
3.3.2 Optimized Design of Annular Element Geometry 59
3.4 Evaluation of Radiation Pattern by Rayleigh-integral Method 64
3.4.1 Direct Calculation 64
3.4.2 Radiation Pattern by Rayleigh-integral Method 67
3.5 Analysis of Sidelobes 69

3.5.1 Element Vibration 69
3.5.2 Accuracy discussion on FEA and R-I methods 73
3.5.3 Potential Reasons for the Sidelobe 76
3.6 Summary 78
Chapter 4 Methods of Sidelobe Suppression 81
4.1 Introduction 81
4.2 Sidelobe Suppression by Broadband 81
4.2.1 Bandwidth Improvement by Tuning 82
4.2.2 Element Behaviours by FEA 84
4.2.3 Imaging Responses 85
4.3 Sidelobe Suppression by Geometric Change 88
4.3.1 Sidelobe Analysis of EA Annular Array 88
4.3.2 Sidelobe Suppression by Novel Array Geometry 92
4.3.3 Analysis of the R-I Patterns 95
4.4 Summary 97
Chapter 5 High Frequency Equal Width Annular Array 99
5.1 Introduction 99
5.2 Performances of Equal Width Annular Array 100
5.2.1 Element Responses 100
5.2.2 Imaging Responses 105
5.3 Discussions on Equal Width Annular Array 106
5.3.1 Discussion on Pressure Pulses at Focal Point 110
5.3.2 Discussion on Resolution and Contrast 111
5.3.3 Discussion on Sidelobe and Pedestal Lobe 113
5.3.4 Discussion on Fabrication Difficulties 115
5.3.5 Overall Discussion 115

5.4 Summary 116
Chapter 6 High Frequency Linear Array 119
6.1 Introduction 119
6.2 Methodology 120
6.3 Design of a Conventional Linear Array 123
6.3.1 R-I Evaluation of Array Beam Pattern 123
6.3.2 Influence of Kerfs Filler on Element Vibration 125
6.4 Imaging Performances of the Linear Array 130
6.4.1 Influence of the Kerfs Vibration 131
6.4.2 Imaging Patterns of Very High Frequency Linear Array 133
6.5 Summary 136
Chapter 7 Novel High Frequency Linear Array 137
7.1 Introduction 137
7.2 Design of a Novel High Frequency Linear Array 139
7.2.1 Method of Grating Lobe Suppression 139
7.2.2 Details in the Design of Novel Array by KLM Model 141
7.3 Performances of the Novel Linear Array 144
7.3.1 Element Responses by FEA 145
7.3.2 Imaging Performances 150
7.3.3 Compound Beam Patterns 157
7.4 Optimization of Grating Lobe Suppression 159
7.4.1 R-I Evaluation 160
7.4.2 FEA Patterns 163
7.5 Summary 164
Chapter 8 Conclusions & Future work 167
8.1 Conclusions 167

8.1.1 High Frequency Annular Array 167

8.1.2 High Frequency Linear Array 169

8.2 Future Work 170

Appendix A 173

Appendix B 179

Appendix C 181

Appendix D 193

Appendix E 197

Reference 201

List of Figures

Figure 1.1 Types of transducer: (a) 1-D linear array, (b) 2-D (phased) array, and (c) annular array ...3

Figure 2.1 Cross section of a single-element transducer 8

Figure 2.2 PZT elementary cell: (a) cubic lattice above Curie point and (b) tetragonal lattice below Curie point including an electrical dipole [27] 11

Figure 2.3 The movements of electrical dipoles in the Weiss domains (a) before poling (b) in poling and (c) after poling [27] 12

Figure 2.4 Vibration modes of a free piezoelectric resonator of which the cross section in XZ plane is displayed, symbol *f* denotes the frequency [28] 15

Figure 2.5 Diagrams of (a) 1-3 and (b) 2-2 connectivity composite [47, 48] 21

Figure 2.6 Pulse-echo response to form the ultrasonic imaging [57] 23

Figure 2.7 A focused beam generated by an ultrasonic transducer 23

Figure 2.8 Diagram of a typical (a) electrical beamforming and (b) beam steering 24

Figure 2.9 2-way radiation pattern of a focused transducer 26

Figure 2.10 Schematic diagram of radiation pattern by a focused transducer 27

Figure 2.11 Comparison between B-scan and B/D scan for single-element transducers [66] 29

Figure 2.12 Dynamic focusing in reception for array transducers [57] 30

Figure 2.13 Three port network to analogise a piezoelectric transducer [17] 32

Figure 2.14 1-D KLM model for T-mode, Port 1 & 2 for acoustic outputs, and Port 3 for the inputs of electrical signals [68] 32

Figure 2.15 ABCD matrices derived from KLM model representing the overall transducer 33

Figure 2.16 Round-trip 1D model, (a) refers to transmitter and (b) for receiver [78] 36

Figure 2.17 The network of electrical tuning in a transducer 37

Figure 2.18 Radiating source with arbitrary shape for Rayleigh integral [79] 39

Figure 2.19 Geometry of a rectangular element 42

Figure 2.20 The cross section of a 1-D or 2-D linear array 42

Figure 2.21 Cross section of a typical linear array [17] 46

Figure 3.1 The front view of a typical 7-element equal area annular array 51

Figure 3.2 Finite element model of a 2-D cross section of a 7-element EA annular array 54

Figure 3.3 (a) Amplitude and (b) phase angle of outermost element impedance spectrum; "FEA real" and "KLM real" denote the FEA and KLM responses of real array (with kerfs) respectively, while "KLM ideal" is the KLM responses of ideal array (no kerfs) 58

Figure 3.4 (a) IL spectrum of the outmost element using (a) the tuning only designed for the element, (b)and the one using conventional design 59

Figure 3.5 IL spectrums of outermost (7th) element by using OD, CD and KLM 61

Figure 3.6 Normalized pressure response at focal point with conventional design (CD) and optimized design (OD) in (a) time domain and (b) frequency domain, respectively..... 62

Figure 3.7 2-way beam patterns of the arrays with OD and CD 63

Figure 3.8 (a) The diagram of array aperture and (b) the diagram to describe Rayleigh-integral method..... 65

Figure 3.9 Gauss pulse to fit the element pulse by FEA..... 67

Figure 3.10 Radiation pattern of EA array with optimized and conventional design by using (a) numerical and (b) FEA method 68

Figure 3.11 (a) The position of the 3 points to get pressure *p_inner* at inner edge, *p_mid* at the middle and *p_outer* at outer edge; (b), (c) show these pressures for 1^{st} element in time and frequency domain; (d), (e) for 4^{th} element; (f), (g) for 7^{th} element 70

Figure 3.12 Pressure distribution along the excited element surface 72

Figure 3.13 Radiation patterns by R-I method using (a) various N_{ap} but N_{th}=256, and (b) N_{ap}=128 but various N_{th}..... 73

Figure 3.14 Radiation patterns by the three methods 74

Figure 3.15 (a) Radiation patterns of the 1mm array by different methods, (b) the same patterns but in the region near sidelobe..... 74

Figure 3.16 2-way pattern of the partly and fully excited EA array by FEA 76

Figure 3.17 The R-I patterns with the Gauss pulse of (a) BW=30% and (b) BW=40%, with the comparison of FEA results 77

Figure 4.1 The influence of electric (R_s) and mechanical tuning (Z_m) on (a) fractional bandwidth and (b) IL peak value 82

Figure 4.2 IL spectrums of the three elements using (a) Z_m =16MRayls and (b) double matching .. 85

Figure 4.3 Beam patterns of the array using the three matching options by FEA 86

Figure 4.4 The pressure pulses at focal point in both (a) time and (b) frequency domain for the array with different matching 87

Figure 4.5 The cross section of an EA annular array to focus in the medium 89

Figure 4.6 Front view of a 7-element EW annular array 92

Figure 4.7 R-I patterns of (a) EW array and (b) EA array with various bandwidth 94

Figure 5.1 (a) Amplitude and (b) phase of the impedance spectrums of the 3 elements by FEA .. 100

Figure 5.2 IL spectrum of the three EW elements by FEA compared to KLM model 101

Figure 5.3 (a) The position of the 3 points to get pressure *p_inner* at inner edge, *p_mid* at the middle and *p_outer* at outer edge; (b), (c) show these pressures for 1st element in time and frequency domain; (d), (e) for 4th element; (f), (g) for 7th element 103

Figure 5.4 Pressure distribution along the excited element surface 104

Figure 5.5 Pressure pulse at focal plane in (a) time and (b) frequency domain 105

Figure 5.6 Radiation patterns, “EW_FEA” and “EW_R-I” refer to the pattern of EW array by FEA and R-I method, respectively; and “EA_FEA” is the pattern of EA array by FEA 106

Figure 5.7 Pressure pulses at focal point: (a), (b) show the pulses of both EA and EW array with *N*=6; (c), (d) for *N*=7; (e), (f) for *N*=8; (g), (h) for *N*=9 and (i), (j) for *N*=10 108

Figure 5.8 Beam patterns of EA and EW arrays with (a) *N*=6; (b) *N*=7, (c) *N*=8, (d) *N*=9 and (e) *N*=10 109

Figure 6.1 Schematic diagram of a linear array (or 2-2 composite), where *d* is the thickness, *a* and *b* denotes the width of ceramic and polymer respectively, and *P* for the polarization direction [47] 120

Figure 6.2 2D FEA model of a typical linear array 121

Figure 6.3 The Gauss pulse of a linear element to fit its element pulse by KLM model 123

Figure 6.4 R-I patterns of the linear array width different kerfs width w_g 124

Figure 6.5 (a), (b) shows the impedance and phase spectrum of the element in the linear array using Epoxy 1; (c),(d) for the array using Epoxy 2; and (e), (f) for Epoxy 3 126

Figure 6.6 IL spectrums of the element in the arrays using the three epoxies, with the KLM response as a comparison 128

Figure 6.7 (a), (b) shows the pressure pulses at the centre of the element in the linear array using the three kerfs fillers; (c), (d) for the pulses at the outer edge; and (e), (f) for the pulses at the centre of the nearest kerfs 129

Figure 6.8 Pressure pulses at the focal point for the linear array using the three kerfs filler in (a) time and (b) frequency domain 131

Figure 6.9 Radiation patterns of the three linear arrays and the one by R-I method 132

Figure 6.10 (a), (b) Pressure pulses at the focal point for the 45MHz linear array; and (c), (d) show the responses of the 60MHz array 134

Figure 6.11 (a), (b) Pressure pulses at the focal point for the 45MHz linear array; and (c), (d) show the responses of the 60MHz array 134

Figure 7.1 Cross section of (a) conventional and (b) novel 1-D linear array 140

Figure 7.2 IL responses by the two matching options in (a) LFI and (b) HFI with *n*=1.5 142

Figure 7.3 IL spectrums of the novel array element in (a) LFI and (b) HFI with different *n* 143

Figure 7.4 (a), (b) show the impedance and phase spectrum of the element in LFI for the novel array with *n*=1.5; (c), (d) for *n*=2; (e), (f) for *n*=2.5; and (g), (h) for *n*=3 146

Figure 7.5 (a), (b) show the impedance and phase spectrum of the element in HFI for the novel array with *n*=1.5; (c), (d) for *n*=2; (e), (f) for *n*=2.5; and (g), (h) for *n*=3 147

Figure 7.6 (a), (b) show the IL spectrums in LFI and HFI respectively, for the element in the novel array with *n*=1.5; (c), (d) for *n*=2; (e), (f) for *n*=2.5; and (g), (h) for *n*=3 149

Figure 7.7 Pressure pulse at focal point in (a) time and (b) frequency domain, for the array with *n*=1.5 in LFI and the lower-frequency conventional array 151

Figure 7.8 Pressure pulses at focal point in (a) time and (b) frequency domain, for the array with *n*=1.5 in HFI and the higher-frequency conventional array 151

Figure 7.9 Radiation patterns of the novel array with n=1.5 and the conventional array in the process of (a) LFI and (b) HFI 153

Figure 7.10 Pressure pulses at focal point in (a) time and (b) frequency domain, for the novel array with *n*=2, 2.5 and 3 in LFI 154

Figure 7.11 Pressure pulses at focal point in time domain for the array in HFI with (a) *n*=2, (b) *n*=2.5 and (c) *n*=3; (d) then shows their frequency domain responses 154

Figure 7.12 Radiation patterns for the novel arrays with various *n* in (a) LFI and (b) HFI 156

Figure 7.13 The compound beam patterns of the novel array with (a) *n*=1.5, (b) *n*=2, (c) *n*=2.5 and (d) *n*=3, compared to the patterns of their corresponding conventional array showing operating frequency about (a) 40MHz, (b) 50MHz, (c) 60MHz and (d) 70MHz 158

Figure 7.14 Angular patterns for the arrays with different frequencies 160

Figure 7.15 Curves of the angular position ϑ versus (a) operating frequency f and (b) $1/f$ 162

Figure 7.16 Angular beam patterns of the three arrays, conv. refers to conventional array..... 163

List of Tables

Table 1.1 Comparison of Imaging Modalities [4] 2

Table 2.1 Piezoelectric equations relating these parameters (i, j=1, 2, 3; λ, μ=1-6) [26] 13

Table 2.2 Piezoelectric equations relating these parameters (*i*, *j*=1, 2, 3; *λ*, *μ*=1-6) 13

Table 2.3 Relations among the piezoelectric material constants [26] 13

Table 2.4 Comparisons of common piezoelectric materials 19

Table 2.5 Parameters in 1-D KLM model of TE mode 32

Table 2.6 Parameters of transfer matrices derived from KLM model 34

Table 2.7 Comparisons among the transducer of single element, linear and annular array 49

Table 3.1 Properties of the layers used in the FEA model of annular array 54

Table 3.2 Area of EA elements using conventional design with different kerfs width 57

Table 3.3 Radius and area of the annular elements using optimized design with 30μm kerfs 60

Table 3.4 Parameters from IL spectrums by using CD, OD and KLM 61

Table 3.5 Parameters obtained by pressure responses at focal point 62

Table 3.6 Imaging parameters obtained by 2-way beam pattern 63

Table 3.7 Parameters from the radiation patterns by both R-I and FEA method 68

Table 3.8 Pressure parameters of the three elements in EA array 71

Table 4.1 IL_{max} with maximum bandwidth *BW* with different matching layer(s) 84

Table 4.2 Parameters of the matching materials for Z_m=16MRayls and double matching 84

Table 4.3 Parameters including IL peak IL_{max}, central frequency f_c and bandwidth *BW* 85

Table 4.4 Imaging parameters from the patterns of the array with different matching 86

Table 4.5 Parameters from the pressure at focal point of the array with different matching 87

Table 4.6 Phase difference φ_{dif} of every element pulse at off-axis point (r_f, *F*); subscript *N* and *–N* denote the right and left parts of each element, respectively 91

Table 4.7 Phase difference φ_{dif} of the pulse in every EW element at off-axis point (r_f, *F*) 93

Table 4.8 Parameters obtained by the R-I patterns of EA and EW array with element pulses with different bandwidth 94

Table 4.9 Z_t and normalized P_{max} for every element in EA and EW arrays 96

Table 5.1 Element pulse responses derived from IL spectrum for EW array 101

Table 5.2 Pressure parameters of the three elements in EW array 103

Table 5.3 Parameters obtained by pressure response at focal point 105

Table 5.4 Imaging parameters of the radiation patterns 106

Table 5.5 Pressure parameters of the pulses at focal point for the arrays with different *N* 108

Table 5.6 Imaging parameters for the arrays with different *N* 110

Table 5.7 Ratio of P_{max} of EW array to the one of EA array by using FHT and FEA 111

Table 5.8 Resolution and contrast of EA and EW arrays by FEA 112

Table 5.9 Position of the pedestal lobes for EW arrays, 'Linear' here refers to grating lobe position in linear array which is calculated by Equation (4.9) 114

Table 5.10 Width of "outermost" element in EA and EW arrays (*N* for the total element number) 115

Table 5.11 Summary and comparison between EA and EW arrays 116

Table 6.1 Properties of materials used in linear array, superscript * means that sound speed *c* of PZ34 is actually c^B used only in the beam mode 122

Table 6.2 Properties of the three epoxies used as kerfs filler 125

Table 6.3 Parameters of IL spectrums for the arrays using three epoxies by FEA and KLM 128

Table 6.4 Parameters of the pulses at the focal point 131

Table 6.5 Beam Parameters of the three arrays, compared to the R-I results 132

Table 6.6 The lateral position of the grating lobes using different methods 135

Table 7.1 Band parameters of the novel array element with different *n* 143

Table 7.2 Band parameters of the novel array element with various *n* by both FEA and KLM, *n*=1 here represents the conventional array (LFI=HFI) 149

Table 7.3 Parameters of the pressure pulses at focal point for the novel array with *n*=1.5, and the conventional array in both LFI and HFI 152

Table 7.4 Imaging parameters of beam patterns for the novel array with *n*=1.5 and conventional array in both LFI and HFI 153

Table 7.5 Parameters of pressure at focal point for the novel array with *n*=2, 2.5 and 3..... 155

Table 7.6 Imaging parameters in both LFI and HFI for the novel arrays with *n*=2, 2.5 and 3..... 156

Table 7.7 The ratios for the novel arrays with *n*=1.5, 2, 2.5 and 3 157

Table 7.8 Imaging parameters of compound beam for the novel array with *n*=1.5, compared to the results of a 40MHz conventional array 158

Table 7.9 Levels and positions of MML and GL for the array with various frequencies..... 161

Table 7.10 Imaging parameters of the three arrays 164

DECLARATION OF AUTHORSHIP

I, YICHEN QIAN

declare that the thesis entitled

Design of High Frequency Ultrasonic Array Transducers for Medical Imaging

and the work presented in the thesis is both my own, and have been generated by me as the result of my own original research. I confirm that:

- this work was done wholly or mainly while in candidature for a research degree at this University;
- where any part of this thesis has previously been submitted for a degree or any other qualification at this University or any other institution, this has been clearly stated;
- where I have consulted the published work of others, this is always clearly attributed;
- where I have quoted from the work of others, the source is always given. With the exception of such quotations, this thesis is entirely my own work;
- I have acknowledged all main sources of help;
- where the thesis is based on work done by myself jointly with others, I have made clear exactly what was done by others and what I have contributed myself;
- none of this work has been published before submission, or [delete as appropriate] parts of this work have been published as: [please list references]

Signed: ……..

Date: …….

Acknowledgements

I would like to express my utmost gratitude to Dr. Nick Harris for being my supervisor and his great guidance throughout this PhD project. I also wish to really thank to my second supervisors - Prof. Steve Beeby and Prof. Neil White for giving me support and sharing their valuable knowledge during the 4-year PhD period.

I would also like to express my great appreciation to Dr. Peter Glynne-Jones, Dr. Russel Torah, Dr. Andy Cranny and Dr. Dibin Zhu for their kindest support in this research. And a special thank to Dr. Peter Glynne-Jones, your support for addressing the problems in my first Journal paper largely helped its publication.

To my colleagues and friends, many thanks for your help not only in my research but also my personal life, particularly to Dr. John Tudor, Dr. Somphop Rodamporn, Dr. Ghaithaa Manla, Dr. Swee Leong Kok, Dr. Noreha Abdul Malik, Ivo Ayala, Yang Wei and Yi Li.

Last but not least, the most special thanks are given to the two oldest friends throughout my 26-year life, my parents. I have spoken to you guys every week, so actually there is nothing really special for you, but simply 4 words: No You! No me!

Definitions and Abbreviations

AL	Acoustic loss
B-scan	Brightness-scan
B-mode	Beam mode
CW	Continuous wave
cos	Cosine function
cot	Cotangent function
DOF	Depth of field
EA	Equal area
EPD	Element Path Difference
EW	Equal width
EL	Electrical loss
FEA	Finite Element Analysis
FFT	Fast Fourier Transform
FHT	Fast Hankel Transform
HF	High frequency
HFI	Higher frequency imaging
HFM	High-frequency matching
IL	Insertion loss
L-mode	Lateral mode
LE-mode	Longitudinal-extensional mode
LFI	Lower frequency imaging
LFM	Low-frequency matching
log	Logarithm function (=$\log_{10}$)
PZT	Lead zirconate titanate ($Pb(Zr,Ti)O_3$)
PT	Lead titanate ($PbTiO_3$)
R-I	Rayleigh-integral
SIR	Spatial impulse response
sin	Sine function
T-mode	Thickness mode
tan	Tangent function
TL	Transducer loss
TS-mode	Thickness shear mode

Chapter 1 Introduction

1.1 Overview of Medical Ultrasound Imaging

The beginnings of ultrasound in medical imaging can in principle, be traced back to the development of sonar by P. Langevin during World War I [1]. Piezoelectricity, discovered by Langevin's teacher, Pierre Curie, is used in transducers to realize practical echo ranging in water, with the original aim of detecting submarines. However, the technique of using ultrasound for echo-ranging was not applied to the human body for imaging until Firestone invented a reasonably compact instrument (reflectoscope) in 1940's [2]. A transmitter excites a sequence of ultrasonic pulses via a piezoelectric transducer into the human body. Echoes from different target objects are received and amplified, and then displayed on an oscilloscope as a record of amplitude versus time. This procedure is so-called "A-scan", with "A" representing amplitude. Wild and Reid then demonstrated ultrasound imaging as an useful clinical tool in early 1950's by analyzing the data from A-scan [3].

In the 1960's, B-scan, with B representing "brightness", was developed and showed its promising potential in medical imaging. The key element to differentiate a pulse-echo system that B-scan uses and echo-ranging system that A mode uses is the control of the transducer motion [4]. In early B-scan system, a single transducer aperture was moved by the position controller, triggered by the periodic timing of transmit pulse. At each mechanical controlled stop point, a scan line is sent to an object and echoes are received and displayed as spots with different brightness which is proportional to the echo amplitude. By the use of this mechanical scanning across the object, multiple lines produce a 2-D gray-scale image. In the 1970's, the introduction of linear arrays and electronic beamforming enabled real-time 2-D images [4-6]. Developments in digital electronics and materials in the past few decades have improved the image quality and flexibility in B-scans. It has now become one of the most popular imaging tools to visualize obscure structures in human body; and accounts for about one third of all diagnostic imaging procedures [7, 8].

Compared to other medical modalities including conventional X-Ray, computed tomography (CT) and magnetic resonance imaging (MRI) [4], ultrasound also has various advantages as detailed in Table 1.1. Diagnostic ultrasound is non-invasive, and does not have any cumulative biological side

effects due to the lack of harmful electromagnetic radiation. Two other strengths of ultrasound imaging is the low cost and excellent portability. However, resolution and penetration depth of ultrasound devices, the two parameters to judge the quality of image, are determined by operating frequency [9]. Most medical ultrasound systems operate in the frequency range of 1 to 10MHz, and can resolve objects approximately 1mm in size [10], showing comparable resolution to other imaging techniques. Finer resolution can be achieved by increasing the frequency. For the ultrasound system working in this low frequency range (1 to 10MHz), penetration depth is of the order of 10cm which is enough for conventional medical imaging applications such as abdominal, obstetrical and cardiological studies [7].

Table 1.1 Comparison of Imaging Modalities [4]

Modality	Ultrasound	X-ray	CT	MRI
Resolution	Frequency dependent 0.3 - 3mm	≈1mm	≈1mm	≈1mm
Penetration	Frequency dependent 3-25cm	Excellent	Excellent	Excellent
Safety	Very good	Ionizing radiation	Ionizing radiation	Very good
Cost	$	$	$$$$	$$$$$$$$
Portability	Excellent	Good	Poor	Poor

In recent years, significant effort has been made into the area of high frequency (>30MHz) ultrasound. High frequency (HF) ultrasound allows the imaging of subsurface structures with microscopic resolution (<100μm), which is also described as ultrasound biomicroscopy (UBM). The price of this improved resolution is the loss in penetration depth because of the increase in attenuation in fluid (tissue is generally regarded as fluid whose attenuation increases exponentially with frequency [11]). For a transducer operating at 50MHz, increased attenuation limits the penetration to less than 1cm. Therefore, HF ultrasound is mostly useful in medical area such as ophthalmology and dermatology, where resolutions are critical but penetration requirements are small [10, 12].

Transducers for HF imaging systems approach the micro-scale in their sizes, and fabrication challenges become a significant factor when processing the design of transducers. Two groups of transducers are generally used in the HF domain. Single-element transducers only consist of one large element. By the use of lens, they generate the image in a fixed focal plane determined by a

pre-set *f*-number. A mechanical scan must be used to form a 2D image. Though the fixed focal plane limits its usage in ultrasonic diagnosis, it is still the most widely adopted transducer in HF imaging largely due to its relatively simple fabrication.

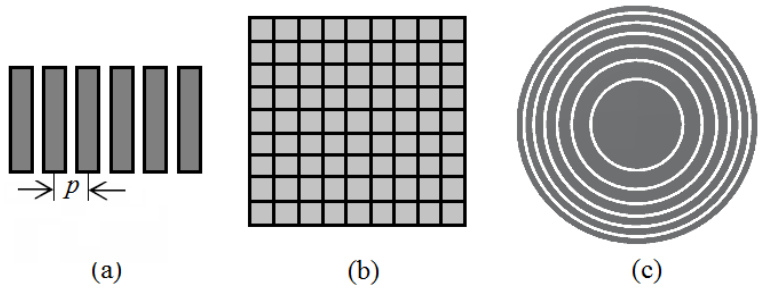

Figure 1.1 Types of transducer: (a) 1-D linear array, (b) 2-D (phased) array, and (c) annular array

To realize dynamic focusing (the focal plane is no longer fixed but adjustable), a different approach, utilising an array transducer, must be developed. Array transducers are usually classified as three groups, including 1D linear array, 2D linear array and annular array, as illustrated by Figure 1.1. Linear arrays including both 1D and 2D one have been successfully used in the relatively low-frequency imaging range (1-10MHz) [13-15]. They comprise of a large numbers of array elements, and each element is excited by an electrical signal with a certain amount of relative delay to generate dynamic focusing. However, linear array transducers are rarely used in the HF range because of the very challenging fabrication requirements, especially the difficulties to realize the very small pitch between adjacent elements.

An interesting alternative for some applications is the annular array showing much fewer elements and no strict requirement of pitch width. The fabrication is largely eased, meanwhile, annular arrays also produce a radial-symmetric acoustic imaging pattern showing better resolution in the focal plane compared to the linear array [16]. All of these have attracted researchers in the past few years. However, dynamic focusing by annular structures can be only realized in the axial direction, and a mechanical scan in the lateral direction is still required. Therefore the annular array may be described as a compromise between single-element and linear array transducers.

1.2 Research Scale

The research presented in this thesis discussed the design of HF ultrasonic array transducer for medical imaging, including both linear and annular arrays. The general objective is to develop novel array designs showing good ultrasonic imaging properties judged by bandwidth, resolutions and the level of side lobes, together with the consideration of fabrication challenges. The absolute improvement in image quality at the expense of highly complex fabrication is not the aim, rather the maintenance of good quality imaging using simpler and therefore potentially lower-cost transducers. To summarize, the array transducer is designed to have good imaging qualities with realizable and relatively easy fabrication techniques.

The research mainly consists of two parts, the design of annular and 1D linear array in HF applications. So far almost all annular array have the geometry of equal area, namely every array element shares the same area. However, by this investigation, the array is found to show an unexpected high sidelobe in the focal plane. It is caused by the influence of the transverse waves travelling across the element surface, which has not been discussed in detail according to the author's knowledge. Its relation to the unexpected sidelobe is revealed in this thesis. To reduce the influence of the transverse waves or suppress the sidelobe, a novel annular array based on the geometry of equal width is developed. No sidelobe is found in the equal width array, but another lobe far from the focal axis appears and this can be regarded as equivalent to the grating lobe in linear array. The comparison between the novel equal width annular array and the conventional equal area annular array is presented.

In terms of HF linear arrays, the grating lobe becomes the main issue in the design. The avoidance of this lobe is determined by the element pitch. The pitch width is required to be at most one wavelength (λ) - if beam steering is minimal. For example, a 70MHz linear array must have a width of element pitch less than 21μm to remove the grating lobe out of the focal plane, and indeed, if significant beam steering is required, this 1 wavelength requirement is increased up to λ/2. This very small element pitch is very hard for current fabrication techniques to realize. Instead of putting effort on further improvement in the already very challenging fabrication techniques to minimize the element pitch, the research here has developed a novel structure of linear arrays to suppress the high grating lobe by using currently available techniques. The imaging performances

of the novel arrays demonstrate the effectiveness of the grating lobe suppression. In other words, the element pitch can breach the rule of element spacing, or become even larger than 1λ (or λ/2, dependent on steering requirement). Consequently, the novel array offers the potential to ease the requirements needed for fabrication.

1.3 Published Papers

1. Qian, Y., Harris, N. R. and Beeby, S. P., *Design of a Novel High Frequency Ultrasound Annular Array*. Procedia Chemistry, 2009, 1: p. 413-416.

2. Qian, Y., Harris, N. R., Glynne-Jones, P. and Beeby, S. P., *A new 2-D model of a thin annular disk using a modified assumption*. IEEE Transactions on Ultrasonics, Ferroelectrics and Frequency Control, 2010, 57 (2): p. 421-426.

3. Qian, Y. C. and Harris, N., *Development of high frequency annular array with a novel structure for medical imaging*. Procedia Engineering, 2010, 5: p. 1276 – 1279.

1.4 Outline of Thesis

The overall structure of the thesis takes the form of 8 chapters, including this introductory chapter. The next chapter, Chapter 2, reviews the previous research done on the ultrasonic transducer. It mainly consists of three parts, the background, the design principle and the comparisons of the current transducers. The section of background briefly describes the transducer components, the piezoelectric effect and the imaging principle. The section of design principle then reveals some essential numerical methods to design and evaluate the transducer. At the end, the comparisons of the current transducers, including the types of single-element, annular and linear array, are discussed especially in HF applications.

Chapter 3 investigates the performances of the equal area annular array. It begins with the optimization of the array in HF applications, showing better performances compared to the conventional design. The next part of the chapter is to discuss the unexpected sidelobe appearing in the focal plane. It is essential to suppress the lobe.

Chapter 4 explains the two potential methods to suppress the high sidelobe in equal area annular array, including the improvement in element bandwidth and the geometric change. Although bandwidth enlargement fails to suppress the lobe, the high- impedance single matching developed in the investigation improves the traditional matching principle. However, for suppressing the sidelobe, only the geometric change is effective and leads to a novel equal width annular array (element showing identical width instead of identical area). The imaging pattern of the novel array is discussed by a numerical method based on the Rayleigh Integral.

Chapter 5 details the performances of the novel equal width annular array. The comparisons between equal width and equal area array are presented in various fields, with showing the influence of element number on the array responses.

Chapter 6 is focused on the design of a linear array in HF applications. The kerfs (or grooves) between the adjacent element are found to show significant influence on the radiation pattern, however, few researchers have addressed this issue. The design of the kerfs is presented.

Chapter 7 reveals the method to suppress the grating lobe appearing in HF linear arrays. By using the relatively easy fabrication techniques, a novel structure is developed and shows its effectiveness. The suppression can be even enlarged by the optimizations in novel array. The comparisons between novel and conventional linear array are also provided.

Finally in Chapter 8, the conclusions of the research are carried out, and the future work is presented.

Chapter 2 Literature Review

2.1 Introduction

In this Chapter, the design of the transducers, especially in high frequency (HF) applications, is reviewed. The chapter begins with the review of transducer components, the piezoelectric, matching and backing layer. And the piezoelectric layer described as the heart of transducers is then detailed. Vibration modes of the piezoelectric layer are investigated and found to be dependent on the shape of piezoelectric element shape. The materials used as piezoelectric layer are then discussed and compared to each other.

Before starting the transducer design, it is essential to review the imaging principle, quality and techniques, since images are the final targets of a medical transducer. Several numerical models are then used to evaluate the performances of the transducer, including the responses of elements and the imaging patterns. Two of the classical models used to show the element responses, named as Mason and KLM model, are instructed. Both electrical and mechanical tuning can be designed by the two models. Here KLM model is further developed to a matrix model combined with several transmission lines representing every single layer. The matrix method is advanced due to its compatibility with computing techniques. In addition, SIR (spatial impulse response) method is the one to show the radiation pattern of a transducer numerically. The directivity can also be derived by SIR, which is a useful tool to predict the lobe positions in beam patterns.

Last but not least, current transducers for HF applications, mainly including single-element, linear and annular array, are introduced and compared. The two fields of fabrication and imaging of the transducers are reviewed. Single-element transducer shows fixed focus and is well investigated since its relatively easy fabrication process. Therefore, this thesis will only focus on array transducers including both linear and annular ones, which could achieve dynamic focusing but remain challenging to fabricate.

2.2 Transducer components

The transducer is a vital part in any ultrasonic imaging system for generating ultrasound and directing it into fluid (specifically the human body), and therefore it determines the quality of the ultrasound data. A cross-section of a typical single-element ultrasound transducer is displayed in Figure 2.1. The backing layer, piezoelectric layer and matching layers are the 3 main components. A lens is essential for single-element transducers, but optional for array ones. The insulator and the metal outer casing function as a grounding housing to reduce acoustic interference and physically protect the transducer.

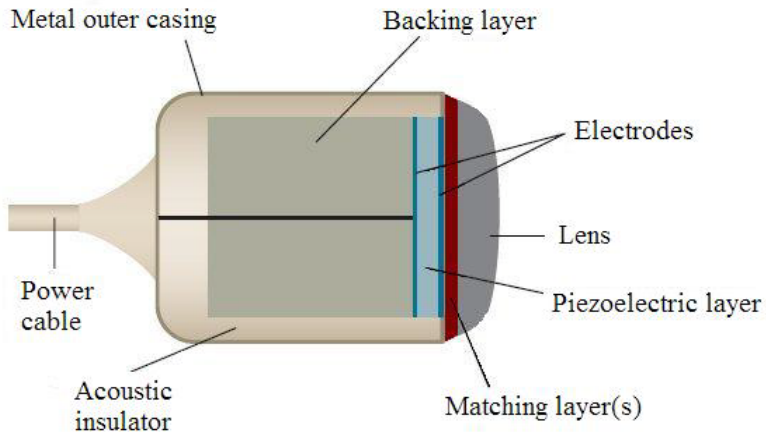

Figure 2.1 Cross section of a single-element transducer

2.2.1 Piezoelectric Layer

The piezoelectric layer is the active transducing element, which converts electrical energy to acoustical energy and vice versa. The most common piezoelectric materials used in current medical ultrasound transducers are ceramic such as lead zirconate titanate ($Pb(Zr,Ti)O_3$ or PZT, which possesses very strong piezoelectric effect [17]. A voltage pulse is applied on the front and back surface of the ceramic to excite a mechanical expansion resonance in its thickness direction. The generated pressure pulses are travelled into the tissue and bounced back by the imaging target. The echo is then received and converted to electrical signals by the ceramic again for measurement. Most of the ceramic layers resonate in thickness mode (T-mode), of which he resonant frequency f_0 can be evaluated by the following equation [4]:

$$f_0 = \frac{c}{2d} \tag{2.1}$$

where *c* is the sound speed for thickness mode in piezoelectric material, and *d* is the thickness of piezoelectric layer. For a given material, 50MHz array needs approximately 50μm thick ceramic layer. The higher the frequency is, the thinner the layer thickness required.

Besides the commonly-used ceramic, several other materials can also be the good candidates to form piezoelectric layer, such as piezoelectric polymer [18], single crystal (i.e. quartz) [19], piezoelectric composite [20]. Each of them shows different influences on the performances of the transducer by its characteristics, and will be detailed in Section 2.3.

2.2.2 Matching Layer

Ideally, the acoustic impedance of piezoelectric layer should be close to the one of tissue in order to allow the efficient transmission of the pulses to and from the tissue. However, the majority of piezoelectric materials such as the commonly-used ceramic, have very high acoustic impedances (>30MRayls). This is a large difference compared to tissue impedance (≈1.5MRayls). Most of the energy is reflected and lost at the interface between transducer and fluid.

Therefore, a ¼ wavelength thick matching layer is introduced to provide the acoustic matching between the ceramic and tissue, similar to the function of an anti-reflective coating used on optical lens. For a transducer with a single matching layer, its acoustic impedance follows the equation given below [4]:

$$Z_m = \sqrt{Z_0 Z_R} \tag{2.2}$$

where Z_m, Z_0, Z_R is the acoustical impedance of matching material, piezoelectric material and fluid (or tissue), respectively. The effect of matching layer is the full energy transmission at centre frequency ideally, and also an improvement in element bandwidth. Further improvement in bandwidth can be achieved by using multiple matching layers, of which the design rules could reference to the work done by T. Inoue [21]. Finding materials with impedances of the correct magnitude is difficult. Thus loading powders into epoxies are commonly used to form matching material, of which the acoustic impedance can be adjusted by the percentage of loaded powder to meet the design requirements of transducers [22].

2.2.3 Backing Layer

The energy generated in the transducer can radiate in both the forward direction and the reverse direction. The purpose of the matching layer is to encourage energy to be propagated in the forward direction with low loss. The backing layer is designed to attenuate any signal emanating from the back surface of the piezoelectric layer, as well as reduce ringing. Ringing is caused by energy resonating within the piezoelectric layer, and so it can be reduced by allowing that energy to be coupled out.

For the energy transmitted into the backing layer, an acoustically lossy material is always preferred to mount on the back of piezoelectric layer to damp out the energy [23]. If the attenuation of the material is sufficient large, no reflections from the back surface of backing layer can be found, otherwise it could cause some spurious signals in imaging.

To minimize the ringing, the acoustic impedance of backing layer can be matched to piezoelectric material. But as a result, half of the energy will be transferred into the backing layer and then lost. A very short pulse could be obtained, but with a very low amplitude. Thus compromise is always taken between sensitivity and bandwidth. Therefore, the acoustic impedance of backing layer is usually slightly lower than the one of piezoelectric layer in order to improve sensitivity at the cost of slightly increased pulse length or ringing. The epoxies loaded by fine powders such as tungsten are commonly used as backing materials [22]. The purpose of loading powder into epoxies is to change the acoustic impedance similarly to the technique used for matching layer design.

2.3 Heart of the Transducer – Piezoelectric Layer

Piezoelectric layer is regarded as the heart of ultrasonic transducer, since it's the only active part to generate ultrasound by electrical signals and turns the received echoes to electrical signals.

2.3.1 Piezoelectric Effect

Piezoelectric effect was first discovered by Jacques and Pierre Curie in 1880, which can be briefly explained as — when a stress is applied to the material, an electrical potential difference is applied across the material, called as direct piezoelectric effect; or conversely, the application of an

electrical filed across the material changes its physical dimensions, called as inverse piezoelectric effect. The nature of piezoelectric effect is related to the electric dipole moments in a unit cell of crystal, in other word, it cannot exist in a completely isotropic material [24]. For a crystal to exhibit piezoelectric effect such as quartz or tourmaline which has been used for ultrasonic transducer for many year [25], its structure should have no centre of symmetry. When a stress is applied on the surface of crystals, it will alter the separation between the positive and negative charge of its electric dipole, leading to the polarization [26]. This process is reciprocal, which means if the crystal is experienced an electric field, its length increase or decrease according to the electric dipole impacted by the electric field.

Besides the crystal, piezoelectric ceramics are another important group of piezoelectric materials. The general formula of these composite materials is $A^{2}+B^{1}+O_{3}^{2-}$, where *A* denotes a large divalent metal ion like barium or lead, and *B* represents a tetravalent metal ion like titanium or zirconium, and *O* is oxygen. For example, PZT has the molecular structure of $PbTiO_3$. Ceramic can be considered as a mass of minute crystallites, of which the structure changes by the temperature known as Curie point. When the temperature is above Curie point, the ceramic lattice exhibit a simply centre-symmetric structure without any positive or negative charges, as illustrated in Figure 2.2a. While then the temperature is below the Curie point, the centre of positive and negative charge no longer coincides. Hence, an electric dipole is formed in the lattice, as displayed in Figure 2.2b.

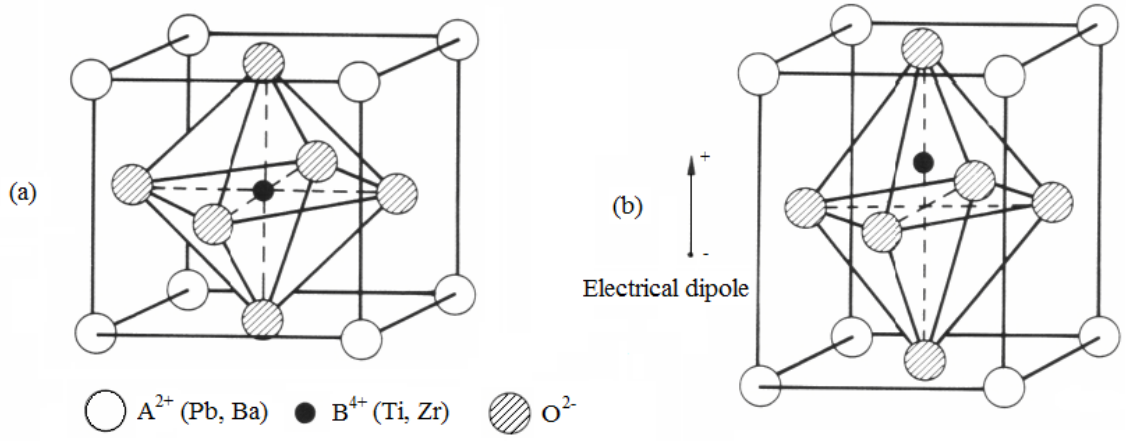

Figure 2.2 PZT elementary cell: (a) cubic lattice above Curie point and (b) tetragonal lattice below Curie point including an electrical dipole [27]

Each electrical dipole is a vector, the neighbouring dipoles tend to be aligned in a region called Weiss domain. Within the domain, all the dipoles are randomly oriented, giving a net dipole moment or a net polarization to the domain. The random distribution of Weiss domains throughout the material can be aligned in one direction by the process called poling. Under a strong poling electrical field applying into ceramic surfaces, domains most nearly aligned with the field will gradually grow at the expense of other domains. When the field is removed, the dipoles remain locked in an approximate poling direction. It gives the ceramic a residual polarization which means the material become anisotropic. Poling is an essential process during PZT manufacturing. Figure 2.3 illustrates the electric dipole movements by poling.

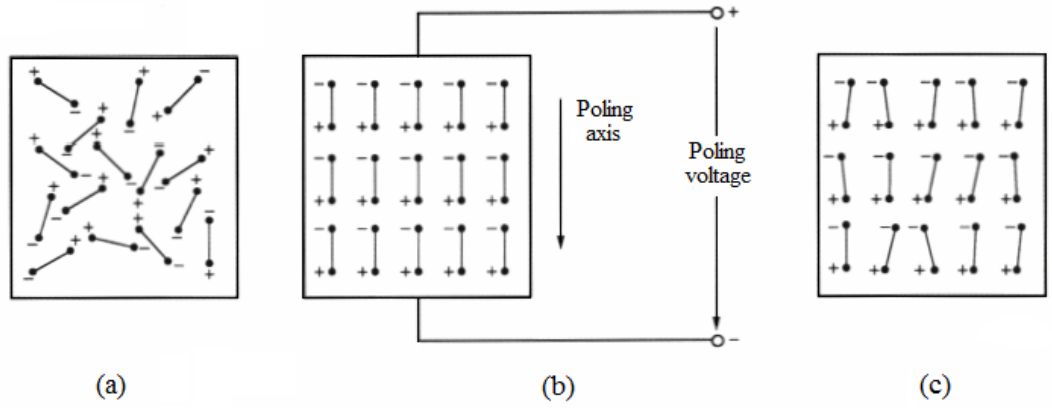

Figure 2.3 The movements of electrical dipoles in the Weiss domains (a) before poling (b) in poling and (c) after poling [27]

2.3.2 Piezoelectric Equations

A piezoelectric material can be characterised by its elastic, piezoelectric and dielectric properties. These constants are related to the strain *S*, stress *T*, dielectric displacement *D* and electric field *E*, which are caused by piezoelectric effect. Their relations are given in Table 2.1 [26], by showing the elastic and dielectric equations.

The subscripts *i*, *j*, *λ* and *μ* are the reduced tensor notations representing the direction of *T*, *S, D* and *E*, as instructed in Table 2.2. The material properties include *c*, *s*, *ε* and *β* for elastic compliance, stiffness, permittivity and impermittivity, respectively; while *e*, *h*, *d* and *g* are all piezoelectric constants. The superscripts in these constants represent the conditions of the measurements. For

example, s^E is the compliance at a constant *E*, and s^D is strain at a constant *D*. The relations among these material properties can be deduced by the piezoelectric equations and revealed in Table 2.3.

Table 2.1 Piezoelectric equations relating these parameters (i, j=1, 2, 3; λ, μ=1-6) [26]

Elastic Equations	Dielectric Equations
$\boldsymbol{T_\lambda = c^E_{\lambda\mu} S_\mu - e_{j\lambda} E_j}$	$D_i = e_{i\mu} S_\mu + \varepsilon^S_{ij} E_j$
$\boldsymbol{T_\lambda = c^D_{\lambda\mu} S_\mu - h_{j\lambda} D_j}$	$E_i = -h_{i\mu} S_\mu + \beta^S_{ij} D_j$
$\boldsymbol{S_\lambda = s^E_{\lambda\mu} S_\mu + d_{j\lambda} E_j}$	$D_i = d_{i\mu} T_\mu + \varepsilon^T_{ij} D_j$
$\boldsymbol{S_\lambda = s^D_{\lambda\mu} T_\mu + g_{j\lambda} D_j}$	$E_i = -g_{i\mu} T_\mu + \beta^S_{ij} D_j$

Table 2.2 Piezoelectric equations relating these parameters (*i*, *j*=1, 2, 3; *λ*, *μ*=1-6)

Reduced subscript	Expanded tensor	Elastic field	Dielectric field
1	xx	longitudinal *S* or *T* in X direction	*E* or *D* in X direction
2	yy	longitudinal *S* or *T* in Y direction	*E* or *D* in Y direction
3	zz	longitudinal *S* or *T* in Z direction	*E* or *D* in Z direction
4	yz, zy	shear *S* or *T* in YZ plane	
5	xz, zx	shear *S* or *T* in XZ plane	
6	xy, yx	shear *S* or *T* in XY plane	

Table 2.3 Relations among the piezoelectric material constants [26]

Relations among the material properties		For
$\boldsymbol{e_{j\lambda} = d_{j\tau} c^E_{\tau\lambda}}$	$d_{j\lambda} = e_{j\tau} s^E_{\tau\lambda}$	τ=1-6
$\boldsymbol{h_{j\lambda} = g_{j\tau} c^D_{\tau\lambda}}$	$g_{j\lambda} = h_{j\tau} s^D_{\tau\lambda}$	
$\boldsymbol{e_{j\lambda} = \varepsilon^S_{kj} h_{k\lambda}}$	$d_{j\lambda} = \varepsilon^T_{kj} g_{k\lambda}$	k=1, 2, 3
$\boldsymbol{h_{j\lambda} = \beta^S_{kj} e_{k\lambda}}$	$g_{j\lambda} = \beta^T_{kj} d_{k\lambda}$	
$\boldsymbol{c^D_{\lambda\mu} - c^E_{\lambda\mu} = h_{k\lambda} e_{k\mu}}$	$s^D_{\lambda\mu} - s^E_{\lambda\mu} = -g_{k\lambda} d_{k\mu}$	k=1, 2, 3
$\boldsymbol{\beta^S_{ij} - \beta^T_{ij} = h_{i\tau} g_{j\tau}}$	$\varepsilon^S_{ij} - \varepsilon^T_{ij} = -e_{i\tau} d_{j\tau}$	τ=1-6

The symmetry of the crystal cell is also taken into the expression of these constants. For example, the elastic compliance s_{12} refers to the strain along x-axis by an applied stress along y- axis, while s_{21} denotes the strain along y-axis to the stress applied along x-axis. Because of the cell symmetry, s_{12} equals to s_{21}. Besides that, most piezoelectric materials used in medical transducers show a high degree of crystallographic symmetry, the complexity of the material properties is largely reduced. For a PZT ceramic, the piezoelectric equations can be expressed in the matrix form with simplified piezoelectric constants, as given by Equation (2.3).

$$\begin{bmatrix} T_1 \\ T_2 \\ T_3 \\ T_4 \\ T_5 \\ T_6 \\ D_1 \\ D_2 \\ D_3 \end{bmatrix} = \begin{bmatrix} c_{11}^E & c_{12}^E & c_{13}^E & 0 & 0 & 0 & 0 & 0 & e_{31} \\ c_{12}^E & c_{11}^E & c_{13}^E & 0 & 0 & 0 & 0 & 0 & e_{31} \\ c_{13}^E & c_{33}^E & c_{33}^E & 0 & 0 & 0 & 0 & 0 & e_{33} \\ 0 & 0 & 0 & c_{44}^E & 0 & 0 & 0 & e_{15} & 0 \\ 0 & 0 & 0 & 0 & c_{44}^E & 0 & e_{15} & 0 & 0 \\ 0 & 0 & 0 & 0 & 0 & c_{66}^E & 0 & 0 & 0 \\ 0 & 0 & 0 & 0 & e_{15} & 0 & \varepsilon_{11}^S & 0 & 0 \\ 0 & 0 & 0 & e_{15} & 0 & 0 & 0 & \varepsilon_{11}^S & 0 \\ e_{31} & e_{31} & e_{33} & 0 & 0 & 0 & 0 & 0 & \varepsilon_{33}^S \end{bmatrix} \cdot \begin{bmatrix} S_1 \\ S_2 \\ S_3 \\ S_4 \\ S_5 \\ S_6 \\ E_1 \\ E_2 \\ E_3 \end{bmatrix} \quad (2.3)$$

Here the equation only shows the relation between [*T, D*] and [*S, E*], while other piezoelectric equations can be expressed in the similar matrix form as well. However, though the equation is largely simplified by many zero constants, it is still too hard to be solved. The further simplifications are required, and found to be dependent on the vibration modes of the piezoelectric layer.

2.3.3 Vibration Modes

A piezoelectric material could vibrate in various directions including lateral, longitudinal (or thickness) and shear ones. But only one vibration direction dominates in a specific geometry since others are so weak to be neglected, and it is described as a vibration mode. The piezoelectric element in a transducer is usually in rectangular shape of its cross-section with the width *w* and the height or thickness *d*. The ratio of *w* to *d* is called aspect ratio *G* and determines the vibration mode.

Selfridge et.al [28] and Onoe et.al [29] have developed the theory of vibration modes for a free resonator with the changes in aspect ratio *G*, as illustrated in Figure 2.4(a). Figure 2.4(b) then shows that the resonator is infinitely long in Y-axis and is applied by the electrical field in its thickness direction (or Z-axis), which is also the poling direction. Here the shear vibration is not counted, since it is always regarded as a very weak mode in medical transducers and thus neglected. Besides that, the vibrations in X and Y direction are identical due to the diagonal symmetry in the property matrix of ceramic in Equation (2.3). Thus the vibrations in X-Z plane (or elevation plane) could represent a single coupling vibrating system.

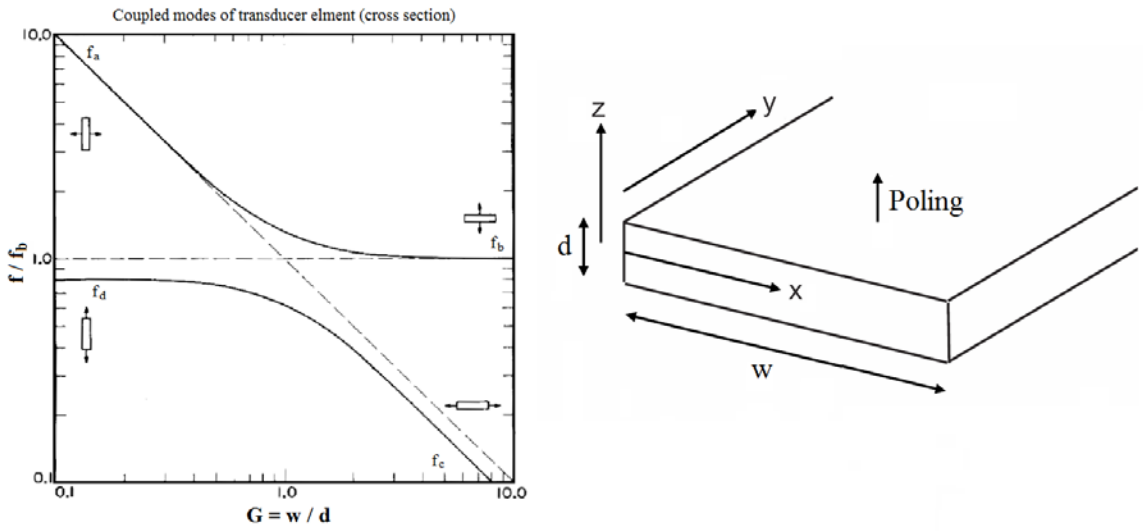

Figure 2.4 Vibration modes of a free piezoelectric resonator of which the cross section in XZ plane is displayed, symbol *f* denotes the frequency [28]

The elements in two types of transducer can be analyzed by Figure 2.4, since they are assumed to be infinitely long in Y-axis. The two transducers are 1-D linear array and single-element transducer, of which the vibration modes are instructed as follows.

2.3.3.1 Vibration Modes of 1-D Linear Array Transducer

For the elements in 1-D linear array, their length in Y direction is much larger than the width in X direction. The assumption of infinite Y-axis is valid and allows plane strain approximation [30]. It reduces the complicated vibrations to be the major two vibration modes in elevation plane, which depends on the aspect ratio *G*. When *G* is very small, the element becomes a narrow and long bar as displayed in the left parts of Figure 2.4(a). The longitudinal-extensional mode (LE-mode) and lateral mode (L-mode) are excited in a lower frequency f_d and a higher one f_a, respectively. To differentiate the LE mode in 2D array element, it is also called beam mode (B-mode). B-mode needs to be excited as the dominant resonance in 1-D linear array element, which generates and receives pressure waves in thickness direction. Thus L-mode needs to be suppressed. If the resonant frequencies of the two modes are too close to each other, B-mode would be largely impacted by L-mode and causes complicated vibrations. Equation (2.4) and (2.5) determine the resonant frequency f_a and f_d for the two modes.

$$f_a = \frac{1}{2w}\sqrt{\frac{c_{11}^D}{\rho}} \tag{2.4}$$

$$f_d = \frac{1}{2d}\sqrt{\frac{c'_{33}}{\rho}} \quad , \qquad c'_{33} = c_{33}^D - \frac{{c_{13}^D}^2}{c_{33}^D} \tag{2.5}$$

where ρ is the density of piezoelectric material. In general, the aspect ratio *G* is suggested to be smaller than 0.7 to separate the two resonant modes, so that they won't be coupled to each other. The precise design of *G* ratio can be obtained by the two equations above.

In addition, coupling factor *k* is introduced to measure the strength of the vibration modes in piezoelectric element. It is defined as the square root of the fraction of energy converted between mechanical and electrical forms for a given mode [31, 32]. The coupling factor of L-mode k_{31} and B-mode k_{33} are expressed as follows,

$$k_{31} = d_{31}/\sqrt{s_{11}^E \varepsilon_{33}^T} \tag{2.6}$$

$$k_{33} = d_{33}/\sqrt{s_{33}^E \varepsilon_{33}^T} \tag{2.7}$$

2.3.3.2 Vibration Modes of Single Element Transducer

The piezoelectric layer in a single-element transducer is a very large plate, in other word, the length and width of the element is much larger than its thickness. It can be represented by the right part of Figure 2.4(a), where *G* is very large. The resonant frequency f_b and f_c refers to the vibrations of thickness mode (T-mode) and L-mode (different from the L-mode in 1D linear array element), respectively. Likewise, T mode is the dominant resonance vibrating in Z direction, and L-mode needs to be suppressed. But the consideration of the aspect ratio is still essential to avoid unwanted lateral mode. In general, *G* is suggested to be larger than 3 to avoid to the coupling by L-mode. The precise design of *G* can be referenced to the two following equations,

$$f_b = \frac{1}{2d}\sqrt{\frac{c_{33}^D}{\rho}} \tag{2.8}$$

$$f_c = \frac{1}{2w}\sqrt{\frac{c'_{11}}{\rho}} \quad , \qquad c'_{11} = c_{11}^D - \frac{{c_{13}^D}^2}{c_{33}^D} \tag{2.9}$$

It should be noticed even though the piezoelectric layer is very thin and already eliminates the L-mode, another mode called thickness shear (TS) is coupled into T-mode and causes complex

vibrations in the free resonator. However, it is found that TS mode becomes quite weak when the piezoelectric layer is loaded (for example water) [32], and the T-mode is still dominant. Similarly, the coupling factors k_t for T-mode and k_p are expressed by Equation (2.10) and (2.11), where σ is Poisson ratio of the material.

$$k_p = k_{31} \cdot \sqrt{2/(1-\sigma)}\ , \qquad \sigma = -s_{12}^E / s_{11}^E \tag{2.10}$$

$$k_t = e_{33} / \sqrt{c_{33}^D \varepsilon_{33}^S} \tag{2.11}$$

2.3.3.3 Vibration Modes of 2-D Linear Array Transducer

The vibration modes of 2-D linear array element are not given by Figure 2.4(a), since its length *L* in Y-axis is very small (*L*<<*d*), instead of infinite long. It leads to another approximation named "plain stress" to the calculate the vibration modes [30]. Like the 1D linear array and single element transducer, the electrical field is applied to its thickness direction, the same as its poling direction. If G ratio is relatively small for this pillar-shaped element, only the longitudinal-extensional (LE) mode is excited in thickness direction at a its resonant frequency f_{LE} [33]. The suggested value of G is generally smaller than 0.7. Equation (2.12) then shows the expression of f_{LE} [32], while the coupling factor k_{33} for 1D linear array can be used to reflect the energy transform efficiency of LE mode.

$$f_{LE} = \frac{1}{2d}\sqrt{\frac{1}{\rho s_{33}^D}} \tag{2.12}$$

2.3.3.4 Vibration Modes of Annular Array Transducer

For an annular element with relatively large *G* (*G*>3 generally), T-mode again becomes the dominant resonance. The L-mode, now described as radial mode (R-mode) in annular geometry, still exists but operates in much lower frequency. The element behaves more like the vibration in single-element transducer. While for *G* with relatively small value (*G*<0.7), the array element shows a dominant B-mode and behaves like a 1D linear array element. Therefore, the resonant frequencies and coupling factors of the T-mode and B-mode are the same as the ones of single-element and 1D linear array transducers. Since the ratio *G* of each element in annular array is

different due to its equal area geometry, it is always essential to avoid complicated coupled vibrations by setting the *G* value larger than 3 for every annulus.

Besides that, the R modes, especially the high-order ones are found to be coupled into T mode for a free resonator regardless of their ratio *G*, but become very weak when the element is loaded. It is similar to the influence of TS mode in rectangular element. The details of R-mode for a thin annulus have been presented by Iula et.al [34]. Many efforts had been put to reveal the coupled vibrations of the free annular resonator by both R mode and T-modes [35-38]. This is because the shear vibration is important, however, it is ignored in the previous analysis [35-38]. We have demonstrated the importance of including shear waves in the analysis in our paper [39], although the detail is not reported in this thesis. Please refer to Appendix C for detail.

2.3.4 Waves produced by transducer element

Although the excited vibration modes are different in the single-element, linear array and annular array transducers, they are all targeting the generation of longitudinal waves that propagate through the fluid medium. These longitudinal waves are dominant in the transducer and travel in the propagation direction to form the radiation pattern. However, the actual elements are not ideal piston-like sources and there are also some other waves alongside the dominant longitudinal waves.

One such wave is shear wave, which has motion perpendicular to the propagation direction. When shear waves propagate on a transducer surface, one motion is polarized to the surface normal and described as shear vertical or SV wave, while another motion is within the surface plane and called shear horizontal or SH wave. SH waves are not very significant in the transducer, since this component cannot cause propagation into the fluid medium [4]. However SV waves do travel transversely along the transducer surface and thus can cause propagation in the fluid. These waves could be generated at the edge of an excited transducer element, since the dominant longitudinal vibration causes a shear stress, due to the Poisson effect. The shear motions then travel along the transducer layers and also transmit energy to nearby elements if there are any.

In addition to shear waves, another group is known as the surface waves. Surface waves have both the longitudinal and transverse wave component travelling along the layered transducer structure. Rayleigh and Lamb waves are usually regarded as the two main types of surface waves in a transducer, both of which shows the longitudinal and transverse wave components. The Rayleigh wave is a special case of the Lamb wave solution when the plate becomes thick compared with a wavelength. However, because the research here is not targeted at the analysis of these surface waves, the detail discussion of these surface waves are not provided, while it is also very hard to clearly explain the formation behind these surface wave components, because they could be very complicated especially in the layered transducer structure.

Nevertheless, all the waves travelling along the transducer surface are described as "surface wave" in the following thesis. It could have the components of shear wave, Rayleigh wave and Lamb wave, etc. Since only the dominant longitudinal waves are needed when the element waves propagate into the fluid medium, the surface waves travelling transversely are thus regarded as unwanted waves and probably lead to the degradation of transducer radiation.

2.3.5 Piezoelectric materials

Table 2.4 Comparisons of common piezoelectric materials

Types of Piezo-material	Ceramic	Composite	Single Crystal	Polymer
Representative Material	PZT-5H	1-3 composite (50% PZT-5A)	PMN-33%PT	PVDF
k_t	0.51	0.68	0.58	0.13
k_{33}	0.75	0.70	0.94	-
Z_0 **(MRayls)**	34	17	34	3.9
$\varepsilon_{33}^S/\varepsilon_0$	1470	430	680-800	6.5
Flexibility	poor	good	poor	excellent
Reference	[31]	[40]	[41]	[42]

The performances of the transducer are strongly related to the piezoelectric materials. For example, the strength of the electro-mechanical vibrations is dependent on the coupling factors, k_t for T mode and k_{33} for B or LE mode. The acoustic impedance Z_0 reflects the efficiency of energy transferred outwards from the piezoelectric layer, and thus determines the matching and backing layers. Relative permittivity $\varepsilon_{33}^S/\varepsilon_0$ is useful in the design of electrical driving or receiving circuit of the transducer. Flexibility is important for a pre-focused array; a lens can be formed by curving the

surface of a transducer if the piezo-material is flexible. In general, 4 types of materials are used as piezoelectric layer, including ceramic, composite, single-crystal and polymer. All of them are compared in Table 2.4.

2.3.5.1 Piezoelectric ceramics

Polycrystalline ceramics (usually called ceramics) are the majority of piezoelectric materials used in ultrasonic transducer, due to their advantages in high relatively high coupling factors, permittivity and fabrication feasibility. Here, a commonly-used PZT-5H is taken as an example. Its relatively high T-mode and LE-mode coupling factors lead to a high sensitive, while large permittivity could make the transducer resistance around 50Ω to reach the maximum transmission of electrical power, since it agrees with the internal resistance of any outside circuits in the imaging system.

However, the large mismatch in acoustic impedances between ceramic and fluid load is its major disadvantage. Though the quarter-wavelength matching layer could provide an almost 100% energy transmission from ceramic to fluid at resonant frequency, the transmission would be reduced when the element vibrates away from resonance. The decrease in energy bandwidth could be expected. In addition, the poor mechanical flexibility of the ceramic also increases the difficulties to realize a geometrically pre-focused transducer [43].

More recently, the ceramic, fine-grained PT ($PbTiO_3$) has been developed for HF transducers [44]. PT material has comparable T-mode coupling factors as PZT ceramics (i.e. PZT-5H), but a much lower L-mode coupling factor. Therefore, PT material would always show a very weak L-mode vibration, regardless of the element shape or aspect ratio *G*. However, the difference to PZT ceramic is the relatively low permittivity of 200 approximately. It could increase the complexity in the outside circuits of imaging system.

2.3.5.2 Piezoelectric composites

Piezoelectric composites have attracted many interests in the applications for HF ultrasound transducers over the past decades [45, 46]. 1-3 and 2-2 connectivity composites are usually used and illustrated in Figure 2.5 [47, 48]. 1-3 composite is actually the shape of 2D linear array with

ceramic and polymer pillars or rods, while 2-2 composite is the shape of 1D linear array with long and narrow bars of ceramic and polymer.

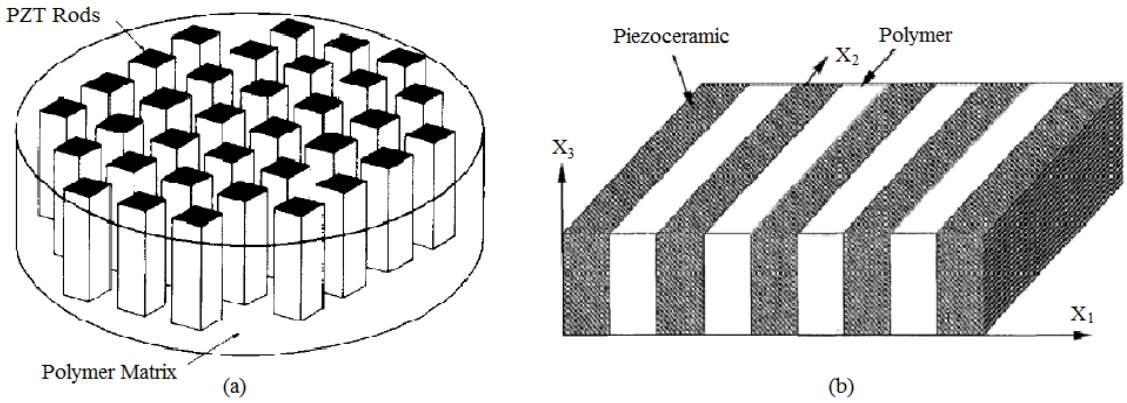

Figure 2.5 Diagrams of (a) 1-3 and (b) 2-2 connectivity composite [47, 48]

The properties of piezo-composites are almost the same as the ones of ceramics, but with lower acoustic impedances. The mismatch to the fluid load is reduced. Though matching layer is still required, the energy transmission is largely improved when the element vibrates off-resonance. As a result, the energy bandwidth will be increased. The injection of polymer into PZT ceramic not only reduces the acoustic impedance of entire structure, but also improves the mechanical flexibility. Besides that, by changing the volume fraction of ceramic in composite, material properties can be modified or optimized for a specific transducer [48, 49]. However, though a large amount of polymer injected could further reduce the acoustic impedance, it also leads to low coupling factors. Trade-off needs be taken between acoustic impedance and coupling factors. Besides that, the relatively low permittivity caused by the injection of polymer in piezo-composite also leads to a slightly complicated outside circuits of the imaging system.

2.3.5.3 Single Crystals and Piezoelectric Polymer

For several decades, polycrystalline ceramics based on the solution of PZT are widely used as the piezoelectric layer for medical transducers, while the single crystal ceramics (or simply called single crystals as quartz) were rarely used due to of their low coupling factors. But it was changed recently by the development of PZN-PT or PMN-PT [41, 50-52]. The two families of PZN-PT and PMN-PT shows high coupling factors, especially the almost 100% k_{33} value, which means a 100% electro-mechanical energy transfer when the element is excited in LE-mode. Besides that, single

crystals also show advantages in HF applications over ceramics in the view of fabrication. The growth of single crystal causes much less deteriorations in material properties than the formation of ceramic layer by screen printing for example, due to the less porosity. Thus single crystals in transducers could show comparable properties to the bulk values [52].

In addition, lead free single crystals such as $LiNbO_3$ are another significant group, with comparable piezoelectric properties to PZN-PT or PMN-PT but much lower permittivity (≈28 for $LiNbO_3$). The elimination of toxic lead components in piezoelectric material gave them a promising future.

In terms of piezoelectric polymer, polyvinylidene fluoride (PVDF) and copolymers of vinylindene fluoride and trifluoroethylene (P(VDF-TrFE)) are the major two polymers used as piezoelectric layer. Good reviews of these materials can be found in the references of [53-55]. The main advantage of piezo-polymers is the very low acoustic impedance, which is even very close to the one of fluid or tissue. No matching layer is actually required, since the very broadband usually above 100% has already been achieved, as well as the large energy transmission from the piezoelectric layer to the fluid load. Besides that, piezo-polymers also show excellent mechanical flexibility so that it can be formed in various shape and easily curved to form pre-focused transducers.

However, the low coupling factors in piezoelectric polymers limits their applications. The lack of energy transferred from electrics to mechanics leads to a much lower sensitivity compared than other piezo-materials. And the very low permittivity of piezo-polymers is also another drawback for fine-scaled HF transducers due to the large mismatch in transducer resistor and the internal resistor of outsides circuit in an imaging system.

2.4 Transducer Imaging

2.4.1 Imaging Principle

The imaging principle of ultrasonic transducers optical imaging systems (i.e. camera), with the detail can be found in the reference of [56]. Ultrasonic transducers are based on the pulse-echo system, the electronic signal applied to the transducer is turned into pressure pulse by piezoelectric effect, and then the pulse is emitted to the fluid (or tissue). The echoes would return

to the transducer surface when the emitted pulse is bounced back by a target in the fluid. The echoes are then transferred into electronic signals to determine the position and brightness of the target. In other word, the transducer not only plays a role as transmitter, but also receiver. The overall 2-way roundtrip imaging is the multiplication of transmitter and receiver, as shown in Figure 2.6.

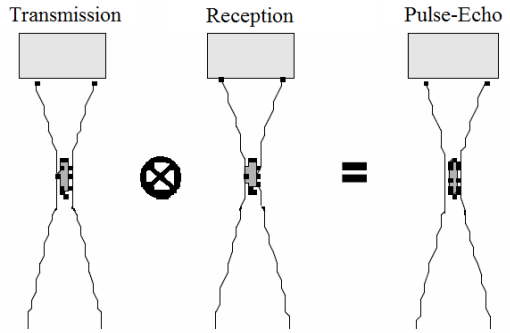

Figure 2.6 Pulse-echo response to form the ultrasonic imaging [57]

A lens is always mounted on the top surface of the single-element transducer to guide the emitted pulses to focus at required focal point that is determined by the curvature of lens, since focused beam could resolve a fine target in the beam focal zone. Figure 2.7 illustrates a focused beam by a transducer, where focal distance is defined as the distance from focal point to transducer top surface. Every beam in a certain position represents a single scan line, the imaging targets on or near the scan line can be resolved and displayed. By moving the scan line across the whole imaging plane, a 2D imaging pattern can be obtained.

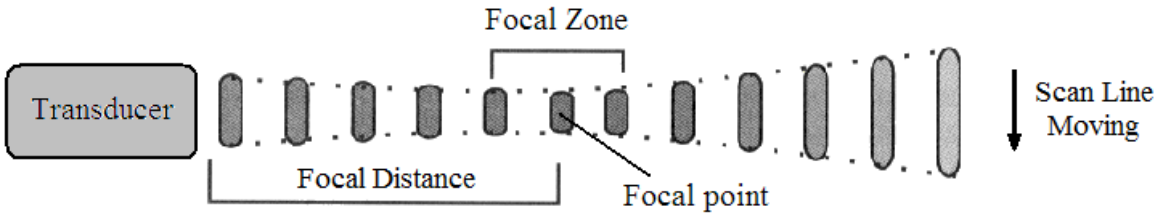

Figure 2.7 A focused beam generated by an ultrasonic transducer

The usage of lens and the movement of scan lines are actually applicable for single-element transducers. For the lens mounted in the transducer, sometime it can be replaced a pre-focused transducer by curving the transducer surface. Nevertheless, either the lens or pre-focused transducer leads to a fixed focal point during focusing. It means only the imaging targets in the focal zone can be well-resolved. Besides that, another major disadvantage is the relatively long

time to obtain a 2D imaging patterns due to the relatively slow scanning motions by mechanical motors. Thus array transducers are more often used to solve the two drawbacks.

For array transducers including 1D linear array, 2D linear array and annular array, lens is not necessary. The focused beam can be formed by applying an electronic signal with a certain amount of time delay or phase shift to each element in the array. By well-designed time delay, the wavefronts of the pressure pulses by every element could form a virtual electronic lens, as illustrated in Figure 2.8(a). The process is also described as electronic beamforming. By changing the time delay, the focal point can be adjusted. Thus the transducer could resolve the targets in various depths. Meanwhile, the beam can be also steered away from the central axis of the array, as displayed in Figure 2.8(b). The mechanical motion for scan is not required. By using electronic signals to adjust focal point and scanning motion, the speed to obtain the imaging pattern would be dramatically improved. In addition, the rules of time delay or phase shift have been well-instructed in the reference of [4, 17].

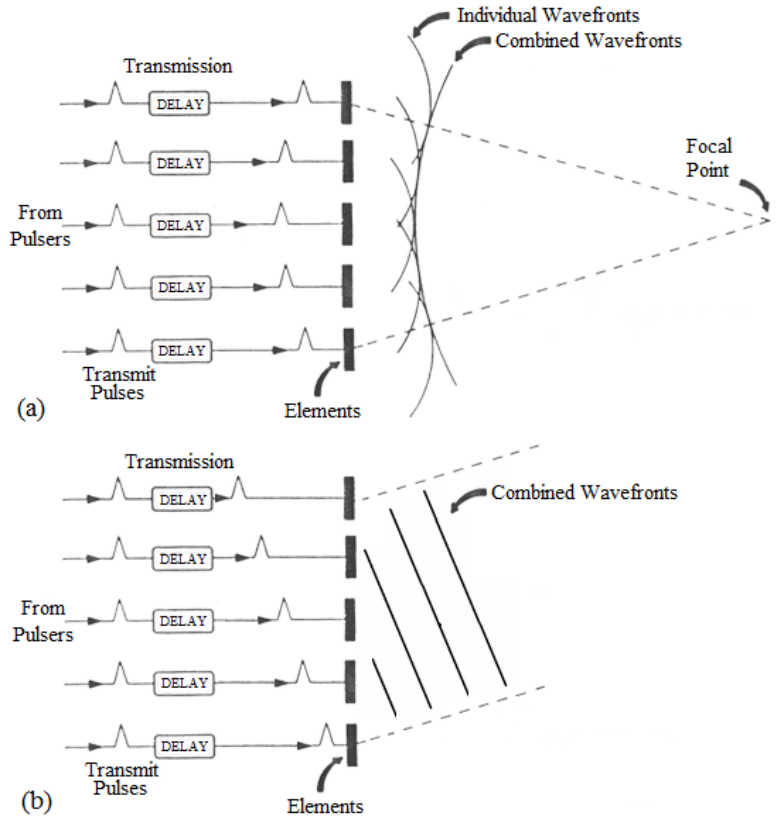

Figure 2.8 Diagram of a typical (a) electrical beamforming and (b) beam steering

However, the imaging techniques described above are based on analogue signals, while recently digital imaging techniques are more widely used in transducer imaging. To briefly describe it here, after the echoes are received by the elements, these analogue signals are firstly amplified and then digitized, for example, they pass through analogue-to-digital converters (ADC). An ADC converts the echo voltages from analogue to a digital form of discrete numbers, which represent the echo amplitude in time domain. The future manipulation of these digitized echoes is accomplished as digital signal process to realize the delay and summation of these signals during receiving process, or a mathematical manipulation of numbers repressing echoes [58]. Finally, the image processor converts the digitized signal into images. The data are then stored in image memory for the instrument display. The digital imaging technique has advantages over the analogue one, since it provides many ways to deal with the imaging data. For example, the spatial compounding technique [59], real-time 3D imaging [60, 61] could be quickly realized by using digital imaging techniques.

2.4.2 Imaging Properties

The quality of the image pattern can be measured the axial resolution, lateral resolution, depth of field (DOF), contrast resolution, side lobe and frame rate [62-64]. All of these imaging parameters are briefly reviewed as follows.

2.4.2.1 Axial and Lateral resolution

Axial and lateral resolution shows the ability of the beam generated by transducer to resolve the small structures axially and laterally, both of which is known as detail resolution and commonly taken as the -6dB beamwidth of the peak value. In terms of axial resolution, it can be also described as the closest distance that two objects are able to be reflected separately along axial direction (scan line). The value of axial resolution R_a is expressed below [58],

$$R_a = \frac{1}{2}cT = \frac{1}{2}\frac{c}{BW} \tag{2.13}$$

where c is sound speed of fluid, T is the -6dB pulse width of the signal received by the transducer (or equivalently the pulse width of the transmitted signal at focal point), and BW denotes the -6dB bandwidth of the pulse in frequency domain. Equation (2.13) indicates that finer axial resolution requires the shorter pulse, or equivalently wider band pulse. The way to improve bandwidth of

pulse is to apply more matching layer or raise the acoustic impedance of backing layer as the cost of sensitivity. There is always a trade-off between sensitivity and axial resolution.

Likewise, lateral resolution describes the closest distance that two object can be reflected separately in the lateral direction (across scan line). The lateral resolution can be obtained from a transmitting-receiving radiation pattern of transducer aperture derived via diffraction theory partly illustrated in [4]. Figure 2.9 illustrates the lateral resolution in the 2-way radiation pattern plotted by the peak amplitude of received signal as a function of the position of the point target in focal plane as A-mode transducer, some of other imaging properties are also given in the figure which will be explained later. In addition, the 1-way transmitted or received radiation pattern has the same responses as 2-way round-trip pattern due to the reciprocity of pulse-echo propagation, but with half amplitude.

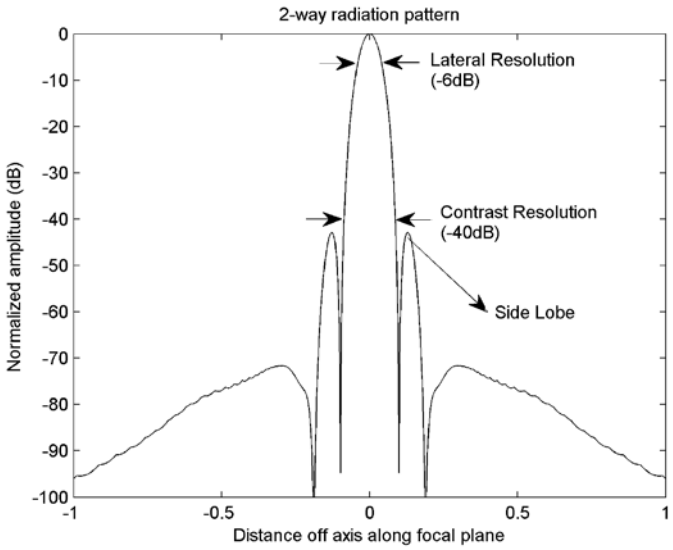

Figure 2.9 2-way radiation pattern of a focused transducer

The value of lateral resolution R_L is defined as -6dB beamwidth of the pattern, and expressed by the following equation,

$$R_L = \lambda \frac{F}{D} = \lambda \cdot f\text{-}number \tag{2.14}$$

where λ is the wavelength of ultrasound wave in fluid, F is the focal length defined as the distance from aperture surface to the focal point, D is aperture length or diameter, and *f-number* is defined as the ratio of focal distance F to aperture length D. The improvement of lateral resolution could

be realized either by increasing operating frequency as the result of a short wavelength, or the strong focusing as the result of small f-number.

2.4.2.2 Contrast Resolution and Side Lobe

The contrast resolution, or simply called contrast, is a measurement of the ability to resolve objects with different reflection coefficients, and is primarily determined by the extent of the beam in the side lobe region. For this reason, contrast is usually measured as the -40dB beamwidth of a 2-way pattern [62]. And sidelobe is defined as the addition lobes in the beam pattern expect the main lobe. Both contrast and side lobes are illustrated in Figure 2.9.
In pulse-echo imaging system, the possibility of distinguishing different tissue is related to the reflection coefficients of tissues, which varies from the level of -20dB to -50dB. If the main lobe is clear of any side lobes down to -50dB, almost all the tissues can be differentiated clearly. Therefore, it is essential to suppress the level of side lobes at least below -40dB, while usually a level of -50 to -60dB is suggested. Otherwise, high side lobe becomes the source of artefacts in the imaging [58].

2.4.2.3 Depth of Field

DOF is another measure of the imaging quality of focusing, and equivalently represents the focal zone illustrated in Figure 2.7. The definition of DOF is the difference between distances where the lateral -6dB beamwidth has doubled over its minimum value as illustrate by Figure 2.10.

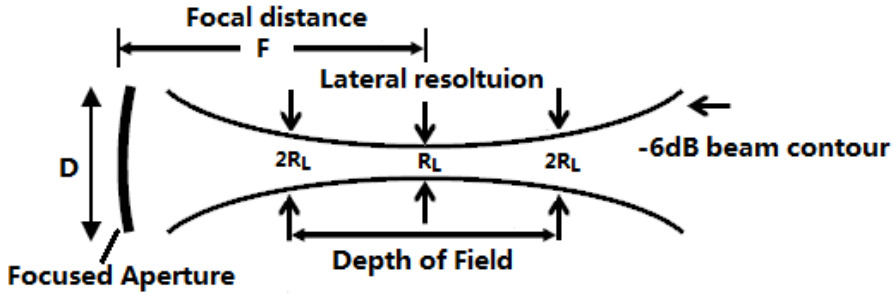

Figure 2.10 Schematic diagram of radiation pattern by a focused transducer

Here *D* represents the length or diameter of the aperture, *F* is the focal distance and R_L denote the lateral resolution. The -6dB beam contour indicates that the beam levels along the two lines are -

6dB off from the peak amplitude (or amplitude at focal point). The value of DOF is approximately given by the equation below [65],

$$DOF \approx 7.1\lambda \cdot (f\text{-}number)^2 \quad (2.15)$$

The images obtained out of DOF region become unclear, and thus a large DOF is essential to provide the imaging patterns in a wide range. By Equation (2.15), DOF depends on the wavelength and f-number. Recall Equation (2.14) of lateral resolution, DOF is proportional to the lateral resolution if f-number is fixed. It means the increase of resolution would cause the reduction in DOF. Trade off or other focusing techniques are required between the two parameters.

2.4.2.4 Frame rate

Frame rate is described as the number of images that can be generated by a transducer per second. In detail, one pulse-echo trip is to form a single scan line. To avoid the misplacement of returning echoes, the second scan line can only be emitted until the transducer receives the previous scan line. By repeating this process for many times, the image in required focal zone is obtained. The frequency of this image is frame rate.

High frame rate is highly demanding in the real time ultrasound imaging to obtain quick and accurate images and more importantly to avoid artefacts by motions of vivo tissues. Real-time imaging is described as a frontier for ultrasound [64]. A single element transducer at frequencies between 50 to 80MHz shows a frame rate lower than 40 frames/s, which is inadequate in real-time applications such as small animal imaging, while a linear array using electronic beam-forming could achieve the required frame rate as high as 400 frames/s. Nevertheless, the relatively low frame rate by a single-element transducer is still large enough for most clinical applications in HF range.

2.4.3 Focusing Techniques

2.4.3.1 Apodization

Apodization is to lower the sidelobes on either side of the main beam by scaling the signals across the aperture. The pressure amplitude along the aperture needs to have rounded edges that taper

toward zero at the end of aperture. However, apodization also leads to an effectively smaller aperture and thus deteriorate the lateral resolution. Trade-offs needs to be considered between lateral resolution and side lobe level.

Many methods can be used to realize apodization, all of which are based on the amplitude weighting of the normal pressure across the aperture. In single element transducer, apodization is realized by tapering the electric field along the aperture, or attenuating the beam on the face of aperture, or changing the physical geometry. In array transducers, it is simply accomplished by applying different voltage amplitude on each element.

2.4.3.2 Dynamic Focusing

For a transducer focused at a certain focal distance, lateral resolution achieves its smallest value at focal point but tends to degrades and become relatively large out of the DOF range. In high frequency transducer, for example, a typical 40MHz single-element transducer with *f*-number of 2 shows a relatively narrow DOF of 1mm approximately. The fixed focal point means that only the targets in this narrow DOF can be resolved, which causes the imaging limitation in HF range. Passmann et.al [66] in 1996 developed a method of B/D scan to improve DOF for a single-element transducer, where B represents the conventional B-mode scan while D denotes the depth scan. Figure 2.11 illustrates the principle of B/D scan, and compares to B-scan.

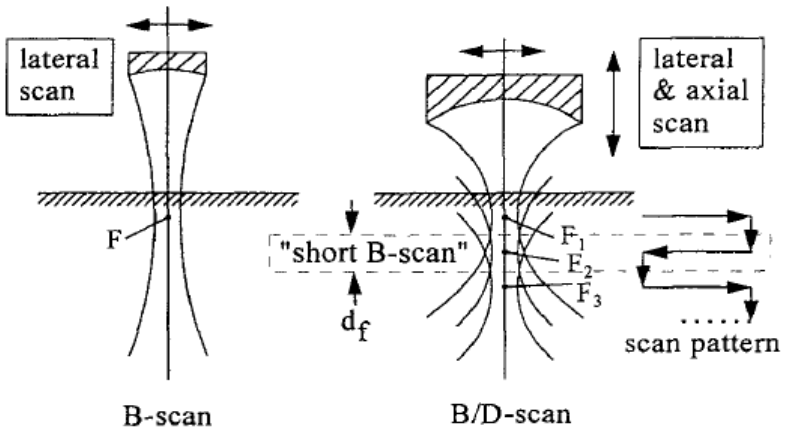

Figure 2.11 Comparison between B-scan and B/D scan for single-element transducers [66]

In the transmission process of B/D scan system, if the imaging region of interest is not moving too fast, the scan depth can be divided into smaller range close to the focal zones of multiple transmit foci. The multiple transmit range are then spliced together to form an overall image, with showing much larger DOF than the single transmit foci by conventional B-scan.

For array transducers, B/D scan becomes a similar method called “dynamic focusing” in the receiving process, of which the principle is illustrated by Figure 2.12 [57]. The scan depth is also divided into many focal zones, and every zone is assigned a receive focal distance, which can be adjusted by the suitable changes in the time delay applied the receiver element. Finally, the individual receive images are spliced together with a separate transmit focus to realize a relatively large DOF. However, both B/D scan and dynamic focusing cause the reduction in frame rate. Since every focal zone requires a frame, the two approaches reduce frame rate by 1/*N*, where *N* is the number of focal zone.

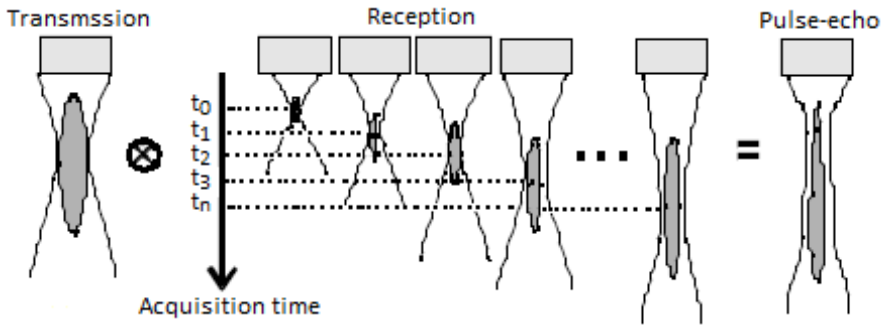

Figure 2.12 Dynamic focusing in reception for array transducers [57]

2.4.3.3 Dynamic Aperture

Dynamic aperture is a technique to further improve the dynamic focusing and only available in array transducers. The multi-focal zones are generated by dynamic focusing, and each of them has different resolution and DOF. The resolution is finest for the focal zone closest to aperture due to the decrease in *f*-number. However, for some imaging applications, the image at low f-number is not recommended due the image distortion by phase aberration [67]. Therefore, it is necessary to have a constant resolution or *f*-number for the focal zones close to aperture. To keep constant f-number, the aperture size needs to be continuously changed by activating or deactivating the

array elements. This process is described as dynamic aperture. A typical *f*-number of 2 is always chosen for constant resolutions.

2.5 Design of Transducers by Numerical Models

The characteristics of transducer can be well described by a 1-D model, or namely a 1-D equivalent circuit model representing one dominant vibration mode. Under different assumptions dependent on the transducer geometry, each vibration mode can be expressed as a 1-D equivalent circuit connecting the field of electricity and mechanism to offer a good understanding of transducer behaviour and an approach for design. The analytical solutions of the wave equations can be obtained by putting the material parameters into the model. To implement a model for a particular structure, the same equivalent circuit can be applied, but with the appropriate constants for the geometry selected.

2.5.1 Classic 1-D models

To connect acoustic and electrical parameters by using the acoustical-electrical analogue, Mason in 1964 derived several models for piezoelectric resonator corresponding to various 1-D vibration modes [32], which is named as Mason model. A further step based on Mason model was made by Kirmholtz, Leedom and Matthaei in 1970 by using transmission lines [68]. This "KLM" model is named after the initials of the authors, shows exactly same solutions to Mason model in various vibration modes but with several advantages for design [69].

As the most applicable for medical transducer such as the single-element and annular array transducer is the T-mode vibration, only 1-D KLM models for T-mode are briefly introduced here. First of all, a piezoelectric transducer can be treated as a three port-network system as displayed in Figure 2.13. The electrical port represents the electrical connection between driving/receiving circuits and transducer. The black box represents the piezoelectric resonator here. And the front and back acoustic port denote the front and rear surface of the piezoelectric resonator, respectively. The backing and matching layer or fluid load can be connected to both acoustic ports mechanically by using the acoustical-electrical analogue into the equivalent circuit. If the acoustic ports are short-circuited, the network represents a free resonator. The 1-D KLM model is

illustrated in Figure 2.14 for T-mode based on the 3-port network. The constants in the model are given in Table 2.5. In addition, either Mason or KLM model of B and LE mode excited in 1-D linear and 2-D array respectively can be found in the literatures [32, 68] for particular design purposes.

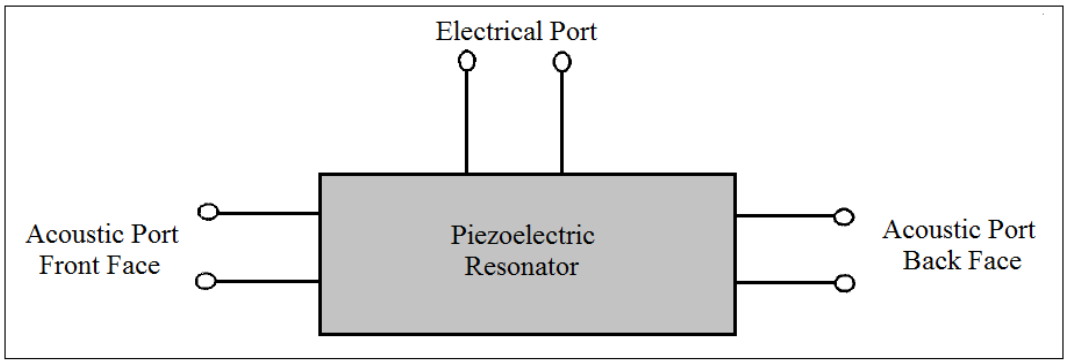

Figure 2.13 Three port network to analogise a piezoelectric transducer [17]

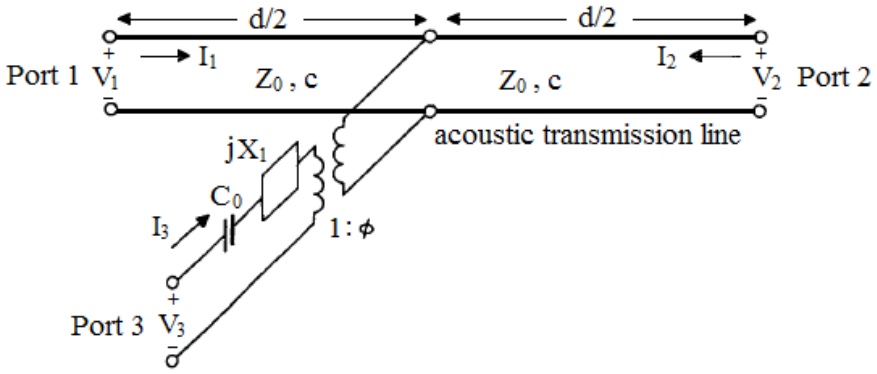

Figure 2.14 1-D KLM model for T-mode, Port 1 & 2 for acoustic outputs, and Port 3 for the inputs of electrical signals [68]

Table 2.5 Parameters in 1-D KLM model of TE mode

Model parameters	Description
$C_0 = \varepsilon_{33}^S \varepsilon_0 S/d$	C_0 – Clamped capacitance, S – surface area
$X_1 = \frac{kt^2 sinc(f/f_0)}{\omega C_0}$	Circuit reactance: f – frequency; ω – angular frequency; f_0 – TE resonant frequency, $f_0 = c/2d$
Z_0 & c	Parameters of transmission line: Z_0 – character impedance; $Z_0 = \rho \cdot c$ c – sound velocity, $c = \sqrt{c_{33}^d/\rho}$ in TE mode

$\varphi = \frac{(2f_0C_0Z_0)^{1/2}}{k_t sinc(f/2f_0)}$	Ratio of electro-mechanical transformer

In Figure 2.14, an artificial acoustic centre is created by splitting the piezoelectric resonator into halves in thickness direction; each part with a thickness of *d/2* is represented by an acoustic transmission line. This partitioning allows the analysis of the two acoustic ports separately to improve transducer design as one of main advantages in KLM model. In the following figure, V_3, I_3 relates to the input voltage and current respectively; V_{12} and I_{12} is for the forces and velocity as acoustic outputs. Port 1 for acoustic back surface will be used to represent forward transmission into fluid or body, while Port 2 for acoustic front surface is for acoustic backing. The optimization of transducer bandwidth, sensitivity can be processed by cascading various loads into the 1-D model. The spectrum of outputs in frequency domain at acoustic ports can be obtained, and pulse responses are calculated using an inverse Fourier transform from the spectrum.

The entire KLM model can be collapsed into a single transfer matrix (or ABCD matrix) between the electrical port (Port 3) and the front acoustic port (Port 2). The overall representation of a transducer including backing, matching layer and the fluid load can be described as a series of simple ABCD matrices cascaded together [70-72], as the matrices show the advances in numerical computation, for example, a computing software known as Matlab. Figure 2.15 illustrates the ABCD matrix derived from 1-D KLM model, where V_S and Z_S in the electrical port denote the applied voltage and inner resistor of voltage, respectively; and Z_R at the front acoustic port is the acoustic impedance of fluid medium. The KLM model using ABCD matrix is used in this research for the transducer design.

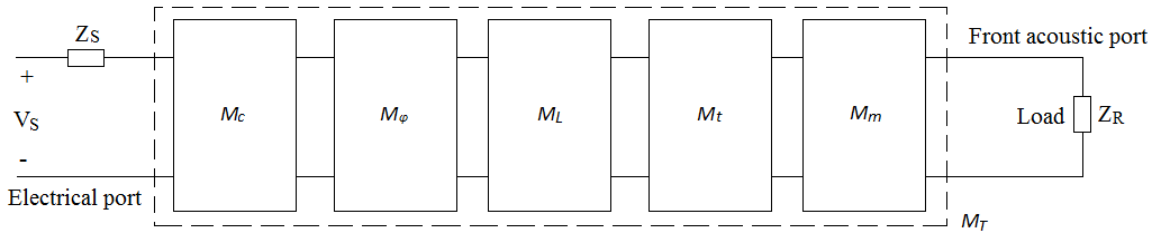

Figure 2.15 ABCD matrices derived from KLM model representing the overall transducer

Matrix M_C refers to the serial reactance in the electrical branch of KLM model. Matrix M_φ is to describe the electro-mechanical transformer. Backing layer can be treated as a resistive load of which the value equals to the acoustic impedance of the material. Thus by using transmission line theory, the whole left branch from the artificial centre in acoustic part of KLM mode can be represented by Matrix M_L. And M_t denotes the right half-thickness transmission line of ceramic element. M_m is for the matching layer(s) if it is mounted in transducer. All the 5 matrices are cascaded and represented by an entire matrix M_T displayed in dashed line, a single ABCD matrix. The parameters of these matrices are listed in Table 2.6.

Table 2.6 Parameters of transfer matrices derived from KLM model

Matrix	Definition	Parameters in matrices
$\boldsymbol{M_C}$	$\begin{vmatrix} 1 & \frac{1}{j\omega C_0} + jX_1 \\ 0 & 1 \end{vmatrix}$	Given in Table 2.4
$\boldsymbol{M_\varphi}$	$\begin{vmatrix} 1/\varphi & 0 \\ 0 & \varphi \end{vmatrix}$	Given in Table 2.4
$\boldsymbol{M_t}$	$\begin{vmatrix} A_t & B_t \\ C_t & D_t \end{vmatrix}$	$A_t = cosh(jkd/2)\,;\ B_t = Z_0\, sinh(jkd/2);$ $C_t = \frac{sinh(jkd/2)}{Z_0}; D_t = cosh(jkd/2);$ k – wave number of ceramic
$\boldsymbol{M_L}$	$\begin{vmatrix} 1 & 0 \\ 1/Z_L & 1 \end{vmatrix}$	$Z_L = (A_t Z_B + B_t)/(C_t Z_B + D_t);$ Z_B – characteristic impedance of backing layer
$\boldsymbol{M_m}$	$\begin{vmatrix} A_m & B_m \\ C_m & D_m \end{vmatrix}$	$A_m = cosh((\alpha + jk_m)d_m);\ B_m = Z_m\, sinh((\alpha + jk_m)d_m)$ $C_m = \frac{sinh((\alpha+jk_m)d_m)}{Z_m}\ ;\ D_m = cosh((\alpha + jk_m)d_m)$ d_m – thickness of matching layer α – attenuation factor of matching layer k_m – wave number of matching material Z_m – characteristic impedance of matching material
$\boldsymbol{M_T}$	$\begin{vmatrix} A & B \\ C & D \end{vmatrix}$	$M_T = M_C \cdot M_\varphi \cdot M_L \cdot M_t \cdot M_m;$

2.5.2 Loss factors involved in 1-D model

In the original 1-D model, the loss factors of practical materials are not involved. To obtain a high accuracy method to evaluate the performance transducer, the complex material constants was

introduced into the model as representatives of loss factors. Losses in piezoelectric ceramics are phenomenological considered to have three coupled mechanisms: dielectric loss (δ_e), elastic loss (δ_m) and piezoelectric loss (γ) [73]. The complex piezoelectric constants with these loss factors can be expressed as [73, 74],

$$s_{ij}^{E*} = s_{ij}^{E}(1 - j\delta_m), \qquad \varepsilon_{ij}^{*} = \varepsilon_{ij}(1 - j\delta_e), \qquad d_{ij}^{*} = d_{ij}(1 - j\gamma) \tag{2.16}$$

where the superscript * denotes the complex parameters. The piezoelectric loss γ is often neglected to simplify the 1-D model. Though there are some arguments of the impact of this loss [74], it is generally accepted that the accurate results by the model without consideration of γ still shows good agreements to experiment results [75, 76]. Key parameters with complex values of TE mode are summarized here [77],

$$\varepsilon_{ij}^{S*} = \varepsilon_{ij}^{S}(1 - j\delta_e) \tag{2.17}$$

$$c_{33}^{D*} = c_{33}^{D}(1 + j\delta) \tag{2.18}$$

$$k_t^{*2} = \frac{k_t^2}{(1+j\delta)(1-j\delta_e)}, \qquad \delta = (1 - k_t^2)\delta_m + k_t^2\delta_e \tag{2.19}$$

where δ is the total loss factor. The equations above are derived under the approximation of $[\delta e, \delta m]^2 << 1$, which is the case of most piezoelectric ceramics. Other vibration mode may have different expressions of parameter expressions, similar process can be used to derive these values to get an accurate 1-D model. In addition, the loss in the matching layer also plays an important role on the sensitivity and bandwidth of transducer. And the attenuation coefficient α is used to describe the loss factor of the material (usually epoxies).

2.5.3 Sensitivity and Bandwidth

Some criteria are required to design a transducer. High sensitivity and broad bandwidth are the two main targets for an excellent transducer performance, but cannot be achieved at the same time. For a round-trip pulse echo configuration, a transducer has two different role of transmitter and received respectively, as displayed in Figure 2.16 by using 1D KLM model.

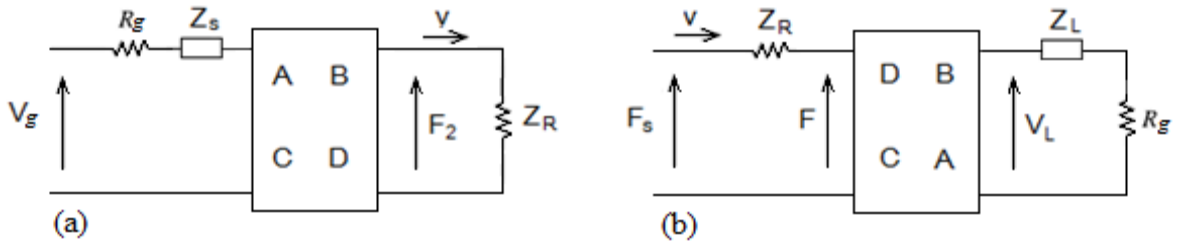

Figure 2.16 Round-trip 1D model, (a) refers to transmitter and (b) for receiver [78]

In Figure 2.16, R_g and Z_s are the inner resistance of voltage source and impedance in driving circuit respectively, while Z_L is the impedance of the receiving circuit impedance Z_L. Symbols "*F*" and "*v*" denote the forces and velocity in acoustic ports. Besides that, if the transmitter has an ABCD matrix to connect the electrical and acoustic port of the transducer, the receiver will have a DCBA matrix due to the reciprocal structure.

Insertion Loss (IL) is then introduced as a measure of round-trip energy efficiency to show the relationship between sensitivity and bandwidth, and defined as the ratio of power delivered from a source into the load with network (namely ABCD matrix) inserted, to the power delivered with network removed [78]. When the condition of $Z_s = Z_L$ is fulfilled, the 1-way transmitter and receiver network becomes reciprocal. Thus IL can be expressed as (in dB unit),

$$IL = 20log\left(\frac{4Re(Z_R)(R_S+R_g)}{\left|AZ_R+B+(Z_S+R_g)(CZ_R+D)\right|^2}\right) \tag{2.20}$$

Since the reciprocal transmission and reception, 1-way transducer loss (TL) equalling to half value of IL is also used in transducer design. The peak value of IL (or TL) implies the transducer sensitivity, while the -6dB frequency width of IL spectrum down from its peak value (or -3dB width of TL) refers to bandwidth.

2.5.4 Electrical and Mechanical Tuning

The 1-way transmission network is usually used in the transducer design. For highest transducer sensitivity, TL needs to be minimized or equivalently the TL peak needs to be maximized. By using the KLM model with transfer matrices, TL could be divided into electrical loss (EL) and acoustic loss (AL) referring to the electrical energy and acoustic energy efficiency, respectively. The relations among three losses are given as: TL = EL + AL in dB unit.

2.5.4.1 Electrical tuning

EL is defined as the ratio of the power reaching the transducer to the maximum power available from the source. To maximize the EL peak, the electrical tuning is applied and displayed in Figure 2.17.

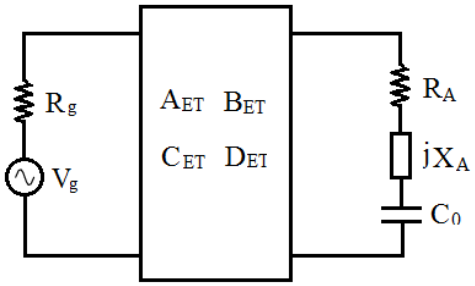

Figure 2.17 The network of electrical tuning in a transducer

In Figure 2.17, V_g and R_g refer to the voltage source and its inner resistance, respectively. The transducer with fluid load is described a series of resistor R_A, reactance X_A, and clamped capacitance C_0 [4]. And the electric tuning network is represented by a transfer matrix "ET" with the parameters of A_{ET}, B_{ET}, C_{ET} and D_{ET}, respectively.

Snook et.al used coaxial cable and transformer for electric tuning [42], while a simple way to apply electrical tuning is realized by adding a series resistor R_s and inductor L_s. Therefore, the electric tuning matrix becomes a simple series impedance Z_s ($Z_s = R_s + j\omega L_s$), and EL can be expressed as,

$$EL = \frac{4R_A R_g}{\left(R_A+R_g+R_s\right)^2+\left(X_A-\frac{1}{\omega C_0}+\omega L_s\right)^2} \tag{2.21}$$

At resonance, the reactance X_A becomes 0, and clamped capacitance is tuned out by inductor $L_s = 1/\omega_0^2 C_0$. If R_s is negligibly small and $R_A = R_g$, maximum electrical power will be transferred into the load RA or transducer. Therefore, EL achieves maximum (→100%) at resonant frequency f_0, which means there is no electrical energy loss during transmission. For a standard circuit of a voltage source, the inner resistance R_g equals to 50Ω [55]. The resistance of loaded transducer in resonance is required to be close to 50Ω, of which the value is given as,

$$R_A(f_0) = R_{A0} = \frac{2k_t^2}{\pi f_0 C_0}\left(\frac{Z_0}{Zllay+Zrlay}\right) \tag{2.22}$$

where Z_{llay} is the input impedance looking from the left face of piezoelectric ceramic, while Z_{rlay} is the one looking from the right face. Z_{llay} often equals to the backing acoustic impedance Z_B if no other layers between backing and ceramic. And Z_{rlay} involves the influence of matching layer which relates to the improvement of acoustic loss AL by mechanical tuning, which is instructed in the next section.

However, R_A shows relatively large variance with different transducers according to Equation (2.22), and is not always close to the standard 50 Ω of R_g. In this research, instead of the tuning in R_A, R_g is tuned to match R_A by simply inserting an ideal transformer between voltage source (V_s and R_g) and tuning matrix "ET" for the convenience of transducer design. As a result, R_g becomes adjustable and has an equivalent tuning effect as R_A tuning.

2.5.4.2 Mechanical tuning

AL is defined as the ratio of the acoustic power reaching the front fluid load, to the total acoustic power converted [4]. If there is no absorption loss along the acoustic path to the front, AL at resonance can be simply expressed as,

$$AL(f_0) = \frac{Z_{rlay}}{Z_{rlay}+Z_{llay}} \tag{2.23}$$

As explained above, Z_{llay} often equals to Z_B as explained above. Thus for an air-backing transducer ($Z_B=0$), AL=1 at resonance. The physical meaning is that all the energy is bounced back at the interface of piezoelectric and backing layer. Although air-backing provides the largest acoustic energy transform, it also shows the narrowest bandwidth or the longest ringing at the front acoustic port (the interface between piezoelectric layer and fluid). Backing layer with higher acoustic impedance could improve the bandwidth, but also largely increase AL. For example, a backing layer with acoustic impedance about 30MRayls only shows the AL value of 5%. Thus quarter-wavelength matching layer(s) is introduced to improve AL. The acoustic impedance Z_m of single matching layer is the root of the multiplication of Z_R and Z_0, as expressed by Equation (2.2).

By using matching layer(s), Z_{rlay} in Equation (2.23) becomes the value of ceramic acoustic impedance Z_0 at resonance. For a backing layer with Z_B of 30MRayls, AL reaches the peak value about 50%. Decreasing the value of Z_B could increase the AL peak, but leads to the reduction in

bandwidth. The suitable choice of backing layer is required to achieve compromise low acoustic loss and broad band. Single matching layer is always used due to the relatively easy fabrication, while applying more matching layers could further enlarge the bandwidth [21]. This process is also known as mechanical tuning.

2.5.5 Model of Transducer Imaging

The imaging is the ultimate target for a medical transducer, and can be evaluated by a numerical model called SIR (Spatial Impulse Response). The model is based on Rayleigh integral by assuming an idealized transducer vibrating in a piston-mode. First of all, Figure 2.18 illustrates the diagram to obtain the pressure at point *P* in the imaging by using Rayleigh integral, where *S* the radiating source located in XY plane; r_0 and r are the distance from original point to the source *S* and the point *P*, respectively.

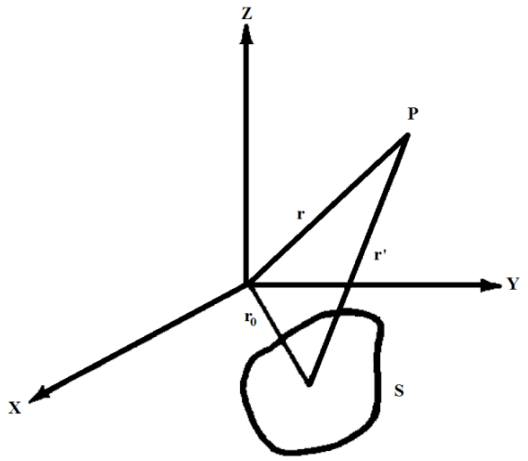

Figure 2.18 Radiating source with arbitrary shape for Rayleigh integral [79]

The Rayleigh integral is then applied to derive the diffraction in the imaging region, thus the velocity potential $\varphi(r,t)$ at point *P* in time domain can be obtained [79],

$$\varphi(r,t) = \int_S \frac{v_n(t-(r-r_0)/c_0)\cdot v_n(r_0)}{2\pi(r-r_0)}\,dS \tag{2.24}$$

where c_0 denotes sound speed of fluid medium, $v_n(r_0)$ is the velocity across the radiating source or aperture, and *dS* here refers to the very small area element of the radiating source *S*. If all of the points at the surface of the source show an identical amplitude and phase, namely an ideal piston, its velocity v_n becomes a parameter only dependent on time *t*. Thus the velocity potential $\varphi(r,t)$ at point *P* can be transferred to,

$$\varphi(r,t) = v_n(t) * h(r,t) \tag{2.25}$$

$$h(r,t) = \int_S \frac{\delta(t-r'/c_0)}{2\pi r'} dS \tag{2.26}$$

where * represents convolution, *r'* is the distance from point *P* to the source as shown in Figure 2.18, and *h(r,t)* is so-called impulse response of the source, or SIR. Thus the radiating source can be treated as a transducer, and the pressure *p(r,t)* at point *P* can be expressed as the convolution of two functions, *pulse(t)* and *h(r,t)*,

$$p(r,t) = \rho \frac{\partial \varphi(r,t)}{\partial t} = \rho \frac{\partial v_n(t)}{\partial t} * h(r,t) = pulse(t) * h(r,t) \tag{2.27}$$

The function *pulse(t)* refers to the pressure pulses generated by a transducer, and defined as a Gaussian-modulated sinusoid signals with different bandwidth to match the anticipated experimental pulses. The radiation pattern is then generated by the maximum amplitude of the pulse envelop for every point in the imaging region. But notice that the pattern by Equation (2.27) is only the transmitter pattern, because pulses are sending from transducer surface to point *P*.

When a transducer is receiving echoes, it has the same response as sending pulses but just reciprocal. Thus the final 2-way radiation pattern is calculated by multiplying the1-way transmitter pattern twice. In a more general case, the receiver pattern could be different from transmitter pattern by using a focusing technique such as dynamic focusing. Therefore, the overall pattern is expressed in Equation (2.28). Likewise, the 2-way pulse responses of every point in imaging region in time domain becomes the convolution of the transmitter and receiver responses, as expressed by Equation (2.29) [80],

$$P_{2-way}(r) = P_t(r) \cdot P_r(r) \tag{2.28}$$

$$p_{2-way}(r,t) = p_t(r,t) * p_r(r,t) \tag{2.29}$$

where $P_{2\text{-}way}$, P_t and P_r is the beam pattern of a 2-way transducer, its transmitter and receiver, respectively; $p_{2\text{-}way}$, p_t and p_r are the pressure pulse in time domain for 2-way response, transmitter and receiver, respectively.

For array transducer, every element is a radiating source but with different phase. Then the impulse response at point *P* becomes the sum of the impulse response of every individual element, as expressed by Equation (2.30),

$$h_a(r,t) = \sum_{n=1}^{N} h_n(r, t - \Delta t_n) \tag{2.30}$$

where $h_a(r, t)$ is the overall impulse response of array, N denote the total number of elements, subscript n represents the n^{th} element, and Δt_n is the time delay applied to each element. If point F is designed to be the focal point of an array, the rule of time delay for each element is given by,

$$\Delta t_n = \frac{r - \sqrt{(x_r - x_n)^2 + z_r^2}}{c} + t_0 \tag{2.31}$$

where (x_r, y_r, z_r) the coordinate position of focal point F, x_n is location of the element centre in X-axis, and t_0 is a constant time value to avoid unphysical negative time delay. In this case, the individual impulse response can be aligned to overlap completely. By using the impulse response of an array given in Equation (2.30), its pressure responses in imaging region can be obtained by Equation (2.27).

2.5.6 Directivity

Directivity is the angular response for a transducer transmitting a continuous wave (CW) in the far field [81, 82], while it is also the impulse response of a transducer. The SIR function $h(r,t)$ in time domain can be transferred $H(r,f)$ in frequency domain by using inverse Fourier transform (IFT). $H(r,f)$ is also called system function. By using the replacement of $f=c/\lambda$, $H(r,f)$ is transferred to $H(r,\lambda)$, which reflects the directivity for a transducer operating at a certain frequency.
For a small rectangular element illustrated in Figure 2.19, where P is a point in imaging region, r denotes the distance between point P and original point, ϑ and φ is azimuth and elevation angle, respectively; while Lx and Ly refers to the length in X-axis and Y-axis, respectively.

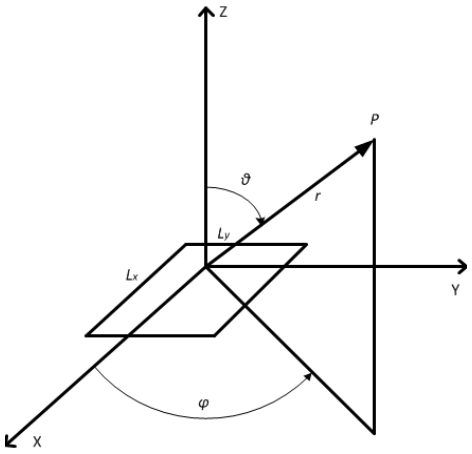

Figure 2.19 Geometry of a rectangular element

If the element vibrates uniformly as an ideal piston, the element system function $H_e(r,\lambda)$ is the production of the system functions of the two line sources, or equivalently $H_e = H_x H_y$ [83]. Equation (2.32) then shows the expression of H_x, which is actually the Fourier transform of its aperture function of the line in X-axis,

$$H_x(\theta,\lambda) = h_{0x} L_x \cdot sinc\left(\frac{L_x \cdot sin\theta}{\lambda}\right), \qquad h_{0x} = \sqrt{c_0/2\pi r} \tag{2.32}$$

where $sinc(x)=sin(\pi x)/\pi x$, r here is treated as a certain constant. The function of H_y has the same expression just by replacing L_x to L_y, and ϑ to φ.

Likewise, for a circular/annular element, the beam pattern in far field is expressed as the following equation, which implies a Hankel transform of the aperture function, where J_0 is the zero order of Bessel function,

$$H(\theta,\lambda) = h_{0x} \int_0^{\infty} A(r_0) J_0\left(\frac{2\pi sin\theta}{\lambda} r_0\right) r_0 dr_0 \tag{2.33}$$

For linear array either in 1-D or 2-D geometry, the directivity can be obtained by a series of line sources, as displayed in Figure 2.20. The function of H_x can be express by Equation (2.34) when the beam is steered at an angel ϑ_s away from the axis.

$$H_x(\theta,\lambda) = \sum_m h_{0x} L_x p w sinc\left(\frac{w sin\theta}{\lambda}\right) \cdot sinc\left[\frac{L_x}{\lambda}\left(sin\theta - \frac{m\lambda}{p} - sin\theta_s\right)\right] \tag{2.34}$$

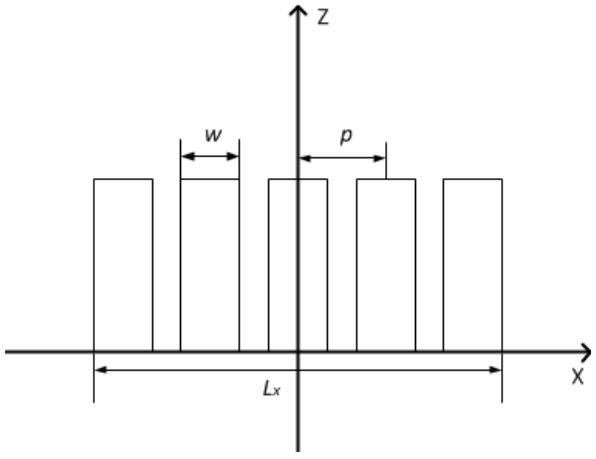

Figure 2.20 The cross section of a 1-D or 2-D linear array

where w is the element width and p for the element space, m is an integral number and is described as lobe order. The first *sinc* term in Equation (2.34) is called the element factor. In the

angle domain, the small size of array element translates into a broad directivity. And the second "*sinc"* term determines the angular position of so-called grating lobe. The relatively large size of array aperture refers to a much narrow directivity. The main lobe (*m*=0) thus appears when $\vartheta = \vartheta_s$, while the periodicity of second *sinc* term is defined as position of grating lobe with its amplitude modulated by the element factor. The angular position ϑ_g of grating lobe is given by Equation (2.35), where *m* is an integer and $m \neq 0$.

$$\theta_g = \pm \arcsin\left(m\lambda/p + sin\theta_s\right) \tag{2.35}$$

The first grating lobes, or *m*= ±1, is the most significant ones due to their highest amplitude among the levels of all grating lobes. When the array beam is not steered (ϑ_s= 0), as in the case of rectangular scan, no grating lobe would appear if the element pitch $p = 1\lambda$. However, when the array is steered, for example ϑ_s= -45^o in the sector scan, the first grating lobe will appear at ϑ_g=17^o. This is not appropriate for the linear arrays that demand angular beam sweeping, thus element pitch *p* must be smaller than $\lambda/2$ to eliminate the grating lobes. In summary, the value of p is usually set to be 1-λ for linear arrays without beam steering and $\lambda/2$ for the ones with steering.

However, it is very hard to derive an expression of directivity for an annular array transducer because of the calculation difficulties in Hankel transform, which involves complicated Bessel function. Nevertheless, the system function $H(r, \lambda)$ can still be obtained by using the numerical SIR method. The sidelobe far away from the focal axis in annular arrays is described as a pedestal lobe showing not too much change in lobe level in a certain region along focal plane. To reveal the relation between pedestal lobe and array aperture, Brown et.al [84] made a great effort by establishing a so-called EPD (element path difference) theory. EPD is found to be generally proportional to the level of pedestal lobe, and defined as the path difference between the pulse travelling from the element inner edge and the pulse travelling from element outer edge to the focal point. By using Fresnel approximation always valid in the annular array with the elements showing the same area, the expression of EPD is simplified and given by Equation (2.36).

$$EPD = D^2/8FN \tag{2.36}$$

where *D* is the diameter of the array aperture, *F* is the focal distance, and *N* denotes the total element number of the array. The equations relating EPD and pedestal level is detailed in the paper published by Brown et.al [84]. Though these equations are based on experimental results

and could be changed by using different material, they certainly provide general evaluations of pedestal lobe level.

2.6 Transducers Fabrication and Comparisons

Fabrication is a significant factor, since the designed transducer must be compatible to the current fabrication techniques in our research, which aims to improve the transducer without increasing the fabrication difficulties. Therefore, it is essential to review the fabrications of HF transducers by current techniques, including the transducer of single element, linear array and annular array.

2.6.1 Single-element Transducer

In high frequency (>30MHz) ultrasonic imaging system, almost all commercially available transducers are based on the single element structure, since its relatively easy fabrication. Single-element transducer basically consist of three single layers, ceramic, backing and matching layer. For the transducer operating in HF range, the thickness of its ceramic layer is generally smaller than 50μm, which is the thickness for a 30MHz transducer approximately. Thus several thick-film fabrication techniques [85-87] can be used to form the layer, for example, screen printing is a commonly-used technique. After the film is sintered, poling is the next step to make the layer piezoelectric. However, by using thick-film technique such as screen printing, the deposited film shows some deterioration in its properties [87]. Using the fine-grained ceramic with grain size less than 1μm could reduce the deterioration and make the film properties close to the bulk values, but at the cost of increasing fabrication difficulties [88]. Therefore, sometime the piezoelectric layer is simply formed by lapping the relatively thick bulk material of several hundreds of microns to several tens of microns, the thickness required by HF transducer. No significant deterioration in material properties would be found. In addition, if thick-film techniques are used, doping some specific ions into the ceramic grain could change the ceramic properties, and optimizes its application in medical transducers [31, 89, 90].

For the formations of passive layers including electrodes, matching and backing layer, electrodes at the top and bottom surface of the ceramic layer can be fabricated by various techniques such as sputtering, evaporation, etc. The thickness of electrode (<1μm) is usually much smaller than other

layers its influence on transducer performances could be neglected. Backing layer made by epoxy is relatively thick (several hundreds of microns), it can be formed by a simply filling process. However, matching layer made by epoxy as well is slightly more complicated since its thickness is usually tens of microns and sensitivity to energy transmission between ceramic and fluid. Spin-coating is the common-technique to form the layer and shows good accuracy in controlling film thickness [88]. Sometime the matching film is also deposited by thick-film techniques, and then lapped down to have a relatively accurate thickness.

Besides that, to form an image, single-element transducers need to be focused by either mounting a lens or curving transducer surface or [42, 63, 88]. The curved surface is actually an equivalent lens, but the fabrication requires a flexible piezoelectric layer such as PVDF. For ceramic transducer, lens is usually used and fabricated apart from the transducer, and then glued to the front surface of transducer. The details of fabrication are well reviewed by Li et.al [91]. However, the minimization of the bonding layer that glues lens and transducer, and the accuracy of the lens curvature are the two main difficulties in fabrication, especially in the fine structure of HF transducer.

Though there are some difficulties in fabricating single-element transducers, the fabrication is still regarded as a relatively easy one since no micro-machining is required, which is essential for HF array transducers. However, single-element transducer only could get the best image only in a very narrow region of DOF due to its fixed focal point. B/D scan is a solution but leads a low frame rate because slow mechanical motions are required in both axial and lateral direction. The drawback of frame rate can be overcome by array transducers, which is also the main target that this research has put effort on.

2.6.2 Linear array

Linear arrays can be divided into 1D and 2D array, while both of them show the same cross-section as displayed in Figure 2.21. Lens is an optional and usually not mounted since the array can steer the focused beam electronically. The fabrication of linear array in HF applications is almost same as the single element, but with an extra dicing and filling technique to form the kerfs (or grooves) between the two adjacent elements.

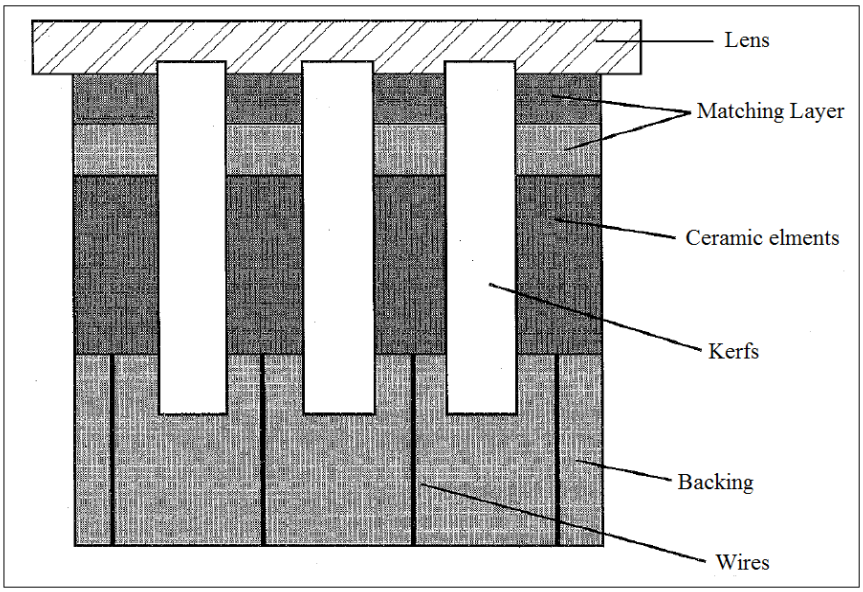

Figure 2.21 Cross section of a typical linear array [17]

When all the layers are formed by the same fabrications processes of single-element transducer, the array transducer is diced to make kerfs, and the kerfs are then backfilled with a polymer to support the whole structure. However, the fabrication difficulties are dependent on the requirement of the width of ceramic and polymer element. 1D array has the same structure as 2-2 composite, while 2D one is related to 1-3 composite. The guidelines of kerfs width w_k and ceramic width w_c applied to 2-2 composite is expressed as follows [92],

$$w_k \leq c_s/(4f_c) \;\; ; \qquad w_c \leq c_l/(4f_c) \tag{2.37}$$

where c_s is the shear velocity of polymer or kerfs material, f_c is the central frequency of transducer, and c_l refers to the longitudinal velocity of B-mode in the ceramic. For a 1D linear array operating at 30MHz, the ceramic width is about 25μm. But the required kerfs width is of 15μm approximately, which is already very challenging for current dicing technique. With higher central frequency, the required kerfs width will be reduced and beyond the capability of current dicing technique.

For 1-3 composite or 2D linear array, Reynold et.al [93] has revealed its spurious lateral modes. And the resonances of these modes are suggested be at least twice larger than the central frequency of transducer. Impedance spectrum obtained either by experiment or simulation is method to check the existence of these unwanted modes. Michau et.al [20] reported a 30MHz 1-3

composite configuration showing a ceramic volume fraction of 51% and a dicing width less than 12μm. Likewise, kerfs width will become unachievable for current dicing technique by the increase of frequency.

Besides that, the requirement of pitch width (1λ for 1D array, and $\lambda/2$ for 2D array) to avoid the grating lobe also leads to the fabrication challenges. For a 30MHz array, the pitch width for 1D array is 50μm and only 25μm for 2D one. Considering the ceramic volume fraction of 50% (a too low value is not recommended due to lack of active area in transducer), the kerfs width becomes 25μm and 12.5μm. Again the current dicing technique will eventually fail to cut the kerfs by the increasing frequency.

Thus only a few researches have successfully fabricated HF linear array, and most of them operate at the frequencies in a relatively low region from 30 to 40MHz [92, 94, 95]. Kerfless linear array [96, 97] operating in very high frequency (even beyond 100MHz) are currently attracting research interests, since no dicing process is required and the element pitch can be made by patterned electrodes using lithography techniques which could achieve very fine spatial resolution. However, strong cross talking among non-diced elements is the main concern [98]. Another alternative to conventional linear array based on piezoelectricity is called CMUT, namely capacitive micro-machined ultrasonic transducer, and without using dicing technique. Many efforts have been made with good imaging outcomes achieved in HF applications [99, 100], but since CMUT is not piezoelectric-based, it is not discussed in this thesis.

2.6.3 Annular array

Annular array is another group of array transducers to solve the very small element pitches of linear arrays in HF applications. Annular array usually consists of several concentric elements with same area. The formation of the layers including ceramic, matching and backing layers are all the same to the previous two groups of transducers, while the separation of the annular elements is also realized by dicing and filling technique. However, 1λ or $\lambda/2$ requirement of pitch width is no longer significant, since no grating lobe would be found in the radiation pattern of annular array transducer. The kerfs in HF annular array usually are diced to 30μm approximately by laser micro-machining [44, 101-103]. Conventional dicing technique by saw blade is not recommended, since it

is not good for cutting curved patterns (i.e. annulus here). Besides that, kerfless annular array without using any dicing but patterned electrode was also designed and fabricated [104, 105], while again cross talking becomes the main concern.

Though there is no significant challenge in dicing the annular array, the decreasing element width in the array could leads to unwanted lateral mode. Elements in annular array are usually in same area. This is to achieve same impedance and phase shift for every element, but also results in the decrease of element width by the increase of element number. For example, a typical 2mm diameter, 7-element, 50μm thick annular array operating about 40-50MHz only shows the width of its outermost element around 50μm. It leads to a very small aspect ratio about 1, while most outer elements shows their aspect ratio smaller than the suggested value of 3. Therefore, lateral modes (R-mode) would be large coupled into main T-mode vibration, if PZT ceramic is used as piezoelectric layer. To eliminate the lateral coupling, PT ($PbTiO_3$) materials are introduced to replace conventional PZT since it shows very small lateral coupling coefficient. Though the lateral modes still exist in outer elements, they become too weak to impact the T-mode vibration. PT is the material that almost all the reported HF annular arrays have used. Some arrays made by piezo-polymer layer (PVDF) were also fabricated [106, 107], but suffered low sensitivity as expected.

In addition, compared to linear arrays, the annular array achieves electronic beamforming in axial direction, but still requires mechanical motions in lateral direction since the annular array could only show focal point on focal axis. The frame rate is lower than linear array but faster than single-element transducer. However, the natural on-axis focus by annular geometry also offers a better resolution than the other two groups of transducer [16]. And annular array need much fewer element (usually <10), the complexity in fabrication and outside circuits would be largely reduced.

2.6.4 Comparisons

The three groups of HF transducers are then compared to each other by the two fields of fabrication and imaging, as reviewed in Table 2.7.

Table 2.7 Comparisons among the transducer of single element, linear and annular array

Transducer	Fabrication	Imaging
Single-element	▪ relatively easy lapping or thick-film techniques ▪ fine-grained ceramic required if thick-film techniques used ▪ no micro-machining ▪ lens required	▪ lens required, fixed focus ▪ narrow DOF ▪ very low frame rate using B/D scan to improve DOF
Linear array	▪ very small kerfs hardly to be diced ▪ large element number ▪ lens optional	▪ dynamic focusing ▪ very fast frame rate ▪ grating lobe appeared if width of element pitch is large
Annular array	▪ no kerfs restriction ▪ kerfs is diced by laser micro-machining ▪ only a few elements ▪ lens optional	▪ dynamic focusing on focal axis ▪ fast frame rate, and mechanical motions in lateral direction ▪ Better resolution than the other two

2.7 Summary

The chapter described background information which is required for the following chapters for the design of HF array transducers including linear and annular ones. The basic of ultrasonic transducer was introduced by showing its components, piezoelectric principle, vibration modes, as well as the transducer imaging. Besides that, a brief overview of the design by using numerical models was provided; the element and imaging response can be predicted and measured by some imaging measurements instructed in the Chapter. The discussion about materials used as piezoelectric layer was also involved, while ceramic is selected in our research since it is the material that most of current transducers used. At the end, the three groups of HF transducers are reviewed and compared in the two fields of transducer fabrication processes and imaging behaviours.

Chapter 3 High Frequency Annular Array

3.1 Introduction

The fabrication of a high frequency (>30MHz) transducer for medical imaging becomes very difficult for conventional linear arrays which require the element space of one wavelength. Only a few researchers have successfully realized the manufacture of a linear array in the high frequency range.

An annular array is developed as an alternative transducer showing two major advantages over the linear arrays. One is that the axis-symmetric geometry gives an intensive axial radiation pattern for the annular array, which is superior to that of a linear array. Another one is the much less challenging fabrication, since no strict restriction on element pitch is required. Annular arrays are usually fabricated by cutting concentric rings into transducer to create a series of annular elements. Dynamic focusing can be realized in the focal axis by applying a suitable phase shift or time delay on every element. Mechanical scans then must be used in the elevation plane, which slightly reduces frame rate.

The geometry of a conventional annular array is a Fresnel plate comprising several equal area (EA) elements. Figure 3.1 shows a typical equal area annular array. The EA design has been adopted by many researchers so far due to the same impedance and more importantly the same phase shift of each element, showing advantages in electrical tuning and beam forming.

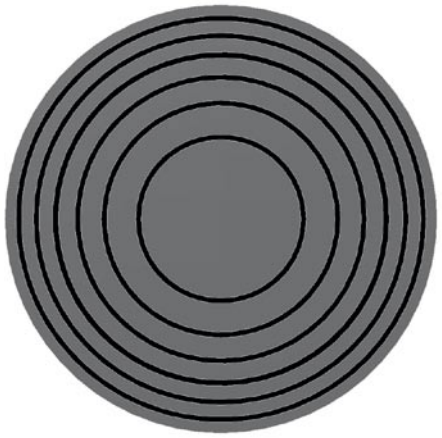

Figure 3.1 The front view of a typical 7-element equal area annular array

However, the geometry given in Figure 3.1 is the ideal case, without the consideration of kerfs between the two nearby element. Kerfs are usually cut by a laser micro-machining technique to separate the elements. The influence of kerfs is usually neglected in the design of an annular array, but it is found that it has significant impact on the design of the annular array in high frequency applications. The optimized design is then developed and presented here for EA arrays with the consideration of kerfs.

A major problem caused by EA geometry is that the width of outer elements must decrease to maintain the same area as inner elements, as illustrated in Figure 3.1. When more elements are added to improve the imaging qualities, the outer elements could become very small, leading to the unwanted lateral modes coupled into thickness mode (T-mode) by using conventional piezoelectric ceramics represented by PZT-5H. The aspect ratio, *G*, of outer elements defined as the ratio of element width to thickness could be far smaller than the suggested value of 3 to eliminate lateral modes from the frequency band. Furthermore, if the kerfs (≈30μm) are taken into account in the real case, the aspect ratio of outer elements could be even smaller. To avoid the lateral coupling, PT (PbTiO3) materials have been developed to replace the conventional ceramics. The material shows a strong T mode vibration but weaker lateral mode.

In this chapter, a typical high frequency equal area annular array is investigated mainly by using Finite Element Analysis (FEA), including the design, element and imaging responses of the array. First of all, an optimized design is developed to show better performances compared to the conventional design, with the consideration of kerfs influence.

Secondly, a numerical method is developed here to evaluate the radiation patterns of the array, and to compare with the patterns obtained by FEA method. Both good imaging quality and agreement are achieved by both numerical and FEA beams, but with an unexpected high sidelobe in FEA patterns.

Last but not least, by analysing the unexpected lobe, it is found that the formation of the lobe is mainly due to the coupling of transverse waves by outer elements. Though transverse waves travelling across the array surface are always found, their influence on beam pattern is not well-

investigated but revealed here. Thus the potential methods to suppress the unexpected lobe are more focused the improvements in the performances of outer elements.

3.2 Methodology

Both Rayleigh-integral and FEA method are used here to show the response of the annular array. In terms of numerical method, 1-D KLM model using transfer matrices reviewed in last chapter is adopted to obtain the element response of an annular array element, including its impedance spectrum, resonant frequency, insertion loss and element pulse shapes.

However, 1D KLM model could hardly evaluate imaging performances of an array transducer. Thus numerical method based on the direct calculation of Rayleigh integral is applied to obtain the numerical radiation patterns, revealing the imaging parameters including lateral and axial resolution, sidelobe information, pulse bandwidth, sensitivity etc.

All the results obtained by the two numerical methods are idealized since all the elements of the array are assumed to vibrate as an ideal piston. But to show array performances experimentally is very expensive and time consuming. Thus the FEA method is used to predict the behaviour of the transducer, which has been demonstrated to show very similar responses as experiments by many previous researchers [98, 105]. The piezoelectric element, circuit, and acoustic analysis can be coupled together to simulate the electric-mechanical responses and the radiation patterns for a whole array transducer.

The finite element model was created by using the FEA software package named ANSYS (version 11.0), and it shows a strong capability to model multi-physical systems, which is quite suited for the piezoelectric analysis showing both the harmonic and transient responses of the pulsed ultrasonic array transducers. The model of annular arrays could be 3-dimensional as in the real device, or a simplified 2D model to represent 3D ones with the axis-symmetric boundary condition. Only the cross section is needed in the analysis, which rotates by the axis virtually to form a 3D array, as illustrated in Figure 3.2. The simplification saves the computing time of the FEA software.

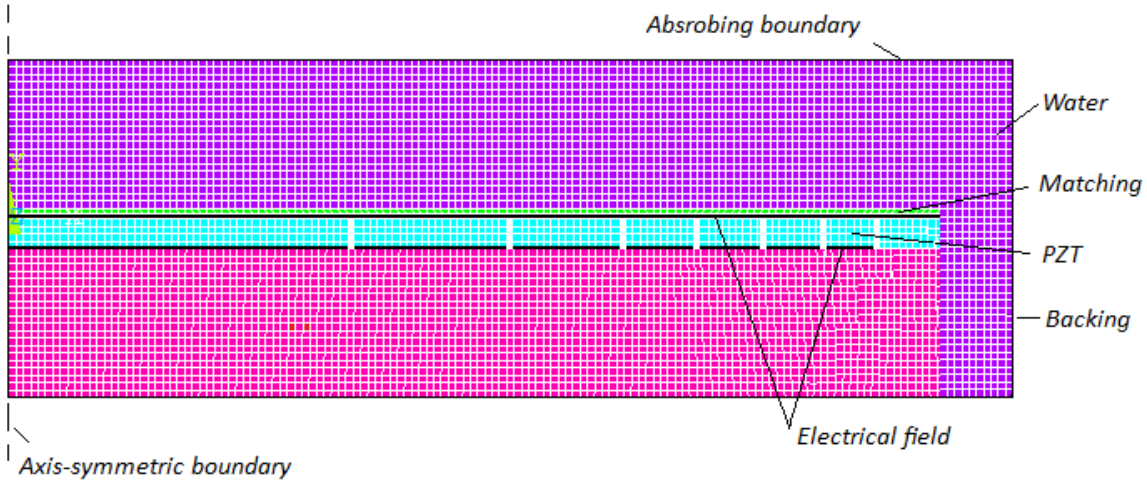

Figure 3.2 Finite element model of a 2-D cross section of a 7-element EA annular array

Most high frequency annular arrays published so far have diameters ranging from 2 to 6mm, the number of elements from 5 to 7, and the f-number around 2 [44, 84, 101, 102, 107]. Therefore, the annular array in this research is designed with general dimensions similar to available devices, having a diameter of 2mm, 7 elements and f-number of 2. The kerfs width is set to be 30µm according to the limits of laser micro-machining. A common PT material, PZ34 provided by "Ferroperm", is used as ceramic layer with a thickness of 50µm to have an operating frequency around 45MHz for the transducer. The designs of the matching and backing layer all follows the design guidelines described in Section 2.5.4.

Table 3.1 Properties of the layers used in the FEA model of annular array

Layers	Material	Ref.	*Z* (MRayls)	*c* (m/s)	Q_m	α (dB/mm ·MHz^{-1})
Matching	Alumina-loaded EPO-TEK 301-2	[22]	7.3	3248	-	≈4
Ceramic	PZ34	[88]	35.4	4661	120	-
Backing	Tungsten-loaded E-solder 3022	[22]	10.0	1600	10	-
Kerfs filler	Araldite	[22]	2.45	2210	-	≈1.2

EPO-TEK 301-2 loaded by Alumina is used as matching layer to have the acoustic impedance of 7.3MRayls for good mechanical tuning, while E-solder 3022 loaded by Tungsten is used as backing layer to show the acoustic impedance of 10MRayls. The loading percentage of the two particles in the two layers follows the principle instructed by Levassort et.al [108, 109]. In addition, it should

be noticed that the matching layer can only be loaded by the non-conductive powder such as Alumina because the patterned electrode attached to top surface of ceramic layer. The material to fill the kerfs, namely kerfs filler, is a commonly-used epoxy - “Araldite”. The key parameters of all these materials are listed in Most high frequency annular arrays published so far have diameters ranging from 2 to 6mm, the number of elements from 5 to 7, and the f-number around 2 [44, 84, 101, 102, 107]. Therefore, the annular array in this research is designed with general dimensions similar to available devices, having a diameter of 2mm, 7 elements and f-number of 2. The kerfs width is set to be 30μm according to the limits of laser micro-machining. A common PT material, PZ34 provided by “Ferroperm”, is used as ceramic layer with a thickness of 50μm to have an operating frequency around 45MHz for the transducer. The designs of the matching and backing layer all follows the design guidelines described in Section 2.5.4.
Table 3.1, including acoustic impedance Z, longitudinal sound speed c, mechanical quality factor Q_m and attenuation coefficient α.

In the model, the electrodes usually made of gold are replaced by a special ANSYS element called as Coupled Electrical Field (CEF). Since electrodes deposited by sputtering are usually at the magnitude of several hundreds of nanometres or even less, their influence on transducer performances can be neglected compared with the other layer thickness of several tens of microns [96, 102] . CEF is a 1-D line element without the definition of thickness or material. It introduces electric signals into the piezoelectric layer, or equivalently it is an extremely thin electrode. The absorbing boundary is applied to the edges of fluid (water) medium to simulate the infinite water load as the real case. The backing layer is set to be sufficiently thick to absorb all the energy transferred into it. Driving circuit of the transducer to achieve electrical tuning was also established in the model, including voltage source, capacitance and inductor.

The finite elements obtained through the meshing process of the model are 4-node quadrilaterals, and the grid on which the element positions are is known as the finite element mesh, as displayed in Figure 3.2. Mesh size needs to be fine enough to get accurate results, but finer mesh demands more computing time. There is always compromise between accuracy and computing time. More than 10 elements per wavelength (or mesh size of λ/10) are usually suggested, while 20 elements are generally believed to show enough accuracy [110, 111]. Here, the mesh size for this annular array is set to be λ/8. Although this is less than λ/10, the mesh refinement study suggests that the

element responses using mesh of λ/8 are quite similar to the one using mesh of λ/20. However, for the simulation of array radiation performance, the mesh study takes a significant amount of computer resources due to the large number of "water" elements in the model. The "water layer" in the mesh study for element responses can be quite small because an "absorbing boundary condition" can be used, but the radiation simulation requires more than 4mm deep water layer and this contains an enormous number of elements even using a coarse mesh of λ/8. The mesh of λ/8 takes more than 72 hours of computing time, and the finer mesh is therefore beyond the capability of our computer. Sp the mesh study for radiation patterns is based on a smaller array with 5 elements, 1mm diameter and f-number of 1 (other properties are same). It is again found that the mesh of $\lambda/8$ shows very similar radiation to the finer mesh up to $\lambda/20$. But this study may not prove an accurate radiation of the larger 2mm array using the mesh of λ/8, compared to the finer mesh, since the much larger "water layer" could lead to some more errors during wave propagation. Nevertheless, the coarse mesh of $\lambda/8$ for the 2mm array is still believed to at least show the trend of the radiation, and the detail discussion can be found in Section 3.5.2. Meanwhile, all the mesh studies are detailed in Appendix D.

In addition, a method based on the Rayleigh-integral is also developed to compare to the FEA radiation patterns, as this is computationally less complicated. It uses a Gaussian modulated signal as the element pulses emanating into the water medium; the pulses are then applied to the Rayleigh-integral to form the radiation pattern. It is to show theoretical results, and the detail can be found in Section 3.4.

3.3 Optimized Design of Equal Area Annular Array Geometry

In the transducer design of a typical EA annular array, the influence of kerfs between nearby elements is always regarded as a minor factor and neglected. However, it is found that the kerfs play a significant role when the array is approaching the field of high frequency applications which leads to a micro-scaled transducer. The following sections reveal the relations between kerfs and array performances, and show the advantages of the optimized design of EA array geometry.

3.3.1 Conventional Design of Annular Element Geometry

By conventional design of EA array, every element shares the same area and follows the equations given by Equation (3.1), but without considering the kerfs,

$$r_n^2 = (n-1)R^2/N \tag{3.1}$$

where r_n is the outer radius with the subscript n representing the index number of each array element, R is the radius of total aperture, and N is the total element number. If the kerfs are taken into account, a simple process to obtain the inner and outer radius of elements is applied.

$$r_{in} = r_{n-1} + w_g/2\,; \qquad r_{i1} = 0$$

$$r_{on} = r_n - w_g/2 \tag{3.2}$$

where r_i and r_o are the inner and outer radius of n^{th} element, respectively, and w_g denotes the width of the kerfs. With the kerfs, the element would no longer be equal area. But it is believed that EA condition could still be valid because the kerfs width is very small compared to the element width and thus shows very little influence on element area. However, the kerfs width becomes comparable to element width and cannot be neglected in high frequency applications, where the aperture size is relatively small.

Under current laser micro-machining technique used for high frequency annular arrays, kerfs can be realizable with width as small as 25μm, while 30μm is the value that could be confidently achieved. Table 3.2 shows the changes of element area S by different kerfs width w_g for a typical 2mm diameter, 7-element annular array. In ideal case (w_g=0), EA condition is strictly followed. With kerfs width increased to 15μm, a decreasing trend of the area from inner to outer elements is found, but their differences are not too much. EA condition might be still valid, though 15μm kerfs are very hard to fabricate. When kerfs width reaches a realizable level of 30μm, a stronger decreasing trend can be seen. The area of the outermost element is almost 1/3 lower than the value of an ideal EA array. Non-EA elements could results in poor element responses.

Table 3.2 Area of EA elements using conventional design with different kerfs width

Element		**1st**	**2nd**	**3rd**	**4th**	**5th**	**6th**	**7th**
***S* (mm²)**	**w_g=0μm**	0.45	0.45	0.45	0.45	0.45	0.45	0.45
	w_g=15μm	0.43	0.41	0.39	0.38	0.37	0.37	0.36
	w_g=30μm	0.41	0.36	0.34	0.32	0.30	0.28	0.27

In Figure 3.3, the impedance spectrum of the outermost element for the real array (with kerfs of 30μm) by using KLM model (denoted as KLM_real) and FEA method (denoted as FEA_real) are displayed. In addition, the responses of the KLM model for the ideal array (without kerfs and denoted as KLM_ideal) is also shown in the same figure for comparison. A good agreement between FEA and KLM results for the real array can be found, with two clear peaks belonging to ceramic resonance (left peak) and matching resonance (right one) respectively. However, the two peaks obtained by FEA are weaker than the ones by KLM, especially in Figure 3.3(a). This is possibly due to more energy dissipation in the 3D FEA model, while KLM model only considers the 1D vibration in thickness direction. In addition, a difference between real and ideal array is expected in the impedance amplitude spectrum, which is caused by the differences in element area.

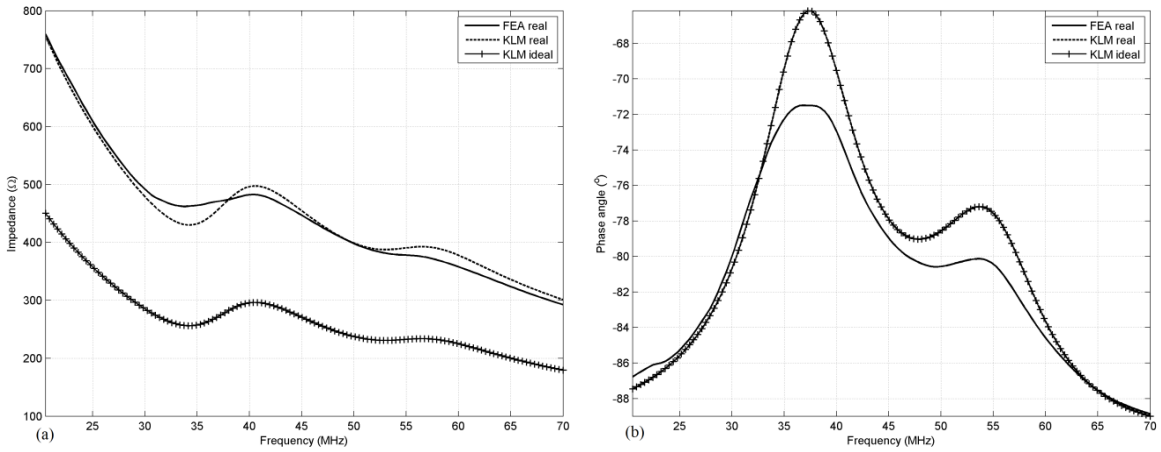

Figure 3.3 (a) Amplitude and (b) phase angle of outermost element impedance spectrum; "FEA real" and "KLM real" denote the FEA and KLM responses of real array (with kerfs) respectively, while "KLM ideal" is the KLM responses of ideal array (no kerfs)

More importantly, this difference in area would impact the electrical tuning, since the values of resistor and inductor in a tuning network is determined by element area. The tuning networks of every element are designed to be all the same because the same element area is expected in an ideal EA array, and it is described as conventional tuning. Thus the conventional design of tuning is no longer suitable for the actual array in high frequency devices, especially for the outermost element. Insertion loss (IL) is always used to measure the element responses including sensitivity and bandwidth. Figure 3.4 (a) shows the IL spectrum of the outermost element with the tuning determined by the actual element area by using KLM and FEA, respectively. Figure 3.4(b) then

displays the same responses but with the conventional tuning. Again the FEA responses shows reasonable agreement to the KLM results, while the loss in amplitude could be caused by more energy dissipation in FEA model. By using the tuning determined by the actual element area, IL spectrum shows higher peak with its position much closer to the central frequency than the one using conventionally tuning. It implies that the element using conventional tuning is not well-tuned for the actual element with reduced area. An optimized geometric design for high frequency annular array is essential to achieve EA condition for every element with the kerfs influence.

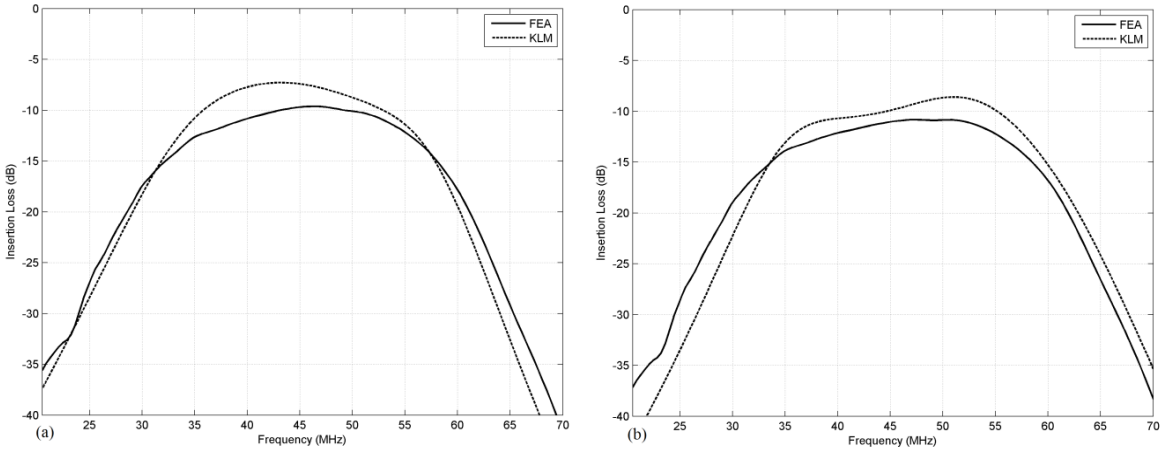

Figure 3.4 (a) IL spectrum of the outmost element using (a) the tuning only designed for the element, (b)and the one using conventional design

3.3.2 Optimized Design of Annular Element Geometry

An optimized design is presented here, which aims at maintaining the exact EA geometry with kerfs influence. Imagine an annular array with *N* elements and (*N-1*) kerfs in the array aperture, the inner radius of next element equals to the outer radius of previous element by ideal geometric design (or conventional design). However, by considering the kerfs, a very similar criterion is described as: the inner radius of next element equals to the outer radius of previous element plus the kerfs width. Thus the following relationship can be obtained, which implies that the total area of an aperture equals to the sum of every element and kerfs area.

$$r_{on}^2 = nr_{o1}^2 + \sum_1^{N-1}[\left(r_{on} + w_g\right)^2 - r_{on}^2] = Nr_{o1}^2 + (N-1)w_g^2 + 2w_g \sum_1^{N-1} r_{on} \tag{3.3}$$

$$r_{in} = r_{o(n-1)} + w_g \tag{3.4}$$

The parameters used in Equation (3.3) and (3.4) are the same as those given in Equation (3.1) and (3.2), while r_{oN} is the outer radius of outermost element or the radius of the aperture. However, Equation (3.3) is very hard to solve. An approaching calculation method to resolve this implicit equation is adopted and realized by Matlab programming. The dimensions of annular array following the EA condition strictly are obtained, as listed in Table 3.3 with 30μm wide kerfs. In addition, the optimized design is also compatible with the conventional design by just setting the kerfs width to 0. Array performances based on the optimized design is then compared to the conventional design by using FEA method, including IL spectrums and focusing responses.

Table 3.3 Radius and area of the annular elements using optimized design with 30μm kerfs

Element	1st	2nd	3rd	4th	5th	6th	7th
S **(mm²)**	0.34	0.34	0.34	0.34	0.34	0.34	0.34

3.3.2.1 IL spectrums

Figure 3.5 compares the IL spectrums of the outermost (7th) element using conventional design (CD) with kerfs, and the one using optimized design (OD). The results of KLM model with perfect electrical tuning is also displayed as a reference. Table 3.4 then details their element responses, where IL_{max} is the peak value of IL representing the element sensitivity, f_c is central frequency and *BW* is -6dB fractional bandwidth. The algorithm used to obtain these parameters from the frequency spectrum is detailed in Appendix E.

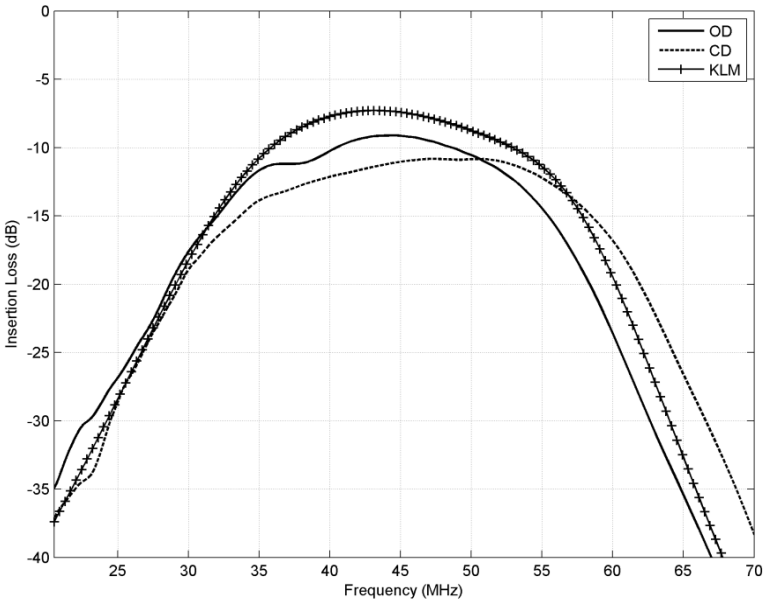

Figure 3.5 IL spectrums of outermost (7th) element by using OD, CD and KLM

Table 3.4 Parameters from IL spectrums by using CD, OD and KLM

Design	IL_{max} (dB)	f_c (MHz)	BW (%)
CD	-10.82	45.88	61.57
OD	-9.11	43.73	53.85
KLM	-7.29	44.84	53.01

The curves of both IL responses using OD and KLM are found to be in similar shapes, and it indicates that OD shows an almost perfect electrical tuning. The slight loss in IL peak for OD case is again due to the extra energy loss in lateral direction in FEA. However, it is also found that the IL spectrum of CD case shows the largest bandwidth, but it doesn't refer to a better electrical tuning. For the element by CD, its IL peak is actually located at the frequency of 52MHz approximately, instead of the position close to the central frequency for the element response by OD or KLM. The IL value around the designed operating frequency of 45MHz approximately is about -11dB. The tuning of CD is not as good as OD. In addition, it can be seen that the IL spectrum of OD shows a slight drop in the region around 35 to 40MHz in Figure 3.5. It is the evidence of the lateral mode, but the mode is very weak because of PZ34 material with very low lateral coupling coefficient. Therefore, the lateral mode shows no significant influence on the element responses.

3.3.3.2 Imaging Responses

Imaging responses are the ultimate target that we need to obtain in the research, since it directly relates to the imaging parameters including bandwidth, sensitivity, resolution, contrast resolution, side lobe level, etc. Following the guidelines instructed in Chapter 2, the responses at focal plane and the beam pattern can be obtained by applying suitable phase shift or time delay to each of the array elements. In the FEA model, only 1-way radiation or the transmission pattern is simulated, since the receiving pattern is identical to the transmission one if the reflection of the object is ideal. 2-way radiation can be obtained simply by the following relationship.

2-way radiation = 2 X (1-way radiation) in dB unit (3.5)

For a typical 2mm, 7-element annular array operating at 45MHz with 30μm-wide kerfs, the often used f-number is set to be 2. In other word, the 2mm aperture is focused at 4mm deep in the fluid medium (water). Figure 3.6 compares the normalized pressure response at focal point of the

arrays with conventional and optimized design. The pressure parameters are then listed in Table 3.5, where P_{max} is the maximum pressure amplitude, and $PL_{(-6)}$ is pulse length referenced to the -6dB level of the pulse envelope. Likewise, the algorithms to get these parameters from the pulse diagram are detailed in Appendix E.

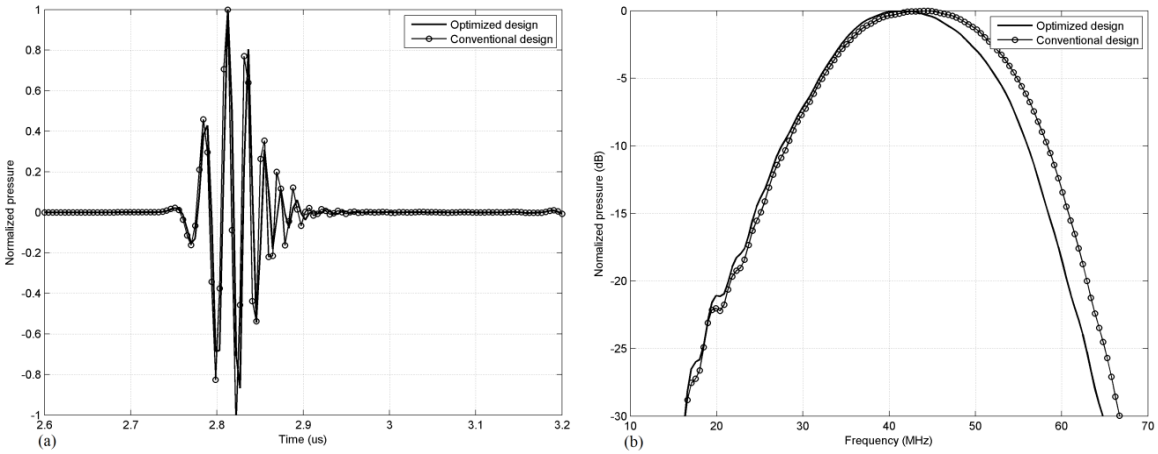

Figure 3.6 Normalized pressure response at focal point with conventional design (CD) and optimized design (OD) in (a) time domain and (b) frequency domain, respectively

Table 3.5 Parameters obtained by pressure responses at focal point

Case	P_{max} (10^5 Pa)	$PL_{(-6)}$ (ns)	f_c (MHz)	BW (%)
OD	2.52	56.8	41.3	55.3
CD	2.58	58.6	43.2	56.9

It is found that OD has a slightly shorter pulse length, but also a narrower bandwidth. The values of P_{max} are comparable for the two cases, suggesting similar sensitivity. It can be claimed that the pressure performances with OD and CD are generally comparable.

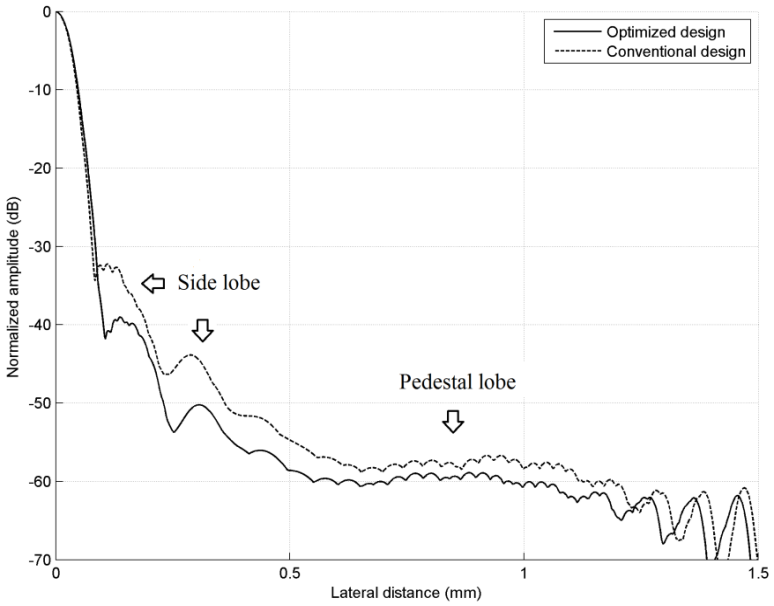

Figure 3.7 2-way beam patterns of the arrays with OD and CD

The 2-way radiation pattern is displayed in Figure 3.7 with the their imaging parameters detailed in Table 3.6, including lateral resolution *Res*, contrast resolution *CR*, level of nearest sidelobe *SL* and the level of pedestal lobe *PeL*. Only half of the beam pattern has been shown due to axis-symmetric geometry of the array aperture, with the positions of two sidelobes and pedestal lobe pointed out.

Table 3.6 Imaging parameters obtained by 2-way beam pattern

Case	*Res* (μm)	*CR* (μm)	*SL* (dB)	*PeL* (dB)
CD	71.4	385.8	-32.2	-56.7
OD	74.8	202.9	-39.0	-58.9

It can be found that the radiation pattern of OD is better than the one of CD. In detail, the pattern of OD shows better contrast resolution, lower sidelobes and pedestal lobe. Though the resolution of OD is slightly lower than the one of CD, the two values are still comparable and close to the theoretical value about 75μm calculated by Equation (2.14). By the comparisons of pressure pulse responses and imaging performances given in Table 3.5 and Table 3.6, respectively, it can be claimed that OD is generally better than CD. Therefore, the following investigations for annular arrays are all based on the optimized design.

However, the nearest sidelobe in both the two patterns is found higher than -40dB, while the suggested level is usually below -50dB [62]. Though OD design already shows an improvement in sidelobe level, it is still essential to find a method to suppress the sidelobes, especially the nearest one. Otherwise, the high sidelobe could results in artefacts in images.

3.4 Evaluation of Radiation Pattern by Rayleigh-integral Method

To suppress the high sidelobe appeared in the patterns displayed by Figure 3.7, it is essential to find a numerical method to predict and analyze the radiation pattern. Rayleigh-Sommerfeld integral is a good estimator to evaluate the acoustic diffraction produced by an ideal radiation piston. The integral is reviewed in section 2.5.5 and again expressed below,

$$\varphi(\vec{r},t) = \int_S \frac{v_n(\overrightarrow{r_0},t-R/c)}{2\pi R} dS \tag{3.6}$$

where $\varphi(r,t)$ is the time-dependent velocity potential of a point in radiation field with its position represented by vector r; v_n is the particle velocity of a point on the piston surface with its position represented by vector r_0; R is for the distance from vector r to vector r_0, and S denotes the surface area of the piston. Thus the velocity v and pressure p at a certain position r in fluid field can be obtained by following equations, where ρ_0 is the density of fluid.

$$v(\vec{r},t) = -\nabla\varphi(\vec{r},t) \tag{3.7}$$

$$p(\vec{r},t) = \rho_0 \partial\varphi(\vec{r},t)/\partial t \tag{3.8}$$

By substituting Equation (3.6) into Equation (3.7) and (3.8), pressure p can be transferred to forms as expressed below,

$$p(\vec{r},t) = \rho_0 \cdot \int_S \frac{g(\overrightarrow{r_0},t-R/c)}{2\pi R} dS \quad ; \qquad g(\overrightarrow{r_0},t) = \partial v_n/\partial t \tag{3.9}$$

Equation (3.9) means that the pressure $p(r, t)$ is the overlap of all the pulses emanated from a radiating piston with different time delay dependent on distance R. The radiation pattern is then plotted by the amplitude of pressure $p(r, t)$ at its corresponding position.

3.4.1 Direct Calculation

The SIR (spatial impulse response) method is always applied to solve the Rayleigh integral to show the acoustic field for either a single-element or array transducer. A programme named as “Field II”

has been developed based on SIR method by Technical University of Denmark, with its details instructed in the references [112, 113].

However, although “Field II” programme successfully evaluates the radiation pattern for linear arrays with high efficiency, it meets difficulties in the evaluations of the annular array. No direct method to solve annular geometry has been given in the programme. Thus we have developed another programme to solve the Rayleigh integral directly by using Matlab. Both the imaging field and radiating aperture are divided into numerous tiny elements. Every single element is assumed to show one pressure pulse. Thus the Rayleigh integral given by Equation (3.9) is discretized and can be solved numerically. However, the direct method is inefficient due to the large numbers of tiny elements. But it is suitable for the transducers with different geometry and pulse shapes emitted from aperture surface, since both geometry and pulses can be adjusted by the numerous tiny elements along aperture. For the geometry of annular array, the key procedures are instructed as follows, with its Matlab programme detailed in Appendix A.

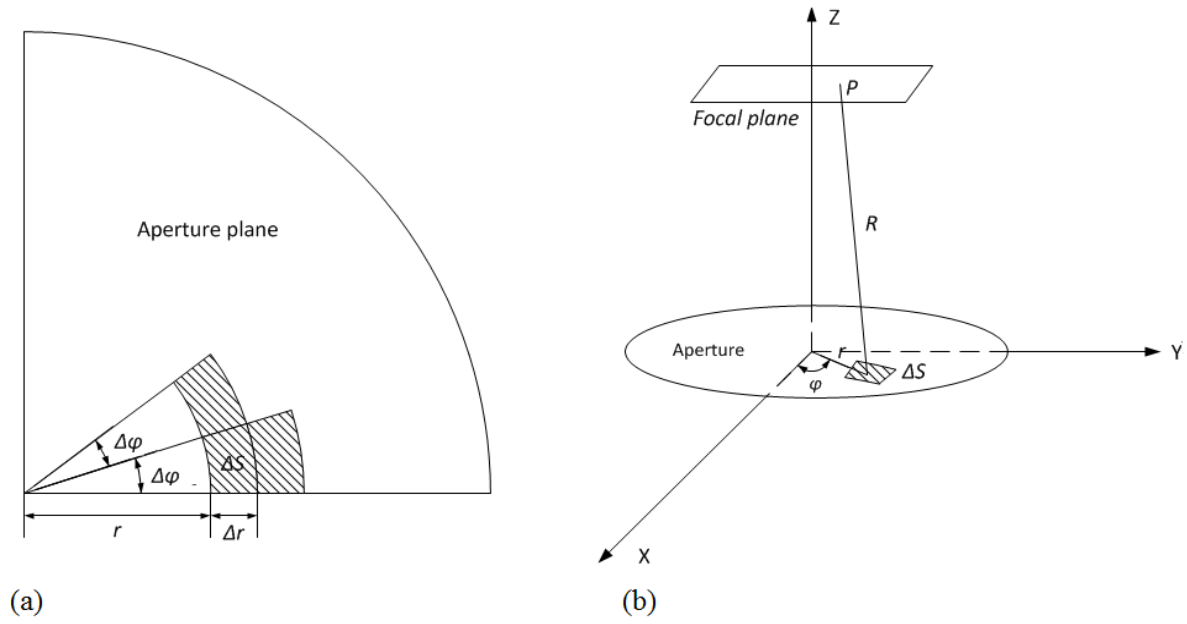

Figure 3.8 (a) The diagram of array aperture and (b) the diagram to describe Rayleigh-integral method

First of all, the polar coordinate is introduced to describe every point along the annular array aperture with the coordinate of (r, φ), where r is the radius and φ is the azimuth angle as displayed in Figure 3.8(a). The aperture is then discretized to many tiny elements, and three of them are

magnified to be clearly seen in Figure 3.8(a) (shaded region). The increment of radius and azimuth angle is set to be Δr and $\Delta\varphi$ for these tiny elements, respectively. Since Δr and $\Delta\varphi$ is very small, the surface integral dS in the Rayleigh integral becomes the element area ΔS with its expression of $\Delta S = r\Delta r\Delta\varphi$. Therefore, the pressure at a certain point P in the focal plane (the plane perpendicular to Z-axis) becomes the summation of all the pressure of all the tiny elements ΔS along the aperture with their time delay R/c, as illustrated in Figure 3.8(b). Equation (3.10) is then used to describe pressure at the focal plane, which is equivalently a discrete Rayleigh integral. Here the subscripts n_r and n_φ denote the number of points along the radial and azimuth directions respectively, and $\vec{r}$ is a vector to describe the position of the point P at the focal plane.

$$p(\vec{r},t) = \rho_0 \sum_{n_r,n_\varphi} \frac{g(t-R/c)}{2\pi R} \cdot r_{(n_r)} \Delta r \Delta\varphi \tag{3.10}$$

To obtain the radiation pattern in the plane, only the vector $\vec{r}$ along the line with its cylindrical coordinate of (r_f, 0, F) need to be observed due to the axis-symmetric condition, where r_f is the vector radius at the plane and F is the focal distance. Thus the distance R is expressed as,

$$R = \sqrt{\left(r_f - r_{n_r} \cdot \cos\left(\varphi_{n_\varphi}\right)\right)^2 + \left(r_{n_r} \sin\left(\varphi_{n_\varphi}\right)\right)^2 + F^2} \tag{3.11}$$

Notice that for an annular array to focus at a certain focal point, the time delay t_f and phase shift φ_f is required for each element and follows the rules re-expressed as follows, where subscript N denotes the array element number.

$$t_{f(N)} = t_0 - \frac{R_{cN}^2}{2Fc} \quad ; \quad \varphi_{f(N)} = 2\pi f \cdot t_{f(N)} \tag{3.12}$$

With considering the time delay for focusing, the pulse in the Rayleigh integral now becomes of the form $g(t\text{-}t_d)$ for every array element, where t_d is defined as the overall time delay and expressed as follow,

$$t_d = R/c + t_{f(N)} \tag{3.13}$$

Obviously, the accuracy of the radiation evaluation by using direct solution of Rayleigh integral depends on the value of small area ΔS, or equivalently the small radius ΔR and small azimuth angle $\Delta\varphi$. But very small ΔS also leads to the increased computing time. Compromise needs to be taken between the area ΔS and computing time.

3.4.2 Radiation Pattern by Rayleigh-integral Method

The radiation pattern of the same annular array used in the FEA models is evaluated by the Rayleigh-integral (R-I) method described above, including the arrays with both conventional and optimized design. The R-I radiation pattern is expected be comparable to the FEA results.
Since the array geometry is defined, the overall time delay t_d (or phase shift (φ_d) for every element can be obtained. Thus Equation (3.10) could be solved when the element pulse *g(t)* is defined.

The R-I evaluation will be eventually compared to the FEA results, therefore it is essential to find a numerical pulse *g(t)* to fit the FEA result. A Gaussian modulated sinusoidal pulse (Gauss pulse) is found to show reasonable agreement, as illustrated in Figure 3.9. The element pulse by FEA is obtained from the centre point of 1st element, which is believed to show a good response without significant element edge effect or reflection. Both the pulses of Gauss and FEA are normalized in the figure. The detail profiles of Gauss pulse are referenced by its band parameters showing the bandwidth of 53%, the central frequency of 44MHz and the trailing pulse envelope (TPE) level of -25dB in the Matlab programme.

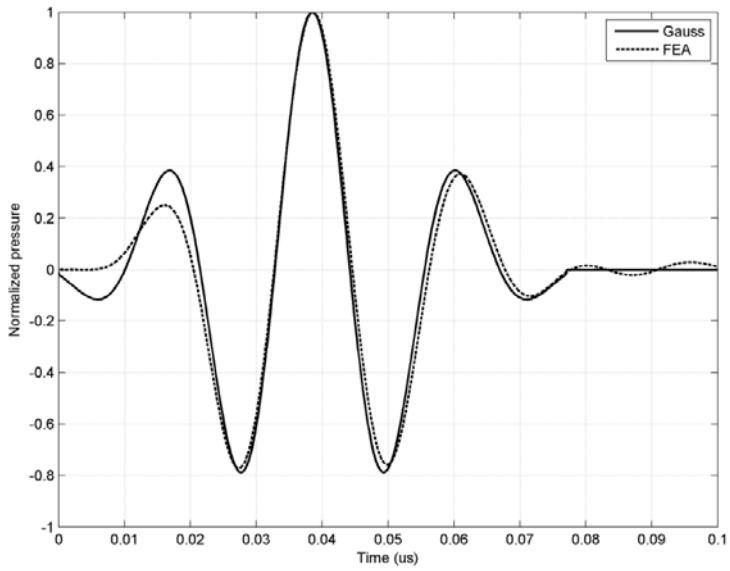

Figure 3.9 Gauss pulse to fit the element pulse by FEA

Thus we firstly evaluated the radiation patterns of the EA array with both conventional and optimized design, as illustrated in Figure 3.10(a). The patterns obtained by FEA are re-displayed in Figure 3.10(b) for comparisons.

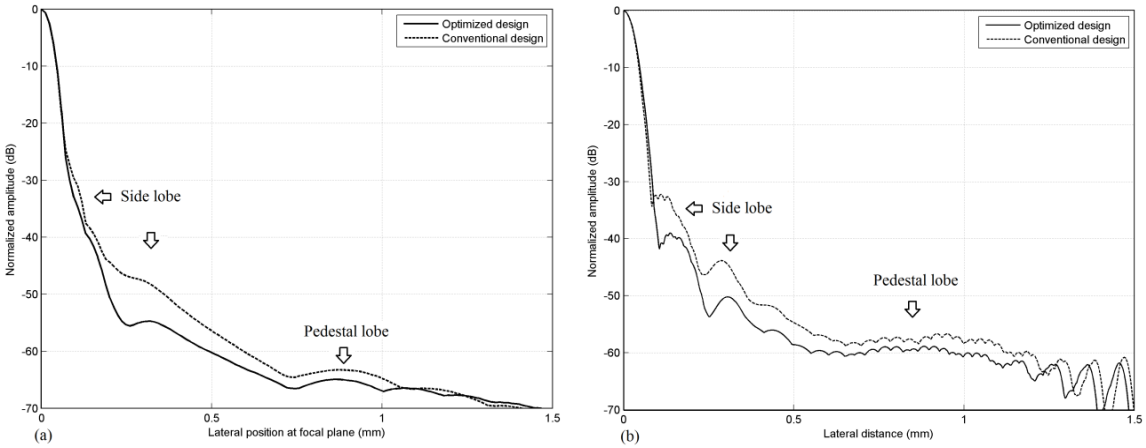

Figure 3.10 Radiation pattern of EA array with optimized and conventional design by using (a) numerical and (b) FEA method

It can be found that the improvement of optimized EA array is confirmed by using R-I method, and shows similar curve shapes compared to FEA results. The pedestal lobe found in numerical method generally agrees with the FEA response, while the difference in sidelobe region is also found. The nearest sidelobe in FEA pattern is not strongly reflected in the R-I results, though the R-I curves become slightly rippled in this region. However, the second nearest sidelobe in FEA pattern has been predicted by the R-I evaluation, though the lobes in R-I pattern are much smoother. Table 3.7 details the imaging parameters from the patterns, where X_{SL1} and *SL1* denotes the lateral position and the peak level of the nearest sidelobe respectively, and X_{SL2} and *SL2* similarly are the ones of 2nd nearest sidelobe; X_{PeL} then indicates the lateral position of pedestal lobe. The abbreviation conv. and opt. represents the array with conventional and optimized design respectively.

Table 3.7 Parameters from the radiation patterns by both R-I and FEA method

Array	Method	*Res* (μm)	X_{SL1} (μm)	*SL1* (dB)	X_{SL2} (μm)	*SL2* (dB)	X_{PeL} (μm)	*PeL* (dB)
conv.	R-I	69.7	-	-	313.8	-48.0	877.7	-63.2
	FEA	71.4	110.7	-32.2	288.4	-43.9	951.5	-56.7
opt.	R-I	71.1	-	-	316.4	-54.7	865.6	-64.9
	FEA	74.8	137.6	-39.0	306.0	-50.2	882.8	-58.9

The resolution and the lobe position (two sidelobes and pedestal lobe) show a general agreement between the R-I and FEA method, but there is a difference in the lower beam level and weaker nearest sidelobe in the R-I pattern. The differences may be caused by the ideal uniform pulse

along the element surface in R-I method, as well as the accuracy concern caused by coarse mesh in FEA method. The related discussion will be detailed in the following section, especially in the region of the nearest sidelobe, which shows the largest difference.

3.5 Analysis of Sidelobes

This section reveals the factors that might be related to the unwanted nearest sidelobe in the FEA pattern, and thus gives the potential direction to suppress the lobe. The details discussion begins with the analysis of the element vibration in the array.

3.5.1 Element Vibration

For the R-I evaluation of radiation patterns, a single element is assumed to behave as an ideal piston with uniform vibration in the thickness direction. However, the vibrations of an array element are more complicated as illustrated by the FEA responses, and include non-ideal oscillations probably caused by the surface wave. To show the element vibration in the annular array, three representative elements (1st, 4th and 7th) are excited one by one, with their pressure observed at the 3 points as illustrated by Figure 3.11(a). Notice that the "inner edge" of 1st element is actually the centre due to axis-symmetric geometry, thus the "middle" becomes the middle position of half the 1st element, while the outer edge is still the outer edge.

Figure 3.11 (b)-(g) then shows the pressure responses in both time and frequency domain. Since the pressure pulses in time domain show some ringing tails, which could lead to abrupt changes in the frequency domain when FFT (Fast Fourier Transform) is applied, a fitting method is used to smooth the frequency spectrum for a reasonable measurement of band parameters. The algorithm of this fitting model is detailed in Appendix F. In addition, all the pulses in the time domain are normalized to the maximum amplitude of the pressure at the 3 observing points of the excited element.

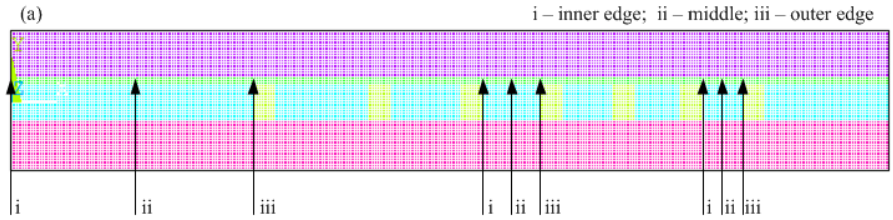

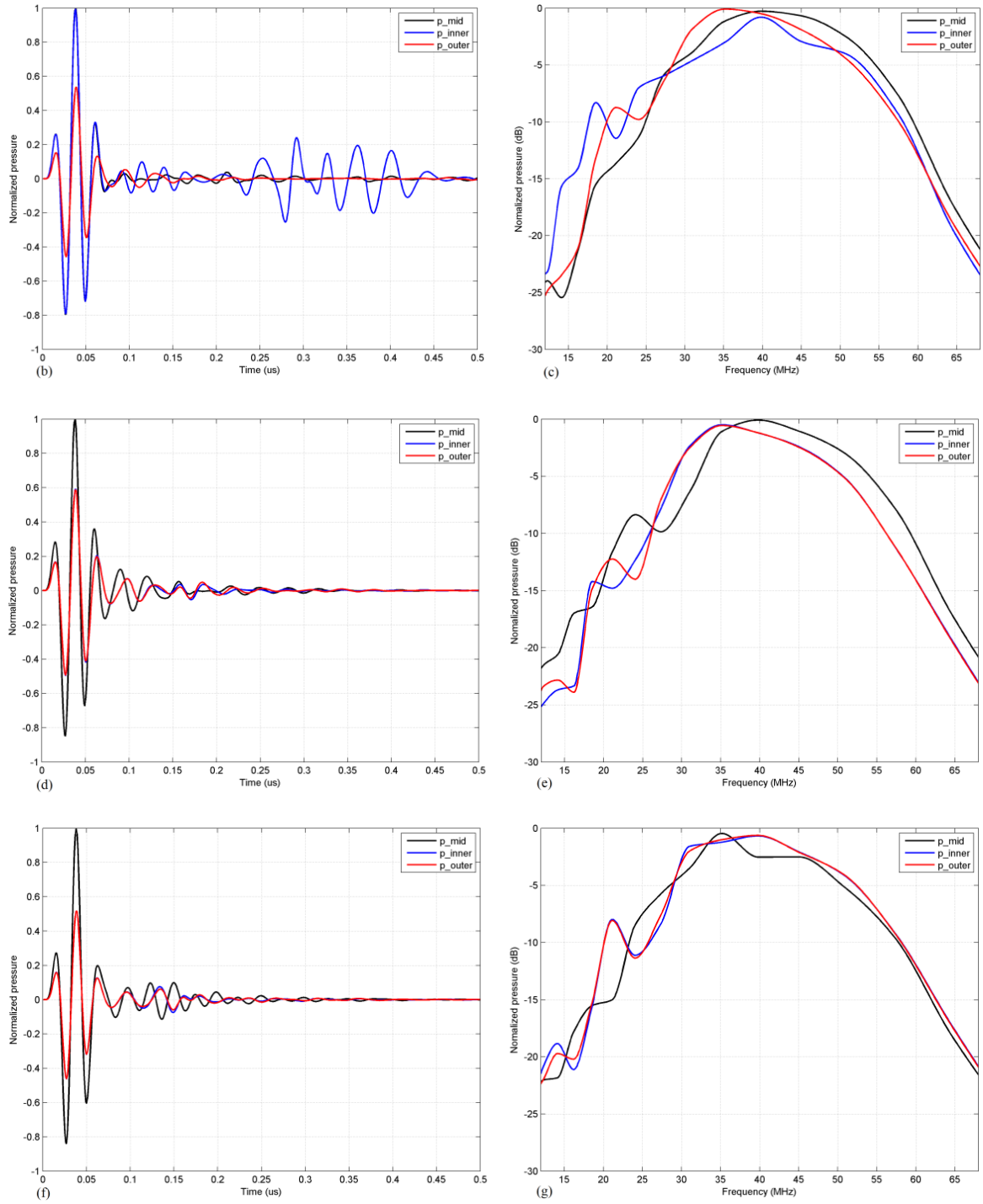

Figure 3.11 (a) The position of the 3 points to get pressure *p_inner* at inner edge, *p_mid* at the middle and *p_outer* at outer edge; (b), (c) show these pressures for 1st element in time and frequency domain; (d), (e) for 4th element; (f), (g) for 7th element

Table 3.8 Pressure parameters of the three elements in EA array

Element number		1st	4th	7th
p_inner	P_{max} (10^4 Pa)	2.73	1.51	1.38
	$PL_{(-6)}$ (ns)	35.4	37.4	34.3
	f_c (MHz)	39.7	40.4	41.3
	BW (%)	71.5	56.6	59.2
p_mid	P_{max} (10^4 Pa)	2.75	2.55	2.66
	$PL_{(-6)}$ (ns)	35.0	35.4	33.3
	f_c (MHz)	41.4	43.1	39.7
	BW (%)	65.6	52.3	62.9
p_outer	P_{max} (10^4 Pa)	1.48	1.50	1.38
	$PL_{(-6)}$ (ns)	34.9	37.1	34.3
	f_c (MHz)	40.3	40.2	41.2
	BW (%)	59.3	58.2	60.1

Table 3.8 then lists the pulse parameters obtained by Figure 3.11, including the maximum pulse amplitude P_{max} and -6dB pulse length $PL_{(-6)}$ in time domain; centre frequency f_c and fractional bandwidth *BW* in frequency domain. From Table 3.8, the pulses at all the observing points of the three elements have very similar $PL_{(-6)}$ and f_c. But the *BW* value shows some variance with some values exceeding 60%, or even 70%.This increment in *BW* is found to be caused by the smoothing effect of the fitting model to avoid abrupt changes in the band spectrum, for example, *p_inner* for the 1st element as discussed in Appendix F. Nevertheless, the bands for the three elements in frequency domain shown in (c), (e), (g) are similar to each other, as well as their main pulses (excluding the ringing tail) in the time domain as displayed in Figure 3.11 (b), (d), (f). All of these imply that the T-mode vibration is dominant in these element oscillations.

However, the ringing tails are found in the three elements and are also reflected as some spurious modes around 20MHz in their corresponding band patterns. This could be the evidence of the influence of the surface waves, especially the pulse *p_inner* for the 1st element. In Figure 3.11(b), a lower-frequency pulse is found well after the main higher-frequency pulse, implying a lower velocity, which is evidence for the propagation of surface waves in the array aperture. The transverse components of these waves travel inwards along the element surface and add constructively at the axis due to the axis-symmetric geometry. As a result, relatively large longitudinal waves would be found. These waves may be surface-like waves, but the propagation of these waves within an array is very complicated, since the waves carried by PZT layer are perturbed by kerfs, matching and backing layers. These lower-frequency waves won't impact the

pressure pulse at focal point when the array is focused, since they arrive later and probably destructively interfere, thus leaving only the higher-frequency waves (main pulse) to constructively interfere. However, the influence of these surface waves or ringing on the radiation pattern away from focal point remains uncertain.

In addition, it is also found that the pressure peak P_{max} at the element edges is always lower than the centre as shown in Table 3.8. Unlike the ideal piston-like oscillation showing uniform vibration along the element surface, the pressure pulse decays at the edges in the FEA response. This is confirmed by Figure 3.12, showing the pressure distribution at the surface of the three elements when their centre achieves P_{max}. The gray area represents the excited element, while the white part is the surface away from the element. Again only half of the 1st element is displayed as the axis-symmetric geometry.

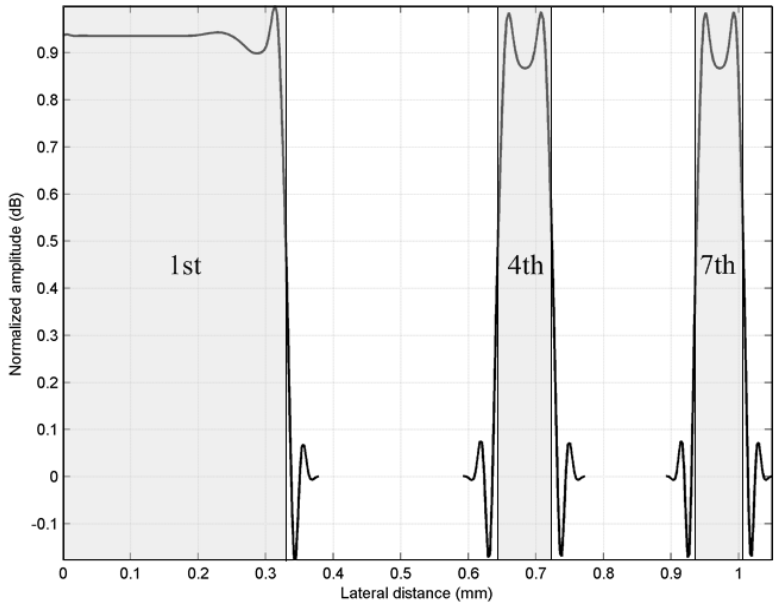

Figure 3.12 Pressure distribution along the excited element surface

It can be seen that the oscillation around the edges is always different from the centre. However, the non-ideal edge motion seems to not really affect the 1st element; uniform vibration is found at most parts of its surface. For the outer elements (4th and 7th), their surface vibration seems more rippled likely due to their smaller element width, but generally around the amplitude level of 0.9. The non-uniform surface vibration is found, but also not very severe; whether this less smooth oscillation (especially in outer elements) impacts the radiation pattern remains uncertain.

3.5.2 Accuracy discussion on FEA and R-I methods

The R-I radiation pattern uses a Gauss pulse as the element pressure pulse based on the assumption of ideal uniform piston-like element vibration, but seems quite different from the FEA pattern, as illustrated in Figure 3.10. The possible reasons could be either inaccuracy coming from the R-I method since the actual element vibration is non-uniform, or the inaccuracy from FEA method due to the coarse mesh of $\lambda/8$ used. Therefore, another method is developed to investigate the difference between R-I and FEA patterns. The method firstly uses FEA to obtain the pulse responses at the aperture surface. In this way, FEA modelling only needs a small amount of water and can make use of an absorbing boundary condition. A very fine mesh can be used since the size of the FEA model is largely reduced, thus the FEA data to represent the aperture vibration can be assumed to be accurate. After that, the FEA data are applied to the R-I integral to get the radiation pattern. This method combines both FEA and R-I method, and is called FEA&R-I method. Although FEA data are used in this method, it still uses R-I method to obtain radiation and thus regarded as a modified R-I based method. A refinement study of the two factors, Δr and $\Delta\varphi$ which are believed to impact the accuracy in the R-I based methods, is quickly processed and illustrated in Figure 3.13. Here, N_{ap} is the number of elements along the aperture plane ($\Delta r=r/N_{ap}$, r - aperture radius), and N_{th} is the number of elements in the angle φ ($\Delta\varphi=360^o/N_{th}$, $\varphi=360^o$).

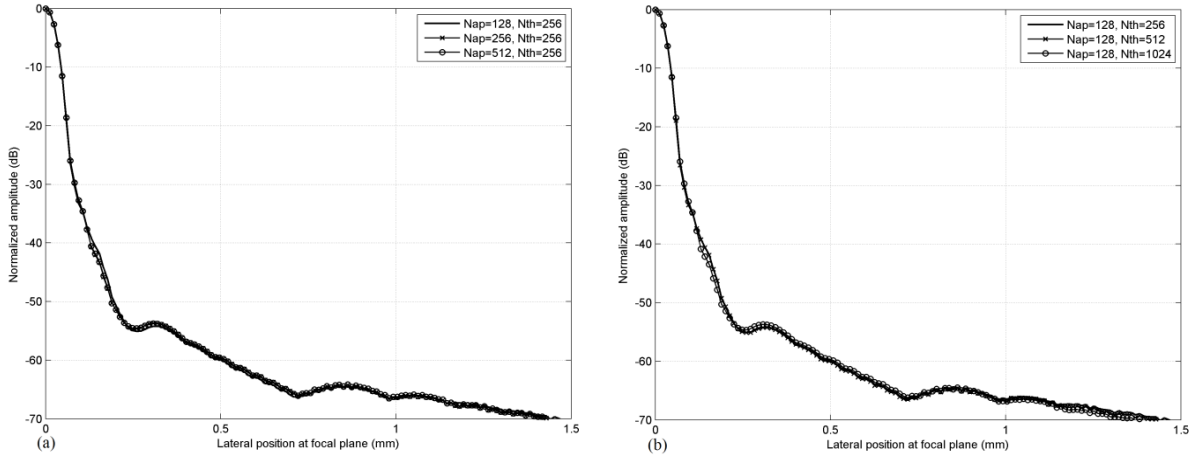

Figure 3.13 Radiation patterns by R-I method using (a) various N_{ap} but N_{th}=256, and (b) N_{ap}=128 but various N_{th}

It can be seen that there is no significant difference found in the patterns with increasing either N_{ap} or N_{th}, a N_{ap} of 128 and N_{th} of 256 is believed to show relatively accurate results by using R-I based methods.

Figure 3.14 then shows the radiation patterns of the 2mm annular array by using FEA, FEA&R-I and R-I method, respectively. It should be noticed that the accuracy of the two R-I based methods is also impacted by the factors of Δr and $\Delta\varphi$, according to the discretized R-I equation, namely Equation (3.10).

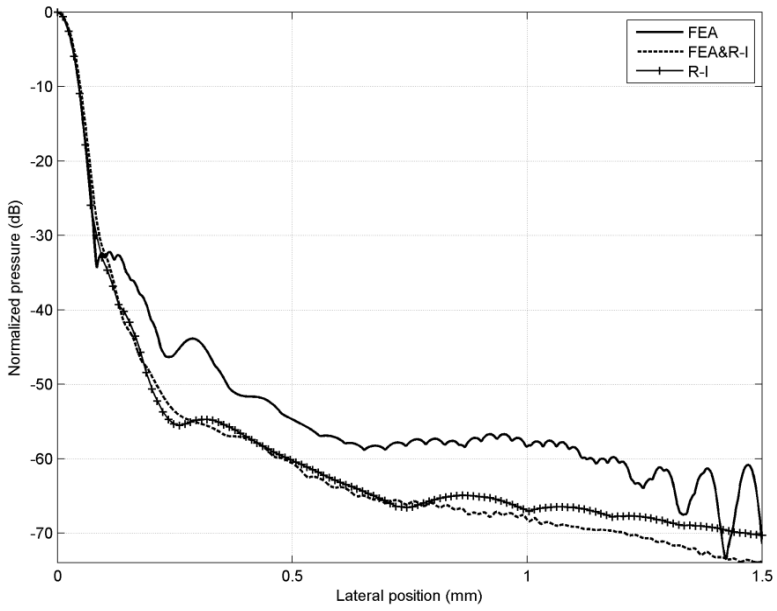

Figure 3.14 Radiation patterns by the three methods

From Figure 3.14, there is no significant difference between R-I and FEA&R-I pattern, but the FEA results has disagreement to the two R-I based results. This implies that the FEA pattern might not be very accurate likely due to the coarse mesh of $\lambda/8$.

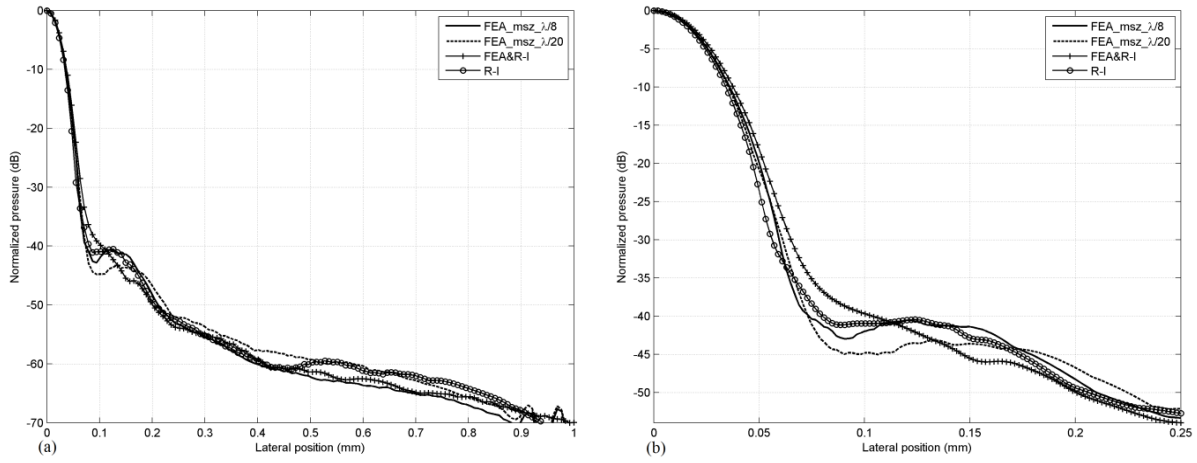

Figure 3.15 (a) Radiation patterns of the 1mm array by different methods, (b) the same patterns but in the region near sidelobe.

However, as discussed in Section 3.2, it is not possible to do a mesh refinement study for the 2mm, 45MHz array because of the limitation in our computer, while a smaller 1mm, 30MHz array model can be done due to the largely reduced number of FEA elements. The radiation of this 1mm array with mesh of $\lambda/8$ is found quite similar to the one using mesh of $\lambda/20$, with the detail given in Appendix D. Thus the two R-I based methods are applied to show the pattern of the 1mm array and compared to the FEA patterns with mesh of $\lambda/8$ and $\lambda/20$, as illustrated in Figure 3.15. Notice that "FEA_msz_$\lambda/8$" and "FEA_msz_$\lambda/20$" represent the patterns using FEA method with mesh size of $\lambda/8$ and $\lambda/20$, respectively.

It can be seen that a generally good agreement can be found among the patterns by the different methods, and a sidelobe can be found in the range from 0.1mm to 0.2mm. However, there are still some slight differences found, for example, the lower sidelobe level in the patterns by FEA with mesh of $\lambda/20$ and the slightly smoother sidelobe in the patterns by FEA&R-I method. These differences are again related to the accuracy issues of these methods. For the R-I method, the Gauss pulse is the source of inaccuracy; while for FEA and FEA&R-I method, the mesh size used to get FEA data could be the source. Nevertheless, the patterns for the small 1mm array model are generally comparable with using all these methods.

In terms of the larger 2mm array, the array we are targeted, its FEA pattern with mesh of $\lambda/8$ might not be accurate, and the nearest sidelobe might be reduced and become smoother if a finer mesh is applied. However, since a similar sidelobe is found in the patterns of the smaller 1mm array, it is still believed that the beam level is relatively stronger in this "sidelobe" region of 2mm array. It may be still necessary to suppress the nearest "sidelobe" level in the 2mm array pattern, at least this could provide a clear main lobe or equivalently improve the contrast since the beam level in the region about 150μm (or "sidelobe" region) from the focal axis is reduced. In addition, since the patterns by R-I and FEA&R-I method are similar to each other, only the R-I method is used in the following research as another tool for array radiation analysis. This is due to the R-I method being computationally less intensive and therefore quicker than the FEA&R-I method, which needs FEA data as element pulse inputs.

3.5.3 Potential Reasons for the Sidelobe

Two potential reasons are found that could explain the sidelobe formation. One is the vibrations in the outer elements, and another one is related to the influence of element bandwidth. Both FEA and R-I methods are used here for the analysis of the 2mm array.

In an array transducer, every element has its own contribution to the radiation pattern. The pulses from the elements constructively interfere at the focal point and form a large main lobe, because all the pulses share the same phase. But away from the focal point, the phase differs and makes the pulses either overlap or suppress each other to form the sidelobe and pedestal lobe in the annular array, for example. Therefore, the element contribution to radiation pattern is analyzed. By considering the large amount of time required for FEA modelling, only the first 4 inner elements are excited (partly-excite), instead of exciting the elements one by one. The pattern is then compared to the fully-excited array pattern, as illustrated by Figure 3.16. Both R-I and FEA method are used.

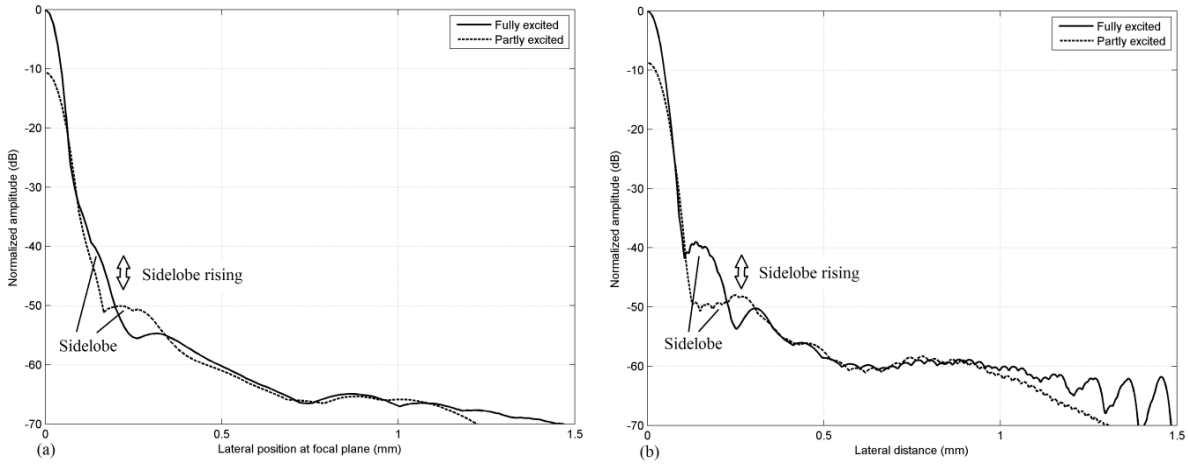

Figure 3.16 2-way pattern of the partly and fully excited EA array by FEA

First of all, it can be found that the pedestal lobe for both partly and fully excited arrays show the same level in the patterns by either R-I or FEA method. This agrees with the expectation made by Brown et.al [84] claiming that the level of pedestal lobe only depends on the value of EPD (element path difference), as the EPD for every element is the same in an EA annular array. The pedestal level would not be impacted by the changes in the number of exited elements. Secondly, since the contribution of every element to the main lobe peak is the same, the ratio of the main lobe peak of partly-excited array to the fully-excited array is expected to be close to 4/7 (≈0.57). It

is then found to be about 0.60 by FEA and 0.54 by R-I method. A good agreement has been achieved. This again implies that FEA radiation might not very accurate in the sidelobe region and beam level, but still could give some useful information and general trend of the radiation for the 2mm annular array.

More importantly, by using the FEA method, the pattern for the partly-exited array shows a smooth sidelobe in the range from 150 to 300μm, but an obvious sidelobe appears when the array is fully excited. By using the R-I method, the pattern for the partly-excited array also shows a smooth sidelobe in the same range, and the similar sidelobe rising can be found as well when the array is fully excited. However, the difference is that the sidelobe in the R-I pattern of fully-excited array is not obvious, while the beam level of this weak sidelobe is about -40dB, close to the level of the obvious sidelobe in FEA pattern. This implies that the pulses from outer elements are more likely to be overlapped to cause this sidelobe. By calculating the increment of sidelobe rising in the two patterns, the ratio of the level in partly excited array to fully excited one is about 0.58 with either R-I or FEA method used. This is very close to the ratio of the main lobe increment (≈0.60). It again suggests the strong overlap for the pulses emanated from the outer elements in the region of the weak nearest sidelobe.

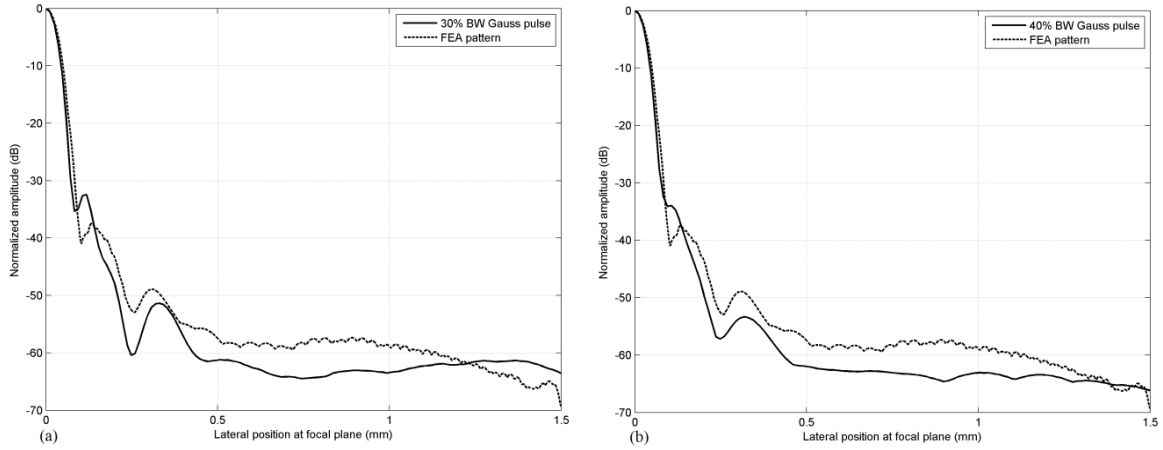

Figure 3.17 The R-I patterns with the Gauss pulse of (a) BW=30% and (b) BW=40%, with the comparison of FEA results

In addition, the element bandwidth is also believed to be related to the sidelobe, since the increase in bandwidth could suppress the unwanted sidelobe [4]. Its influence can be revealed by the R-I patterns using the Gauss pulse with decreased bandwidth (30% and 40%), as illustrated in

Figure 3.17. One reason to use R-I method is that the bandwidth change in R-I method can be easily and quickly achieved by changes in Gauss pulse settings. Here, the FEA pattern is re-displayed for comparison, while its element bandwidth is around 53%.

It can be seen that the nearest sidelobe in the R-I pattern appears when the bandwidth decreases, and the second sidelobe located around 400μm also becomes stronger in R-I patterns. General agreement in the positions of the two lobes can also be found between R-I and FEA patterns. The influence of element bandwidth on sidelobe can be clearly seen.

In addition, the ringing tail likely caused by the surface waves and the non-uniform vibration at the element surface, both of which were discussed in Section 3.5.1, might also have some effect on the radiation pattern. But due to the complexity of these non-ideal motions, their influence on the pattern is hard to measure.

Nevertheless, potential ways to suppress the nearest sidelobe could be related to the changes in the outer elements or the overall bandwidth. The detail about the sidelobe suppression is then discussed in the next Chapter.

3.6 Summary

The EA annular array analyzed in this research is set to have 2mm diameter, 7-elements, 45MHz centre frequency and f-number of 2. The choice of this specific array is based on the previous work on high frequency annular arrays, and it is regarded as a typical equal area high frequency annular array transducer. However, it is concluded that the results for this array can be applied across a whole range of arrays, and is not limited to this particular array. For example, the optimized design developed for the equal area annular array can be used in all equal area annular array transducers, in particular the array with aperture diameter around 2mm or smaller, since the kerfs width cannot be neglected in these cases. Meanwhile, the potential ways to suppress the sidelobe for this specific array might also be extended to other high frequency annular array transducers if the sidelobe is found. The summary of all the analysis is given as follows.

The conventional geometry design of an annular array in high frequency range shows its weakness in the consideration of kerfs, since the kerf width cannot be neglected due to a relatively small aperture. The EA condition would no longer be fully met by using the conventional design and leads to poor element tuning. Thus an optimized design with the consideration of kerfs is developed to give the exactly same area for every element. The element response and focal pulse of the array using this optimized design are comparable to the one using conventional design, and an improved imaging pattern is found. Both sidelobe and pedestal lobes are lower when the optimized design is used.

However, a sidelobe nearest to the focal axis is found in the FEA pattern of the EA array, but there is an accuracy concern due to the use of a coarse mesh. However, only a weak sidelobe is found in the patterns with using R-I and FEA&-R-I method, which is based on the direct calculation of the Rayleigh integral and is expected to provide a relatively accurate result. Although there are some disagreements in the patterns by FEA and the two R-I based methods, the FEA pattern is still believed to show the general trend of the array radiation. It is still necessary to suppress the sidelobe which might be weak if finer mesh is used in FEA, and this would at least increase the transducer contrast. Both the FEA and R-I patterns suggests that the sidelobe could be related to the outer elements based on the analysis of partly and fully-excited arrays, while element bandwidth also shows its influence on the sidelobes. The two potential methods to suppress the lobe are thus related to the changes in outer elements and element bandwidth, respectively. In addition, the non-ideal oscillation of the element might also have influence on the radiation, but the magnitude of this effect is uncertain.

Chapter 4 Methods of Sidelobe Suppression

4.1 Introduction

As the high sidelobe described in Chapter 3 could cause artefacts in the imaging patterns, it is essential to suppress the unwanted sidelobe that arises in the patterns of equal area (EA) annular array. From analysis in the last Chapter, the outer elements and bandwidth both show their influence on this sidelobe. Thus two methods to suppress the lobe are discussed here.

The first method is based on the increase of element bandwidth, which is believed to be effective on sidelobe suppression [4]. However, for high frequency transducers using PZT as ceramic layer, only double matching could achieve a relatively large bandwidth, but this suffers from fabrication difficulties. Alternatively, a high impedance single matching layer is developed and found to show bandwidth comparable to the double layer matching. The performances of this single high impedance matching procedure are then evaluated by both KLM and FEA model, likewise, its radiation pattern is also examined by both R-I and FEA method to check the effect on sidelobe suppression.

The second method concentrates on the mechanism of sidelobe formation. The pulse phase from outer element is designed to be make the pulse less overlapped based on a change in the array geometry, since the nearest sidelobe is found to be related to the element position in the aperture. Therefore, irrespective of the long or short element pulse, or equivalently narrow- or broad-band array, the nearest sidelobe is expected to be always suppressed. This method is firstly examined by R-I method here, while the discussion of its FEA performances is presented in next Chapter.

4.2 Sidelobe Suppression by Broadband

This 2mm diameter, 7-element annular array is found to have a bandwidth around 53% by the data given in Table 3.4 (KLM and OD entries). The further enlargement of this bandwidth is expected to suppress the unwanted sidelobe.

4.2.1 Bandwidth Improvement by Tuning

Almost all the annular array published so far had the bandwidth ranging from 20%-55% [44, 101, 102, 104, 106, 107, 114], while all these arrays used ceramic as their piezoelectric layers and a single matching layer. PVDF sometimes was also used as piezoelectric layer because of its very low acoustic impedance. Its mismatch to fluid medium is largely reduced. As a result, very wide bandwidth (larger than 100%) can be achieved, but at the cost of very low IL peak (<-30dB) because of the poor coupling coefficient of the material.

Besides that, using double matching instead of single matching could also improve the bandwidth at a lower cost of sensitivity, and gives a maximum bandwidth as high as 70%. The band could be even wider with more matching layers involved. However, double matching is rarely used in high frequency ultrasonic transducer, probably because of the fabrication challenges of the very thin matching layers with their thickness in the range of 5-20μm. It is already hard to lap down one matching layer to such a thin thickness, to realize two layers would considerably increases the fabrication difficulties. The accuracy of the layer thickness is another key factor; an error of several microns could already be another quarter-wavelength in high frequency applications. Coating more matching layers increases the probability of thickness errors and thus impacts the band performances. Therefore, PZT ceramic and single matching layer becomes the first choice in high frequency transducers.

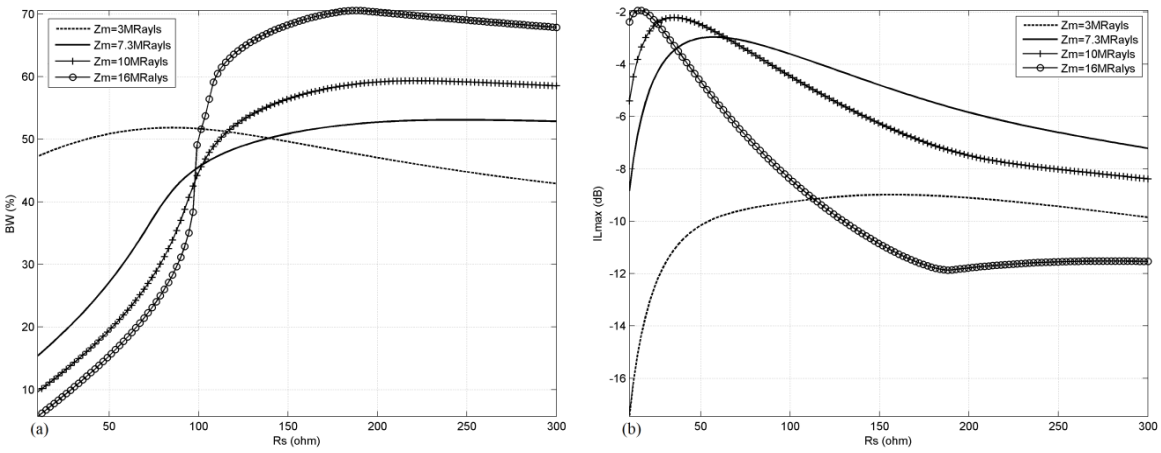

Figure 4.1 The influence of electric (R_s) and mechanical tuning (Z_m) on (a) fractional bandwidth and (b) IL peak value

However, another option to improve bandwidth is found by optimizing the tuning. Mechanical tuning is optimized by changing acoustic impedance(s) of matching layer(s), while the electrical tuning is optimized by changing tuning resistor *Rs*, as illustrated by Figure 4.1. It shows the bandwidth and sensitivity reflected by IL peak value (IL_{max}) for a typical 2mm, 7-element and 45MHz annular array with single matching layer, by different R_s and Z_m. All the responses are obtained by KLM model.

It can be seen that except the case of Z_m=3MRayls, the maximum achievable bandwidth by different matching layer at the location of Rs around 210Ω, a value generally following Equation (2.22). In terms of mechanical tuning, the matching layer of Z_m=3MRayls is sometime used in high frequency transducers because of the fabrication convenience. Most epoxies and polymers that could be relatively easy to coat to form a thin layer show their Z_m in the range of 2-4MRayls, but at the cost of low bandwidth and sensitivity. To realize so-called perfect matching, the epoxies must be loaded by other heavy particles to reach Z_m of 7.3MRayls, while it leads to the maximum bandwidth of 55% approximately by Figure 4.1. Here the perfect matching layer and the R_s following Equation (2.22) are described as the conventional tuning.

So far, materials of Z_m>10MRayls haven't been used as single matching layer. But it is found that the high acoustic impedance matching can give higher bandwidth. Although there is a loss found in the element sensitivity (or IL peak), the overall responses might be still comparable to the array using double matching layer, which is not easy to fabricate in high frequency transducer. Here, it is assumed that the two matching layers are realizable in our models just for comparison. The maximally flat approach is adopted in the design of matching layers. It aims at showing the flattest (or widest) frequency band, as expressed below [4],

$$Z_{m1} = Z_0^{4/7} Z_w^{3/7}\ ; \qquad Z_{m2} = Z_0^{1/3} Z_w^{2/3} \tag{4.1}$$

where Z_{m1}, Z_{m2}, Z_0 and Z_w are the acoustic impedance of the 1st matching layer (attached to the ceramic layer), the 2nd matching layer (attached to the fluid medium), ceramic material and water, respectively. Table 4.1 then lists the maximum bandwidth *BW* with its corresponding tuning resistor R_s, central frequency f_c and IL peak for the 4 matching options shown in Figure 4.1. The responses of double matching are also given. The materials for ceramic, backing layer and kerfs filler are all the same to the ones used in the previous model of the annular array.

Table 4.1 IL_{max} with maximum bandwidth *BW* with different matching layer(s)

Z_m (MRayls)	3	7.3	10	16	Double Matching
R_s (Ω)	86.8	237.2	218.8	190	210
f_c (MHz)	45.3	45.2	45.2	45.3	41.5
BW (%)	51.9	53.1	59.34	70.6	73.0
IL_{max} (dB)	-9.4	-6.4	-7.7	-11.5	-9.2

Improvement in bandwidth is found by using either higher acoustic impedance matching or double matching, while the slight loss in IL peak is also expected. Though the single matching of Z_m=16MRayls shows slightly narrower *BW* and lower IL, it has the central frequency closer to the designed value about 45MHz compared to the one of double matching. Generally, these two matching options are comparable. The application of single high acoustic impedance matching could be a good solution of the fabrication difficulties in double matching.

4.2.2 Element Behaviours by FEA

The numerical outcomes of the use of high acoustic impedance (Z_m=16MRayls) single matching are now evaluated by FEA, as well as the double matching. The materials used for these two matching options are listed in Table 4.2. A glass material could be found with an impedance of 16MRayls, while the epoxy "EPO-TEK 301-2" is loaded by different particles to achieve the required acoustic impedance of the 1st and 2nd layer in double matching.

Table 4.2 Parameters of the matching materials for Z_m=16MRayls and double matching

Layers	Material	Ref.	*Z* (MRayls)	*c* (m/s)	α (dB/mm ·MHz^{-1})
Single matching	Glass-flint	ONDA	16.0	4500	Very low
Double matching (Layer 1)	Tungsten-loaded EPO-TEK 301-2	[22]	9.15	1550	≈0.8
Double matching (Layer 2)	Alumina-loaded EPO-TEK 301-2	[22]	4.3	2620	≈0.5

*ONDA: ONDA Corporation, http://www.ondacorp.com/

First of all, the IL spectrums of the three representative elements (1st, 4th and 7th) of the EA annular array by using the two matching options are illustrated in Figure 4.2, with their band parameters listed in Table 4.3. The results of the conventional tuning (Z_m=7.3MRayls) are re-listed here for comparison.

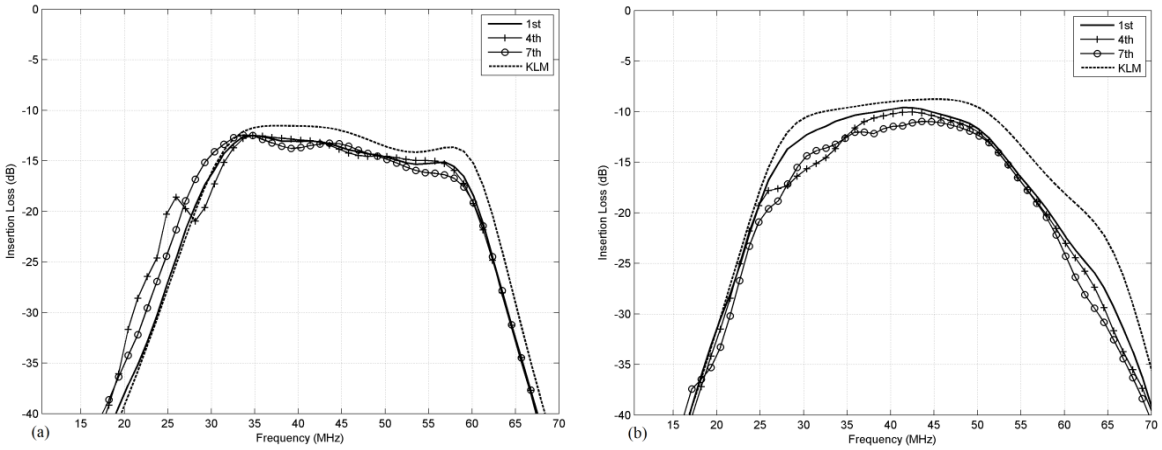

Figure 4.2 IL spectrums of the three elements using (a) Z_m =16MRayls and (b) double matching

Table 4.3 Parameters including IL peak IL_{max}, central frequency f_c and bandwidth BW

Element	Z_m=7.3MRayls			Z_m=16MRayls			Double matching		
	IL_{max} (dB)	f_c (MHz)	BW (%)	IL_{max} (dB)	f_c (MHz)	BW (%)	IL_{max} (dB)	f_c (MHz)	BW (%)
1st FEA	-8.4	44.1	53.5	-12.5	44.4	70.8	-9.6	40.4	67.8
4th FEA	-8.3	44.1	52.9	-12.5	44.8	66.8	-10.0	41.9	58.3
7th FEA	-8.7	43.8	54.5	-12.4	43.5	74.5	-11.0	41.6	64.2
KLM	-7.3	44.8	53.0	-11.5	45.3	70.7	-8.8	41.4	72.7

The results of FEA for all these matching options agree well with the ones of KLM model, but some differences are still found. FEA responses shows slightly lower IL peaks compared to the KLM results due to the extra lateral energy loss in FEA. Besides that, an additional minor peak is found in the FEA spectrum of the 4th element with Z_m=16MRayls; and the band of 4th and 7th element with double matching become more rippled in FEA. The minor peak is related to the weak lateral mode of PZ34 ceramic appearing around 27MHz, while the rippled band is ascribed to the lateral modes of PZ34 ceramic and the two matching layers. Nevertheless, these lateral modes show limited influence on frequency band, though the bandwidth of these elements are slightly smaller than their KLM results. Nevertheless, high-impedance matching layer shows comparable element responses to the double matching layer, especially the broad band.

4.2.3 Imaging Responses

FEA method is applied to show the imaging performances, including the beam pattern and pressure response at focal point for the arrays using the options of conventional matching

(Z_m=7.3MRayls), high-impedance matching (Z_m=16MRayls) and double matching. Their patterns are displayed in Figure 4.3, with the imaging parameters listed in Table 4.4. The definitions of the parameters can be referenced to Table 3.7.

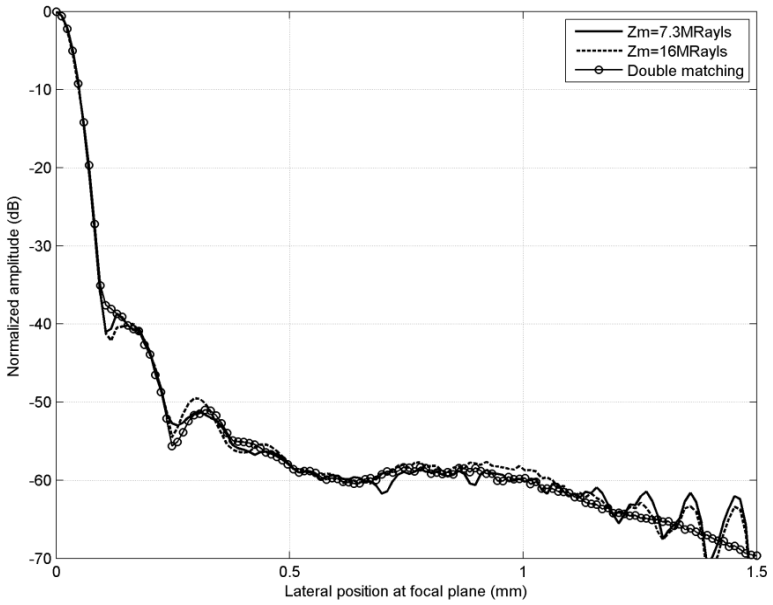

Figure 4.3 Beam patterns of the array using the three matching options by FEA

Table 4.4 Imaging parameters from the patterns of the array with different matching

Matching	***Res*** **(μm)**	X_{SL1} **(μm)**	SL_1 **(dB)**	X_{SL2} **(μm)**	SL_2 **(dB)**	X_{PeL} **(μm)**	***PeL*** **(dB)**
Z_m**=7.3MRayls**	74.8	137.6	-39.0	306.0	-50.2	882.8	-58.9
Z_m**=16MRayls**	74.5	162.2	-39.9	300.0	-49.5	887.4	-57.7
Double matching	77.0	(150)	(-40)	322.9	-50.1	864.4	-58.4

* (150), (-40) means that no clear peak is found in the lobe

It can be seen that all the patterns are generally similar, with the similar level and position of second sidelobe and pedestal lobe. But no significant suppression of the nearest sidelobe is found by using single matching of Z_m=16MRayls. Although the pattern of double matching might is smoother than the other two in the region of nearest sidelobe, the lobe level only shows -1dB drop. The expected sidelobe suppression by a broadband array is not found. The possible reasons might be related to the non-ideal motions at the element surface, since both the ringing tails due to surface waves and non-uniform surface vibrations are found in the arrays with Z_m=16MRayls and double matching layer and possibly cause some complicated oscillations after the main pulse.

This ringing could limit the bandwidth improvement in the pressure pulses emanated from every element, or the actual bandwidth increment in element pulses are not as large as the value that IL spectrum shows.

However, the failure of broadband array in sidelobe suppression doesn't mean it is totally useless in the imaging performances. It does show positive effect on another important imaging measure, the pressure pulse at focal point. Figure 4.4 illustrates the pressure pulses at focal point in both time and frequency domain by the arrays using the three matching options. The parameters obtained from the pressure responses are listed in Table 4.5, including maximum amplitude P_{max}, -6dB pulse length $PL_{(-6)}$, central frequency f_c and fractional bandwidth BW.

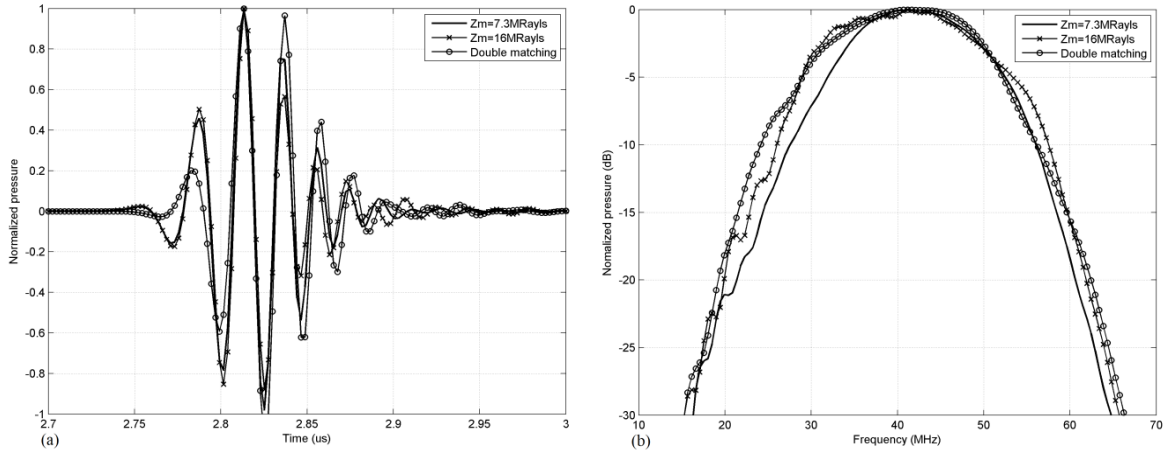

Figure 4.4 The pressure pulses at focal point in both (a) time and (b) frequency domain for the array with different matching

Table 4.5 Parameters from the pressure at focal point of the array with different matching

Matching	P_{max} (10^5 Pa)	$PL_{(-6)}$ (ns)	f_c (MHz)	BW (%)
Z_m=7.3MRayls	2.52	56.8	41.3	55.3
Z_m=16MRayls	2.43	51.7	41.6	63.3
Double matching	2.89	53.9	40.5	61.2

It can be found the pulses of the array with Z_m=16MRayls has the smallest P_{max}, which agrees with the lowest IL peaks listed in Table 4.3 by using FEA. And P_{max} of double matching is the largest, though it shows relatively low IL peak. The pulse of all the arrays are found short and without significant ringing, since the main pulse emanated from every element is designed to be subject to constructive interference at the focal point. In addition, the central frequencies of the pulse at

focal point also agree well with the expectations obtained by the IL spectrums of array elements. The improvement in pressure bandwidth is demonstrated with at least 10% increment by using single matching of Z_m=16MRayls, which is even larger than the double matching. As a result, better axial resolution is achieved.

To summarize, the high impedance single matching (Z_m=16MRayls) shows some bandwidth improvement in IL spectrums by using an optimized tuning. Although the enlarged bandwidth is at the cost of IL peak or sensitivity, the high impedance matching is still comparable to the double matching, or even better. In terms of the imaging performances, only very limited suppression in sidelobe can be seen, probably due to the non-ideal motions at the elements. Nevertheless, the broad band arrays do have positive effect on the pulse at focal point, showing improved axial resolution. More importantly, single high impedance matching could be very useful in high-frequency single element transducers to replace the double matching design, since the single-element transducer shows a simple and more-ideal element oscillation. The bandwidth improvement could be more effective on radiation pattern. This is detailed in one of our submitted papers.

4.3 Sidelobe Suppression by Geometric Change

The cross coupling in the outer elements is found to be the main source of the unexpected sidelobe in FEA patterns, but it cannot be significantly reduced by using broad band array. Therefore, we here describe a method of sidelobe suppression based on geometric modification. First of all, the mechanism of sidelobe formation is investigated by numerical method.

4.3.1 Sidelobe Analysis of EA Annular Array

The numerical evaluation of radiation patterns based on the solution of the Rayleigh integral was discussed in Section 3.4. Two factors in the integral are found to be crucial to determine the pressure along the focal plane. One is the distance R between a point at the focal plane to another one at the array aperture, of which the expression is given by Equation (3.11). When the pressure pulse from a single point at the array aperture arrives at a certain point at the focal plane, its

amplitude is inversely proportional to R. Another factor is the total time delay t_d given by Equation (3.13), determining the phase of the element pulse at focal plane.

The pattern is then obtained by the summation of numerous pulses travelling from element aperture to the focal plane, or R-I method. However, it is hard to analyze the influence of ever single element on sidelobe formation because there are numerous pulses involved. Therefore, a simple "assumption" is made here, the pressure pulses of every element are represented by the pulse at its centre point R_c, as is illustrated in Figure 4.5.

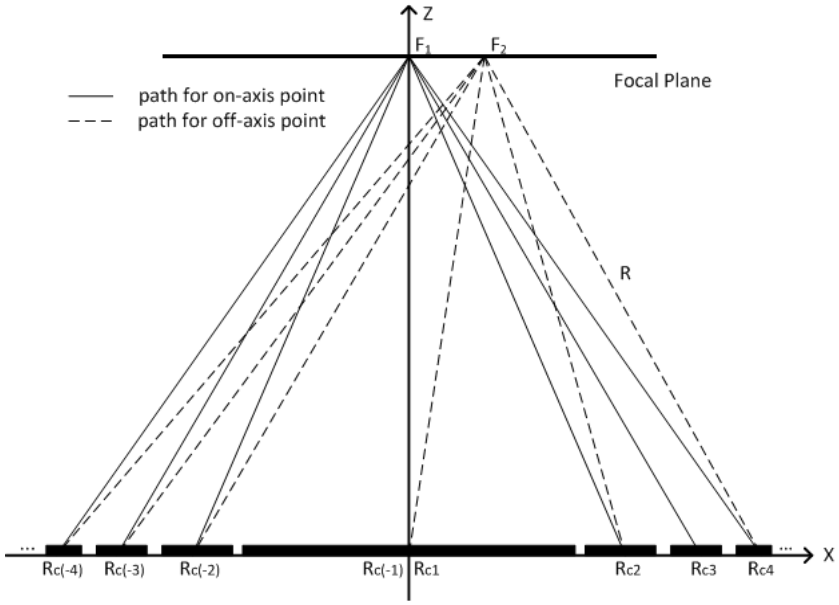

Figure 4.5 The cross section of an EA annular array to focus in the medium

It should be noticed that every element is an annulus and actually shows two centre points in the cross-section except the 1st element, namely both the right and left centres are displayed in Figure 4.5. To represent both the two centre points, subscript *N and –N* are introduced, where *N* is the element number. The positive *N* represents the right centres of the annular element, while the negative *N* denotes the left ones. However, since 1st element only has one centre, the assumption, $R_{c(1)}=R_{c(-1)}=0$ is defined. The distance *R* is also displayed in the figure to the points on- and off-axis along the focal point, and *R* is sometimes called "Element Path" [84]. In addition, the off-axis point F_2 at the focal is set to have the coordination (r_f, F), where r_f denotes distance away from the focal axis and F is focal distance.

However, the assumption of representing an element as a point is far too simple and would lead to inaccuracy. But it at least could reveal the relation between element pulse and sidelobe, as detailed later. The pulse of every element at a certain point in the focal plane only has two factors of R and t_d, the expression of the two factors then becomes the following equations with the total phase shift φ_d simply transferred by t_d, where t_{fN} is given in Equation (3.12)

$$t_{dN} = R_N/c + t_{fN}; \qquad \varphi_{dN} = t_{dN} \cdot 2\pi f \tag{4.2}$$

$$R_N = |F_2 - R_{cN}| = \sqrt{\left(r_f - R_{cN}\right)^2 + F^2} \tag{4.3}$$

The array to be analyzed here is the same one modelled by both R-I and FEA method, having 7 EA annular elements, 2mm diameter, 4mm focal distance and 45MHz operating frequency. The unexpected sidelobe located in the range of 100-200μm in the FEA pattern displayed by Figure 3.7 is of most interest, thus the distance r_f away from focal axis is set to be 140μm which is also the location of sidelobe peak. With the element centre R_{cN} (positive N) ranging from 0-1mm, it is found that the distances R_N to the off-axis position F_2 for every element are very close to each other. It implies that the amplitude of each element pulse at the point of (r_f, F) is similar. The R factor is not important in the region of nearest sidelobe.

However, the very small change in distance R might cause large change in time delay t_d or phase shift φ_d, while t_d or φ_d is the only influential factor that determines the overlapping of the 7 element pulses at the off-axis position. By using Equation (4.2) and (4.3), t_d and φ_d are calculated but found to be very large values that are hard to analyze. Therefore, another parameter named phase difference φ_{dif} is introduced and defined as the difference of the φ_d in the two nearby elements. Likewise, time difference t_{var} is also defined. Equation (4.4) then shows the expression of both φ_{dif} and t_{dif}.

$$\varphi_{dif(N)} = \varphi_{dN} - \varphi_{d(N-1)}; \qquad t_{dif(N)} = t_{dN} - t_{d(N-1)} \tag{4.4}$$

Notice that the undefined φ_{d0} appears when N=0 and 1 in above equations, hence, it is assumed that $\varphi_{d0} = \varphi_{d1} = \varphi_{d(-1)}$. This assumption leads to the phase/time difference of 0 for the central element; it physically means that the single centre point of 1st element does not show any phase or time difference. With a given r_f of 140μm, the values of φ_{dif} are listed in Table 4.6.

Table 4.6 Phase difference φ_{dif} of every element pulse at off-axis point (r_f, F); subscript N and $-N$ denote the right and left parts of each element, respectively

EA Element	1st	2nd	3rd	4th	5th	6th	7th
$\varphi_{dif(N)}$ (°)	0	-159.7	-52.8	-43.3	-37.8	-34.1	-31.4
$\varphi_{dif(-N)}$ (°)	0	-158.7	-52.2	-42.6	-37.1	-33.4	-30.4

The phase differences in the right part of the array are firstly investigated, the close values of φ_{dif} for the outer 3 elements indicate that their phase shift φ_d varies within the range of approximately 100°. The strong overlapping of the pulse would occur in this phase range if the pulse is not very short or with very broad band. On the other hand, the inner elements then show a relatively large φ_{dif}, especially the first two. The largely varied φ_d implies the complicate pulse overlap or suppression, but at least no strong overlapping would appear.

In terms of the left part in the array, the phase differences of the elements are quite similar to their right parts, thus a similar pulse overlap or suppression is expected. However, the overall pattern (or sidelobe) is the combination of the element pulses in both left and right parts; these pulses may be coupled and results in complicated overlap or suppression.

Thus the phase differences between left and right parts are analyzed. However, since the phase differences listed in Table 4.6 is the one between the two nearby element centres. The phase difference between the left and right element is directly calculated by $\varphi_{d(N1)} - \varphi_{d(N2)}$, where subscript N1 and N2 are the number of the element in either left or right part of the array. The smallest phase difference is found between $\varphi_{d(2)}$ and $\varphi_{d(-2)}$ showing the value about 320°, while the largest value is between $\varphi_{d(7)}$ and $\varphi_{d(-7)}$ with the value of 710° approximately. Since the element pulses in ultrasonic transducers are usually quite short, at least the main pulse, the phase differences ranging from 320° to 710° could already be large enough to separate the pulses from either suppression or overlap. In other words, the pulse overlap in the nearest sidelobe region only depends on one part of the array, either left or right.

To summarize, the outer elements show the phase shift close to each other, the corresponding strong pulse overlap becomes the main source of the nearest sidelobe. Though the lobe is not clear with broad band array by using R-I evaluation, the cross coupling in FEA actually reduces the

bandwidth and make the high sidelobe apparent again. A method is then applied to reduce the pulse overlap in outer elements regardless of bandwidth by changing the geometry of annular array.

4.3.2 Sidelobe Suppression by Novel Array Geometry

The small phase difference in outer elements potentially causes the strong pulse overlap and leads to the nearest sidelobe. The separation of these phase differences could effectively decrease the pulse overlapping. Fresnel approximation expressed in Equation (4.5) is used to deduce Equation (4.2) to show the relation between phase and the element.

$$\rho = \sqrt{X^2 + Y^2} = Y + X^2/2Y \tag{4.5}$$

The approximation is always valid when $Y >> X$. Thus by using Fresnel approximation on distance R given by Equation (4.3), where the condition of "$F >> |r_f - R_{cN}|$" generally valid, Equation (4.2) is transferred into the following forms,

$$t_{dN} = T_0 - \frac{r_f \cdot R_{cN}}{Fc} \quad ; \quad \varphi_{dN} = t_{dN} \cdot 2\pi f \tag{4.6}$$

$$T_0 = \frac{r_f^2}{2Fc} + \frac{F}{c} + t_0 \tag{4.7}$$

where T_0 is a constant regardless of element centre position if the off-axis point at focal plane are determined. By Equation (4.6), it is found that the time delay or phase shift only depends on the positions of element centres.

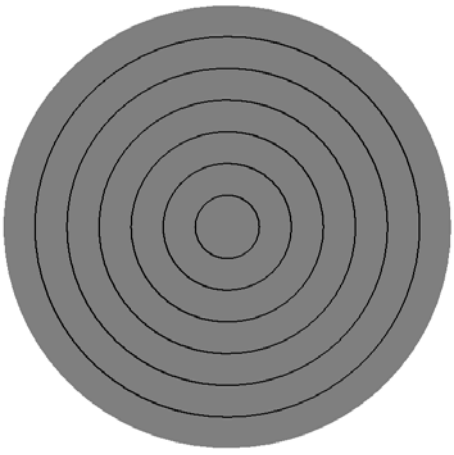

Figure 4.6 Front view of a 7-element EW annular array

Therefore, the close phase shifts in EA outer element is due to their close centre positions. The separation of the element centre could leads to the separation of phase shifts and less pulse overlapping, so the sidelobes could be reduced. Thus different from geometry of EA annular array, an equal width (EW) annular array is developed and illustrated in Figure 4.6, of which its elements in either left or right parts all share the same width. Notice that the width of 1st element is assumed to be its radius, the actual width is doubled to its radius since its left and right parts are combined together to form a disk.

As a result, the outer elements in EW array are more separated, while the inner ones become closer to each other compared to EA array. Thus the phase difference between the two nearby elements are expected to be same due to the equal separation in element centre except the 1st and 2nd element, as listed in Table 4.7. Meanwhile, the distance *R* by Equation (4.3) for every element still changes very little so that its influence is nominal.

Table 4.7 Phase difference φ_{dif} of the pulse in every EW element at off-axis point (r_f, F)

EW Element	1st	2nd	3rd	4th	5th	6th	7th
$\varphi_{dif(N)}$ (°)	0	-80.9	-53.7	-53.3	-52.7	-52.0	-51.0
$\varphi_{dif(-N)}$ (°)	0	-80.7	-53.3	-52.8	-52.0	-51.0	-49.9

It can be found that the phase differences for most EW elements are in the level of -52°, the larger value between 1st the 2nd element is caused by the doubled width of 1st element. Likewise, only one part of the array elements determines the sidelobe. Compared to the phase difference of EA annular array listed in Table 4.6, the phase differences in the outer elements of EW array become larger, the strong overlap in sidelobe region would be reduced. Meanwhile, though the phase differences in inner element of EW array is smaller, their values are still relatively large to prevent the strong overlap. Therefore, the high nearest sidelobe will be suppressed by EW geometry, regardless of either long or short element pulses.

With the consideration of kerfs between the adjacent elements, the design of EW geometry follows the equations given below,

$$r_{i(n)} = \frac{R}{N}(n-1) + \frac{w_g}{2} \quad ; \qquad r_{o(n)} = \frac{R}{N} \cdot n - \frac{w_g}{2} \tag{4.8}$$

where R, N and w_g is the aperture radius, total element number and the gap width between nearby elements, respectively. And $r_{i(n)}$ and $r_{o(n)}$ are the inner and outer radius of the n^{th} element respectively. In particular, since the 1^{st} element is not an annulus but a disk, inner radius has no physical meaning and is assumed to be 0 to describe the element centre instead.

The R-I evaluation is then used to obtain the patterns of EW array to show its effectiveness on sidelobe suppression. Like the model of EA array, the EW array also has 7 elements, 2mm aperture, 45MHz operating frequency and a 4mm focal distance. Since the transverse waves could potentially reduce the bandwidth, the patterns of EW arrays by the pulses with BW of 30%, 40% and 53% are displayed in Figure 4.7 and compared to the ones of EA array. Specifically, BW=53% is regarded as the bandwidth obtained by perfect matching or an ideal response.

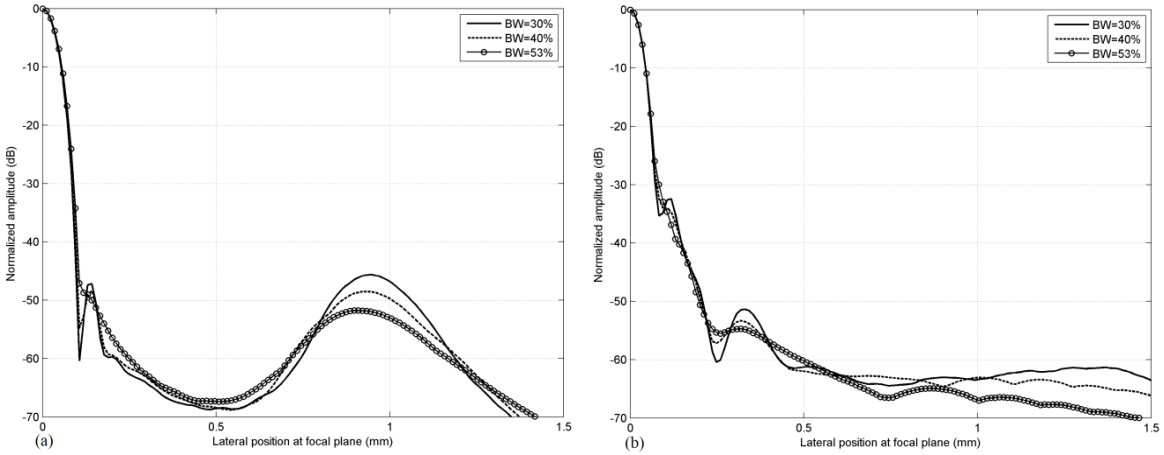

Figure 4.7 R-I patterns of (a) EW array and (b) EA array with various bandwidth

Table 4.8 Parameters obtained by the R-I patterns of EA and EW array with element pulses with different bandwidth

***BW* (%)**	***Array***	P_{max}	***Res* (μm)**	X_{SL1} **(μm)**	SL_1 **(dB)**	X_{SL2} **(μm)**	SL_2 **(dB)**	X_{PeL} **(μm)**	***PeL* (dB)**
30	**EA**	1.0	70.1	113.1	-32.1	329.5	-51.7	894.0	-63.1
	EW	0.8	84.0	136.2	-46.8	-	-	943.7	-45.6
40	**EA**	1.0	70.4	106.4	-34.0	319.1	-53.3	994.7	-63.1
	EW	0.8	85.5	139.8	-48.3	-	-	924.7	-48.5
53	**EA**	1.0	71.0	-	-	316.2	-54.7	865.8	-64.9
	EW	0.8	88.2	(121)	(-48.6)	-	-	906.8	-51.8

* (121), (-48.6) means that only a very weak lobe peak is found

Table 4.8 then lists the imaging parameters of EW arrays and compared to the results of EA array, including P_{max} denotes the maximum pressure or main lobe peak and is normalized by the largest value of P_{max} in the table, the definitions of other parameters can be referenced to Table 4.4.

Similar to EA array patterns, the nearest sidelobe become apparent for the pulse with lower bandwidth, but somehow invisible for pulse with broad band as expected. Only a weak lobe is found in EW pattern by 53% BW pulse. More importantly, the nearest sidelobe levels for the element pulse with 30% and 40% in EW array are much lower than the ones in EA array. The suppression of sidelobe with EW array has been proved by R-I method.

But unfortunately, another lobe in EW array appears in the region of pedestal lobe in EA array. And the differences between the patterns of EA and EW array are also found in their main lobe peak and resolution. The details will be instructed in the following section.

4.3.3 Analysis of the R-I Patterns

EW arrays are found to show a lower main lobe peak P_{max} compared to the EA arrays. It is caused by the differences in element area between the two arrays. Different element area leads to different natural focal distance Z_t. It is a focal distance where the on-axis pressure P_{max} of each element achieves its maximum value. Since Z_t is proportional to the element area ($Z_t = S/(\pi\lambda)$; S – element area, λ wavelength), large variance in Z_t is expected in EW array elements, while the same value in EA array elements. For the annular array showing the focal distance F of 4mm at focal axis, the maximum pressure amplitude or main lobe peak $P_{e(max)}$ of every single element at focal point is determined by the distance between F and Zt. The values of Z_t and $P_{e(max)}$ are listed in Table 4.9 for every element in both EA and EW arrays. Here, $P_{e(max)}$ is obtained by directly using Hankel transform of the element aperture. Although the resulting beam of the single element is an impulse response, the main lobe peak $P_{e(max)}$ maintains the same when the pulse function is convolved into the impulse response. Thus a so-called FHT (Fast Hankel Transform) method is used instead of R-I method, because FHT has the same accuracy in predicting the main lobe peak and much quicker efficiency. And all P_{max} in the table are normalized to the appropriate element in the EA array.

Table 4.9 Z_t and normalized P_{max} for every element in EA and EW arrays

Element		1st	2nd	3rd	4th	5th	6th	7th
EA	Z_t **(mm)**	2.9	2.9	2.9	2.9	2.9	2.9	2.9
	P_{max}	1.0	1.0	1.0	1.0	1.0	1.0	1.0
EW	Z_t **(mm)**	0.44	1.29	2.15	3.01	3.87	4.73	5.59
	P_{max}	0.21	0.61	0.94	1.17	1.25	1.20	1.02

Same P_{max} is found in all EA elements, and achieves the maximum value in 5th element of EW array because of its closet Z_t to the focal distance F of 4mm. Since overall main lobe peak of the array aperture is the summation of the main lobe peak for every individual element, it is found that the overall peak in EW array is approximately about 80% of EA array. It agrees very well with the P_{max} results of EW array to EA arrays in Table 4.8. The good agreement proves that the difference in P_{max} is caused by the difference in element area, or namely Z_t.

The EW array is also found to have a relatively larger resolution than EA array. It may be explained by the distribution of element. In theory, the resolution of an aperture only depends on the f-number if the lens applied to the aperture is perfectly curved. However, in array transducer, the electronic phase shift is applied to each element to simulate the physical lens. The wavefronts of the element pulses illustrated in Figure 2.8 form a so-called electronic lens. However, the curvature of the electronic lens is not as perfect as mechanical one, since wavefronts from a single element is usually flat but not curved. It is also the reason that the resolution of an array transducer in FEA or experiment is always slightly larger than the theoretical value. More importantly, the elements in EA array show same area, which means that every element has the same contribution to the electronic lens. In detail, the same amount of element area refers to the same amount of the changes in the centre angle of the lens. For example, the widest 1st element is show a certain amount of centre angel closet to focal axis; to have the same change in centre angle far from the focal axis, the narrowest 7th element is required. The elements in EA array contain the same changes in lens curvature. On the contrary, the 1st element in EW is narrowest while 7th is widest. The outer elements in EW array have much more curvature change than EA ones, therefore, the electronic lens formed by EW array is not as good as the one of EA array and leads to the larger resolution.

Besides that, a large lobe is found in the pedestal lobe region in the patterns of EW array. It is found that the lobe is actually the grating lobe usually appearing in linear array. This is probably due to that the EW elements is also linearly distributed along the array aperture. The position of grating lobe can be obtained by the following equation [4],

$$\theta_g = \arcsin(\lambda/p) \quad ; \quad r_g = F \cdot \tan(\theta_g) \tag{4.9}$$

where ϑ_g and r_g is the angular and lateral position respectively, p denotes the element pitch and equals to R/N in EW array, and F is the focal distance. Thus the calculated value r_g is about 0.96mm, and generally agree with the lobe position of FEA ranging from 0.9 to 0.95mm. Similar to the linear array, the level of pedestal lobe decreases with increasing element bandwidth, as demonstrated by Figure 4.5(a) as well.

4.4 Summary

First of all, the method of using broadband array to suppress the unwanted sidelobe seems not very effective, very little improvement is found in nearest sidelobe region even for a nearly 70% bandwidth array. The possible reason might be related to effect of the complicated non-ideal element vibration. Nevertheless, the broadband arrays do show some positive effect on the pressure pulse at the focal point, a wider band can be seen compared to the conventional single matching. As a result, finer axial resolution is achieved. Furthermore, a high impedance single matching with optimized tuning is proved to show comparable bandwidth to double matching. It could be a good replacement of double matching in high frequency transducer, especially the single-element one.

In terms of the second method based on geometry change, the novel EW annular array shows a large suppression of the nearest sidelobe compared with the EA array. By using the simplified form of Rayleigh integral, it is found that the accumulation of the pulses from every element actually relates to the element position, EW annular array is thus designed to enlarge the difference of phase shifts in outer elements to reduce the chances for their pulses to be overlapped in the sidelobe region. The changes in the sidelobe formation show the effectiveness on sidelobe suppression, and this is demonstrated by R-I evaluations. The FEA performances of EW annular array will be discussed in the next Chapter.

Chapter 5 High Frequency Equal Width Annular Array

5.1 Introduction

The R-I pattern of the equal width (EW) annular array shows successful suppression of the nearest sidelobe appearing in the pattern of the equal area (EA) annular array. The FEA method is then applied to model the EW array responses by again investigating the element and imaging performances. Although the FEA method for the 2mm array might not be very accurate, it still could provide some useful information and a general comparison to the R-I evaluation.

One of the element parameters analysed is the spectrum analysis including the element impedance and insertion loss (IL). Both the impedance and IL spectrum for the EW array are expected, and also found to be, quite similar to the EA ones. This is due to the same materials used in the transducer, as well as the dominant T-mode vibration of the piezoelectric ceramic PZ34 regardless of element width. Another part is the element pulse responses in the time domain, the responses of the EW array are also found to be similar to the EA ones, but with slightly weaker ringing tails.

More importantly, the FEA imaging responses of the EW array shows the sidelobe suppression, while the pedestal lobe becomes apparent. This agrees with the analysis given by R-I method in the last Chapter. In addition, the pressure pulse at the focal point is also given by FEA, and found to show very similar pulse properties compared to the EA array, while the difference is the slightly weaker ringing in the focal pulse of the EW array. This might be related to the weaker ringing tails in the EW element pulse responses. Nevertheless, both EA and EW array shows a comparable pulse response at focal point, as well as the sidelobe suppression. Although the pedestal lobe in EW array has a significant increment, its overall sidelobe level is still lower than the EA array.

However, the FEA responses of the EW and EA arrays so far is based on a 7-element geometry, while their imaging performances are found to be related to the total element number. The discussion about the arrays with different element number is taken by the following 4 aspects - pressure pulses at focal point, resolution, sidelobes and the fabrication. The comparison between EA and EW array in these fields suggests that EW array has advantages in the performances of

sidelobe suppression, less ringing, and the fabrication; while the cost could be the resolution but this is also dependent on element number.

5.2 Performances of Equal Width Annular Array

The improvement on sidelobe suppression is demonstrated by the R-I evaluations of equal width (EW) annular array. FEA method is then used to show the effectiveness of the EW array on sidelobe suppression. Likewise, the EW array has all the same characteristics as EA array, except the element size in radial direction. In detail, the array has 7-element, 2mm diameter, 30μm kerfs, 45MHz operating frequency, 4mm focal distance (or f-number of 2) and the same material for every layer (PZ34 as ceramic, loaded epoxy for 10MRayls backing and 7.3MRayls single matching layer).

5.2.1 Element Responses

The response of every element in EW array is firstly analyzed, to reveal its sensitivity, bandwidth, lateral mode and coupling by its impedance, IL (insertion loss) spectrum and pressure output. The 3 elements in the central (1^{st}), middle (4^{th}) and outermost (7^{th}) position are investigated as the representatives of the whole EW array. Figure 5.1 displays the amplitude and phase angle of their impedance spectrums by FEA.

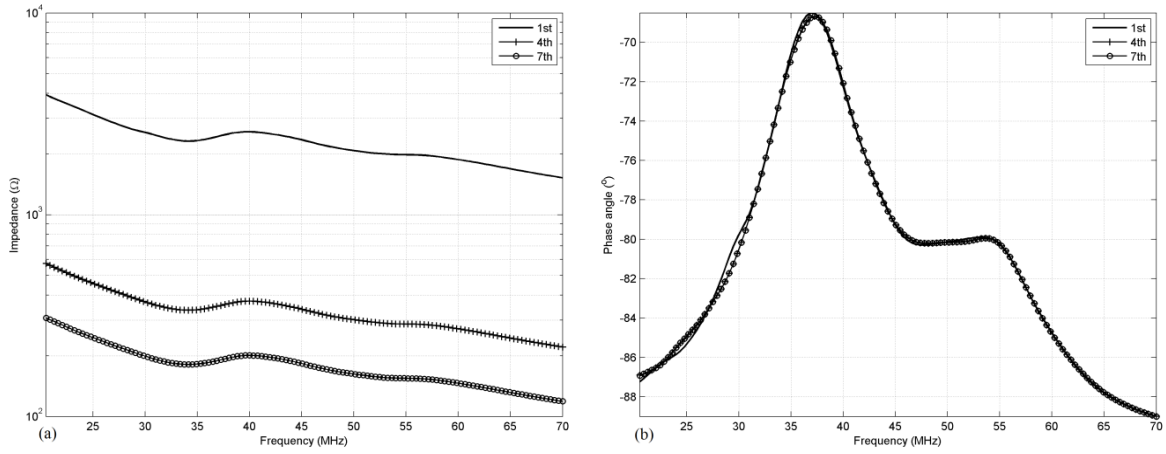

Figure 5.1 (a) Amplitude and (b) phase of the impedance spectrums of the 3 elements by FEA

The amplitude of the impedance decreases by the increase of element number due to the differences in element area. The phase spectrum implies that all these elements almost show

same resonances with the obvious resonance of T-mode (left peak) and matching layer (right peak), and no other spurious modes. IL spectrum is then illustrated in Figure 5.2, with the response of KLM model as a reference. Good agreement between KLM and FEA has been achieved, and all the array elements show a clean and broad band. The band parameters for the three elements and KLM model are listed in Table 5.1, including IL peak IL_{max}, central frequency f_c and fractional bandwidth *BW*.

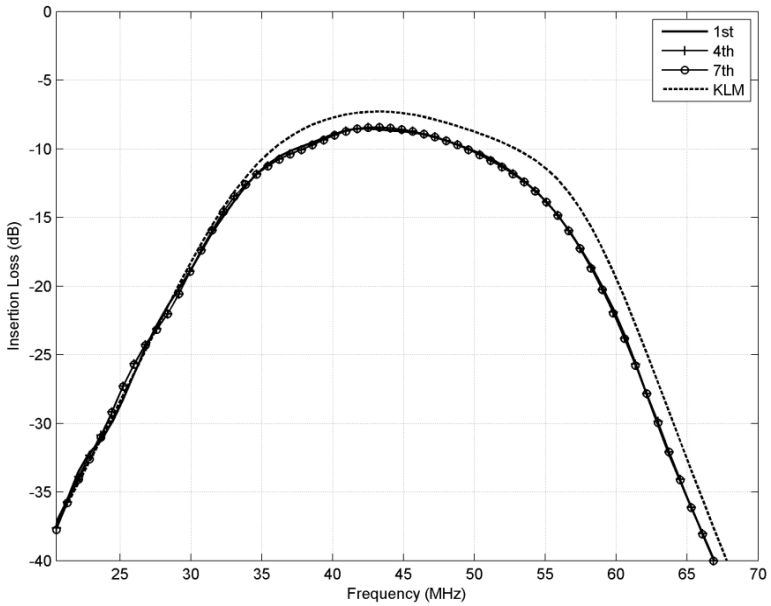

Figure 5.2 IL spectrum of the three EW elements by FEA compared to KLM model

Table 5.1 Element pulse responses derived from IL spectrum for EW array

Element	IL_{max}(dB)	f_c(MHz)	*BW* (%)
1st	-8.5	44.1	52.3
4th	-8.4	44.0	52.6
7th	-8.4	44.0	52.6
1D model	-7.3	44.8	53.0

Compared to the KLM results, the slight loss in IL_{max} is again found in FEA method and due to the extra lateral energy dissipation in the array. Compare to the IL spectrums of EA array displayed in Figure 3.5, the responses in EW elements are more identical to each other without any evidence of weak minor peaks in outermost elements. The weak lateral mode has been moved out of the interested band by increase of width in outer elements.

The vibration of the three EW elements (excited one by one) is also examined by FEA method, as illustrated in Figure 5.3. Likewise, the element pulse is shown at the three positions displayed in Figure 5.3(a). The time domain pulses are transferred into frequency domain by FFT, and again 1/3 octave fitting is applied to band spectrum to avoid abrupt changes probably caused by the ringing.

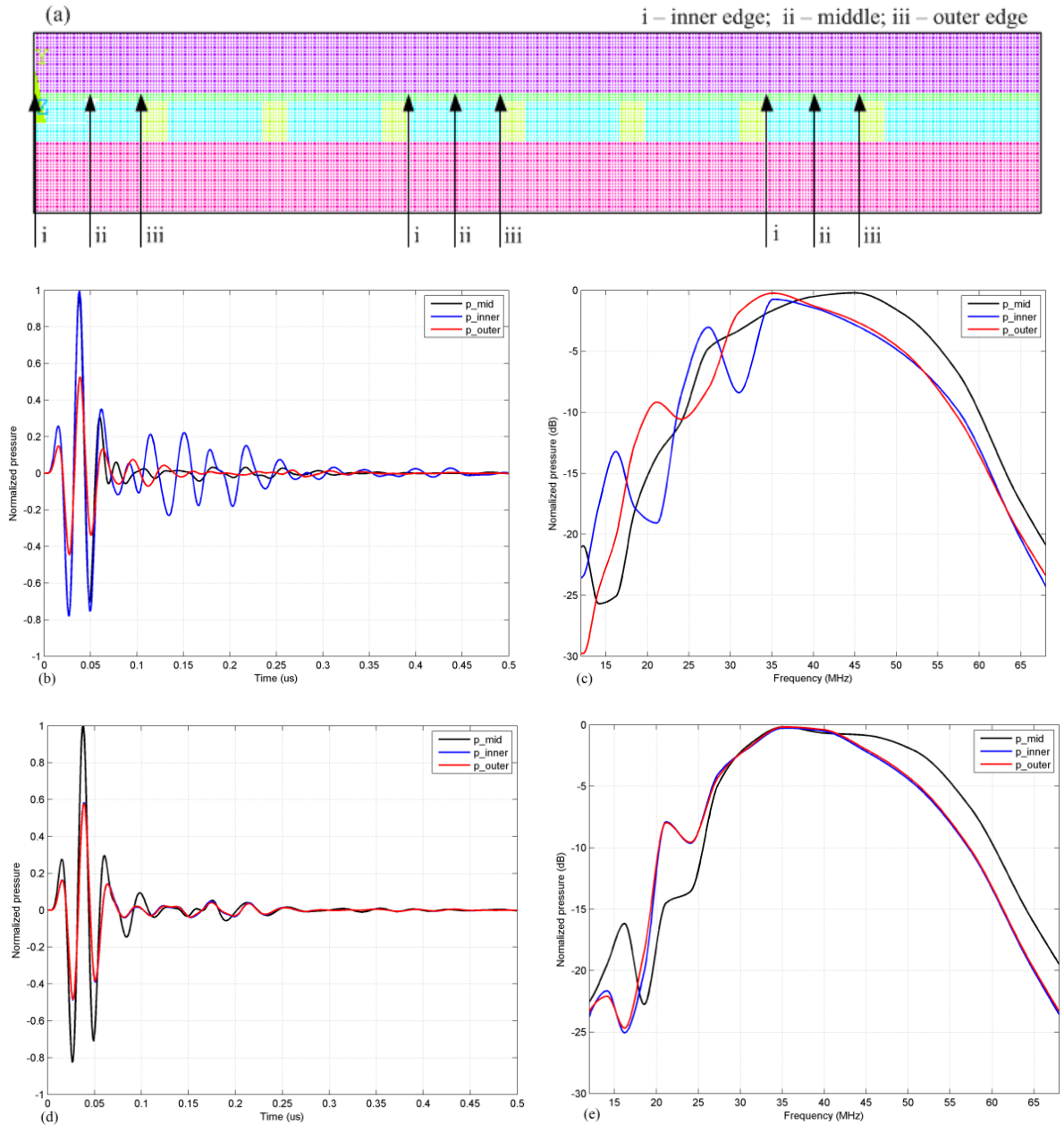

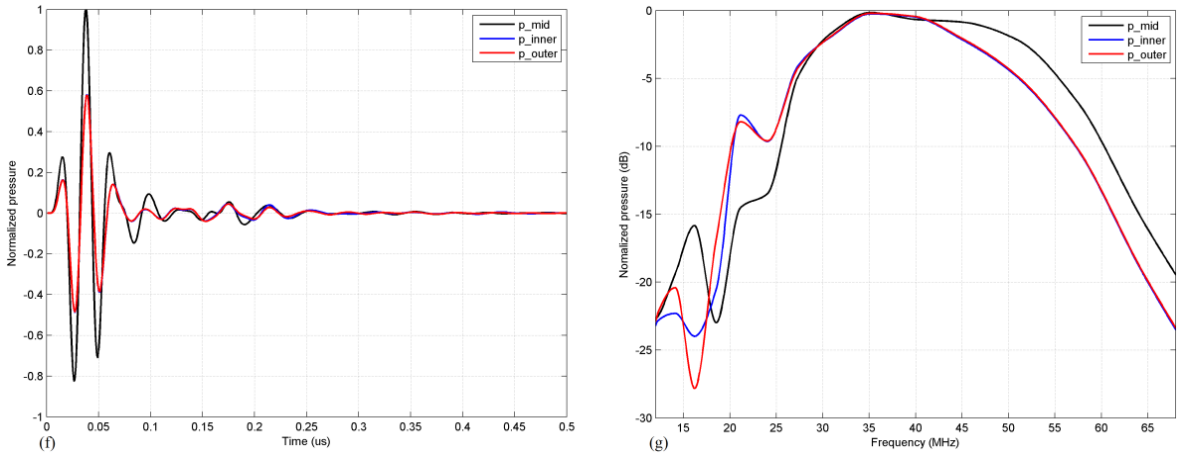

Figure 5.3 (a) The position of the 3 points to get pressure *p_inner* at inner edge, *p_mid* at the middle and *p_outer* at outer edge; (b), (c) show these pressures for 1st element in time and frequency domain; (d), (e) for 4th element; (f), (g) for 7th element

Table 5.2 then lists the related pressure parameters including the maximum pulse amplitude P_{max} and -6dB pulse length $PL_{(-6)}$ in time domain; centre frequency f_c and fractional bandwidth *BW* in frequency domain.

Table 5.2 Pressure parameters of the three elements in EW array

Element number		1st	4th	7th
p_inner	P_{max} (10^4 Pa)	2.78	1.52	1.52
	$PL_{(-6)}$ (ns)	36.5	35.8	35.7
	f_c (MHz)	42.6	39.5	39.6
	BW (%)	46.3	63.3	63.3
p_mid	P_{max} (10^4 Pa)	2.71	2.61	2.61
	$PL_{(-6)}$ (ns)	34.8	34.4	34.4
	f_c (MHz)	41.5	41.6	41.6
	BW (%)	68.6	67.4	63.3
p_outer	P_{max} (10^4 Pa)	1.47	1.51	1.51
	$PL_{(-6)}$ (ns)	34.9	35.5	35.5
	f_c (MHz)	40.6	39.6	39.6
	BW (%)	55.8	63.1	63.1

It can be seen that ringing tail is still found after the main pulses, and this is again caused by the surface waves. Similar to the responses of EA array element, the centre (represented by *p_inner*) of the 1st element in EW array also shows relatively large afterwards ringing, and this is due to the axis-symmetric boundary. In addition, the ringing in EW array elements, especially the outer ones, seems slightly weaker than the EA array ones displayed in Figure 3.11, while the only difference

between EA and EW array is the increased width for EW outer elements. This implies a potential relation between ringing level and element width; in other word, the ringing might be slightly reduced by the increase of the element width.

Likewise, the pressure parameters listed in Table 5.2 for EW array are compared to the data listed in Table 3.8 for EA array, and are found to be quite similar. The central frequencies for EW elements are all around 40MHz, agreeing well with the theoretical expectation. The bandwidths are larger than the KLM-model predicted value of 53%, probably due to the applied fitting model which smoothes the band spectrum. However, only the inner edge (actually the centre) of the 1st element shows a relatively narrow band, and this is caused by the strong ringing. Nevertheless, the pressure pulse in EW elements shows short main pulse and broad band, while the ringing tail is also found.

In addition, the edge vibration of the three elements in EW array is also lower than the centre vibration, as same as the responses of the EA array. This implies a non-uniform surface vibration of the element, as illustrated in Figure 5.4. Compared to the surface vibration for EA array shown in Figure 3.12, probably only slight differences are found in the two outer elements, while the 1st element in EW array seems to have less uniform vibration than the EA array due to the large decrease in element width, however, the difference is not very significant. Again similar to EA array, though non-uniform vibration is found in EW array, its amplitude is generally around 0.9.

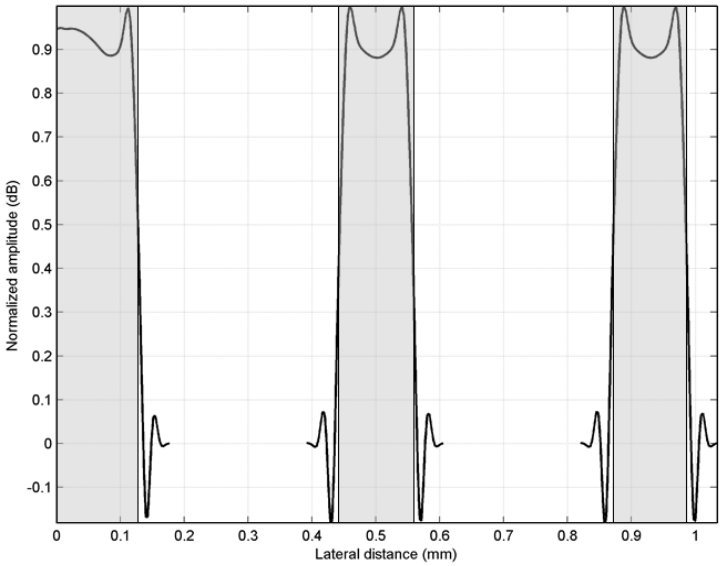

Figure 5.4 Pressure distribution along the excited element surface

5.2.2 Imaging Responses

Different time delay/phase shift is introduced to every element in EW array to form a focal zone at distance of 4mm. First of all, the pressure pulse at focal plane is obtained by FEA and displayed in Figure 5.5, and compared to the one of EA array. Table 5.3 lists the pulse parameters, including P_{max}, $PL_{(-6)}$, f_c, BW, and -20dB pulse length $PL_{(-20)}$ to measure the length of ringing tail.

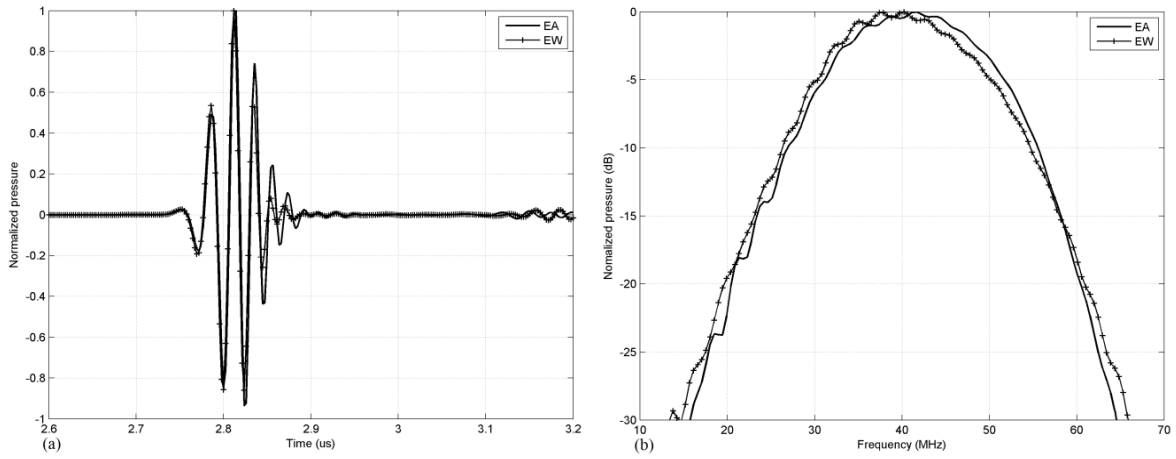

Figure 5.5 Pressure pulse at focal plane in (a) time and (b) frequency domain

Table 5.3 Parameters obtained by pressure response at focal point

Array	P_{max} (10^5 Pa)	$PL_{(-6)}$ (ns)	$PL_{(-20)}$ (ns)	f_c (MHz)	BW (%)
EA	2.52	56.8	113.1	41.3	55.3
EW	2.12	52.5	90.8	40.2	55.5

Short pulse with broad band and little ringing has been achieved by the EW array, and comparable to the EA array. The reduction of P_{max} is also expected due to the difference of natural focal distance as analyzed in Section 4.3.3. The ratio of P_{max} in the EW array to the one in the EA array is about 84%, which generally agrees with the value of 80% evaluated by R-I method and listed in Table 4.9. The pulse lengths including both -6dB and-20dB ones in EW array are shorter than the ones in EA array; it probably benefits from the slightly weaker ringing in EW array elements.

The 2-way radiation pattern of the EW array is then obtained by FEA and compared to the one the one of EA array by FEA, as illustrated in Figure 5.6. The pattern of EW array by R-I method is also displayed in the figure for reference only. The related imaging parameters are listed in Table 5.4,

including lateral resolution *Res*, contrast resolution *CR*, the position of sidelobe X_{SL} and its level *SL*, the position of pedestal lobe X_{PeL} and its level *PeL*.

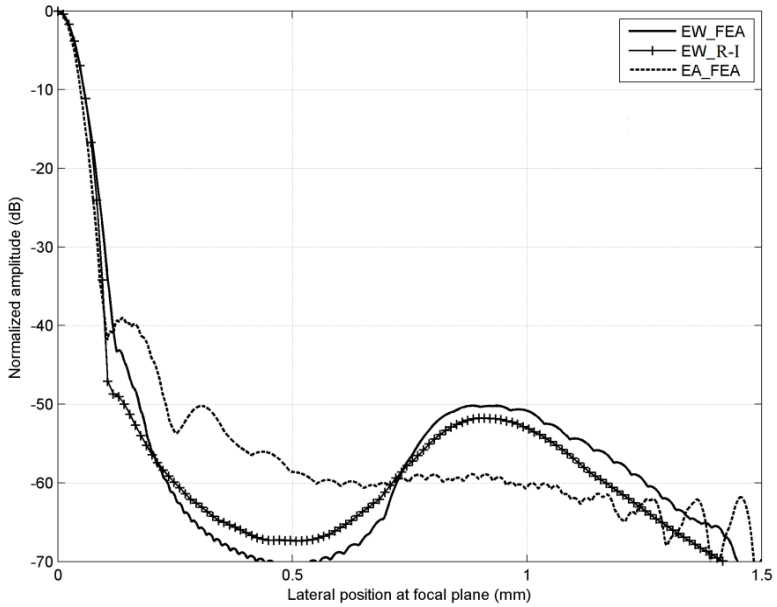

Figure 5.6 Radiation patterns, "EW_FEA" and "EW_R-I" refer to the pattern of EW array by FEA and R-I method, respectively; and "EA_FEA" is the pattern of EA array by FEA

Table 5.4 Imaging parameters of the radiation patterns

Array	Method	*Res* (μm)	*CR* (μm)	X_{SL} (μm)	*SL* (dB)	X_{PeL} (μm)	*PeL* (dB)
EA	FEA	74.8	202.9	137.6	-39.0	910.8	-58.9
EW	Num	88.2	198.6	(121.1)	(-48.6)	906.8	-51.8
	FEA	86.1	234.0	(130.5)	(-43.1)	886.3	-50.2

(121), (-48.6) etc. means that no obvious lobe is found

It can be seen that the EW array shows the suppression of the nearest sidelobes; its main lobe has a smooth decreasing trend without any obvious sidelobe in the region of 0-0.5mm, or only a very weak sidelobe around 130μm away from the focal axis. Meanwhile, the increase in resolutions (both lateral and contrast) and the extra pedestal lobe are also found compared to the pattern of EA array. This generally agrees with the analysis of R-I patterns instructed in Section 4.3.3.

5.3 Discussions on Equal Width Annular Array

The imaging performances of a 7-element EW array are given above, but they are found to be strongly impacted by the element width, or the total element number *N*. To reveal the relation,

Figure 5.7 displays the normalized pulses at the focal point for EA and EW arrays with different *N* ranging from 6 to 10 by using FEA method. The related pressure parameters are listed in Table 5.6, the denotation of the parameters can be referenced to Table 5.3.

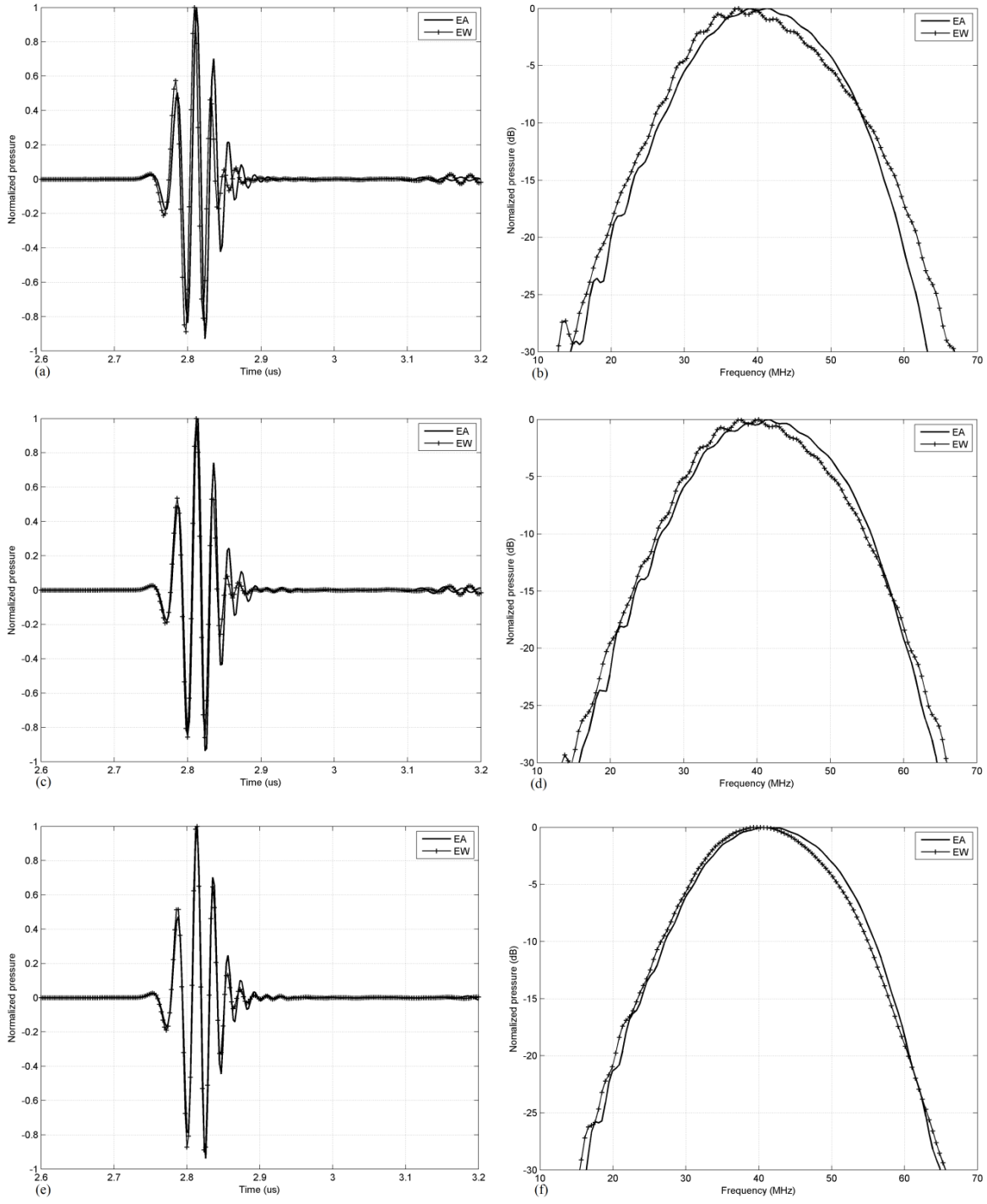

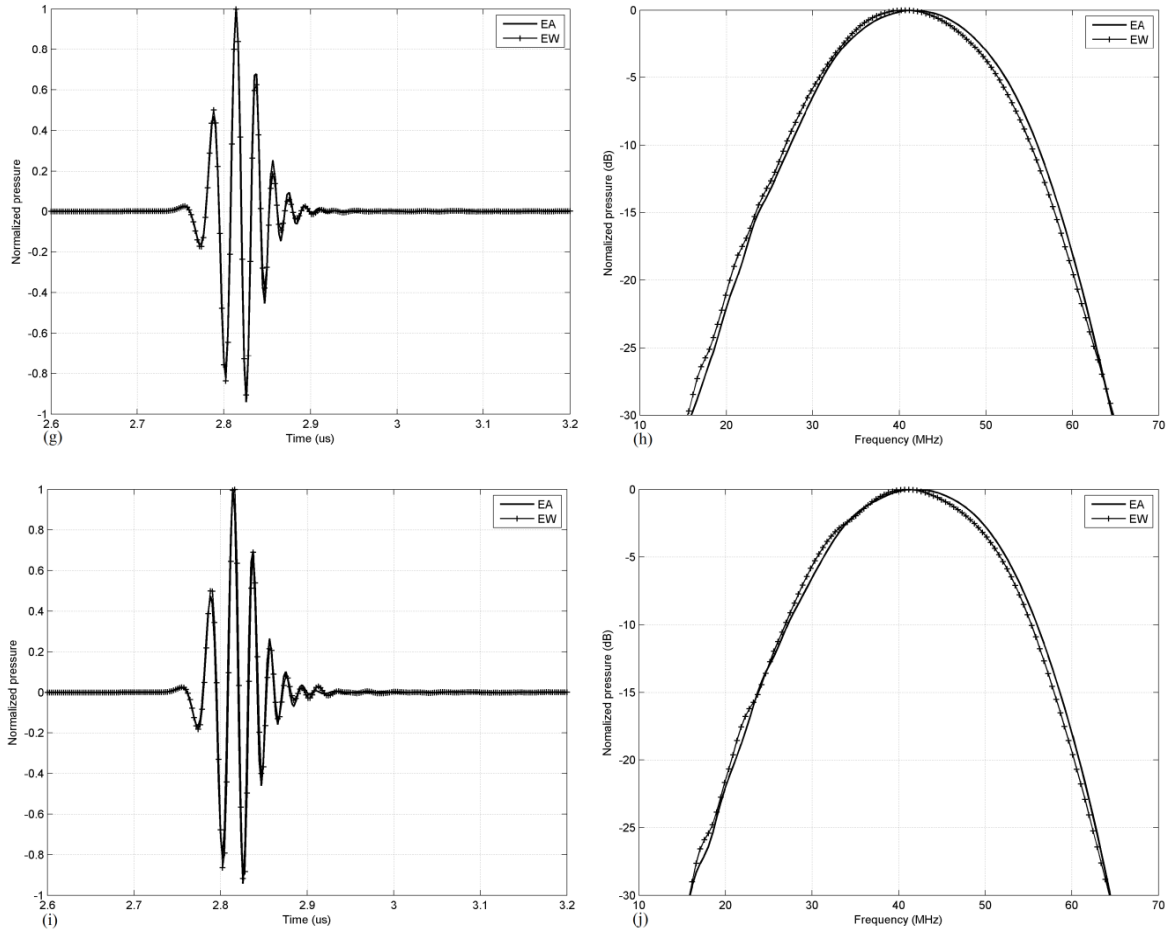

Figure 5.7 Pressure pulses at focal point: (a), (b) show the pulses of both EA and EW array with *N*=6; (c), (d) for *N*=7; (e), (f) for *N*=8; (g), (h) for *N*=9 and (i), (j) for *N*=10

Table 5.5 Pressure parameters of the pulses at focal point for the arrays with different *N*

N	Array	P_{max} (10^5Pa)	$PL_{(-6)}$ (ns)	$PL_{(-20)}$ (ns)	f_c (MHz)	*BW* (%)
6	**EA**	2.24	57.7	109.9	40.6	54.3
	EW	1.77	51.1	87.5	39.7	56.5
7	**EA**	2.52	56.8	113.1	41.3	55.3
	EW	2.12	52.5	90.8	40.2	55.5
8	**EA**	2.63	56.3	112.7	41.6	55.5
	EW	2.32	53.8	95.8	40.8	54.4
9	**EA**	2.64	56.1	110.8	41.7	54.5
	EW	2.42	54.7	101.1	41.1	54.7
10	**EA**	2.58	56.1	111.5	41.9	54.4
	EW	2.47	54.5	106.8	41.2	55.6

The radiation patterns of these arrays with different *N* are then illustrated in Figure 5.8. The imaging parameters are listed in Table 5.6, with their denotations referenced to Table 5.4. The discussions of the EW annular array are presented in the following section, and based on the fields of the pressure pulses at focal point and the beam patterns.

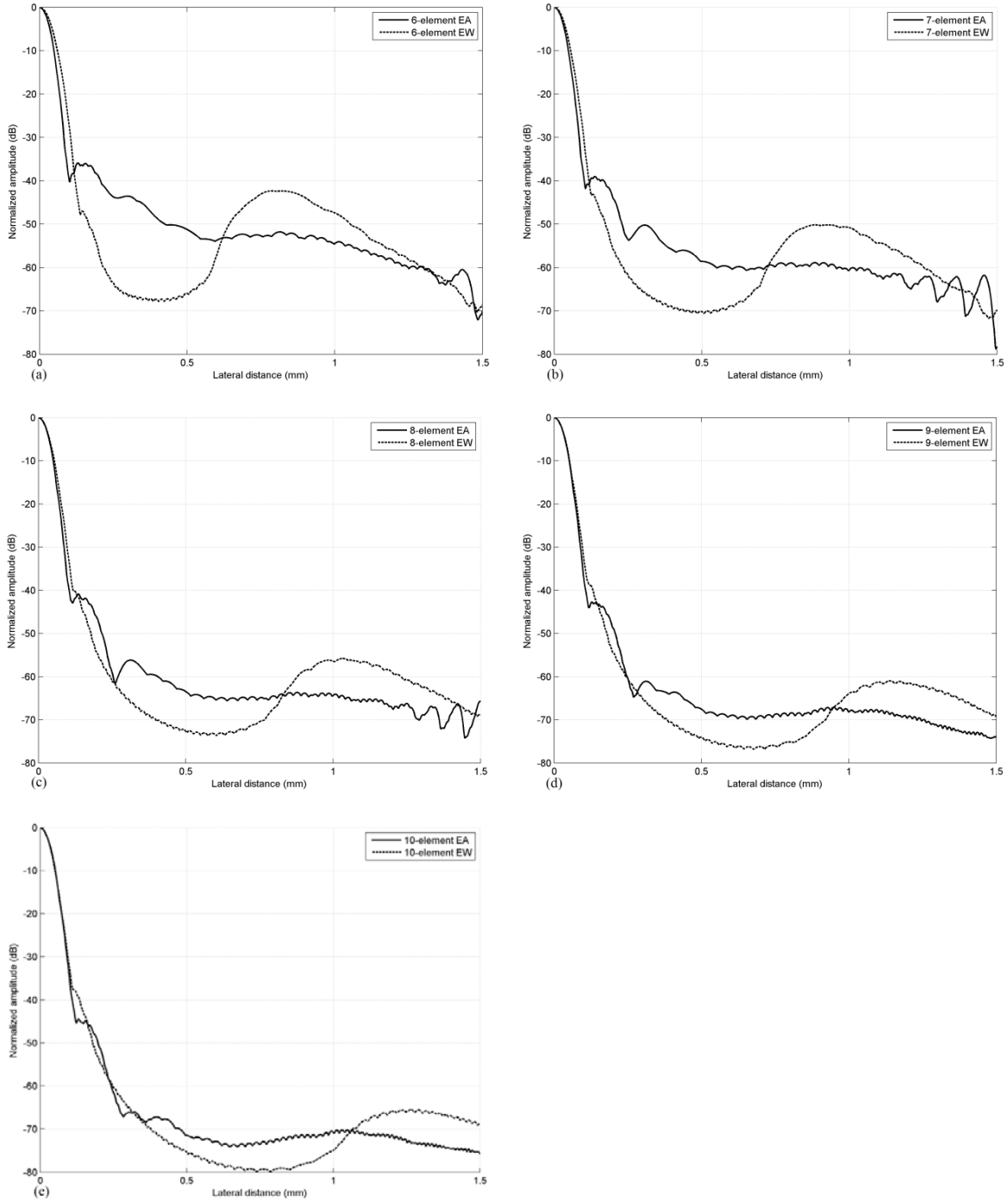

Figure 5.8 Beam patterns of EA and EW arrays with (a) *N*=6; (b) *N*=7, (c) *N*=8, (d) *N*=9 and (e) *N*=10

Table 5.6 Imaging parameters for the arrays with different *N*

N	Array	*Res* (μm)	*CR* (μm)	X_{SL} (μm)	*SL* (dB)	X_{PeL} (μm)	*PeL* (dB)
6	EA	76.7	201.3	130.0	-35.9	815.3	51.8
	EW	94.3	214.2	(144.3)	(-47.0)	788.3	-42.3
7	EA	74.8	202.9	137.6	-39.0	882.8	-58.9
	EW	86.1	234.0	(130.5)	(-43.1)	886.3	-50.2
8	EA	78.2	207.8	134.7	-40.9	798.7	-64.5
	EW	81.3	234.9	(112.8)	(-40.2)	1032.0	-55.8
9	EA	80.2	212.9	128.1	-42.7	946.9	-67.1
	EW	81.9	263.5	(131.7)	(-40.0)	1139.1	-61.0
10	EA	80.3	217.6	130.6	-44.5	1030.0	-70.2
	EW	77.8	269.2	(121.4)	(-38.1)	1291.0	-65.6

(144.3), (-47.0), etc. means the lobe is not obvious

5.3.1 Discussion on Pressure Pulses at Focal Point

The discussion here is based on Figure 5.7 and Table 5.5. In EA arrays with different element number *N*, the maximum amplitudes P_{max} or equivalently main lobe peak generally keeps the same level, except for the array with *N*=6. In terms of EW arrays, an increasing trend can be seen by the increase of element number. Meanwhile, the value of P_{max} in EW array is always smaller than the one in EA array with a certain element number. All of these can be explained by the change in element nature focal distance.

For EA arrays with *N*=6, their elements all have the natural focal distance Z_t above the designed focal distance *F* of 4mm and results in a near-field pattern, instead of the required far-field pattern. But by applying more elements to the array, the natural focal distance moves below the focal distance and leads to the far-field pattern for every element. Since the overall main lobe peak is then the summation of the individual peak, the values of P_{max} are generally same for the array with different *N* if all its elements have the far-field at focal distance. Likewise, the EW arrays with smaller *N* have the outer element showing the near-field due to their large area, while fewer and fewer elements have near-field by the increase of element number since the area of outer elements are correspondingly reduced. Thus increasing trend of P_{max} is expected in EW array and eventually become comparable to the one in EA array with a large *N*.

To demonstrate the analysis above, FHT (Fast Hankel Transform), as another theoretical analysis tool, is applied to obtain the maximum pressure amplitude at focal point of every element. Their amplitude is then summed up to obtain the overall main lobe peak of a focused array. The comparison between FHT and FEA pressure of the array with different *N* is given in Table 5.7, where P_{EA} and P_{EW} refer to the normalized P_{max} in EA and EW array, respectively. The values of P_{EA} and P_{EW} by using FHT method are normalized by the maximum P_{max} in all the arrays using FHT, while the values of the two parameters by using FEA are normalized by the maximum P_{max} in the arrays using FEA. A good agreement between the results of FHT and FEA has been achieved.

Table 5.7 Ratio of P_{max} of EW array to the one of EA array by using FHT and FEA

N		**6**	**7**	**8**	**9**	**10**
$\mathbf{P_{EA}}$	**FHT**	0.91	0.98	1.00	0.99	0.97
	FEA	0.85	0.95	1.00	1.00	0.98
$\mathbf{P_{EW}}$	**FHT**	0.64	0.78	0.87	0.91	0.94
	FEA	0.67	0.80	0.88	0.92	0.94

Besides that, the pulse length *PL* (including the -6dB and -20dB) in EW array seems a bit smaller than the values in EA arrays, especially with the smaller element number *N*. It might be due to the weaker ringing tails in EW array element, as discussed in Section 5.2.1. However, the difference between pulse lengths in EA and EW arrays also reduces with the increasing *N*, and this is probably related to the decreased difference in their element widths. The ringing in every element for the two arrays would have no real difference, and it is also believed that the pressure pulses at focal point for the two types of array will eventually become the same with a sufficient large *N*.

5.3.2 Discussion on Resolution and Contrast

The discussion here is mainly based on Table 5.6. For convenience, lateral resolution here is described as “resolution”, while contrast resolution is named “contrast”. Table 5.8 re-listed the two parameters already given in Table 5.6 for clear comparison. It should be noticed that the contrast values of the EA arrays with relatively small element number (*N*=6 and 7) are very large and thus not given, this is due to the strong influence of their nearest sidelobe which is about -40dB (the level to measure *CR*).

Table 5.8 Resolution and contrast of EA and EW arrays by FEA

N		**6**	**7**	**8**	**9**	**10**
***Res* (μm)**	EA	76.7	74.8	78.2	80.2	80.3
	EW	94.3	86.1	81.3	81.9	80.3
***CR* (μm)**	EA	-	-	207.8	212.9	217.6
	EW	214.2	234.0	234.9	263.5	269.2

In terms of resolution, this is related to the so-called electronic lens of the array transducers discussed in Section 4.3.3. The electric lens formed by the wavefronts of each element in EW array is not as good as the one formed by EA array. Therefore, the resolution of EW array is always larger than the one of EA array for the same total element number *N*. However, by the increase of element number, though the outer elements in EW array still refers to a larger change in lens curvature compared to EA array, the difference between electric and physical lens keeps decreasing. Eventually the resolution of EW array would become comparable to EA one with a relatively large *N*.

For the EA arrays, a general increasing trend is found in the resolution of EA array by the increase of element number *N*, which is the opposite of that found for the EW array. Two related reasons might be found. One is probably due to the non-uniform vibration in the narrow outer elements in the arrays with large *N*. The very narrow element vibrates more like a point, instead of a piston. Its contribution to the main lobe is thus reduced and causes a potential degrading of resolution. Another reason is very likely to be the increasing area that kerfs occupy. The kerfs width keeps the same despite the increase of element numbers, this leads to the fact that more and more area at the surface of the array aperture become inactive. Hence, the overall contribution of the array elements to the main lobe is also decreased and also causes the resolution to degrade as well.

In terms of contrast, the responses seem more complicated, due to the influence of the sidelobes in the patterns. For EA arrays, the *CR* for the array with N=6 and 7 is not defined, because their sidelobe is above -40dB hampering the measurement of *CR*. For the ones with higher *N*, the sidelobe is below -40dB, and the contrast resolution shows an increasing trend with increasing *N*; this agrees with the behaviour of its resolution described in the last paragraph. In other word, the main lobe becomes slightly wider.

However, for EW arrays, their sidelobe is much weaker and a smooth main lobe can be clearly found, the *CR* can be measured through the arrays for all different *N*. Like the EA array, an increasing trend is also found in *CR* values for EW arrays with increasing *N*. But this disagrees with the behaviours of the resolution in EW array. The reason is found to be related to the sidelobe, which is not obvious and coupled into the main lobe. Although the main lobe is generally smooth, the evidence of this weak and coupled sidelobe can still be found - a discontinuous change always around 150μm away from focal axis in the EW array patterns. Meanwhile, the level of this coupled sidelobe also increases by the increment in *N*, and eventually becomes around -40dB. This then leads to a large CR when it is measured at -40dB. As a result, contrast shows an increasing trend and becomes larger than EA array with a large *N*.

To summarize, EA array shows better resolution than EW array, but the resolution of EW array eventually becomes comparable to EA arrays by the increase of *N*. Although the contrast of both two types of arrays increases with *N*, the EW array has a higher contrast than EA ones if the element number *N* is large.

5.3.3 Discussion on Sidelobe and Pedestal Lobe

The discussion here is mainly based on Figure 5.8 and Table 5.6. The level of sidelobe in EA array is expected to show a decreasing trend with the increase of element number and demonstrated by its FEA pattern. Because with more elements involved in focusing, more element pulses are overlapped more strongly in the main lobe, but less strongly in the region away from focal axis. For the same reason, the level of the pattern away from the main lobe decreases by the increasing N, and it can be easily proved by the FEA evolutions.

However, the level of the sidelobe in EW array, though it is weak and coupled into the main lobe, still shows an increasing trend by the increase of element number instead. It is found to be caused by the reduced effect of the sidelobe suppression in EW array. Recall the analysis in Chapter 4, the sidelobe suppression by EW geometry is based on the relatively large phase difference for the pulses in the sidelobe region. This makes these pulses to have fewer chances to be strongly overlapped and thus leads to the sidelobe suppression. But with the increase of element number *N*, the element position of EW array also becomes closer to each other. This means that the phase

difference related to the element position also becomes smaller, in other word, the pulses in the sidelobe region would probably still have some, or even large chances to be overlapped. The effect of sidelobe suppression is therefore reduced. Nevertheless, the increased sidelobe in EW array with large *N* is fortunately coupled into the main lobe. Thus the main lobe is still regarded as a smooth one, but at the cost of a relatively large contrast discussed the last section.

In terms of the "pedestal" lobe illustrated in Figure 5.8, similarly, its level in both EA and EW arrays decreases by the increase of element number as expected. Since the pedestal lobe in EA array is usually very weak and thus is not discussed here, while its relation with *N* can be found in the reference [84]. For the EW arrays, the R-I analysis in Section 4.3.3 reveals that the "pedestal" lobe is actually a kind of grating lobe usually appearing in linear array, which is further demonstrated by Table 5.9. It lists the positions of grating lobe of the *N*-element linear arrays with same element width of the corresponding EW array by using Equation (4.9), with the comparison of the positions of pedestal lobe in EW arrays by FEA method already listed in Table 5.6.

Table 5.9 Position of the pedestal lobes for EW arrays, 'Linear' here refers to grating lobe position in linear array which is calculated by Equation (4.9)

N		**6**	**7**	**8**	**9**	**10**
X_{PeL} **(mm)**	**Linear**	0.82	0.96	1.11	1.26	1.41
	FEA	0.79	0.89	1.03	1.12	1.29

The FEA results generally agree well with the theoretical ones of linear array. The slight difference in lobe position is acceptable, since the lobe is very smooth over a relatively large range, while the value of X_{PeL} only takes the position of the lobe peaks.

To summarize, the nearest sidelobe in EA array is suppressed clearly by the EW array with small *N* (*N*=6, 7), but becomes comparable for the arrays with *N*=8 and 9, and even lower than the EW array with *N*=10. Nevertheless, the sidelobe in EW array is not obvious and coupled into main lobe, while it is clearly separated from the main lobe in the patterns of EA arrays. For the pedestal lobe, the lobe levels in EA arrays are already very low, while a large lobe can be seen in the patterns of EW arrays. However, the lobe level in EW array decreases by the increasing *N* and eventually achieves a relatively low level (below -60dB) as well.

5.3.4 Discussion on Fabrication Difficulties

Element number of both EA and EW array shows significant influence on imaging behaviours, while it also has the limitation due to difficulties in fabricating very narrow annular element. Table 5.10 then lists the width of the outermost element w_N using kerfs widths of 30μm.

Table 5.10 Width of "outermost" element in EA and EW arrays (*N* for the total element number)

N		**6**	**7**	**8**	**9**	**10**
w_N **(μm)**	EA	69.0	55.9	46.3	38.9	33.1
	EW	136.7	112.9	95.0	81.1	70.0

The 10-element EA array shows the narrowest width of 33.1μm for its outermost element. Though the element still can be fabricated by the current dicing techniques, it would eventually becomes impossible to realize when the aperture contains more and more elements, or when the aperture becomes smaller and smaller. And the width of outermost element decreases much faster in EA array than EW array. For example, if the array aperture is halved to be 1mm in diameter, the level always used in the intravascular imaging, the w_N of a 10-element EA array is only 8.6μm, the level too hard to fabricate. But in EW geometry, w_N is about 20μm, small but achievable.

Since the imaging parameters of EA and EW array eventually become comparable with a sufficient large element number, there will be no significant difference between these two arrays. Thus the EW array has the advantages in fabrication of the arrays with large *N* or a small aperture.

5.3.5 Overall Discussion

The discussions about imaging parameters of EA and EW array are presented above and can be summarized in the following table:

Table 5.11 Summary and comparison between EA and EW arrays

Parameters	EA array	EW array
Pressure amplitude	▪ Larger value; ▪ Similar with different *N*	▪ Smaller value; ▪ But increases by *N* and finally become comparable to EA array
Pulse length	▪ Longer; ▪ keeps similar value with different *N*	▪ Shorter; ▪ But increases by *N* and finally become comparable to EA array
Bandwidth	▪ Broad	▪ Broad
Resolution	▪ Better ▪ Slight increase in the arrays with large *N*	▪ Poorer especially for small *N*; ▪ But become finer and comparable to EA array with larger *N*
Contrast	▪ Better expect the case of *N*=6 and 7 due to high sidelobe	▪ Better for the case of *N*=6 and 7 due to sidelobe suppression; ▪ But poorer for other *N* and shows an increasing trend by *N*
Sidelobe	▪ Higher lobe level; ▪ Decreases by increasing *N*; ▪ Clear and separated lobe	▪ Lower lobe level; ▪ increases by increasing *N*; ▪ Weak and coupled into main lobe
Pedestal lobe	▪ Lower; ▪ Decreases by *N*	▪ Higher; ▪ Decreases by *N*
Fabrication	▪ Fabrication challenges in narrow outer elements	▪ Advantage in fabricating the array with larger *N* or smaller aperture

5.4 Summary

Based on the R-I analysis in Chapter 4, a way to suppress the high sidelobe in EA array is found by using the EW array and verified by FEA method. Though the EW array leads to the increased complication of electrical network including the tuning circuit, it is regarded as a minor negative factor since it can be overcome by current techniques. The suppression of sidelobe is the aim and the main advantage of EW array.

However, the suppression of sidelobe is paid for by the increase of pedestal lobe, but the overall lobe level in the EW array is lower than the EA array with 7 elements. The imaging parameters of

EA and EW arrays with different element number are then compared and discussed in several fields. The EW array with small element number *N* has its advantage in sidelobe suppression and shorter pulse length compared to the EA array, but at the cost of slight increase in resolution. By the increase of *N*, the imaging performances of EW array eventually become comparable to the EA array, because no significant difference are found in the two arrays when *N* is very large. Besides that, the discussion of fabrication difficulties suggests that EW array is advanced in realizing the array transducer with small aperture or large element number. Generally speaking, the EW annular array shows a good improvement of conventional EA array in the high frequency imaging.

Chapter 6 High Frequency Linear Array

6.1 Introduction

In terms of real-time imaging, linear array is advanced compared to both annular array and single-element transducer, because of its feasibility in 2D beam steering by only applying the electronic signals to change the phase of the element. However, the other two types of transducer require the mechanical movement (only lateral movement for annular array, while both axially and laterally for single-element transducer) to scan through the target imaging plane. The slow mechanical motors results in the low frame rate, while the linear array without using mechanical motors has a much faster electronic beamforming.

However, in high frequency (>30MHz) imaging, linear arrays still have challenges in fabrication following more than a decade of study. It would be even more difficult to realize a phased (linear) array, because of the strict requirement of element pitch, namely element-to-element spacing. The desired pitch is about one-λ (λ, wavelength) for the linear array capable of 2D beamforming, while only about λ/2 for the one capable of 3D beamforming [95]. The pitch width larger than these values could cause the appearance of grating lobes, and leads to the fake artefact or wrong position of target in the imaging plane [58]. The suppression of grating lobes is always of great importance in the design of linear and linear phased array.

The fabrication of linear (phased) array is usually processed by a dicing and filling technique. Kerfs are diced through all the layers in the array and then filled with epoxy to form 2-2 ceramic-epoxy composite structure for linear array, and 1-3 composite for linear phased array. Current dicing techniques, including mechanical dicing and laser micro-machining could comfortably realize kerf width of 20-30μm. It gives the achievable pitch width of approximately 40μm, this corresponds to a maximum array centre frequency of approximately 40MHz (λ=40μm) for the linear array without beam steering, and only 20MHz (λ/2=40μm) for the one requiring large beam steering [95]. The increase of the frequency effectively enlarges the pitch and introduces the grating lobes.

In this chapter, only 1-D linear array (called linear array in the following discussion) is presented, since the 2-D phased array has very similar design principle as the 1-D one. First of all, the design of a conventional high frequency linear array is investigated, showing the impedance spectrums,

element vibrations, pulse responses and radiation patterns by using both R-I and FEA method. And it is found that the kerfs width have significant influence on the radiation pattern, though it is always regarded as the secondary important factor. Secondly, using the high attenuated kerfs filler, it is possible to reduce the influence of kerf width (which causes an addition lobe similar to the grating lobe in the radiation pattern), even for an array that fulfil the requirement of one-λ pitch width. Besides that, for a very high frequency (>45MHz) linear array, the additional lobe caused by kerfs no longer appears because the attenuation of the kerfs filler increases with the increase of operating frequency. However, the grating lobe is apparent due to the large pitch width (>1λ) caused by fabrication difficulties, though it is essential to suppress for imaging.

6.2 Methodology

Similarly, KLM model as a numerical method and FEA method to simulate the performances of practical device are both used. KLM model presented in Chapter 2 is based on the T-mode vibration, which refers to the dominant vibration of a thin plate with very large width and length. However, the dominant resonance of the ceramic in linear array is beam mode generated by a very long but narrow bar, as illustrated in Figure 6.1.

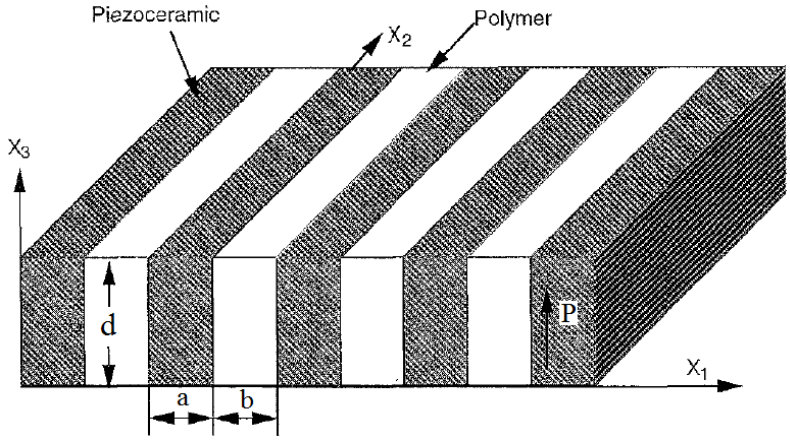

Figure 6.1 Schematic diagram of a linear array (or 2-2 composite), where *d* is the thickness, *a* and *b* denotes the width of ceramic and polymer respectively, and *P* for the polarization direction [47]

The length of the ceramic in X_2 direction is very long compared to its width in X_1 direction and thickness in X_3 direction. Thus it can be treated as an infinite long beam and allows a 1-D beam mode model. To use the KLM model based on thickness mode for the 1-D beam mode, several

changes are made by replacing the parameters of permittivity ε_{33}^{s}, sound speed c and coupling factor k_t, and expressed as follows:

$$\varepsilon_{33}^{s\,B} = 1/\beta_{33}^{S\,B} \quad , \quad \beta_{33}^{S\,B} = \beta_{33}^{S} - h_{13}^{2}/c_{11}^{D} \tag{6.1}$$

$$c^{B} = \sqrt{c_{33}^{D\,B}/\rho} \quad , \quad c_{33}^{D\,B} = c_{33}^{D} - c_{13}^{D\,2}/c_{11}^{D} \tag{6.2}$$

$$k_t^{B} = h_{33}^{B\,2}\varepsilon_{33}^{s\,B}/c_{33}^{D\,B} \quad , \quad h_{33}^{B} = h_{33} - c_{13}^{D}/c_{11}^{D} \cdot h_{13} \tag{6.3}$$

where the parameters with superscript "*B*" represents the newly replaced ones used in KLM model for beam mode, others are the material properties of piezo-ceramic. The detail of the replacements and the rectified beam mode KLM model is presented in Appendix B.

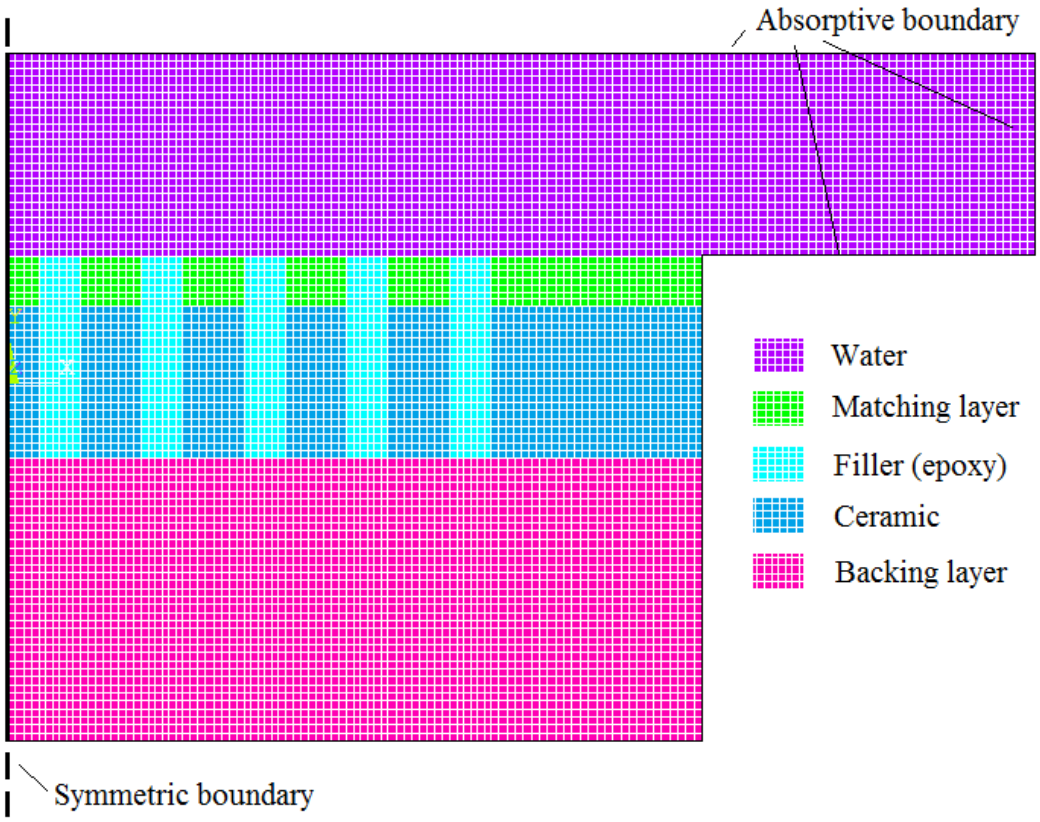

Figure 6.2 2D FEA model of a typical linear array

Likewise, FEA is another main method in the design since it has been proved to show close results compared to experimental ones. A simplified 2D model is established to represent the actual 3D arrays. Only the performances of cross section in X_{13} (or azimuth) plane are simulated by using plane strain condition available in the FEA software Ansys 11.0. The cross section in X_{23} (or

elevation) plane is assumed to be an infinite long beam. The assumption is always valid in 1D linear array. The 2D FEA model of linear array is then illustrated in Figure 6.2.

Similar to the FEA model for annular array, the absorptive boundary is applied to represent the larger water medium by much smaller element area. And only half of the array needs to be analyzed due to the symmetric boundary. Backing layer is again designed to be sufficient thick to absorb all the energy transmitted backwards by the ceramic elements. Electrodes are applied to the bottom and top surfaces of ceramic elements and also represented by CEF elements available in Ansys.

Instead of the annular array, many PZT can be used as the ceramic layer such as the commonly-used PZT-5H, since there is no requirement of the very low lateral coupling coefficient in the beam mode vibration. But PZ34 is still selected as the ceramic material just because of the convenience from the already-established KLM and FEA model of annular array, which can be easily transferred to the models of linear array. For the same reason, the materials of matching and backing layer are the same as annular array. The key properties of all these materials are again given in Table 6.1, where Z, c, Q_m and α denotes the characteristic impedance, longitudinal velocity, quality factor and attenuation coefficient, respectively.

Table 6.1 Properties of materials used in linear array, superscript * means that sound speed c of PZ34 is actually c^B used only in the beam mode

Layers	Material	Ref.	Z (MRayls)	c (m/s)	Q_m	α (dB/mm ·MHz^{-1})
Matching	Alumina-loaded EPO-TEK 301-2	[22]	7.3	3248	-	≈4
Ceramic	PZ34	[88]	35.4	4690*	120	-
Backing	Tungsten-loaded E-solder 3022	[22]	10.0	1600	10	-

The material of kerfs filler is not listed in Table 6.1, because it is found that the attenuation of the kerfs material shows significant influence on the element performances. The influence will be reveal in the following discussion. In addition, it should be noticed that the matching layer in linear array is diced to stop the transmission of the transverse waves, which is found to largely impact the radiation pattern.

6.3 Design of a Conventional Linear Array

A 30MHz conventional linear array is firstly designed and investigated, with the consideration of imaging quality and fabrication difficulties. The key feature of imaging quality mainly refers to the avoidance of grating lobe. For the array operating at 30MHz, the element pitch to remove the lobe out of imaging plane is required to be less than 50μm which is one-λ.

Meanwhile, under the current conventional dicing and filling technique, kerfs width of 20μm is a reasonable level to be realized, smaller kerf width would significantly increase the fabrication difficulties. Thus the ceramic width is designed to be a maximum value of 30μm, and leads to the maximum ceramic volume of 60%. The low ceramic volume is not recommended since the effective aperture decreases with the ceramic volume.

6.3.1 R-I Evaluation of Array Beam Pattern

The 30MHz linear array with 50μm pitch is expect to show no evidence of grating lobe, but it is found that the width of kerfs strongly impact the array beam pattern. R-I method is firstly used since the inaccuracy issue in annular array would be resolved in linear array. Thus to obtain the R-I patterns, Gauss pulse is firstly determined to fit the element pulse by KLM model, as illustrated by Figure 6.3. The profile of Gauss pulse is set to have the bandwidth of 55%, central frequency of 32MHz and TPE level of -25dB.

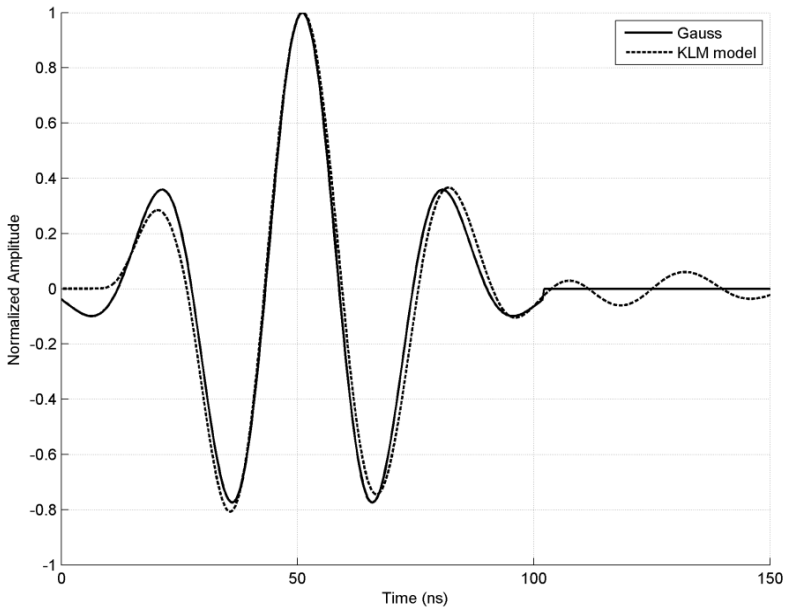

Figure 6.3 The Gauss pulse of a linear element to fit its element pulse by KLM model

In general, good agreement has been achieved by the two pulses. Although the element pulse by KLM model might have some differences compared to the one by FEA due to the influence of edge effect and transverse waves, the pulse difference is believed to be not large enough to cause any significant errors in the R-I evaluation of radiation patterns.

To reveal the relations between kerfs width and beam patterns, the R-I patterns of the linear arrays with 9 elements and 50μm pitch but different kerfs widths are compared in the Figure 6.4 displayed below. The kerfs width ranges from 0 to 25μm, or the corresponding ceramic volume ranging from 100% to 50%.

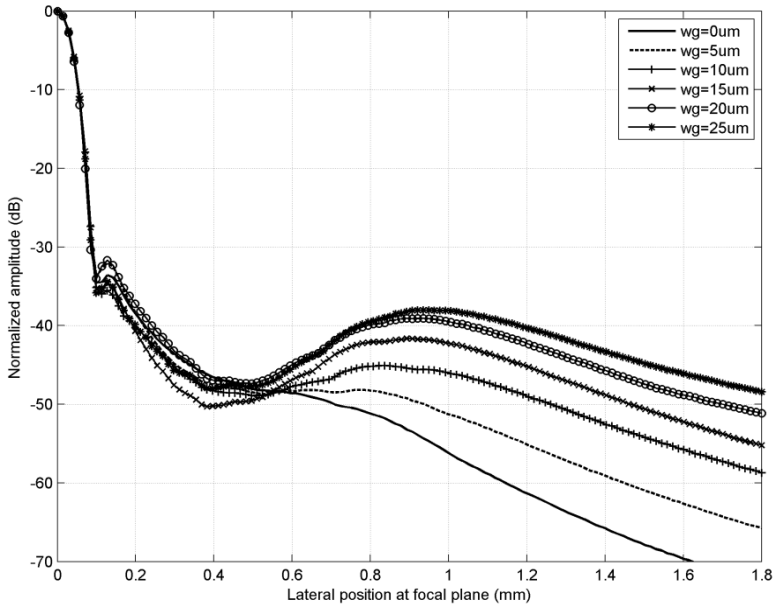

Figure 6.4 R-I patterns of the linear array width different kerfs width w_g

It can be seen that the ideal linear array with no kerfs shows the radiation pattern without any pedestal lobe as expected. But by the increase of kerfs width or the reduction of ceramic volume, additional lobe appears around 1mm with its level keeping increasing. The reason of this lobe is not clear, but it is certainly caused by the kerfs. Meanwhile the sidelobe appearing about 130μm is also found and caused by the bandwidth of the element pulse. Bandwidth of 55% is large enough to suppress the sidelobe in annular array, but seems not in linear array. The level of the sidelobe may be also impacted by the kerfs width but not very strongly, since only a weak increasing trend is found by the increase of kerfs width. However, the resolution measured by -6dB bandwidth

keeps the same regardless of the changes in kerfs width, while the reduction in ceramic volume certainly decreases the sensitivity or the main lobe peak.

Recall that in the analysis of the element vibration in annular array, the surfaces waves are very likely to be the reason of the ringing at a certain element. These surface waves also travel transversely across the element surface, and leads to some unwanted vibration in the kerfs part of an element. Different from annular array, the kerfs in linear array occupies about 40% of surface area of the array aperture, thus the kerfs vibration could be significant in the element vibration. Furthermore, in the patterns generated by R-I evaluation (Figure 6.4), the vibrations in the kerfs are assumed to be none, while the potential complicated kerfs vibration would probably lead to the further deterioration in radiation pattern.

6.3.2 Influence of Kerfs Filler on Element Vibration

To stop the transmission of the transverse waves, the kerfs are always cut through the matching layer and then filled with a highly attenuated material. Therefore, three different epoxies are chosen as the kerfs filler for the linear array with 9-element, 50μm pitch and 30MHz operating frequency. Their key properties are then listed in Table 6.2, including the acoustic impedance Z, longitudinal velocity v_L, shear velocity v_S, and attenuation coefficient α.

Table 6.2 Properties of the three epoxies used as kerfs filler

No.	Material	Ref.	Z (MRayls)	v_L (m/s)	v_S (m/s)	α (dB/mm ·MHz^{-1})	Viscosity
1	Araldite	[22]	2.45	2210	972	1.2	low, easily pourable
2	Eccogel 1365 loaded by 6% Al_2O_3	[23]	2.6	1700	795	4.8	low, easily pourable
3	EC-2CN:PbO (1:1.5 wt.)	[115]	2.1	975	456	8.8	medium, pourable

All of these epoxies show close acoustic impedance ranging from 2-3MRayls. By the differences in attenuation coefficient, “Araldite” represents the low attenuation material labelled as Epoxy 1; ”Ecco-gel 1365” loaded by Al_2O_3 powder denotes the medium attenuation material labelled as Epoxy 2; while “EC-2CN” loaded by PbO powder is for the high attenuation material labelled as Epoxy 3. Besides that, viscosity is another important factor in the fabrication process. The kerfs

filler need to be pourable enough to fill into the fine-scaled kerfs between elements. Both Epoxy 1 and 2 show low viscosity and thus easily pourable. Though Epoxy 3 has a relatively high viscosity, it is still pourable and already used in the filling process.

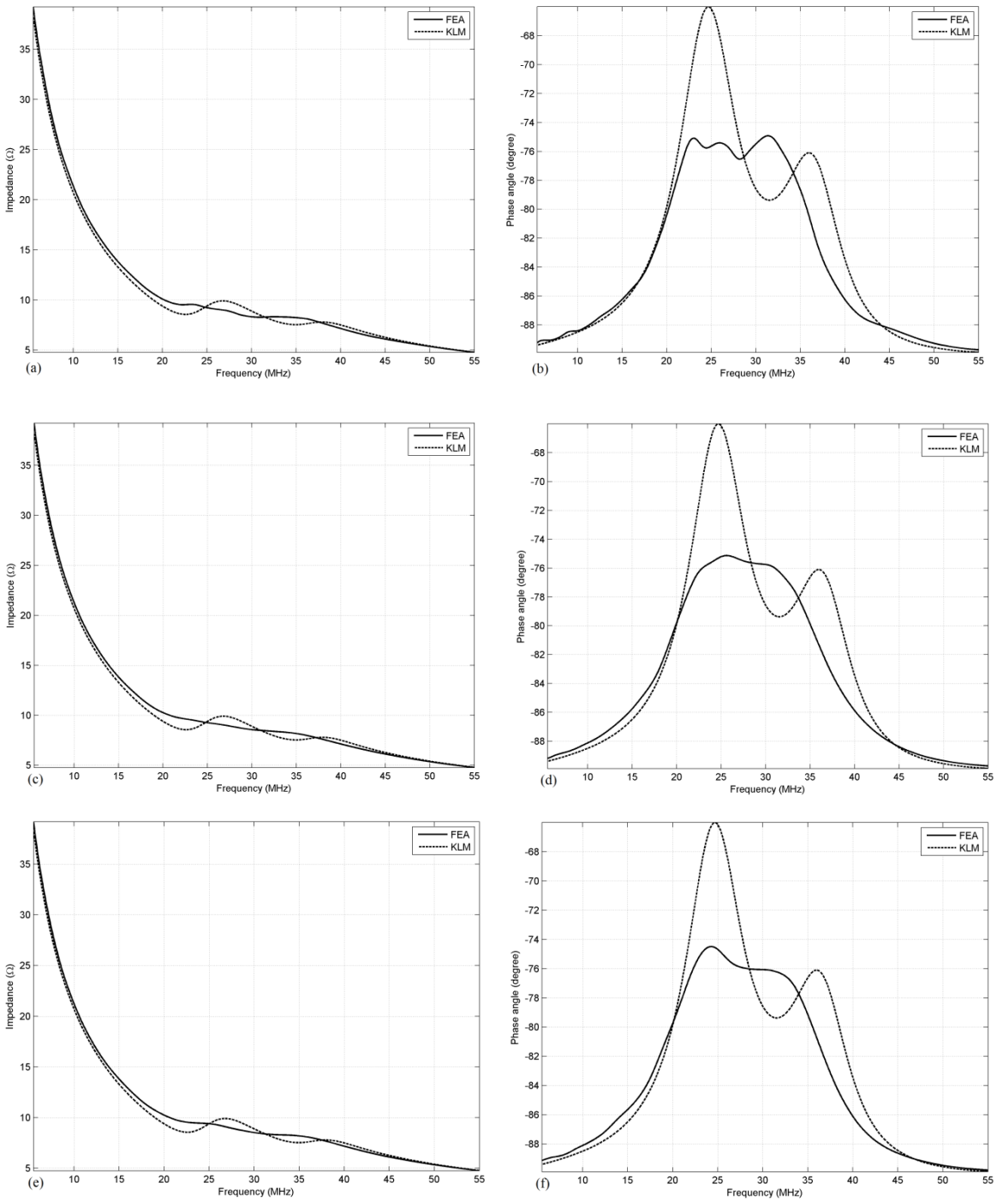

Figure 6.5 (a), (b) shows the impedance and phase spectrum of the element in the linear array using Epoxy 1; (c),(d) for the array using Epoxy 2; and (e), (f) for Epoxy 3

First of all, the impedance spectrum of a single element in the linear arrays by using the three kerfs fillers is investigated and compared to the responses by the modified KLM model, as displayed in Figure 6.5.

However, by examining the FEA phase spectrum of the array filled by Epoxy 1, some other spurious modes are found in the region of ceramic peak at 25MHz approximately. They largely impact the ceramic resonance and also shift the peak of matching layer slightly leftwards. These modes are found to be caused by the shear resonance of the kerfs material. The shear resonant frequency f_{ks} of the kerfs filler can be obtained by the following equation [46], showing the value of 24.3MHz.

$$f_{ks} = \frac{v_s}{2w_g} \tag{6.4}$$

To avoid the coupling by kerfs in linear array which is basically a 2-2 composite, it is always suggested that the shear resonance of kerfs filler should appear at least as twice large as the operating frequency of the transducer[49]. But it can only be realized by doubling the shear velocity of the material or halving the kerfs width. The further reduction in kerfs width is already impossible for current high frequency arrays due to the fabrication difficulties. Meanwhile, most epoxies used as kerfs filler show their shear velocity ranging from 800 to 1500m/s; it's too hard to find a material showing sufficient large shear velocity. Nevertheless, for the arrays using Epoxy 2 and Epoxy 3, the coupling of shear resonance to the major T-mode is less strong. One reason can be ascribed to the decrease of the shear velocity. It leads to the shear resonant frequency of 20MHz for Epoxy 2 and 11MHz for Epoxy 3. And another reason is probably the larger attenuation so that the shear resonance is further weakened.

However, it is found that the shear resonance in impedance spectrums does not influence the element vibration (the ceramic partition). Figure 6.6 illustrates the IL (insertion loss) spectrums of the arrays with the three kerfs filler and compares to the results of KLM model, with the parameters listed in Table 6.3, including IL peak value IL_{max}, central frequency f_c and fractional bandwidth *BW*.

The central frequency and bandwidth of the three arrays are generally comparable and agree well with the KLM model. But their peak values are much lower than the KLM results, and it is thought

to be caused the energy dissipation in the lateral direction, since KLM model only considers the 1D vibration in thickness direction, while the energy in FEA (or experiment) also transmits laterally and attenuates in the kerfs material. Besides that, a slight decreasing trend in the IL_{max} with the increase of the attenuation in kerfs filler is found by FEA. This also implies there is some energy loss in the lateral direction or kerfs. However, the influence of kerfs attenuation on the IL peaks seems quite limited, because there is about 2dB difference between the lowest and the highest.

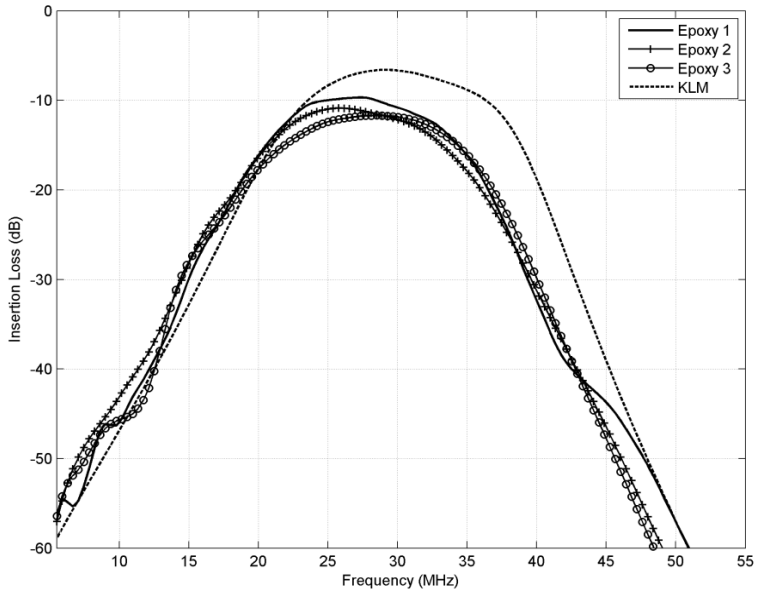

Figure 6.6 IL spectrums of the element in the arrays using the three epoxies, with the KLM response as a comparison

Table 6.3 Parameters of IL spectrums for the arrays using three epoxies by FEA and KLM

Design	IL_{max} (dB)	f_c (MHz)	BW_f (%)
Epoxy 1	-9.68	27.5	52.9
Epoxy 2	-10.9	27.1	54.1
Epoxy 3	-11.7	27.9	56.9
KLM	-6.60	30.0	53.0

Thus clean T-mode vibrations are expected in the ceramic partition of the element, while the vibrations in the kerfs are determined by kerfs filler. Figure 6.7 displays the pressure pulses at the element centre, outer edge and the centre of its nearest kerfs in both time and frequency domain, when only a single element is excited in the linear array by using the three kerfs fillers. Notice that all the pressure pulses in time domain are normalized by the largest amplitude of all the pulses in

the three positions in the three arrays with different kerfs filler, while the ones in frequency domain are normalized by their own amplitude.

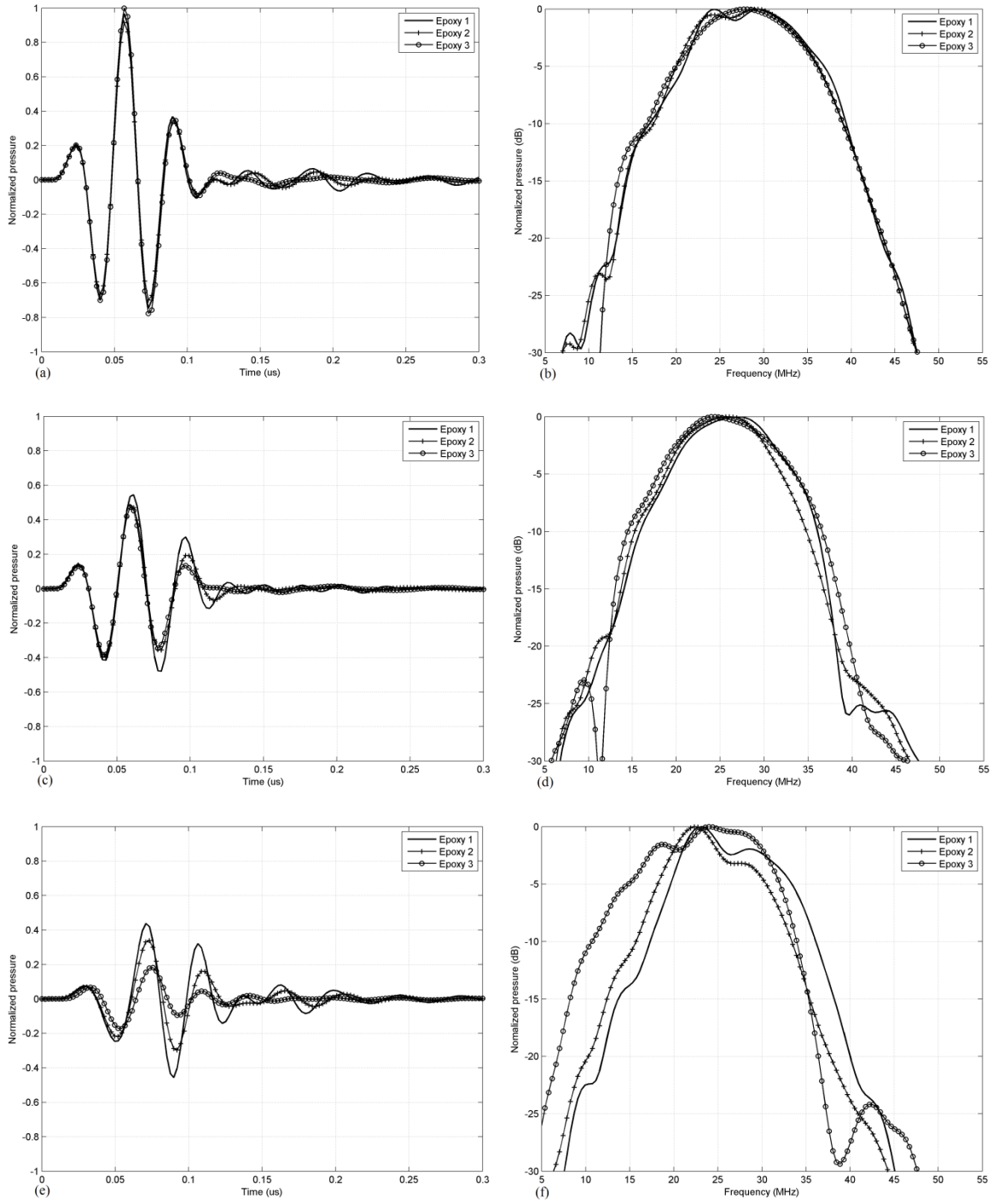

Figure 6.7 (a), (b) shows the pressure pulses at the centre of the element in the linear array using the three kerfs fillers; (c), (d) for the pulses at the outer edge; and (e), (f) for the pulses at the centre of the nearest kerfs

The pulses at element centre and outer edge for the three arrays are generally the same; there is no significant influence of kerfs filler on the vibration of element ceramic partition. By the comparison between the pulses at the centre and outer edge for all the arrays, the amplitude at the outer edge is about half of the amplitude at centre, and a slight lower central frequency. This implies a non-uniform surface vibration at the surface of element ceramic partition, very similar to the surface vibration of annular array element discussed in previous chapters. But in general, all these pulses are in-phase, and show similar responses.

However, the oscillation from the surface of the inactive element kerfs partition can also be clearly seen in Figure 6.7(e), and this is very likely to be caused by the surface waves. These waves appear after the main T-mode vibration in the active ceramic part in an element. This is one of the characteristics for the surfaces waves, as they are travelling transversely across the aperture surface. However, the amplitude of the kerfs vibration is relatively large, almost comparable to the amplitude at the edge of ceramics for the arrays using the first 2 epoxies. But the amplitude becomes relatively low when high-attenuated kerfs filler, Epoxy 3, is used, since a decreasing trend of the amplitude is found by the increasing attenuation of the epoxy used. How the kerfs vibration impacts radiation pattern might be hard to predict at current stage, but there is certainly some influence as discussed in Section 6.3.1. The array using high-attenuated kerfs filler (i.e. Epoxy 3) would be preferable, as it is close to the ideal vibration and probably shows less influence on radiation pattern. The patterns of these linear arrays with different kerfs fillers are then analyzed in the next section by using FEA.

6.4 Imaging Performances of the Linear Array

This section is aimed at obtain the imaging performances of the linear array by FEA method, mainly includes two responses: the pressure at the focal point and the radiation patterns. Since the imaging of the array is expected to be impacted by the kerfs vibration, their relationship is analyzed at first.

6.4.1 Influence of the Kerfs Vibration

The 9-element, 30MHz linear arrays with pitch width of 50μm and f-number of 2 by using the three different kerfs fillers are modelled in FEA. Figure 6.8 illustrates their pressure pulses at the focal point, and both in time and frequency domain.

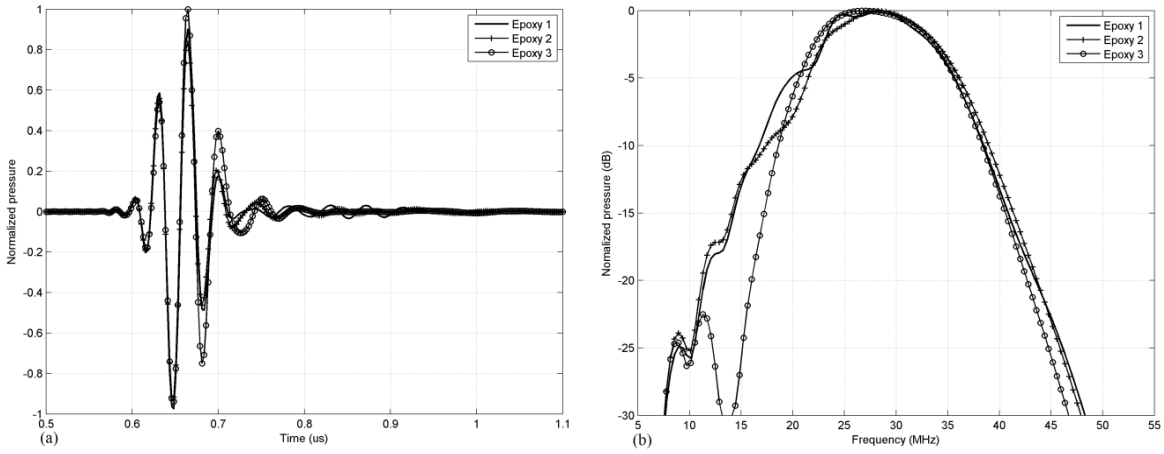

Figure 6.8 Pressure pulses at the focal point for the linear array using the three kerfs filler in (a) time and (b) frequency domain

Similarly, the pulses in time domain are normalized by the largest pulse amplitude, while the ones in frequency domain are normalized by their own maximum amplitude. The pulse parameters are listed in Table 6.4, including maximum amplitude P_{max}, -6dB pulse length $PL_{(-6)}$, -20dB pulse length $PL_{(-20)}$, central frequency f_c and fractional bandwidth BW.

Table 6.4 Parameters of the pulses at the focal point

Parameters	P_{max} (10^4Pa)	$PL_{(-6)}$ (ns)	$PL_{(-20)}$ (ns)	f_c (MHz)	BW (%)
Epoxy 1	2.00	55.8	100.8	27.6	63.1
Epoxy 2	1.89	54.5	107.8	28.9	54.5
Epoxy 3	2.03	64.9	123.5	28.2	57.4

It can be seen that the pressure pulses for all the arrays are generally close to each other, with the similar amplitude, central frequency and bandwidth. Besides that, though large kerfs vibrations are found in the element of the array using kerfs filler “Epoxy 1” and “Epoxy 2”, no significant ringing is found in their focal pulses. It is probably due to the strong and dominant interference of the main T-mode vibration in every element. However, the array using “Epoxy 3” and showing weak kerfs vibration actually has a slightly larger pulse length, mainly because of the additional lobe about 10MHz in the frequency band of the pulse. This component are very likely attributed to

the shear resonance of the kerfs, it is coupled to the main pulse nearly at the end of main pulse and leads to the increase of both -6dB and -20dB pulse length. The shear resonance of the kerfs also exists in the pulses for the array filled by Epoxy 1 and 2, but their resonant frequency is much closer to the central frequency and thus results in the less influence on the main pulse, as well as the shorter pulse length. Nevertheless, the pressure pulses at the focal point for all the arrays could be described as a short and broadband pulse, despite the influence of kerfs vibration.

To reveal the influence of kerfs vibration on the array radiation pattern, Figure 6.9 displays the patterns of the linear arrays using the three kerfs filler at the focal plane, with the comparison of the R-I evaluated pattern. Notice the Gauss pulse used here are set to fit the pressure pulse for a single element, instead of the pulse by KLM model. The pulse shows its profile of 53% bandwidth, 30MHz operating frequency and -25dB TPE. The beam parameters are then listed in Table 6.5, including only the lateral resolution *Res* and contrast resolution *CR*.

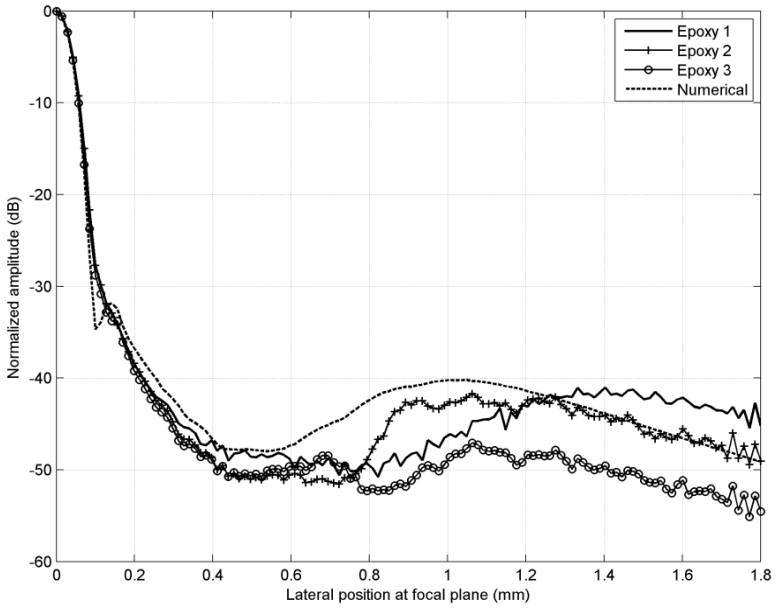

Figure 6.9 Radiation patterns of the three linear arrays and the one by R-I method

Table 6.5 Beam Parameters of the three arrays, compared to the R-I results

Parameters	Epoxy 1	Epoxy 2	Epoxy 3	R-I
***Res* (μm)**	92.7	92.2	89.6	87.7
***CR* (μm)**	439.5	443.9	419.7	508.2

It can be seen that the main lobe of the three arrays are close to each other and generally agree with the R-I result by their similar resolution and contrast. But the patterns of these arrays by FEA method do not show any evidence of nearest sidelobe appearing in R-I pattern about 130μm. It is probably benefit from the actual arc-shaped vibration (kerfs vibration is weaker than the ceramic vibration) in every element. The arc-shaped vibration has the similar function as apodization, which slightly increases the resolution but suppress the sidelobe. Nevertheless, the pattern suggests that the influence of kerfs vibration is not very significant in the region of main lobe.

More importantly, in the region around 1mm, the R-I pattern shows the lobe caused by the large volume of kerfs in the array and is certificated by the FEA responses, the increasing trend of the lobe level can be found in this region for the arrays using “Epoxy 1” and “Epoxy 2”, while the array of “Epoxy 3” keeps a generally same pattern level. However, the lobe patterns seem more complicated than the R-I evaluation, probably due to the complicated kerfs vibrations. Nevertheless, the improvement of the additional lobe by using high attenuated material can be found. In addition, the pattern the array using “Epoxy 3” as kerfs filler is even better than the ideal R-I pattern, while the levels in the same region for the arrays using the other two kerfs fillers are also slightly lower than the R-I one. This might be related the complexity of the kerfs vibrations in FEA, while R-I method assumes the kerfs vibration as none.

6.4.2 Imaging Patterns of Very High Frequency Linear Array

High attenuated kerfs filler shows its effectiveness on the beam improvement by suppression of complicated kerfs vibration for a 30MHz linear array. For an array of higher operating frequency, or namely a very high frequency array, the attenuation would only be stronger, since the attenuation increase by the increase of frequency. Thus the patterns are expected to be much closer to the R-I results with higher operating frequency.

The linear array is designed to have operating frequency of 45MHz and 60MHz by simply changing the thickness of ceramic and matching layer to half and quarter wavelength respectively. The width of element pitch still remains at 50μm (30μm wide ceramic and 20μm wide kerfs), therefore, the grating lobe would appear in the radiation since 50μm is larger than one-λ for the operating

frequency higher than 30MHz.

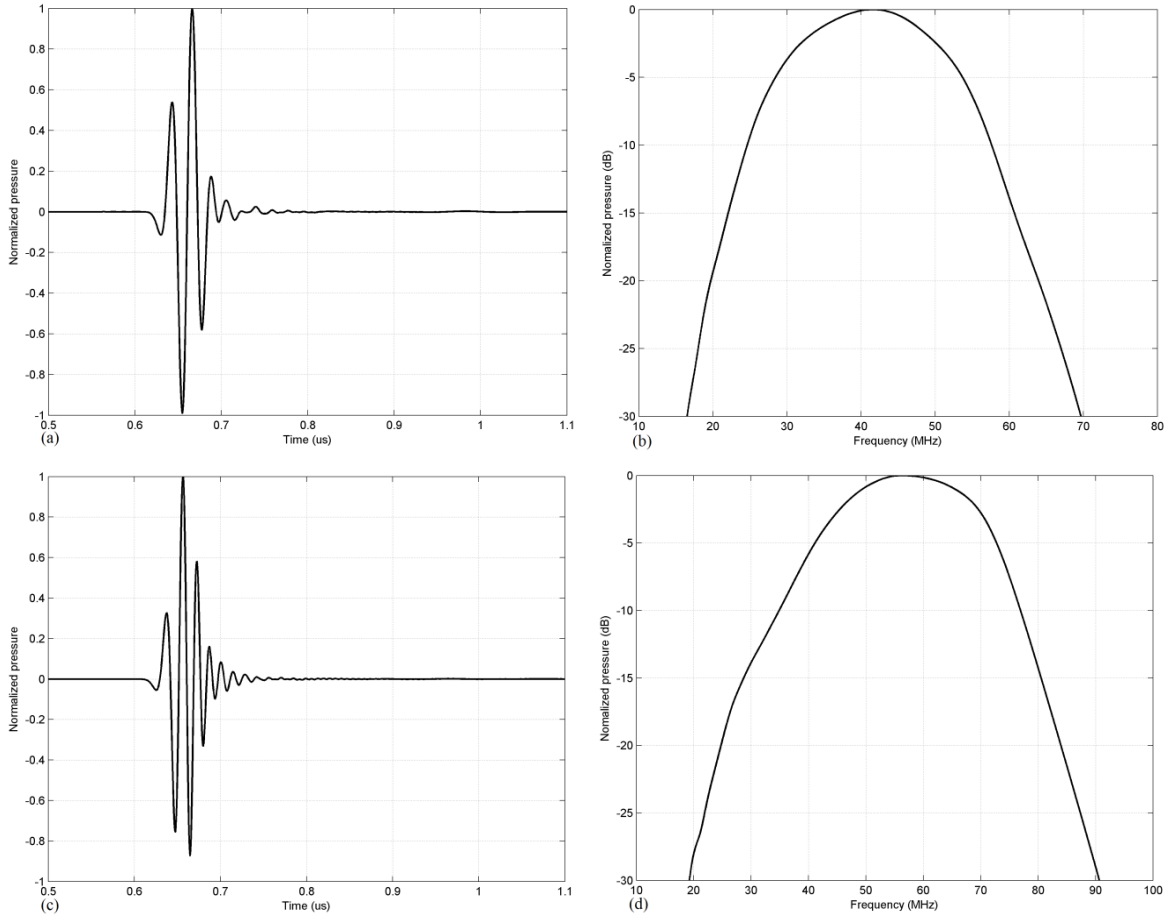

Figure 6.10 (a), (b) Pressure pulses at the focal point for the 45MHz linear array; and (c), (d) show the responses of the 60MHz array

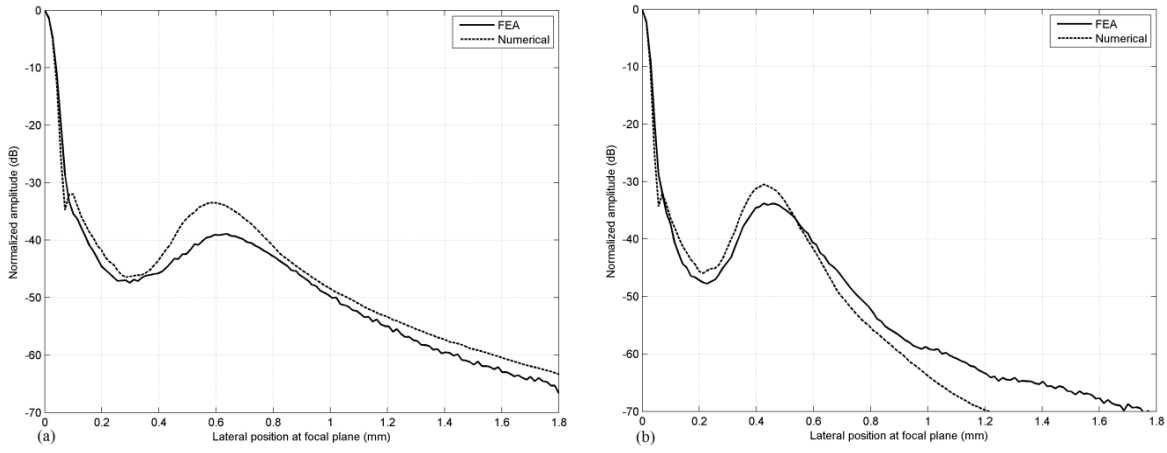

Figure 6.11 (a), (b) Pressure pulses at the focal point for the 45MHz linear array; and (c), (d) show the responses of the 60MHz array

Figure 6.10 firstly shows the normalized pressure pulses at the focal point for the 45MHz and 60MHz array with using the kerfs filler “Epoxy 3”. Figure 6.11 then displays the radiation patterns of the two arrays with the comparison of R-I results. It can be seen that the pressure pulses are short and shows broadband without much ringing, and no additional lower frequency lobe is found in the frequency band. Furthermore, the beam patterns of the two arrays are generally agree with the R-I evaluation, and show no significant influence by either transverse waves or kerfs vibration. Likewise, the nearest sidelobe in the R-I pattern is suppressed by the arc-shaped vibration at the narrow element.

However, large grating lobe is found in the two arrays, with its level increasing by the operating frequency. By the increase of frequency, the wavelength-scaled pitch width also decreases and leads to closer and closer lobe position to the focal axis. The position of the grating lobe obtained from the patterns in Figure 6.10 is also compared to the theoretical value obtained by Equation (4.9), and generally good agreement is achieved as illustrated in Table 6.6.

Table 6.6 The lateral position of the grating lobes using different methods

Lobe position	Array	Theoretical	FEA	R-I
r_g (mm)	≈45MHz array	0.68	0.60	0.57
	≈60MHz array	0.47	0.45	0.43

To suppress the grating lobe, the required pitch width would become very small, for instance, 33μm for 45MHz and only 25μm for 60MHz array. However, the current dicing and filling technique generally could achieve the kerfs width of 20μm. The volume of ceramic in an element pitch would becomes only 39% for 45MHz array and 20% for 60MHz array, if the required pitch width is maintained. The ceramic volume is so small that causes large reduction in sensitivity, and thus is not recommended in the linear array transducers. Therefore, the suppression of grating lobe is not possible in very high frequency (>45MHz) unless there is a newly developed improvement in the current dicing techniques.

6.5 Summary

In the design of a high frequency linear array, the element pitch needs to be at most one-λ wide to move the grating lobe out of the focal plane. The 30MHz array is designed to have 30μm wide ceramic and 20μm kerfs for the one-λ element pitch. However, the one-λ pitch actually is found to be not the only influential factor to determine the grating lobe in the radiation pattern, but also the kerfs width. For an ideal array without any kerfs among elements, the pattern shows no evidence of grating lobe. But by the increase of kerfs width, an additional lobe becomes apparent in a certain region of the pattern with the increasing lobe level as well. It is caused by the vibrations in the kerfs. Therefore, high attenuated epoxy is used as the kerfs filler to damp the kerfs vibration. By FEA method, the level of additional lobe decreases by the increase of the attenuation of the kerfs filler. In addition, there is also a nearest sidelobe found in the R-I pattern, this lobe is actually suppressed in FEA response because of the “natural apodization” (or the arc-shaped vibration) by the linear array element.

In addition, the grating lobe would appear if the array maintains the same pitch width and ceramic volume in very high frequency (>45MHz) linear array. However, the pitch width could be reduced to the required level of one-λ, but leads to the very low ceramic volume in the array since the smallest kerfs width that current dicing technique could achieve is very limited. Therefore, it is essential to find out a method to suppress the grating lobe, but the only possible way seems to be the improvement of current fabrication techniques.

Chapter 7 Novel High Frequency Linear Array

7.1 Introduction

Because of the difficulties in current dicing techniques, the high grating lobe becomes unavoidable in the very high frequency linear array. Besides the effort to find an improved fabrication technique, a novel array using the similar principle instructed by Moshfeghi et.al [116] is now developed to suppress the grating lobe.

By using the novel structure, the linear array is able to operate in two different frequencies, instead of only one for conventional linear array. The radiation pattern obtained by the lower-frequency process is designed to show no evidence of grating lobe. Though the pattern formed by higher-frequency process has a large grating lobe, the lobe is expected to be suppressed by the pattern with lower frequency through a process named spatial compounding [58]. In this technique, every image formed by the transducer with different requirement is recorded, and then combined together or averaged to yield a single (compound) image. Because the compound image contains N_i images, the frame rate will be also reduced by N_i. The technique is widely used in transducers to improve their imaging quality [59, 117]. In the novel linear array, two images (one higher frequency, and one lower) is compounded, thus the frame rate will be halved compared to conventional B-scan transducers.

As a result, the compound pattern shows the suppression of grating lobe. For example, a 9-element novel array operating at the two frequencies of 30MHz and 80MHz approximately reduces the grating lobe level about 4 to 5dB, compared to a 70MHz conventional linear array with similar resolution as the novel array. However, as the cost of the lobe suppression, the frame rate of the novel array would be halved by the compound process, but it is regarded as a minor disadvantage because the frame rate in linear array without using any mechanical scan is already very fast.

Although the grating lobe is suppressed by the novel array, its level is still found to be higher than -40dB, far from the recommended level of -50dB in the ultrasonic imaging [62]. It is caused by the very small number (only 9) of the excited element, while a common linear array has at least 32-

elements. With more elements involved in the linear array either the conventional or the novel one, the level of its grating lobe could be further reduced [4].

A way to optimize the suppression of grating lobe is also found. In the original design of the novel array, the higher-frequency pattern with grating lobe is compounded into the lower frequency pattern without grating lobe to realize the suppression. However, the region of lower-frequency pattern where the grating lobe is coupled into is actually not the lowest beam region. To further suppress the grating lobe, we could make the grating lobe appearing in the higher-frequency pattern to be coupled into the region of the lower-frequency pattern where the beam level is almost the lowest. As a result, an optimized decrement of 6dB in general can be achieved in lobe level compared to the conventional array.

There is a similar technique also reported, called harmonic imaging. To briefly describe it here, transducers emanate pulses with their fundamental frequency f_0, while the returning echoes only have the n^{th}-order (usually n=2) harmonic frequency ($n \cdot f_0$) by using a band-pass filter [58]. Thus the low-frequency transmitting pattern is compounded to the high-frequency receiving pattern to form an image. However, harmonic imaging needs a transducer to have sufficient bandwidth to cover both fundamental and n^{th}-order harmonic frequency. But it seems unlikely to have enough large bandwidth to cover the two frequencies in high-frequency range [118-120], for example, 30-90MHz as the novel linear array attempts to realize. In addition, the band for either low or high frequency pulses in harmonic imaging needs to be relatively narrow to fit within the overall transducer band, as this leads to a relatively long pulse response and causes the degradation in axial resolution. But a short pulse in the two frequencies can be achieved in the novel array. Although the novel array has a drawback as the frame rate is halved, it has advantages in the high frequency field compared to the harmonic imaging.

In this chapter, the design of the novel array is firstly presented, and KLM model is the main tool to evaluate the feasibility of the novel structure. Secondly, the performances of the novel array are examined by using FEA method. Because the limitation of our current computer, the novel array with small number of elements is modelled and compared to the conventional array. The suppression in grating lobe has been successfully achieved. At the end, the method to further suppress the grating lobe by the optimization in the design of novel array is revealed.

7.2 Design of a Novel High Frequency Linear Array

The radiation pattern of a 30MHz linear array has shown the expected resolution and no obvious lobe away from the focal axis, if high attenuated kerfs filler, EC-2CN loaded by PbO powder, is used. However, if the operating frequency of the transducer is increased to achieve better resolution, the grating lobe would appear if the pitch width is remained the same as 30MHz array since it breaches the one-λ rule. The same pitch is aimed to maintain same amount of ceramic volume, as well as the kerfs width which is limited by current dicing technique.

Here, instead of using an advanced dicing technique to reduce the achievable kerfs width, an approach based on the novel structure of linear array is developed to suppress the grating lobe in very high frequency linear array, without changing the ceramic volume and the already very small kerfs width.

7.2.1 Method of Grating Lobe Suppression

Moshfeghi et.al [116] in 1987 published a method to reduce sidelobe level by using different aperture size of transmitter and receiver in an array transducer, with the compromise of slight decrease in imaging resolution. This method is briefly introduced here: a transducer actually reacts as both transmitter and receiver, and their aperture sizes depend on the active area in the array. The position of sidelobe is determined by the aperture. Since the final 2-way radiation pattern is the compound of the 1-way transmitter pattern and receiver pattern, the sidelobe could appear in different position during transmitting or receiving. By the suitable design of the active area in transmitter and receiver aperture, their sidelobes can be cancelled to each other or largely suppressed. Meanwhile, because one of the 1-way patterns is generated by a smaller transmitter or receiver in this method and thus leads to a larger resolution, the compound resolution of overall 2-way pattern also shows decrease.

However, this method does not work in the suppression of grating lobe, since the position of grating lobe is determined by the wavelength-scaled width of element pitch, instead of the aperture size. But its principle can be adopted to develop a way to suppress the grating lobe. 30MHz linear array with 50μm pitch shows no evidence of grating lobe, while the array with higher frequency and the same pitch is expected to show a grating lobe in its pattern. Thus if we

compound the pattern of the higher-frequency array with grating lobe into the pattern of the lower-frequency array without grating lobe, the suppression of grating lobe can be realized. But similarly, a loss in resolution of the compound pattern is expected because of the lower-frequency pattern.

To implement this idea, a single array transducer needs to operate at both lower and higher frequency. The low-frequency pattern is firstly formed without any grating lobe as a “transmitter”, while the high-frequency pattern is later formed as a “receiver”. Hence, a novel structure is then developed and illustrated in Figure 7.1, where *n* is called enlargement ratio defined as the ratio total thickness of the two ceramic layers to the one of bottom ceramic layer; *p* denotes the pitch width, *d* is for thickness for first ceramic layer, and *n·d* is for the total thickness of the two ceramic layer in this novel structure.

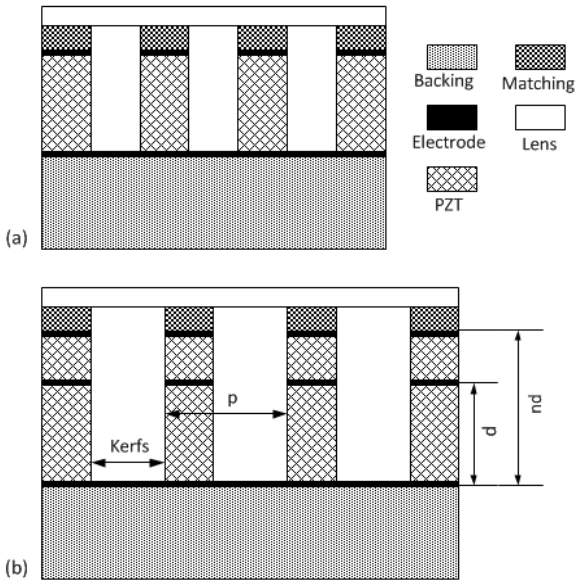

Figure 7.1 Cross section of (a) conventional and (b) novel 1-D linear array

In the novel array, the lower-frequency pattern is firstly realized by only exciting the top and bottom electrode. In other words, both ceramic layers are excited and responded at a lower resonant frequency dependent on the ceramic thickness to form the first radiation pattern without grating lobe. The influence of middle electrode on resonance can be neglected since its thickness is generally very small (less than 1μm if sputtering is used). The first process is described as “Lower Frequency Imaging” (LFI). Then only the middle and bottom electrodes are excited to

activate the only bottom ceramic layer, which shows a higher resonant frequency because of the reduced thickness of active ceramic layer. This process is called “Higher Frequency Imaging” (HFI). Though grating lobe appears at HFI, it would be suppressed in the compound imaging of HFI and LFI. Additionally, the ratio of resonant frequency for HFI to the one for LFI is equivalent to enlargement ratio *n* because the frequency is inverse proportional to the active ceramic layer.

Besides that, the frame rate of the image in novel linear array is half of the one in conventional linear array, because the system compounds the two independent LFI and HFI patterns and thus doubles the time to obtain the overall image. Nevertheless, since the frame rate of a linear array is already very fast, the half of it could be still regarded as an enough fast enough scan to obtain the images in medical applications.

7.2.2 Details in the Design of Novel Array by KLM Model

The novel structure is expected to suppress the grating lobe, but there are still two concerns in the design. First of all, the thickness of matching layer cannot be changed in the process of either LFI or HFT. As a result, its thickness could only be matched to one imaging process, since its thickness is no longer a quarter of the wavelength in another imaging process. The second concern is related to the top inactive ceramic layer in HFI process, which reacts as a dielectric layer. The additional layer could cause some deterioration in element bandwidth.

In terms of the concern of matching layer, the thickness of matching layer has to be designed as quarter-wavelength only suitable for one process. The matching layer matched to LFI is described as LFM (low-frequency matching) option, while the one matched to HFI is called HFM (high-frequency matching) options. It is expected that HFM could show better bandwidth than LFM for the array element, because the perfect matching by HFM could reduce deterioration of the band caused by the additional ceramic layer in HFI. Though it also leads to the mismatch in LFI that could reduce bandwidth, it might be still acceptable because of no additional ceramic layer involved. It is the compromise to have two decent band spectrums in HFI and LFI by using HFM, instead of one “perfect” band in LFI but one poor band in HFI by using LFM.

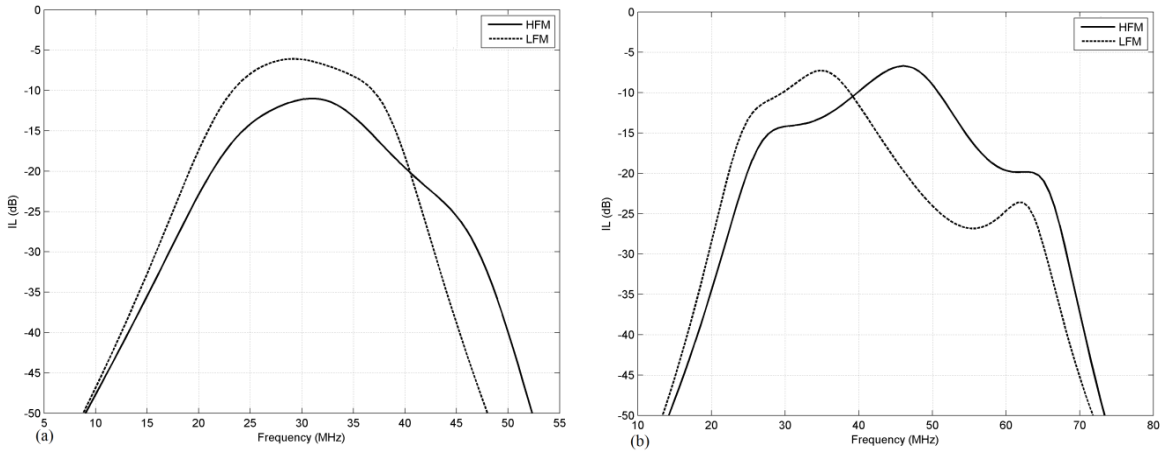

Figure 7.2 IL responses by the two matching options in (a) LFI and (b) HFI with *n*=1.5

KLM model is then applied to compare the frequency responses for the two matching layer options in the process of LFI and HFI. The materials used for all the layers are the same as the ones in conventional linear array presented in last Chapter. Similarly, the lateral geometric parameters of an element are 30μm for ceramic pillar width and 20μm for kerfs width. Figure 7.2 illustrates the IL (insertion loss) spectrum of an array element using the 30MHz beamformer (LFI) as a base and a 45MHz HFI, or equivalently with the enlargement ratio *n* of 1.5 for example.

It can be seen that the matching layer using LFM shows very narrow bandwidth in HFI, while large improvement is found by using HFM. Though the decrease of IL peak (or sensitivity) by HFM is also found in LFI, but without too much deterioration in bandwidth. Therefore, the HFM shows the required compromise in the element band both in HFI and LFI, and chosen to be the matching layer of the novel array for further investigations.

However, Figure 7.2 only shows the element response for the transducer with enlargement ratio *n* of 1.5, while it is found that the ratio n also shows its influence in the HFI band because of the additional inactive ceramic layer. Figure 7.3 then compares the IL spectrums of the element for the array with different *n* ranging from 1 to 3, when the total thickness "$n \cdot d$" of the two ceramic layers are fixed. Notice that ratio *n* of 1 represents the conventional array. Their band parameters are listed in Table 7.1, including IL peak value IL_{max}, central frequency f_c and fractional bandwidth *BW*.

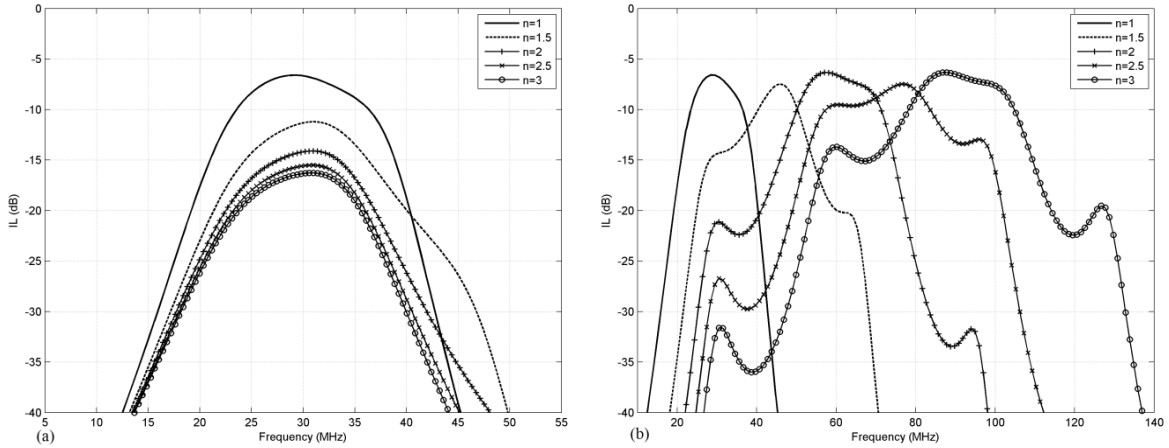

Figure 7.3 IL spectrums of the novel array element in (a) LFI and (b) HFI with different *n*

Table 7.1 Band parameters of the novel array element with different *n*

n	**LFI**			**HFI**		
	IL_{max} (dB)	f_c (MHz)	*BW* (%)	IL_{max} (dB)	f_c (MHz)	*BW* (%)
1	-6.57	30.0	53.4	-6.57	30.0	53.4
1.5	-11.2	30.4	49.7	-7.46	43.8	41.7
2	-14.1	29.7	48.9	-6.34	60.6	41.3
2.5	-15.5	29.5	49.3	-7.48	75.6	58.8
3	-16.3	29.4	49.7	-6.33	91.0	35.4

In LFI, it can be found that the IL peak (or sensitivity) IL_{max} decreases by the increase of enlargement ratio *n* in LFI due to the increasing mismatch between ceramic and fluid, but with smaller and smaller the decrement. The central frequency and bandwidth are generally in a similar level. It suggests that LFI could keep the same operating frequency and broad band to suppress the grating lobe in HFI with different *n*.

In HFI, the IL_{max} in the array of *n*=1, 2 and 3 (all integers) shows generally similar level, while a slight drop is found in the array of *n*=1.5 and 2.5. It is due to the influence of the additional and inactive ceramic layer. For the array with integral n, the thickness d_a of additional ceramic layer is (*n*-1) times of the thickness *d* of active ceramic layer, while *d* in HFI is actually half-wavelength ($\lambda/2$). Thus d_a is (*n*-1) times of $\lambda/2$ and the additional ceramic layer becomes a $\lambda/2$ transmission line. Since the $\lambda/2$ transmission line has the identical impedance transfer at the resonance, the matching layer is still matched to the active ceramic at least at the resonance, and thus the same IL peak is expected. On the other hand, for the array with *n*=1.5 and 2.5, the transmission line of the additional ceramic layer becomes the times of quarter-wavelength, the input impedance to

the matching layer is different from one of active ceramic, the mismatch in impedance would occur. However, since the additional ceramic layer is quarter-wavelength thick and acts like an additional matching layer, the mismatch is not very strong and thus only causes slight decrease in IL peak.

Besides that, the central frequency f_c increases by the increasing n, and the ratio of the two f_c also agrees with the ratio of their n. It is due to the decreased thickness of active ceramic layer. However, there is a large drop in the bandwidth in the novel arrays (n>1) compared to conventional array (n=1), expect the one of n=2.5. It is caused by the rippled frequency band. There are mainly two minor lobes away from the IL peak for the array with large n. One is located at left of the main peak, and another is at right. These lobes are ascribed to the additional ceramic layer, which deteriorates the tuning away from main resonance. Thus the lobes are then coupled into the main resonance and results in the reduction in bandwidth. The array of n=1.5 is an exception, because the two minor lobes are relatively close to the main lobe and thus actually increase the bandwidth slightly.

Generally, the novel structure shows LFI with different ratio n by the same central frequency and broad band, while the central frequency increased by ratio n is also found in HFI. Though there is reduction of IL peak in LFI and bandwidth in HFI, the novel array generally achieves the requirement of LFI and HFI by KLM method.

7.3 Performances of the Novel Linear Array

FEA method is then applied to verify the design of the novel linear array by the KLM model. In FEA model, it should be noticed that the FEA model of the novel array uses the kerfs filler of “Epoxy 3”, since it is essential to reduce the influence of the unwanted kerfs vibration on radiation pattern in LFI. The performances of the novel linear array include two fields, the element responses and the array imaging.

7.3.1 Element Responses by FEA

First of all, Figure 7.4 illustrates the impedance spectrum of the element in LFI for the novel array with different *n* ranging from 1.5 to 3, while the responses in HFI are displayed in Figure 7.5. The results by KLM model is also displayed and compared to the FEA results. It can be seen that very good agreement has been achieved between FEA and KLM, no lateral or kerfs resonances are found in the all the impedance spectrums. Though there are several additional resonances for the spectrums in HFI, they belong to the resonance of additional ceramic layer. Furthermore, the decrease in the amplitude around the resonances especially in the phase spectrums is caused by the extra energy loss in the lateral direction.

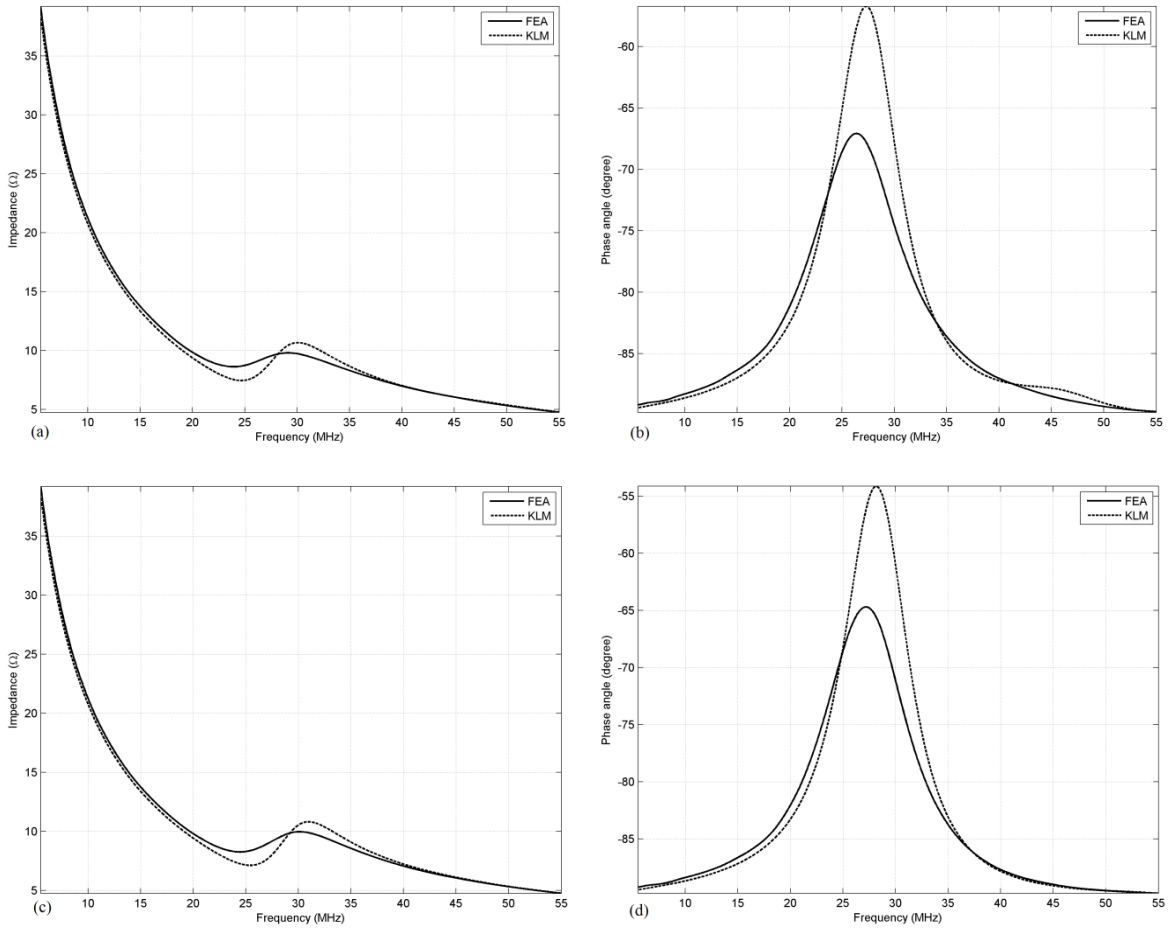

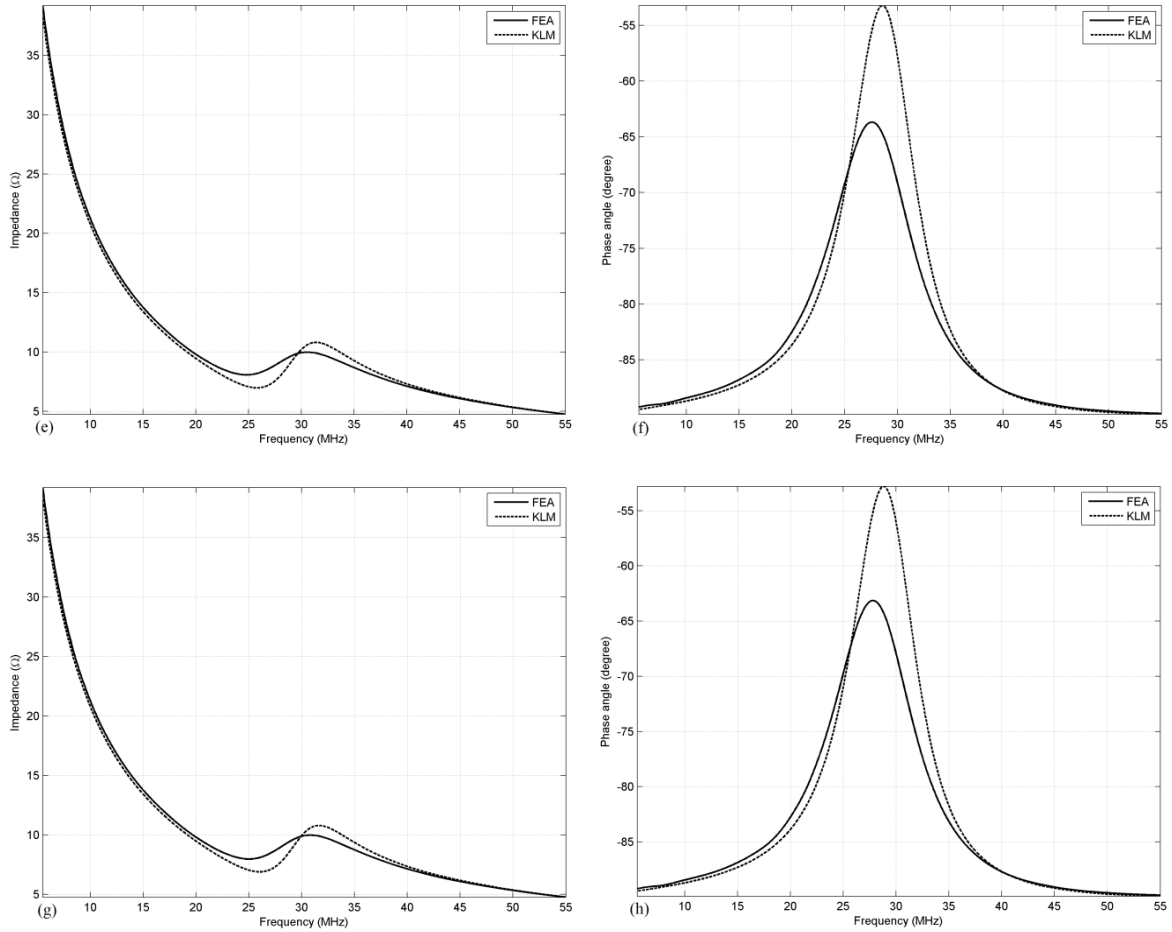

Figure 7.4 (a), (b) show the impedance and phase spectrum of the element in LFI for the novel array with *n*=1.5; (c), (d) for *n*=2; (e), (f) for *n*=2.5; and (g), (h) for *n*=3

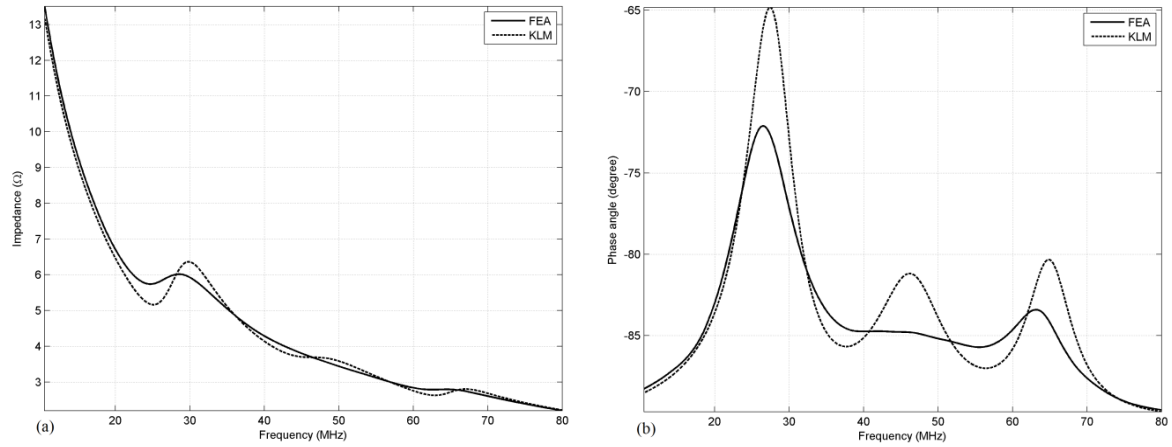

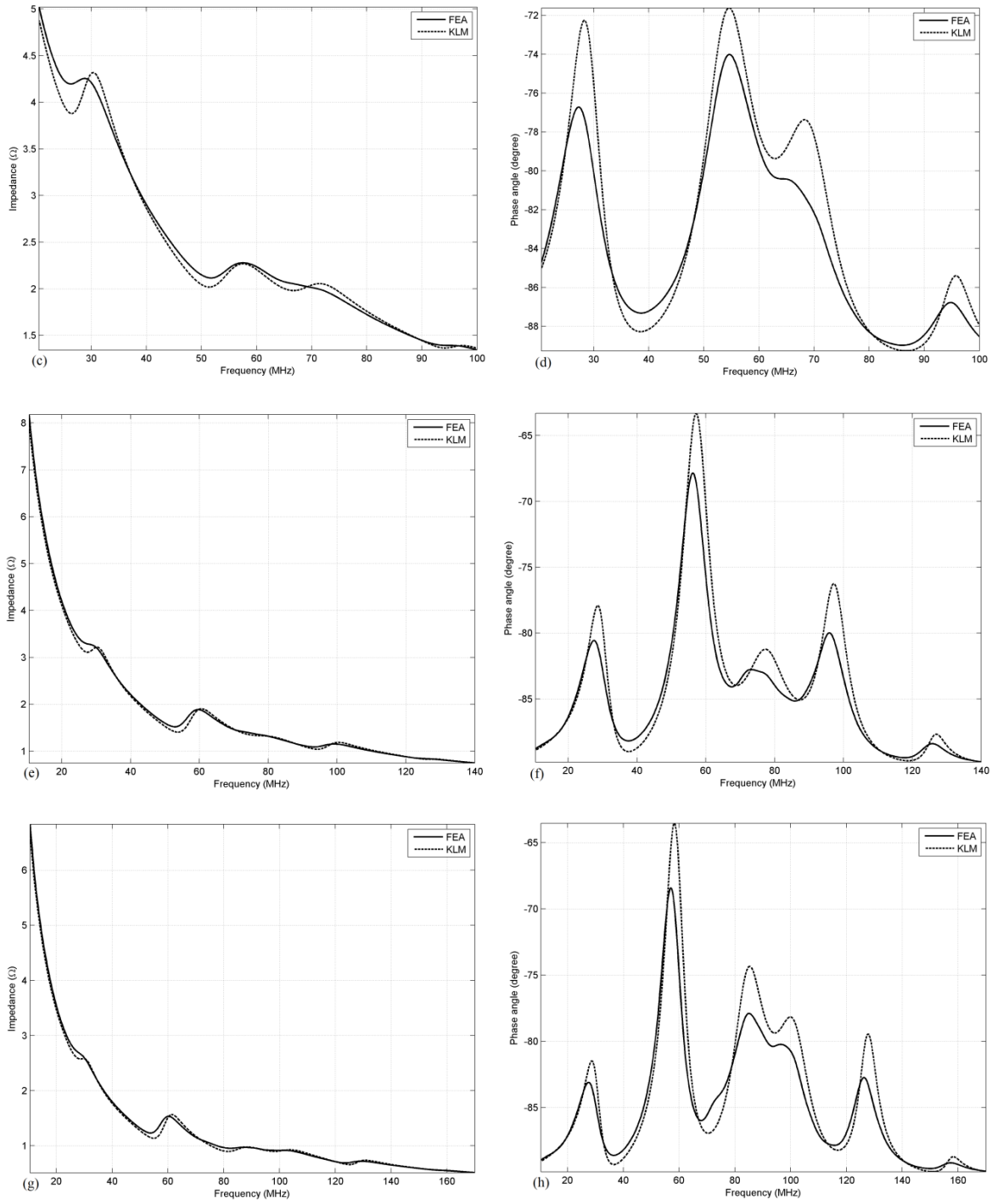

Figure 7.5 (a), (b) show the impedance and phase spectrum of the element in HFI for the novel array with *n*=1.5; (c), (d) for *n*=2; (e), (f) for *n*=2.5; and (g), (h) for *n*=3

Figure 7.6 then illustrates the IL spectrums of the element in both LFI and HFI for the novel array with different *n* ranging from 1.5 to 3 by using FEA method, with the comparison to the results of KLM model. The related band parameters are listed Table 7.2.

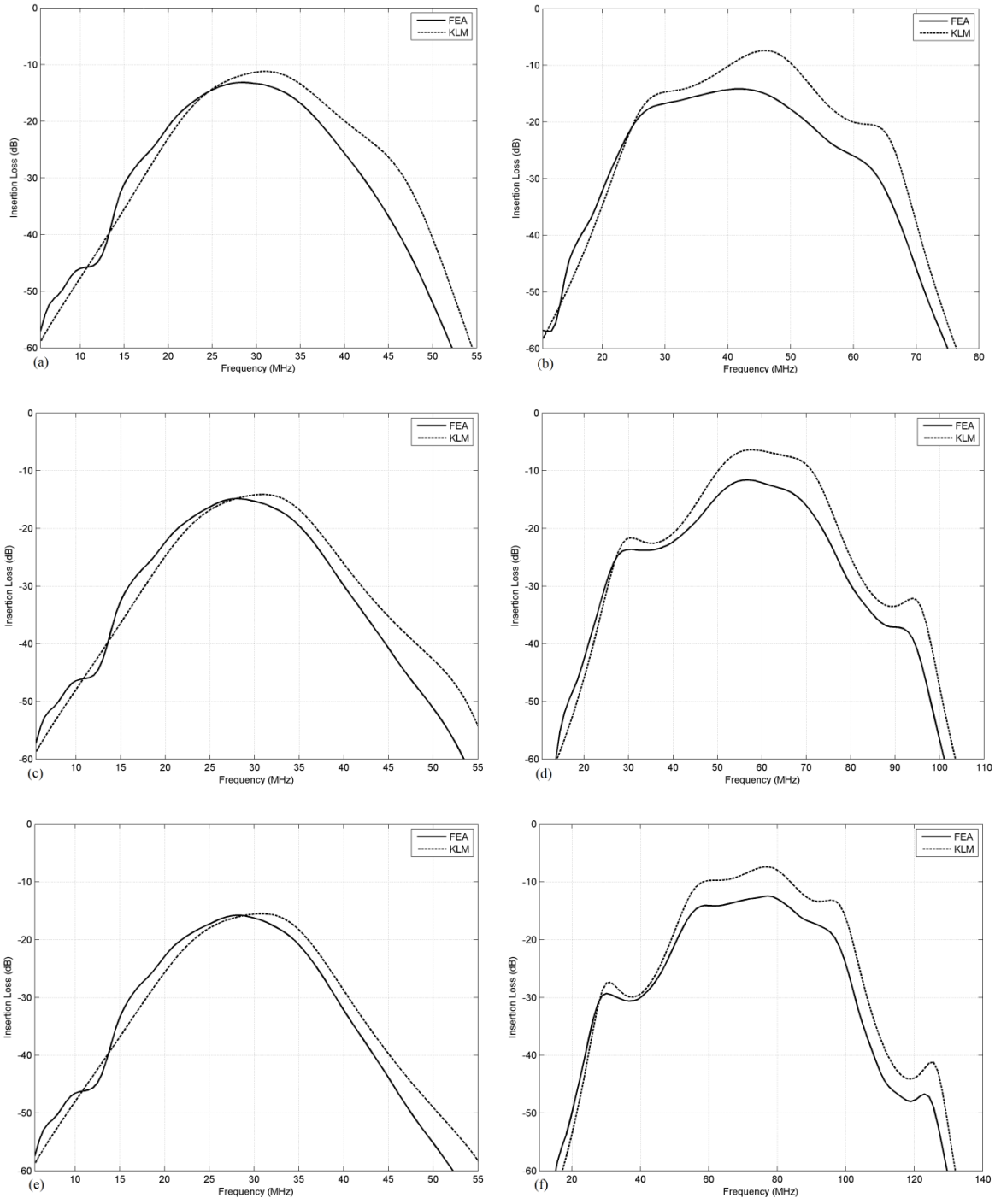
FEA
KLM
Insertion Loss (dB)
Frequency (MHz)
(a)
(b)
(c)
(d)
(e)
(f)

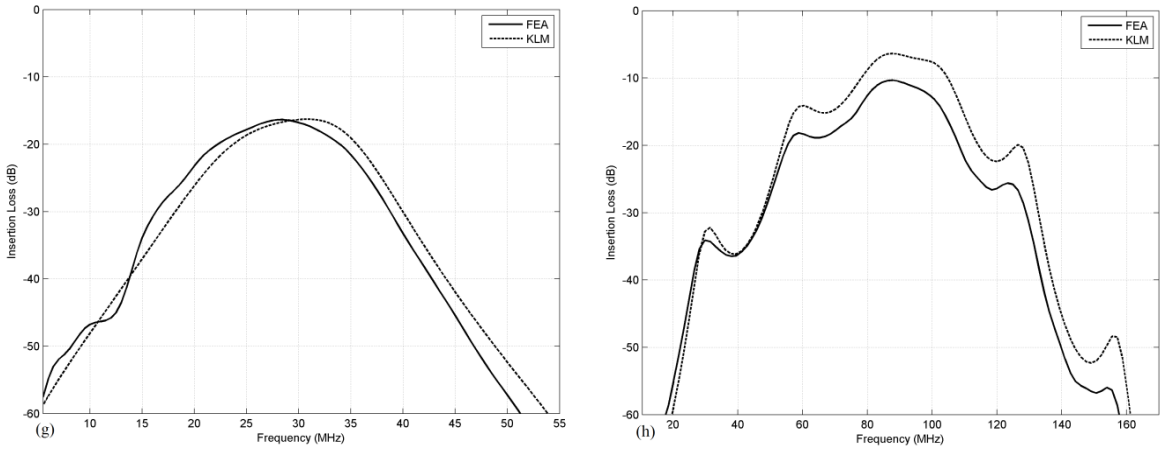

Figure 7.6 (a), (b) show the IL spectrums in LFI and HFI respectively, for the element in the novel array with *n*=1.5; (c), (d) for *n*=2; (e), (f) for *n*=2.5; and (g), (h) for *n*=3

Table 7.2 Band parameters of the novel array element with various *n* by both FEA and KLM, *n*=1 here represents the conventional array (LFI=HFI)

n	Method	LFI			HFI		
		IL_{max} (dB)	f_c (MHz)	BW (%)	IL_{max} (dB)	f_c (MHz)	*BW* (%)
1	**KLM**	-6.57	30.0	53.4	-	-	-
	FEA	-11.7	27.9	56.9	-	-	-
1.5	**KLM**	-11.2	30.4	49.7	-7.46	43.8	41.7
	FEA	-13.2	28.7	54.3	-14.2	39.0	70.8
2	**KLM**	-14.1	29.7	48.9	-6.34	60.6	41.3
	FEA	-14.8	28.3	52.7	-11.6	59.0	42.4
2.5	**KLM**	-15.5	29.5	49.3	-7.48	75.6	58.8
	FEA	-15.8	28.1	53.1	-12.5	73.4	58.6
3	**KLM**	-16.3	29.4	49.7	-6.33	91.0	35.4
	FEA	-16.3	27.9	53.6	-10.3	89.6	34.2

The HFI responses of the conventional array (*n*=1) is not given since they are the same as LFI. By the influence of the lateral energy loss taken into account in FEA, the IL peak of FEA is generally smaller than the one of FEA. However, large decrement in FEA is found for the novel array in HFI, as well as the conventional array. But only a small amount (0-2dB) can be seen in LFI for the novel arrays (*n*≥1.5). It is probably caused by the influence of matching layer. For the conventional array and the novel arrays in HFI, the KLM model predicts a good impedance matching around resonance which provides a very large IL peak. But it is not achievable in FEA or reality due to the extra lateral energy loss, and thus largely reduced. On the contrary, the novel arrays with various ratio *n* in LFI show large impedance mismatch since the matching layers are no longer quarter-

wavelength thick. Since much energy has already lost in the transmission in the thickness direction, the extra lateral energy loss thus becomes much smaller and leads to much less influence on the decrease of IL peak. Nevertheless, the IL peaks for the novel linear ranges from -11.7 to -16.3dB in LFI, and from -10.3 to -14.2dB. By the consideration of many previous researches on conventional linear arrays, the IL peak obtained generally ranges from -10 to -20dB [121, 122]. Hence, the IL peak for novel array is comparable to others.

Besides that, the central frequency and bandwidth in novel arrays by FEA generally agree with the results of KLM model, expect the array with n=1.5 in HFI. By checking Figure 7.6(b) showing the HFI response of the array with n=1.5, a large drop in the IL peak is found in the FEA response, compared to the KLM one. But only a small reduction can be seen in the other two weak lobes alongside the main lobe. Similar behaviour can be also found in other HFI of the novel arrays. But for the array with n=1.5, the left weak lobe is coupled into the reduced main lobe so that leads to the increase in bandwidth and the decrease in central frequency. And for other arrays, the weakened main lobe is still much stronger than others minor lobes. Therefore, no lobe coupling occurs in FEA and their band parameters are close to KLM results. The bandwidths of the novel array in LFI are all above 50% in FEA and thus regarded as broad band, while narrow bandwidth is found in HFI for some arrays (34% for n=3 and 42% for n=2).

In addition, the analysis of transverse waves and kerfs vibrations for these novel linear arrays are not given here, because the high-attenuated material has been used as kerfs filler. It is believed to diminish the influence of transverse waves on the radiation patterns.

7.3.2 Imaging Performances

The linear array is designed to be focused with an f-number of 2. The element pitch is 50μm wide and 9 elements are excited in total for the focusing process, and it leads to the active aperture width of 450μm and the focal distance of 0.9mm. Though the actual high frequency linear array usually has the focal distance about 4mm and contains more than 20 elements, the small-scaled model established in our research still could provide sufficient imaging information, and with a much quicker computing time of FEA.

The novel arrays in LFI have the central frequency around 30MHz and are expected to show no evidence of grating lobes in the focal plane, while the grating lobe appears in HFI since the rule of one-λ pitch is breached. First of all, the novel array with enlargement ratio *n* of 1.5 is investigated, to reveal the pressure pulses at focal plane and the beam patterns in both LFI and HFI.

Figure 7.7 and Figure 7.8 display the pressure pulse at the focal point in LFI and HFI by using FEA, respectively. All the pulses are normalized by their own maximum amplitude in both time and frequency domain.

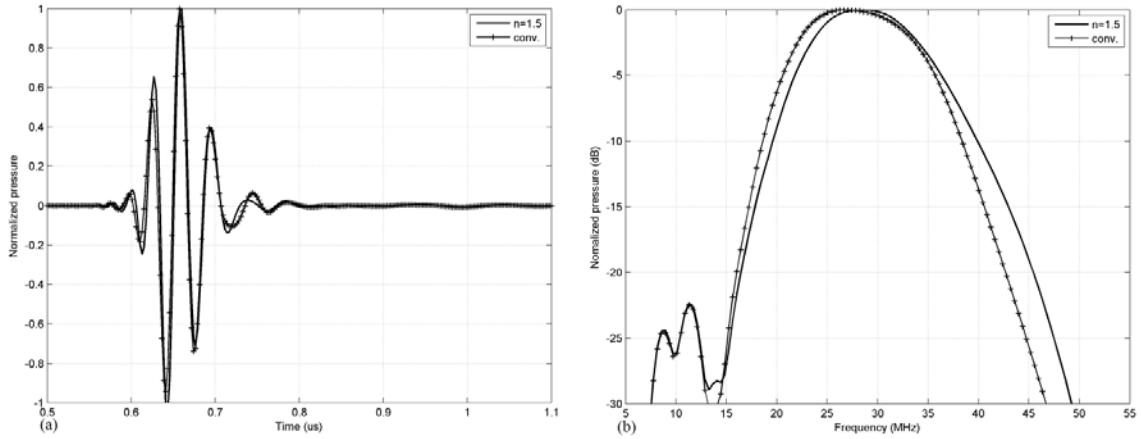

Figure 7.7 Pressure pulse at focal point in (a) time and (b) frequency domain, for the array with *n*=1.5 in LFI and the lower-frequency conventional array

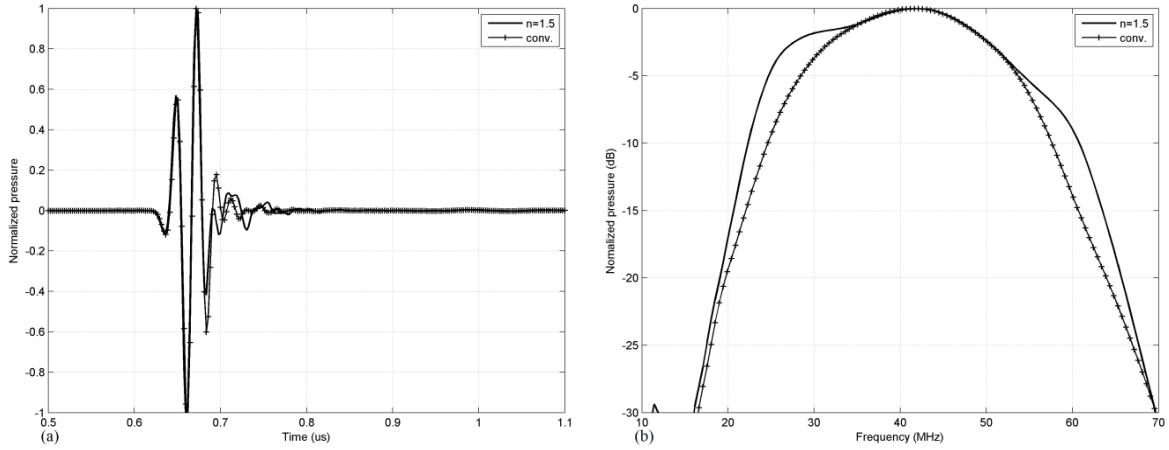

Figure 7.8 Pressure pulses at focal point in (a) time and (b) frequency domain, for the array with *n*=1.5 in HFI and the higher-frequency conventional array

Their parameters are then listed in Table 7.3, including the maximum pulse amplitude P_{max}, -6dB pulse length $PL_{(-6)}$, -20dB pulse length $PL_{(-20)}$, central frequency f_c and fractional bandwidth BW. Notice that both pulse lengths are transferred to the unit of T, where T is the pulse period (T=1/f_c). Meanwhile, the performances of a conventional linear array operating at lower (30MHz) and higher frequency (45MHz) are also given to represent the LFI and HFI of conventional array respectively for comparison, and denoted as "conv.".

Table 7.3 Parameters of the pressure pulses at focal point for the novel array with n=1.5, and the conventional array in both LFI and HFI

Imaging	N	P_{max} (10^4Pa)	f_c (MHz)	$PL_{(-6)}$ (T)	$PL_{(-20)}$ (T)	BW (%)
LFI	conv.	2.03	28.2	1.83	3.49	57.4
	1.5	1.86	29.2	1.88	3.44	54.2
HFI	conv.	3.52	41.1	1.55	2.69	66.3
	1.5	3.33	40.1	1.35	3.94	79.6

It can be seen that the pulse shape in the novel array are almost the same as the one of the conventional array in both LFI and HFI, while some slight differences can be found in their parameters. First of all, the pressure amplitude P_{max} in novel array is slightly smaller than the one of conventional array, because of the lower IL peaks in the novel array element. However, the major differences are found in the -20dB pulse length and the bandwidth in the process of HFI. The length of the novel array is much longer than the conventional one, while its bandwidth is much broader. They are both caused by the additional minor resonance around 28MHz in the frequency domain of novel array for HFI, which can be also found in its element IL spectrum. The minor peak contains low-frequency components and thus leads to some additional ringing at the end of the main pulse, while it is also coupled to the main TE resonance and results in the increase of bandwidth.

The radiation patterns of the novel array with n=1.5 and the conventional array are then displayed in Figure 7.9 for both of LFI and HFI by using FEA method. Their imaging parameters are listed in Table 7.4, including the lateral resolution Res, contrast resolution CR, level of grating lobe GL, the lateral position X_{GL} and angular position ϑ_{GL} of grating lobe. Notice that angle ϑ_{GL} can be simply obtained by the equation of $\vartheta_{GL} = \tan^{-1}(X_{GL}/F)$, where F is focal distance.

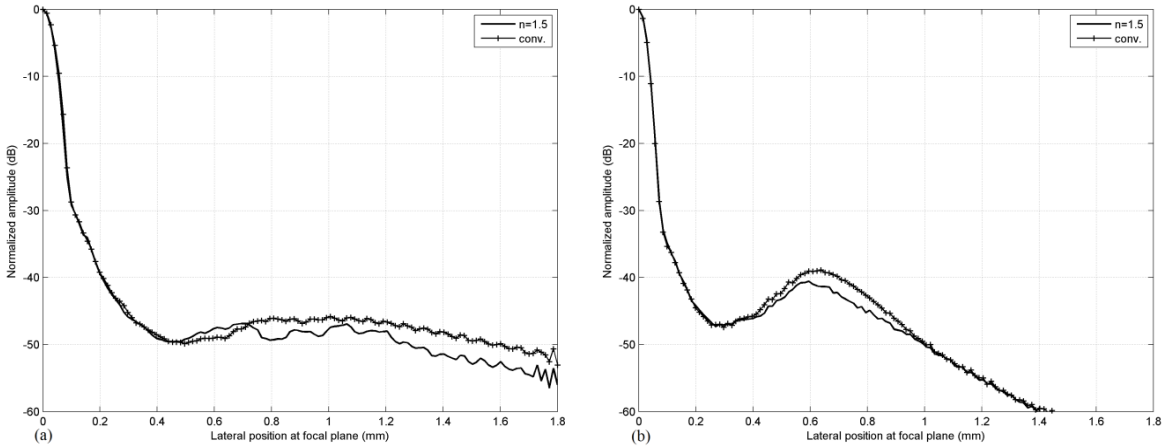

Figure 7.9 Radiation patterns of the novel array with n=1.5 and the conventional array in the process of (a) LFI and (b) HFI

Table 7.4 Imaging parameters of beam patterns for the novel array with *n*=1.5 and conventional array in both LFI and HFI

Imaging	Array	*Res* (μm)	*CR* (μm)	*GL* (dB)	X_{GL} (mm)	ϑ_{GL} (°)
LFI	conv.	89.6	419.7	(-45.8)	(1.00)	(48.0)
	Novel	83.9	412.4	(-47.4)	1.07	(49.9)
HFI	conv.	63.8	296.8	-38.2	0.64	35.6
	novel	63.8	258.6	-40.5	0.60	33.6

*(-45.8), (-47.4) means the lobe is very smooth and not obvious

As expected, grating lobe is not found in LFI (the smooth lobe is caused by the element kerfs), but occurs in HFI with. The beam patterns and their imaging parameters in both novel and conventional array are generally comparable. The angular positions of grating lobe in HFI show the very good agreement with the theoretical evaluation by using Equation (4.9), while a slight 2dB reduction in the level of grating lobe is found in the HFI of the novel array compared and might be due to the better bandwidth of element pulses.

Likewise, the pressure pulses at focal point for the novel array with *n*=2, 2.5 and 3 are analyzed by FEA. The performances of the array in LFI are illustrated in Figure 7.10, while the ones in HFI are displayed Figure 7.11.

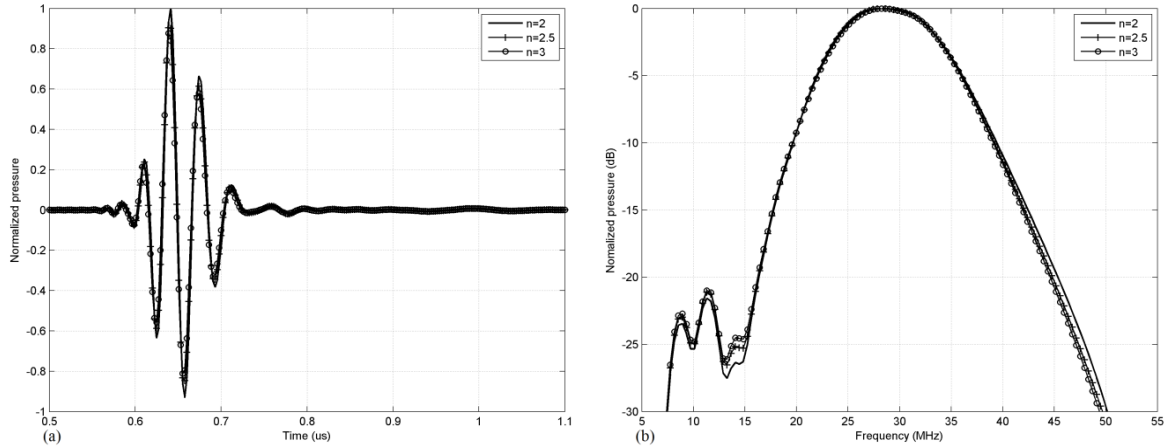

Figure 7.10 Pressure pulses at focal point in (a) time and (b) frequency domain, for the novel array with *n*=2, 2.5 and 3 in LFI

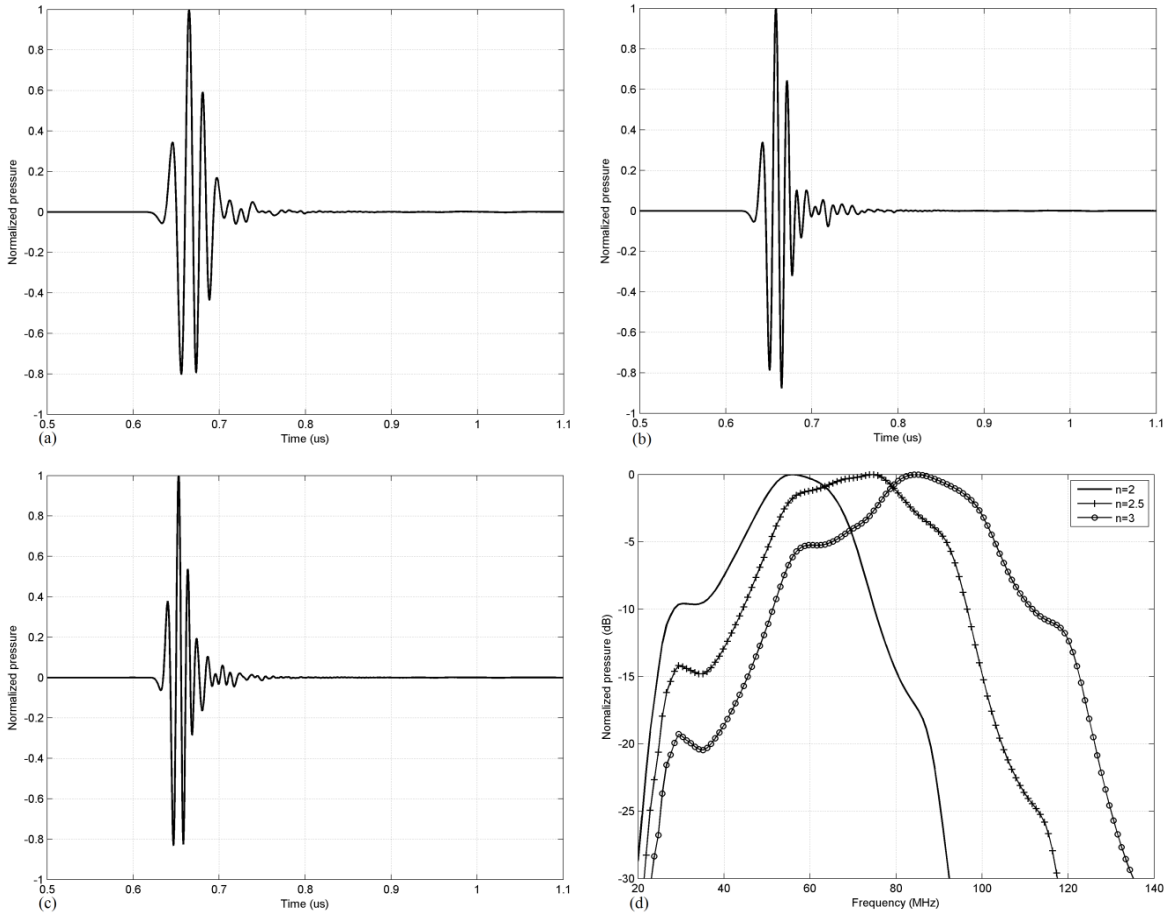

Figure 7.11 Pressure pulses at focal point in time domain for the array in HFI with (a) *n*=2, (b) *n*=2.5 and (c) *n*=3; (d) then shows their frequency domain responses

It can be seen that the pulses for all the novel arrays in LFI are generally identical to each other, and without too much ringing. Some low frequency components around 10MHz are found, which belong to the shear resonance of kerfs filler. In terms of HFI, the pulses are also short with its frequency band close to their corresponding IL spectrums. To measure the quality of these pulses, their parameters are then listed in Table 7.5, and the definition of these parameters can be referenced to Table 7.3.

Table 7.5 Parameters of pressure at focal point for the novel array with n=2, 2.5 and 3

Imaging	n	P_{max} (10^4Pa)	f_c (MHz)	$PL_{(-6)}$ (T)	$PL_{(-20)}$ (T)	BW (%)
	2	1.61	29.1	1.91	3.38	52.7
LFI	2.5	1.49	29.1	1.96	3.46	52.2
	3	1.42	29.1	1.96	3.45	52.0
	2	4.67	57.0	2.09	3.64	50.6
HFI	2.5	6.08	71.3	2.01	4.23	61.2
	3	7.71	80.2	1.77	4.34	59.9

It can be found that is P_{max} show a decreasing trend for the arrays in LFI by the increase of ratio n, showing agreement with the decreasing IL peak in the element response listed by Table 7.2. On the contrary, an increasing trend is found in HFI because of its proportional relationship to the array central frequency f_c in theory [4]. The values of f_c and BW in both LFI and HFI are expected by the ones in their corresponding IL spectrums for the element, but except the ones in HFI for the array with n=3. The possible reason might be due to the slight increase of the minor peaks at 60MHz in its frequency domain. Its lobe level is just above -6dB and leads to the largely the increased BW, as well as the left-shifted f_c.

Besides that, the -6dB pulse length to measure the main T-mode vibration for all the arrays are similar, but the -20dB pulse length to measure the ringing is found to be much longer in HFI for the novel array with n=2.5 and 3. This is caused by the increasing thickness of the additional inactive ceramic layer, thus the resonated T-mode waves in the layer leads to the long ringing tail in the pulse at the focal point.

The radiation patterns in both LFI and HFI for the arrays with ratio n ranging from 2 to 3 are then illustrated by Figure 7.12. Their imaging parameters are listed in Table 7.6, with the same parameter definition as Table 7.4.

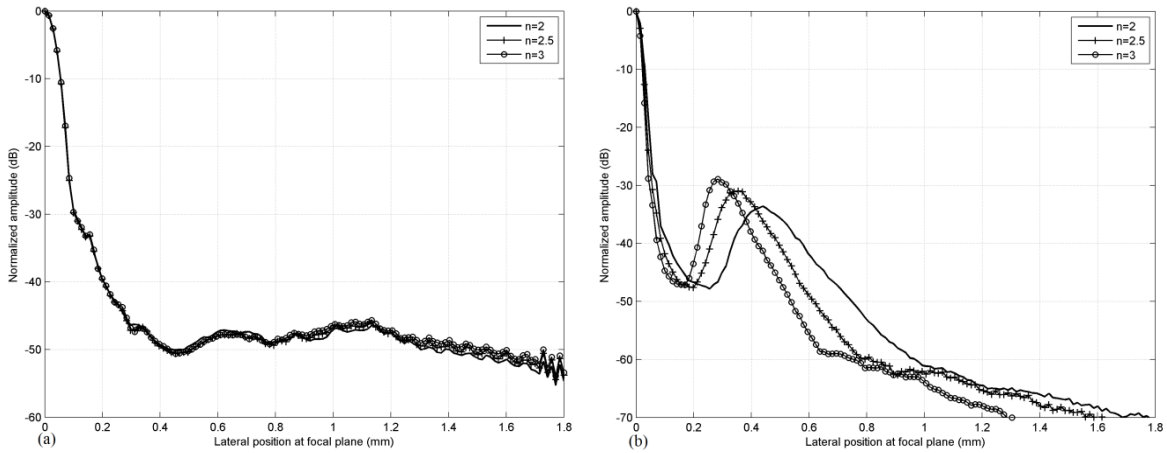

Figure 7.12 Radiation patterns for the novel arrays with various *n* in (a) LFI and (b) HFI

Table 7.6 Imaging parameters in both LFI and HFI for the novel arrays with *n*=2, 2.5 and 3

Imaging	*N*	*Res* (μm)	*CR* (μm)	*GL* (dB)	X_{GL} (mm)	ϑ_{GL} (°)
	2	85.0	408.4	(-46.4)	(1.15)	(52.0)
LFI	2.5	85.2	406.9	(-46.0)	(1.13)	(51.5)
	3	86.5	409.7	(-45.6)	(1.12)	(51.1)
	2	46.8	217.4	-33.6	438.5	25.9
HFI	2.5	40.0	179.6	-30.9	346.6	21.1
	3	33.6	144.7	-28.9	281.7	17.4

*(-45.8), (-47.4) means the lobe is very smooth and not obvious

It can be seen that the patterns of LFI for all the novel arrays are almost same, without an obvious grating lobe. A sidelobe may be found in the region of 150μm approximately. Recall the R-I pattern of a 30MHz conventional array, this sidelobe is also predicted but becomes very weak and thus shows nominal influence in the patterns by FEA. The resolution of LFI is around 85μm while the contrast is about 400μm, the values generally close to the one of the novel array with *n*=1.5 and conventional array as expected.

In terms of HFI, both resolution and contrast decrease by the increase of ratio *n*. Since the proportional relation between resolution *Res* and central frequency f_c, it is expected that the ratio of the *Res* in LFI to HFI should equal to the ratio of the f_c in HFI to LFI for a certain array. Their values are then listed in Table 7.7 for all the novel arrays, where the subscript LFI and HFI refers to the parameters obtained in LFI and HFI respectively.

Table 7.7 The ratios for the novel arrays with *n*=1.5, 2, 2.5 and 3

n	**1.5**	**2**	**2.5**	**3**
Res_{LFI}/Res_{HFI}	1.31	1.82	2.13	2.57
$f_{c(HFI)}/f_{c(LFI)}$	1.37	1.96	2.45	2.76

It can be found that the ratio of resolution is lower, but generally comparable to the ratio of central frequency, since the influential factor in reality (or FEA) is not only dependent on frequency. For example, the non-uniform vibration on the element could increase the resolution and leads to the reduction in the ratio of resolution. Furthermore, both the two ratio is close to the value of *n*, because the resonant frequency of PZT is designed to be proportional to the *n* in HFI. The two ratios are also found to be lower than *n*, and it is due to central frequency in the element band is always smaller than resonant frequency.

Besides that, large grating lobes are found in the HFI patterns as expected, since the widths of the element pitches in HFI for all the arrays breach the 1λ rule. Their position become closer to the focal axis and their levels are also higher by the increase of n, because of the larger and larger width of their element pitches.

7.3.3 Compound Beam Patterns

The patterns of LFI and HFI in the novel array are then compounded together to form the final imaging pattern. Figure 7.13 illustrates the compound patterns of all the novel arrays with n=1.5, 2, 2.5 and 3, with the comparison of the patterns by the conventional arrays showing similar lateral resolution for each *n* value. The reason to take resolution as the measuring factor of comparison is due to that it is the first important parameter of imaging quality.

The approximate operating frequency f_{conv} of the conventional array is basically determined by the equation of $f_{conv}=c/Res \cdot f_{num}$, where *c* is sound speed of water and f_{num} is the *f*-number. Hence, with the resolution given by novel arrays, the frequencies of the conventional arrays are designed to be about 40MHz, 50MHz, 60MHz and 70MHz to match the novel arrays with *n*=1.5, 2, 2.5 and 3, respectively. Similar, the imaging parameters are listed in Table 7.8, with their definition given by Table 7.4.

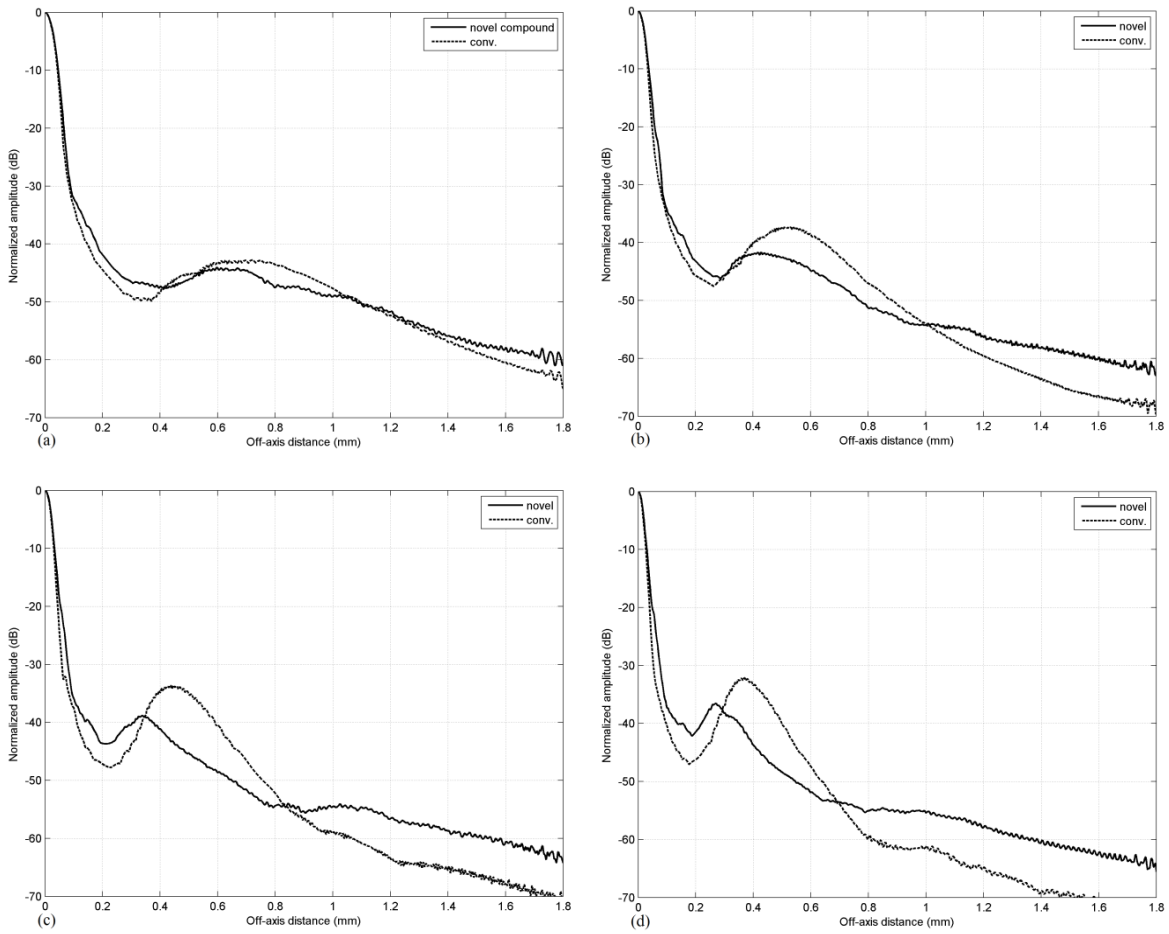

Figure 7.13 The compound beam patterns of the novel array with (a) *n*=1.5, (b) *n*=2, (c) *n*=2.5 and (d) *n*=3, compared to the patterns of their corresponding conventional array showing operating frequency about (a) 40MHz, (b) 50MHz, (c) 60MHz and (d) 70MHz

Table 7.8 Imaging parameters of compound beam for the novel array with *n*=1.5, compared to the results of a 40MHz conventional array

Array	*Res* (μm)	*CR* (μm)	*GL* (dB)	X_{GL} (mm)	ϑ_{GL} (°)
40MHz conv.	67.7	296.8	-42.8	0.72	38.7
***n*=1.5, novel**	71.7	359.3	-44.3	0.60	33.6
50MHz, conv.	53.7	262.1	-37.4	0.53	30.5
***n*=2, novel**	57.2	332.2	-41.7	0.43	25.4
60MHz, conv.	47.4	219.9	-33.6	0.45	26.4
***n*=2.5, novel**	50.5	308.2	-38.8	0.34	20.6
70MHz, conv.	40.0	194.5	-32.1	0.37	22.3
***n*=3, novel**	43.2	271.5	-36.5	0.27	16.7

The resolution of the novel array is generally comparable to its corresponding conventional array or slightly smaller, while the contrast is much larger due to its large value in the LFI pattern. Besides that, the compound pattern only shows a little decrease in the operating frequency compared to the one in HFI. For example, the LFI in the novel array with *n*=3 has the frequency of 30MHz approximately, while its HFI shows the value about 80MHz. And the resolution of its compound pattern is comparable to the 70MHz conventional array, instead of the mean value (about 55MHz) of the frequencies in LFI and HFI. It suggests that the resolution of the compound pattern is more dependent on the one of HFI, while the function of LFI is mainly to reduce the grating lobe.

It can be seen that the grating lobe is still apparent even in the compound pattern, though its level is reduced in different extent compared to the one of the corresponding conventional array. The decrement in grating lobe level is not large for the novel array with *n*=1.5, but keeps increasing by the increase of ratio n. Generally, a -5dB decrease can be achieved in the lobe level by novel arrays, but the level is still quite high in the arrays using large *n* (*n*=2.5 and 3, the level are all above -40dB). It is due to that there are only 9 elements excited in the array, which makes the grating lobe in HFI too large to be suppressed. It is also the reason that the lobe position in compound pattern is very close to the one in HFI pattern. However, the level of grating lobe could be further lowered by more elements involved in the focusing [4].

7.4 Optimization of Grating Lobe Suppression

It is found that the grating lobe suppressed by the novel linear array can be further reduced by the optimization in the design of the operating frequencies of LFI and HFI. The basic idea is to the make the grating lobe in HFI to be coupled into a very low beam level in LFI. The R-I method to evaluate the beam pattern is firstly used to reveal the principle of the optimization, while FEA method is then adopted to demonstrate the effectiveness of the optimization in the suppression of grating lobe.

7.4.1 R-I Evaluation

In the novel arrays with different ratio n, their HFI patterns are compounded by the LFI patterns all showing the operating frequency of 30MHz approximately. By the increase of ratio n, the grating lobe in HFI appears much closer to its main lobe and locates at the region of main lobe in the corresponding LFI. But the LFI beam level at the same location is actually not the minimum, since it could be further reduced by the increase of operating frequency in LFI.

To analyze the lobe positions in both LFI and HFI for novel arrays, the R-I method based on Rayleigh integral is used. Though the pattern evaluated by R-I method only shows the responses of an ideal piston-mode array, it still shows the almost same responses in terms of the lobe position for the patterns in actual arrays including the LFI and HFI in novel arrays. Thus, Figure 7.14 illustrates the R-I patterns of the linear arrays with operating frequencies ranging from 30 to 50MHz to represent the LFI patterns. Notice that the X axis in the pattern is the angular position instead of the lateral one, since it only relates to the element pitch and operating frequency, regardless of any geometric changes in the array such as element number or aperture size. The angular position ϑ_{GL} can be simply obtained by using the equation of "$\vartheta_{GL}=arctan(X_{GL}/F)$", where X_{GL} is lateral position of grating lobe and F is the focal distance. In addition, the lowest level at the edge of main lobe is described as the minimum main lobe as pointed out in the figure.

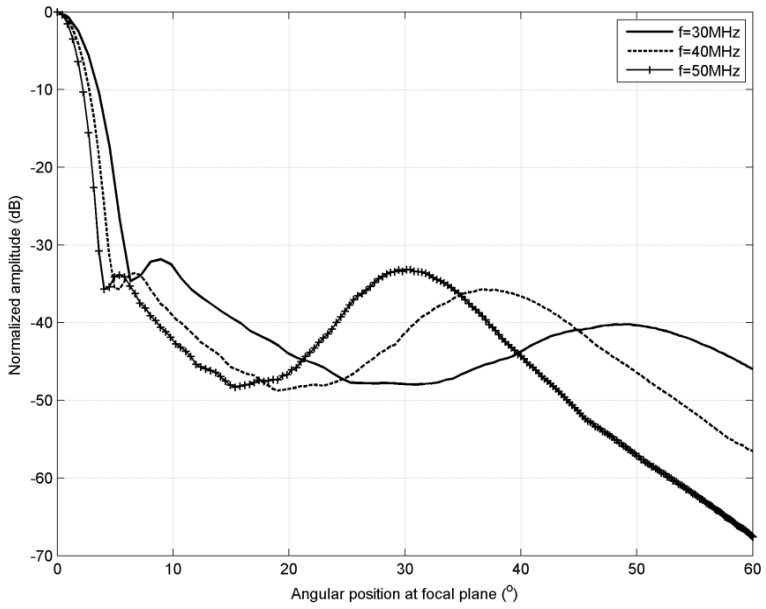

Figure 7.14 Angular patterns for the arrays with different frequencies

It can be seen that the main lobe become narrower as the results of increasing frequency, while both sidelobe and grating lobe can be found away from the focal axis. To reveal the relations of the lobe positions in LFI and HFI, the novel array with ratio *n* of 3 is taken as an example. In HFI, the array shows the peak of its grating lobe at 17^{o} approximately. At the same position, the beam level of 30MHz LFI is the largest, while the values of the two other frequencies are similar and much lower. Therefore, the overall lobe at this position in compound pattern for the novel array with 40 and 50MHz LFI would be lower than the one with 30MHz LFI. Meanwhile, the grating lobe far from the focal axis in LFI patterns can be also suppressed by the HFI patterns. This is because for the array with relatively large *n*, a sharp decreasing trend can be found in the region of HFI where the grating lobe in LFI also locates.

It is reasonable to assume that every HFI pattern can find an LFI pattern where the HFI grating lobe locates at the position of the minimum level of main lobe in LFI, which is described as the optimization of grating lobe suppression. By Figure 7.14, the position of minimum mail lobe and grating lobe are all related to the operating frequency, which is generally determined by the enlargement ratio n. Table 7.9 then lists the levels and positions of the two lobes for the array with the frequencies in the range of 30-90MHz by using the R-I beam evaluation, where f is the operating frequency; L_{MML} and L_{GL} denote the lowest level of minimum main lobe (MML) and the highest peak of grating lobe (GL), respectively; X_{MML} and X_{GL} is then for the lateral position of MML and GL respectively, while ϑ_{MML} and ϑ_{GL} refer to the angular position.

Table 7.9 Levels and positions of MML and GL for the array with various frequencies

f (MHz)	L_{MML} (dB)	X_{MML} (μm)	ϑ_{MML} (^{o})	L_{GL} (dB)	X_{GL} (μm)	ϑ_{GL} (^{o})
30	-48.0	425.2	25.3	-40.2	1049.0	49.4
35	-49.1	360.0	21.8	-37.7	818.8	42.3
40	-48.8	310.6	19.0	-35.7	670.6	36.7
45	-46.4	283.5	17.5	-33.5	581.1	32.9
50	-48.3	247.1	15.4	-33.2	522.4	30.1
55	-48.1	225.9	14.1	-32.1	465.9	27.4
60	-48.0	211.8	13.2	-31.3	430.6	25.6
65	-48.3	190.6	12.0	-30.6	395.3	23.7
70	-48.0	176.5	11.1	-29.9	360.0	21.8
75	-47.8	169.4	10.7	-28.9	338.8	20.6
80	-48.0	155.3	9.79	-28.5	310.6	19.0
85	-48.1	141.2	8.92	-28.2	303.5	18.6
90	-48.3	141.2	8.92	-27.6	289.4	17.8

The level of MML keeps almost the same values by the increase of operating frequency, while a decreasing trend is expected and also found in the level of GL by the theory of EPD [84]. The theory also suggests a decreasing decrement in the GL peak and is demonstrated by the R-I patterns. More interestingly, the positions of both MML and GL both move closer to the focal axis. Based on the data listed in Table 7.9, Figure 7.15 then illustrates the relationships between angular positions of the two lobes and the operating frequency.

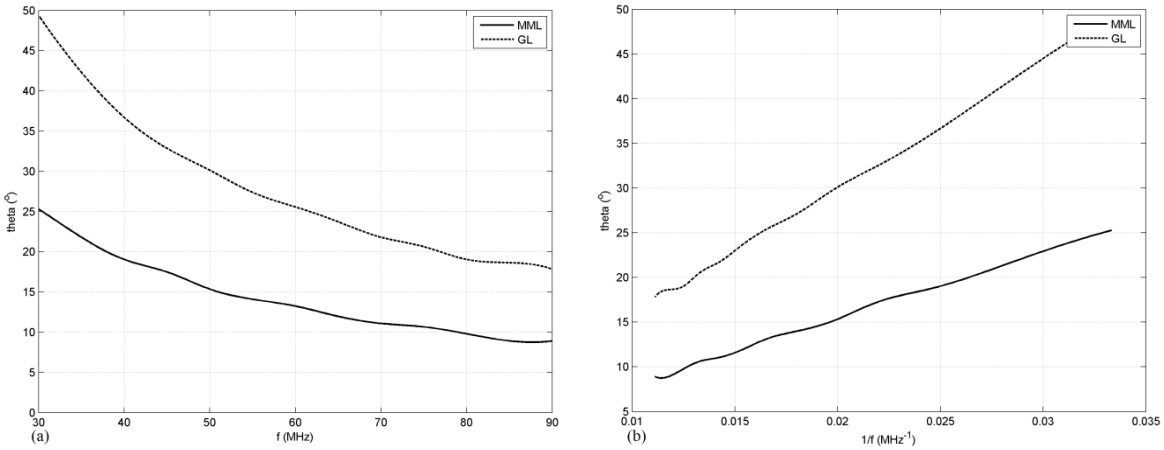

Figure 7.15 Curves of the angular position ϑ versus (a) operating frequency f and (b) $1/f$

It can be found by Figure 7.15(b) that the angular lobe positions are inversely proportional to the operating frequency, but with different slope. To realize the optimization in novel array, a horizontal line can be drawn in Figure 7.15(a) and thus results in two points in the curves of MML and GL, respectively. The X-axis value in MML curve becomes the optimized frequency of LFI, while the value in GL curve is the optimized frequency of HFI.

By Figure 7.15(a), several optimized frequency of both LFI and HFI can be obtained. For example, 60MHz HFI matched to 30MHz LFI; 70MHz HFI matched 35MHz LFI; 80MHz HFI matched to 40MHz LFI, and 90MHz HFI matched to 45MHz LFI. Coincidentally, the ratio of the frequency in HFI and the one in LFI approximately equals 2. It also suggests that the optimized enlargement ratio n is about 2 or slightly larger than 2, because the ratio of central frequency is always slightly smaller than the enlargement ratio.

7.4.2 FEA Patterns

FEA method is then applied to evaluate the optimization and show the suppression of the grating lobe in both HFI and LFI (if there is one). The original design has already shown the response of the novel array with *n*=2 for the 30MHz LFI and 60MHz HFI. The decrement of the grating lobe in its compound pattern is -4.3dB compared to the corresponding response of a conventional array. However, by the FEA data listed in Table 7.8, the largest decrement occurs when the ratio *n* is 2.5, of which the value is -5.3dB. The optimized frequency in HFI is very likely to be around 70MHz, showing the frequency ratio 2.3 and slightly different from the designed frequency ratio of 2. It is probably due to the difference between the FEA and R-I pattern for the array. The MML of the 30MHz LFI is relatively large so that it could cause slightly more errors in the minimum level of MML than other LFI patterns with higher frequency and thus showing narrower MML.

Besides the already-analyzed array with 60MHz HFI and 30MHz HFI, the array with 90MHz HFI and 45MHz LFI is investigated as another example. The FEA results of the element responses including impedance spectrums, IL spectrum and pressure pulses all agree with the KLM model very well as expected, thus they are not displayed.

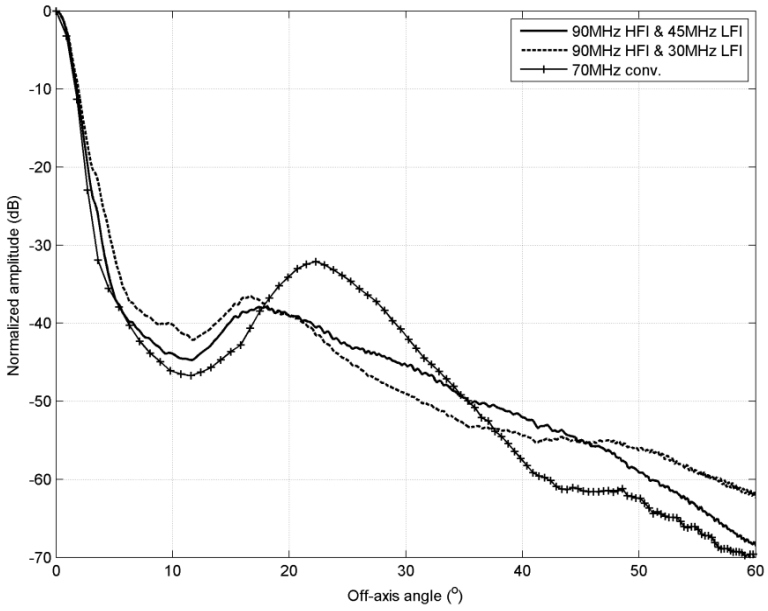

Figure 7.16 Angular beam patterns of the three arrays, conv. refers to conventional array

Only the compound pattern of the array is illustrated here, and compared to patterns of the novel array with 90MHz HFI and 30MHz LFI (already given in Figure 7.13 as the novel array with *n*=3), as

well as the 70MHz conventional array showing similar resolution. Thus Figure 7.16 illustrates the angular patterns of those arrays, with their imaging parameters listed in Table 7.10. In additional, each array is numbered for the convenience in the following description.

Table 7.10 Imaging parameters of the three arrays

Arrays	Num.	*Res* (μm)	*CR* (μm)	*GL* (dB)	X_{GL} (mm)	ϑ_{GL} (°)
70MHz conv.	1	40.0	194.5	-32.1	0.37	22.3
90MHz HFI & 30MHz LFI	2	43.2	271.5	-36.5	0.27	16.7
90MHz HFI & 45MHz LFI	3	41.3	208.5	-37.9	0.29	18.0

It can be found that the grating lobe is further reduced to -37.9dB for the 3rd array, or the array with frequency ratio of 2. Compared to the 1st array, the lobe is -5.8dB down in 3rd array and larger than the decrement of 4.3dB in 2nd array. The optimization of grating lobe suppression has been achieved. However, the 45MHz LFI shows the evidence of grating lobe appears around 34°, and it leads to an increased beam level in the 3rd array in the region from 30-40°, compared to the 2nd array. But the decreasing trend can be still found and no lobe can be seen in this region, the grating lobe in LFI is also suppressed as expected. Besides that, the resolution of 3rd array also becomes finer as the benefit of the LFI with higher frequency. For the same reason, a large decrease in contrast is found compared the 2nd array. The main beam of 3rd array becomes much comparable to the 1st array. To summarize, the optimization of the novel array not only shows its advance in the suppression of grating lobe, but also the improvement in resolution and contrast.

7.5 Summary

Large grating lobe appears in the conventional linear array with very high operating frequency, but can be suppressed by the novel linear array. The novel array is able to operate at two frequencies (or two modes, LFI and HFI). As a result, the LFI pattern without the evidence of grating lobe is used to cancel the grating lobe appearing in HFI by compounding the two patterns. It would leads to the decrease in frame rate but is regarded as a minor disadvantage since the frame rate is already very fast in linear array. The matching layer can be only matched to one frequency which is chosen to be the HFI mode. It could make the bandwidth and IL peak both in reasonable levels, namely bandwidth from 40% to 50% and IL peak from -10 to -15dB for both LFI and HFI of the arrays with different enlargement ratio *n*.

The imaging responses of the novel arrays are then obtained by FEA method. The LFI mode is set to be 30MHz and shows no grating lobe as expected, while the HFI mode is set to be 45MHz, 60MHz, 75MHz and 90MHz corresponding to the enlargement ratio *n* of 1.5, 2, 2.5 and 3 respectively. The pressure pulses at the focal point agree very well with the expectation to show a broadband and short pulse. More importantly, the compound beam patterns of these arrays show the suppression of the grating lobe approximately about -4 to -5dB compared to the conventional linear array with similar resolution. The lobe suppression has been achieved, but its peak level in some compound patterns of the array with large n (*n*=2.5 and 3) are all above -40dB, far away from the recommended level of -50dB. This is due to the few elements (only 9) involved in the focusing, and the level can be further reduced by the increase of element number.

Besides that, the grating lobe can be further reduced by the optimization in the design of novel array by setting a suitable *n*. The principle of the optimization is to put the high grating lobe in HFI to the region of very low beam level in LFI. The results suggests that the enlargement ratio of 2, or slightly larger than 2 is recommended. It could achieve the largest decrease in grating lobe of -6dB approximately, compared to the conventional array with similar resolution. In addition, the optimized novel array also shows finer resolution and contrast than the ones of non-optimized array.

Chapter 8 Conclusions & Future work

8.1 Conclusions

In this thesis, the design and investigation of high frequency array transducers are presented. The improvement of both annular and (1D) linear array is found by designing novel structures. The performances of the novel array are discussed and compared to the conventional array. The outcomes are then concluded here.

8.1.1 High Frequency Annular Array

Annular arrays have been widely used in high frequency medical applications, since there are only a few elements and no strict requirement of kerfs width in the array aperture. Conventional annular array usually consists of several concentric ring elements with showing the same area. The equal area (EA) elements show their benefits in driving or receiving circuit in the imaging system by their same impedance and phase shifts applied for array focusing.

However, it is found that in the high frequency range the kerfs width usually neglected in the EA annular array will impact the array performances. The kerfs width of annular array is about 30μm and confidently diced by laser micro-machining. For a typical 7-element, 2mm diameter annular array operating in the region of 40-50MHz, the conventional design of EA elements would lead to non-EA elements when the kerfs is 30μm wide. Since the electrical tuning by conventional design is based on the same impedance of every element, the actual area difference leads to some errors in electrical tuning and thus impacts the element responses including insertion loss (IL) and bandwidth. An optimized design is then developed with the consideration of kerfs, and the exact EA elements can be achieved. The electrical tuning would become ideal again with improved element responses across the array aperture. As a result, the imaging pattern by optimized EA design is better than the conventional array, and thus the optimized design is adopted in our investigations of EA arrays.

The emanated pulse from every element in time domain is also shown by FEA method. Short and wide-band pulses are obtained by every element, but the ringing tails and non-uniform vibration found in the element might cause some uncertain influence on the radiation pattern. The array is

then modelled by FEA to show its radiation, while a high sidelobe closest to the main lobe is found. A method to evaluate the pattern based on the Rayleigh-integral (R-I) is developed as an analytical tool for the FEA results. The patterns using R-I based methods are generally comparable to the FEA ones, but without the appearance of an obvious nearest sidelobe, this might be related to the inaccuracy issue caused by circular geometry. Nevertheless, the radiation response of the annular elements by FEA suggests that the pulses from outer elements are strongly overlapped in the sidelobe region to cause the sidelobe. To suppress the sidelobe, a potential way is to reduce the overlapping by increasing the phase of the emanated pulses in the sidelobe region. In addition, the transducer bandwidth is always regarded as an influential factor on the sidelobe suppression.

A method of using broad band array is used at first. Although it fails to suppress the sidelobe which might be related to the influence of the ringing and non-uniform vibration in the element, the high-impedance single matching developed in my work is still found to be a significant improvement over traditional single matching. Single matching by conventional mechanical tuning can achieve a maximum bandwidth of about 53% when ceramic is used as piezoelectric layer, but using a high-impedance matching with an acoustic impedance of 16MRaly could improve the bandwidth up to 70%, a value comparable to double matching, by adjusting the effective internal resistor in outside imaging circuits or element impedance.

By the investigation of phase distribution across the array element, the outer elements shows a closer phase in the region of sidelobe at focal plane because of their close position along aperture by EA geometry. However, the phase could be separated by the separation of the element position, thus the element pulses have fewer chances to be overlapped in sidelobe region even it shows narrow bandwidth or equivalently large transverse coupling. Therefore, a novel equal width array is developed, of which every element shows same width instead of same area. The outer elements in EW array are separated, while inner ones distribute closer to each other. The suppression of nearest sidelobe is evidenced by R-I evaluation of beam patterns even with a 30% bandwidth Gauss pulse, but at the cost of a relatively large resolution and a rising in the pedestal lobe. The “pedestal lobe” is found to be related to the grating lobe that is apparent in linear arrays, probably because EW geometry in the cross section is almost the same as linear ones.

FEA method is then used to obtain the performances of EW annular array. And the FEA results show generally good agreement with R-I one. The EW array shows the suppression of nearest sidelobe, the relatively large resolution and high "grating" lobe, compared to the EA array. But this is only for the 7-element annular array. More comparisons and discussions between EA and EW array with different element number have been given in Chapter 5. To conclude, EA array shows better imaging performances than EW array when total element number is relatively small, but with high nearest sidelobe. But with more elements involved, the patterns by EA and EW array becomes generally comparable without strong evidence of the nearest sidelobe. Meanwhile, EW annular array then shows its advantage in fabrication, since EA array with many elements leads to very narrow and unachievable outer elements, while EW array has relatively large outer elements.

8.1.2 High Frequency Linear Array

High frequency (1D) linear array is also investigated and improved by the novel design. Current linear arrays are limited in the frequency range from 30-40MHz due to the restrictions on pitch width by current dicing technique. Grating lobe would appear in the focal plane if higher frequency is operated.

First of all, the research began with conventional 30MHz linear array with the pitch width of 50μm. The kerfs width is set to be 20μm, which is a level that current dicing techniques could comfortably achieve. No grating lobe is expected because the array is matched to the pitch rule of 1λ. However, this is only true for an ideal linear array without kerfs or with very narrow kerfs. The R-I evaluation has shown the influence of relatively large kerfs occupying 40% volume fraction. A smooth lobe has risen up in the region far from the focal axis in the beam pattern, which is also proved by FEA results. The lobe is found to be caused by the large transverse waves coupling in the kerfs, if the common kerfs filler Araldite listed in Table 6.2 is used. By using some high-attenuated epoxies for kerfs filler, the amplitude of the transverse waves in kerfs could largely be reduced, and thus the beam pattern far from the focal axis shows no significant rising of lobes, instead a pedestal lobe can be seen. Nevertheless, using high attenuated kerfs filler is essential in high frequency linear array, especially the one comprising large amount of kerfs volume fraction.

However, grating lobe would appear for this linear array with pitch width of 50μm when the operating frequency exceeds 30MHz. A novel method is then developed for suppressing the high grating lobe in higher frequency linear array. The beam pattern with grating lobe in higher operating frequency is designed to be compounded to a beam pattern without grating lobe. Thus the grating lobe will be suppressed, but at the slight cost of resolution of the higher-frequency pattern. And it also results in half frame rate compared to conventional linear array, although the frame rate reduction is not regarded as a significant factor since it is already very fast in linear array.

The novel structure of the linear array is then developed and mainly consists of two ceramic layers. Only one of them is excited for higher-frequency pattern, while both of them are excited for lower-frequency pattern. Since the thickness of matching layer cannot be changed by the two processes, the layer is then designed to be perfectly matched to higher frequency process because slight mismatch in lower frequency process is still acceptable. By using FEA, the element responses including insertion loss and bandwidth are comparable to conventional arrays. By the compound processes of the two patterns, the suppression of grating lobe can be found as expected. The lobe suppression can be further enlarged by using the optimization of the novel array. As a result, the novel array is designed to compound a 45MHz LFI and 90MHz HFI to form an image. It is able to show the resolution and contrast comparable to a 70MHz conventional array, and with a -6dB lower suppression of the grating lobe. However, the cost of the novel array is a reduction frame rate. In addition, this novel array still showed the grating lobe about -39dB, and it is due to that few elements are excited in the array; the grating lobe can be further reduced to the suggested level of -50dB by exciting more elements.

8.2 Future Work

Overall, though the fabrication issues are considered in the research, the design of the high frequency array transducers are all based on either R-I or FEA results. It is essential to fabricate the novel arrays (both linear and annular one), and especially the fabrication techniques for these array are commonly-used and mature. Afterwards, the testing is also important to examine the experimental results, though FEA is believed to show very similar results as experiments.

Besides that, the transducer operating above 100MHz could provide very fine resolution, but no linear array has been made so far in this very high frequency range, expect the most recent kerfless array. But kerfless array has a main concern of cross talking. The novel structure developed here might be useful. But the level of grating becomes very high in conventional array if the element pitch remains very large to make it realizable by using current dicing techniques. The suppression of the grating lobe of -6dB approximately might not be enough. Nevertheless, it is still worth investigating but the ability of our current computer limits the FEA simulation.

Appendix A

The appendix refers to the numerical solution of Rayleigh integral to evaluate the radiation pattern of an annular array instructed in Section 3.4.1. The algorithm of the method by using a software, Matlab, is given below:

```
% To evaluate the numerical radiation pattern by Rayleigh integral
clear all;clc;close all;

%% Disk parameters
r=1e-3;                         % disk radius
d=50e-6;                        % thickness of PZT disk
n=7;                            % numbers o f elements
wg=30e-6;                       % kerfs width
c=1500;                         % sound speed of water
f=45e6;                         % operating frequency
T=1/f;                          % period
lemda=c/f;                      % wavelength in water
fnumber=2;                      % focal number
F=2*r*fnumber;                  % focal distance

Zm=7.3e6;                       % acoustic impedance of matching layer
Nfp=2^7;                        % element numbers of focal plane
rfp=1.5e-3;                     % total radius of focal plane to observe
roff=linspace(0,rfp,Nfp);       % off-axis position at focal plane

%% Annulus radius
choice=0;                       % choice=0, optimized EA array;
                                % choice=1, conventional EA array
                                % choice=2, EW array
if choice==0
    % ---------- EA array using optimized design --------
    ro=zeros(1,n);              % ro, outer radius
    ro(1)=sqrt(r^2/n);
    tol=0.1e-6;
    dr=0.01e-6;
    while abs(ro(n)-r)>tol
        for i=2:n
            ro(i)=sqrt(i*ro(1)^2+(i-1)*wg^2+sum(ro(1:i-1))*2*wg);
        end
        ro(1)=ro(1)-dr;
    end
    ro(1)=ro(1)+dr;
    ri=zeros(1,n);              % ri, inner radius
    for i=2:n
        ri(i)=ro(i-1)+wg;
    end
    array='EA';
elseif choice==1
    % ---------- EA array using conventional design -------
    rn=zeros(1,n);              % rn, outer radius but no kerfs accounted
    rn(1)=sqrt(r^2/n);
    for i=2:n
        rn(i)=sqrt(r^2/n+rn(i-1)^2);
```

```
    end
    ri=zeros(1,n);            % ri, inner radius
    ro=zeros(1,n);            % ro, outer radius
    ro(1)=rn(1)-wg/2;
    for i=2:n
        ri(i)=rn(i-1)+wg/2;
        ro(i)=rn(i)-wg/2;
    end
    array='EA_con';
elseif choice==2
    % ---------- EW array --------
    rn=zeros(1,n);            % rn, outer radiusbut no kerfs accounted
    for i=1:n
        rn(i)=r/n*i;
    end
    ri=zeros(1,n);            % ri, inner radius
    ro=zeros(1,n);            % ro, outer radius
    ro(1)=rn(1)-wg/2;
    for i=2:n
        ri(i)=rn(i-1)+wg/2;
        ro(i)=rn(i)-wg/2;
    end
    array='EW';
else
    error('The value of "choice" must be 0, 1 or 2')
end

rc=zeros([1,n]);            % rc, element middle position
for i=2:n
    rc(i)=(ro(i)+ri(i))/2;
end

%% Phase shift of every element for on-axis and off-axis focus
% on-axis focus
ton=(F-sqrt(F^2+rc.^2))/c;    % time delay to every element to focus
phon=ton/T*2*pi;              % phase shift

% off-axis focus, ***** every point along aperture radius *****
Nap=2^7;                      % number of points along aperture radius
rap=linspace(0,r,Nap);        % radius of array aperture
drap=r/(Nap-1);               % division between nearby points

% phase shift in polar coordinate
Nth=2^7;
theta=linspace(0,pi,Nth);     % angle in polar system
dth=pi/(Nth-1);               % division of theta matrix
rapx=zeros(Nap,Nth);          % initialize rapx matrix for X axis in
                              % polar system of the points at aperture
rapy=zeros(Nap,Nth);          % initialize rapy matrix for y axis
for i=1:Nap
    for j=1:Nth
        rapy(i,j)=rap(i)*sin(theta(j));
        rapx(i,j)=rap(i)*cos(theta(j));
    end
end
```

```
toff=zeros([Nfp,Nap,Nth]);    % initialize toff matrix,
                              % row - roff position along focal plane;
                              % column - rp position along aperture
for i=1:Nfp
    for j=1:Nap
        for k=1:Nth
            toff(i,j,k)=sqrt((roff(i)-rapx(j,k))^2+rapy(j,k)^2+F^2)/c;
                              % travelling time to the point along
                              % focal plane
        end
    end
end
phoff=toff/T*2*pi;            % total phase shift

%% Phase differences
Le=zeros([1,n]);              % initialize Le matrix
for i=1:n
    % find out the index of rp element belongs to every array elements
    ind_temp=find((abs(rap)>=ri(i))&(abs(rap)<=ro(i)));
                              % array element index number
    eval(['ind',num2str(i),'=',mat2str(ind_temp),';'])
                              % index matrix, ind1-ind7 denotes indices
                              % of the points belonging to 1st – 7th
                              % element
    Le(i)=length(ind_temp);   % length of every ind matrix, since not
                              % all elements along aperture are active

    % phase difference of every element along focal plane
    phd_temp=phoff(:,ind_temp,:)+phon(i);
    td_temp=phd_temp/2/pi*T;
    strCmd1=sprintf('phd%d=phd_temp;',i);
    eval(strCmd1);            %  phd, phase difference

    strCmd2=sprintf('td%d=td_temp;',i);
    eval(strCmd2);            %  td, time difference
    RAPX_temp=rapx(ind_temp,:);
    RAPY_temp=rapy(ind_temp,:);
    eval(['RAPX',num2str(i),'=',mat2str(RAPX_temp),';']);
                              % RAPn, the radius of every element
    eval(['RAPY',num2str(i),'=',mat2str(RAPY_temp),';']);
    clear ind_temp phd_temp td_temp RAPX_temp RAPY_temp
end
Nap=sum(Le);                  % the new active element along aperture,
                              % the element number is now Np

td_all=zeros([Nfp,Nap,Nth]);  % initializing td_all matrix
L=zeros([1,n+1]);             % initializing L matrix showing the
                              % length of phd and td matrix
for i=1:n
    td_temp=eval(['td',num2str(i)]);
    RAPX_temp=eval(['RAPX',num2str(i)]);
    RAPY_temp=eval(['RAPY',num2str(i)]);
    L(i+1)=length(td_temp(1,:,1))+L(i);
    td_all(:,L(i)+1:L(i+1),:)=td_temp;
```

```
    RAPX_all(L(i)+1:L(i+1),:)=RAPX_temp;
                                % RAPX_all, redistributed rapX matrix, to
                                % relate element radius and phd/td_all
    RAPY_all(L(i)+1:L(i+1),:)=RAPY_temp;
                                % RAPY_all, redistributed rapY matrix, to
                                % relate element radius and phd/td_all
    clear td_temp RAPX_temp RAPY_temp
end

td_max=max(max(max(td_all))); % maximum value in td_all matrix
td_min=min(min(min(td_all))); % minimum value in td_all matrix
td_av=(td_max+td_min)/2;      % average value in td_all matrix
td_all=td_all-td_av;          % redistribute td_all matrix
td_max=max(max(max(abs(td_all))));
                              % find the maximum value of new td_all

%% Standard Gauss pulse without phase shift and its deviation
Ntg=500;                      % number of element in tg vector
te=100e-9+td_max;             % end time of the whole pulse
BW=0.30;                      % bandwidth of Gauss pulse
tc=gauspuls('cutoff',f,BW,[],-25);
                              % cutoff time of Gauss pulse
tg=linspace(-tc,tc,Ntg);

% ---- other parameters of Gauss pulse ----
bwr=-6;
ref=10.^(bwr/20);
fv=-BW*BW*f*f/(8*log(ref));
tv = 1/(4*pi*pi*fv);
% ----------------------------------------

yg=exp(-tg.*tg/(2*tv)).* cos(2*pi*f*tg);
                              % expression of Gauss pulse

Nt=2^10;                      % number of element in t vector
t=linspace(-te,te,Nt);
dyg=interp1(tg,yg,t,'spline',0);
                              % redistribute Gauss pulse
dyg=dyg/max(abs(dyg));        % normalized dyg

%% Pressure overlap by Phase Difference Theory (PDT)
t1=zeros([Nap,Nt,Nth]);       % initialize overall time delay
dyg1=zeros([Nth,Nt]);         % initialize the delayed Gauss pulse dyg1
dyg2=zeros([Nap,Nt]);         % initialize the delayed Gauss pulse dyg2
yamp=zeros([1,Nfp]);          % initialize overlapped pulse amplitude

show_bar=waitbar(0,'Please wait');
for i=1:Nfp
    for j=1:Nap;
        for k=1:Nth
            t1_temp=t-td_all(i,j,k);
                              % overall time for element pressures at
                              % roff(i) position along focal plane
            R_temp=sqrt((roff(i)-RAPX_all(j,k))^2+RAPY_all(j,k)^2+F^2);
            dS=sqrt(RAPX_all(j,k)^2+RAPY_all(j,k)^2)*drap*dth;
                              % dS required for 2D intergral
```

```
            dyg1(k,:)=interp1(t,dyg,t1_temp,'spline',0)/(2*pi*R_temp)*dS;
        end
        dyg2(j,:)=sum(dyg1);
    end
    yovlp=sum(dyg2);          % pulse overlap, size of yovlp becomes
                              % [1,Nt,Nth]
    yamp(i)=max(abs(yovlp));  % get maximum amplitude of the overlapped
                              % pulse at roff(i)
    pct=i/Nfp;                % finishing percentage of current loop
    pct=round(pct*100);
    text=['Complete ',num2str(pct),'%'];
    waitbar(pct/100,show_bar,text);
    clear yovlp
end
close(show_bar)

ymax=max(yamp);               % ymax, the beam pattern
yamp_dB=40*log10(yamp/ymax);  % in dB unit

%% Plot
figure(1)
plot(roff*1e3,yamp_dB,'k-','LineWidth',1.5)
axis tight
xlabel('Lateral position at focal plane (mm)');
ylabel('Normalized amplitude (dB)');
grid on
hold off
```

Appendix B

Appendix B explains the 1D KLM model for the linear array element, which shows a dominant longitudinal-extensional (LE) mode. For a typical 1D linear array element as illustrated by Figure B1, the assumptions of *L*>>*w* and *L*>>*d* are always valid, where *L*, *w* and *d* are the length, width and thickness of a single element, respectively.

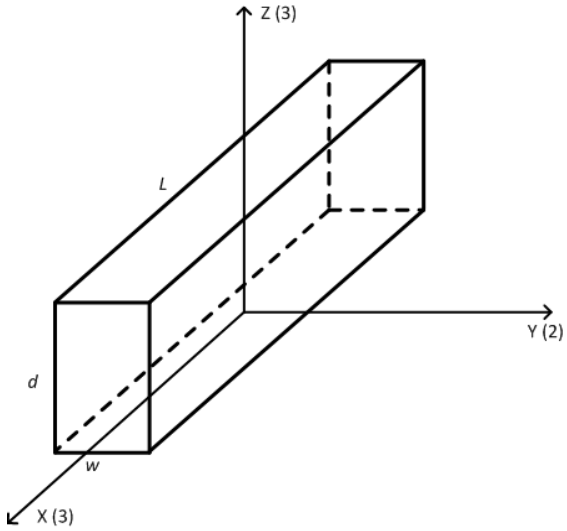

Figure B1 Schematic diagram of an element of a typical 1D linear array

These assumptions in element geometry allow another assumption of plane strain become valid. The plane strain condition shows the following relationships, where the definitions of the parameters can be referenced to the ones instructed by Table 2.1 and Table 2.2.

$$T_1 = S_2 = 0; \quad E_1 = E_2 = D_1 = D_2 = 0; \qquad \partial D_3/\partial z = 0 \tag{B.1}$$

Recall the governing equations expressed by Equation (2.3), it can be transferred to the form given below for the LE-mode by using the conditions expressed in Equation (B.1) and the relationships among piezoelectric constants shown in Table 2.3.

$$T_3 = \left(c_{33}^D - \frac{c_{13}^{D\,2}}{c_{11}^D}\right) \cdot S_3 - \left(h_{33} - \frac{c_{13}^D}{c_{11}^D} h_{13}\right) \cdot D_3 \tag{B.2}$$

$$E_3 = -\left(h_{33} - \frac{c_{13}^D}{c_{11}^D} h_{13}\right) \cdot S_3 + \left(\beta_{33}^S - \frac{h_{13}^2}{c_{11}^D}\right) \cdot D_3 \tag{B.3}$$

where c_{33}^D, c_{13}^D, h_{33}, etc. are all the piezoelectric constants. Compared Equation (B.2) and (B.3) to the governing equations of T-mode (thickness mode) expressed as the following equations,

$$T_3 = c_{33}^D S_3 - h_{33} D_3 \tag{B.4}$$

$$E_3 = -h_{33} S_3 + \beta_{33}^S D_3 \tag{B.5}$$

It can be found that Equation (B.2) and (B.3) has the similar forms of Equation (B.4) and (B.5) However, the 1D KLM instructed in Chapter 2 is only suitable for T-mode vibration. To use the T-mode KLM mode for LE-mode vibration, we can just simply define some new piezoelectric constants with their expressions as follows,

$$\beta_{33}^{S\,B} = \beta_{33}^S - h_{13}^2 / c_{11}^D \tag{B.6}$$

$$c_{33}^{D\,B} = c_{33}^D - {c_{13}^D}^2 / c_{11}^D \tag{B.7}$$

$$h_{33}^B = h_{33} - c_{13}^D / c_{11}^D \cdot h_{13} \tag{B.8}$$

Thus Equation (B.2) and (B.3) have the exactly same forms of Equation (B.4) and (B.5). The LE KLM mode can be obtained by replacing the piezoelectric constants of T-mode KLM model by the corresponding constants with superscript B. In addition, some other constants used in T-model can be also transferred, and expressed below,

$$\varepsilon_{33}^{s\,B} = 1 / \beta_{33}^{S\,B} \tag{B.9}$$

$$c^B = \sqrt{c_{33}^{D\,B} / \rho} \tag{B.10}$$

$$k_t^B = {h_{33}^B}^2 \varepsilon_{33}^{s\,B} / c_{33}^{D\,B} \tag{B.11}$$

Appendix C

This appendix is to review one of our previous paper "A New 2-D model of Thin Annular Disk using Modified Assumption" and given as follows.

A New 2-D Model of a Thin Annular Disk using a Modified Assumption

Y. Qian[1], N. R. Harris[1], P. Glynne-Jones2, S. P. Beeby[1]

1School of Electronics and Computer Science, University of Southampton, University Road, SO17 1BJ Southampton, UK

2School of Engineering Science, University of Southampton, University Road, SO17 1BJ Southampton, UK

Abstract **--** The work describes an improved 2-D model for a thin annulus by using a modified assumption with regard to coupled vibration. With this approach, the impedance spectrum, and displacements due to radial modes, both in radial and thickness direction of a thin ring are obtained. Bending displacement is investigated by finite element analysis (FEA) and matches our model. The bending in the thickness direction is coupled to radial modes and shows several node circles in the high radial overtone frequency range. The model is validated by FEA with excellent agreement between the new theory and FEA results.

***Key Words*—Annular disk; 2-D model; bending, radial mode, coupled vibration**

I. Introduction

Piezoelectric ring transducers are widely used in the fields of underwater and medical applications [1]. Radial (R) only modes for thin ring structures have been well developed in the past decades and illustrated in previous literatures [1-3]. Whereas in these previous models, the R modes included no out-of-plane vibration (apart from Poisson effects), the more accurate model presented in this paper does and discovers that effectively the modelled R modes have a certain amount of bending in their mode shape, which is caused by the R mode and enhanced by the increase of the order of the R mode.

In our analytical model, the technique is based on a new assumption made from the kinematic relationship. This assumption presented here considers the coupled vibration in both thickness and radial direction; previous work [4-7] has used relationships that decouples the vibrations in thickness and radial direction and thus leads to inaccurate results. By FEA simulation (using

software ANSYS 11.0) which has been shown to produce results close to experimental data [8], the analytical results from our model show a very good agreement with FEA results, with the coupled bending vibration obtained accurately in the thickness direction.

In addition, this bending is believed to be the main reason for the non-uniform thickness extensional (TE) vibration that is excited in the far frequency range which is often associated with high overtones of the R mode; the enhanced bending due to high-order R modes is thus strongly coupled into TE vibration. The assumption allowing coupled vibration may be still valid for the TE mode, and could serve as a step to obtain accurate results for the coupled TE vibration, but this has yet to be demonstrated.

II. Model of thin ring using a modified assumption

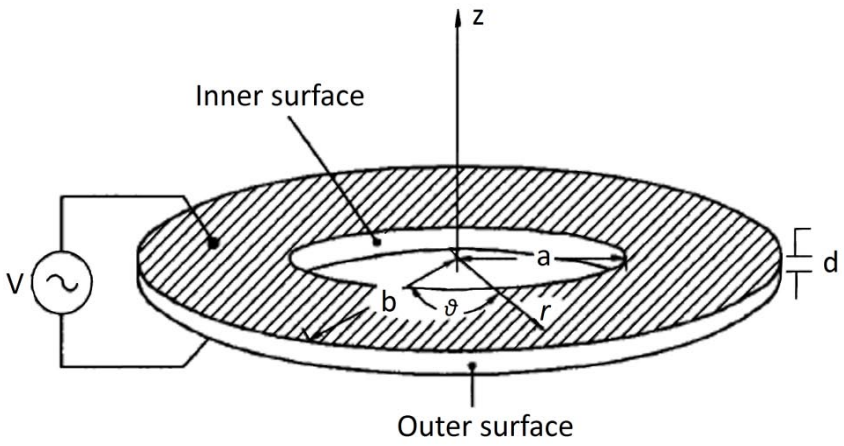

Fig. 1 The geometric structure of a thin ring

Fig 1 shows the structure of a ring defined within axis-symmetric cylindrical coordinates. The angular displacement in θ direction (cylindrical coordinates) can be neglected due to symmetry [1]. The governing equations for piezoelectricity in cylindrical coordinates are given below,

$$T_r = c_{11}^E S_r + c_{12}^E S_\theta + c_{13}^E S_z + e_{31}\partial\varphi/\partial z \quad (1\text{-}1)$$

$$T_\theta = c_{12}^E S_r + c_{11}^E S_\theta + c_{13}^E S_z + e_{31}\partial\varphi/\partial z \quad (1\text{-}2)$$

$$T_z = c_{13}^E (S_r + S_\theta) + c_{33}^E S_z + e_{33}\partial\varphi/\partial z \quad (1\text{-}3)$$

$$T_{rz} = c_{44}^E S_{rz} + e_{15}\partial\varphi/\partial r \quad (1\text{-}4)$$

$$D_r = e_{15} S_{rz} - \varepsilon_{11}^S \partial\varphi/\partial r \quad (1\text{-}5)$$

$$D_z = e_{31}(S_r + S_\theta) + e_{33}S_z - \varepsilon_{33}^S \partial\varphi/\partial z \quad (1\text{-}6)$$

$$S_r = \partial u_r/\partial r,\ S_z = \partial u_z/\partial z,\ S_\theta = u_r/r,\ \ S_{rz} = \frac{\partial u_r}{\partial z} + \frac{\partial u_z}{\partial r} \quad (1\text{-}7)$$

$$E_r = -\partial\varphi/\partial r, \quad E_z = -\partial\varphi/\partial z \quad (1\text{-}8)$$

$$\frac{\partial D_r}{\partial r} + \frac{1}{r}D_r + \frac{\partial D_z}{\partial z} = 0 \quad (1\text{-}9)$$

where $T_{(i,j)}$ is the stress in the defined direction, $S_{(i,j)}$ is the strain, φ represents the electrical potential, E is the electrical field, and D is electric displacement. c_{11}^E, c_{12}^E … c_{44}^E are the elastic stiffness constant; e_{31}, e_{33}, e_{15} are the dielectric constants, ε_{11}^S, ε_{33}^S are the permittivity, u_r and u_z are the radial and thickness displacements, respectively. The differential equations for the 2-D problem are also given,

$$\frac{\partial T_r}{\partial r} + \frac{T_{rr} - T_{\theta\theta}}{r} + \frac{\partial T_{rz}}{\partial z} = \rho\frac{\partial^2 u_r}{\partial t^2};\quad \frac{\partial T_{rz}}{\partial r} + \frac{T_{rz}}{r} + \frac{\partial T_z}{\partial z} = \rho\frac{\partial^2 u_z}{\partial t^2} \quad (2)$$

Since the polarization is in the thickness direction and the ring is supposed to be thin, the classic Kirchhoff's theory is used, and a number of assumptions are made and summarized as follows [1, 9],

$$T_z = T_{rz} = E_r = D_r = 0,\ \varphi = \frac{V}{d}\cdot z,\ S_{rz} = 0 \quad (3)$$

These assumptions are reasonable since the top and bottom surfaces of the thin ring hold the stress free-boundary condition and as the thickness is also small, the stress quantities cannot depart much from zero. Likewise, the linear approximation to voltage through the thickness is also a result of the thin nature of the disk. The zero shear deformation S_{rz} can be deduced by equation (1-4). By the zero shear deformation, the relationship of both radial and thickness displacements can be obtained by classic kinematic relation [10], as expressed in following equation.

$$u_z = \frac{\partial v(z)}{\partial z}\cdot w(r); \qquad u_r = -v(z)\cdot\frac{\partial w(r)}{\partial r} \quad (4)$$

where *v* and *w* are the functions dependant on z and r respectively. For the conventional assumption used in [4-7], the displacements u_r and u_z are decoupled and assumed to be functions only of radius r and thickness *z*, respectively. The modified assumption made in equation (4) realizes the coupled vibration; both *r* and *z* determine the displacements. The new coupled assumption is expected to offer more accurate results. FEA study is used here to verify the analytical model. The FEA representation is modelled in ANSYS and essentially 2-dimensional, consisting of a rectangular element using Solid PLANE13 denoting the piezoelectric resonator, and with an axis-symmetric boundary at the circle centre to represent the 3-D annular structure. A 1-

Volt harmonic voltage is applied onto the top surface of the resonator, and the bottom surface is grounded. Thus harmonic analyses can be applied to obtain impedance and displacement responses. The parameters of the FEA model are listed in Table I.

Table I. RING TRANSDUCER PARAMETERS

PZT ceramic	Inner radius (a)	Outer radius (b)	Width (w=b-a)	Thickness (d)
PZT-8	250 μm	500 μm	250 μm	5 μm

The FEA results show that the u_z in the thickness direction at fixed radius appears as linear function. This is because, although the component *∂v(z)/∂z* of u_z may take the form of a sinusoidal function for thin rings, thickness *z* is quite small compared to the radial wavelength, and this small range of *z* allows a linear approximation.

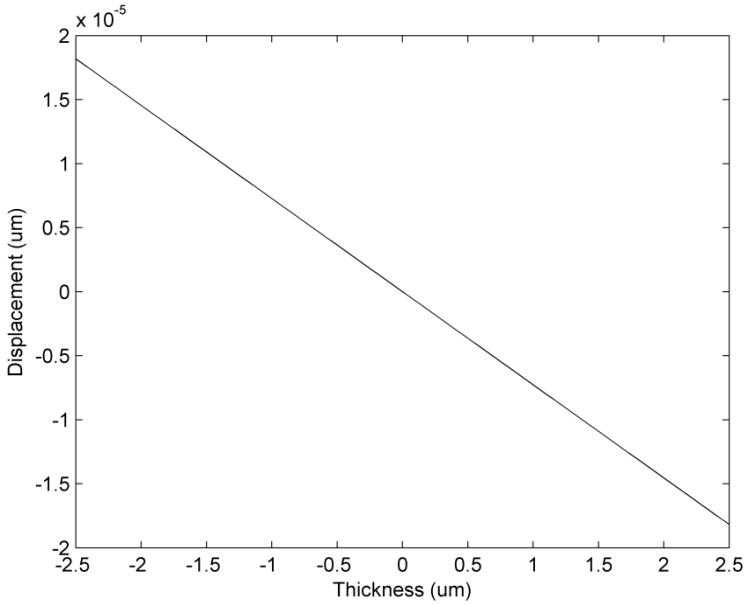

Fig. 2 u_z at fixed radius *r*

As verified in Fig 2, u_z $u_z$for fixed radius *r* and fixed applied voltage *V* is linear which means u_z can be expressed as,

$$u_z = \frac{\partial v(z)}{\partial z} \cdot w(r) = -z \cdot w(r) \quad (5)$$

where the linear coefficient of *z* is absorbed into *w(r)* as this is constant at fixed *r*. Thus by the deduction from equation (4), the radial displacement is obtained,

$$u_r = -v(z) \cdot \frac{\partial w(r)}{\partial r} = \int z \frac{\partial w}{\partial r} dz = (\frac{z^2}{2} + C) \cdot \frac{\partial w}{\partial r} \quad (6)$$

where *C* is a unknown constant generated from the integration. The elastic governing equations from (1-1) to (1-6) can be simplified through Kirchhoff's theory listed in equation (3). The simplified governing equations are obtained,

$$T_r = c_{11}^p \partial u_r/\partial r + c_{12}^p u_r/r + e_{31}^p \partial\varphi/\partial z \quad (7\text{-}1)$$

$$T_\theta = c_{12}^p \partial u_r/\partial r + c_{11}^p u_r/r + e_{31}^p \partial\varphi/\partial z \quad (7\text{-}2)$$

$$D_z = e_{31}^p(\partial u_r/\partial r + u_r/r) - \varepsilon_{33}^p \partial\varphi/\partial z \quad (7\text{-}3)$$

where the parameters with superscript p are given as follow,

$$c_{11}^p = c_{11}^E - c_{13}^{E\,2}/c_{33}^E\,, \quad c_{12}^p = c_{12}^E - c_{13}^{E\,2}/c_{33}^E$$

$$\varepsilon_{33}^p = \varepsilon_{33}^S - e_{33}^2/c_{33}^E\,, \quad e_{31}^p = e_{31} - e_{33}c_{13}^E/c_{33}^E \quad (8)$$

To satisfy the constraint of dielectric displacement $D_{i,j}$ expressed in equation (1-9), the differential of D_z is required to be zero. Considering Kirchhoff's theory ($D_r=0$), we get a constraint from equation (7-3),

$$\frac{\partial D_z}{\partial z} = e_{31}^p\left(\frac{\partial u_r^2}{\partial r \partial z} + \frac{1}{r}\frac{\partial u_r}{\partial z}\right) = 0 \quad (9)$$

Using the conventional assumption with decoupled u_r and u_z, equation (9) is easy to satisfy since the component $\left(\frac{\partial u_r^2}{\partial r \partial z} + \frac{1}{r}\frac{\partial u_r}{\partial z}\right)$ is obvious zero, but this results in disagreement between model and experiment results. However, in our new assumption only suitable values of u_r and u_z are able to make that component zero. A potential solution is apparent if e_{31}^p is set to be zero. Equation (9) is satisfied, but it leads to none piezoelectricity of the material. To avoid this problem, we can make another approximation for radial displacement u_r to satisfy equation (9),

$$u_r = (\frac{z^2}{2} + C)\cdot\frac{\partial w}{\partial r} \approx C\cdot\frac{\partial w}{\partial r} \quad (10)$$

It is assumed that $(Z^2/2)$ is very small compared to the unknown constant *C*. The validity of this approximation will be demonstrated later. Therefore, the radial displacement is only a function of the variable radius *r*, and thus $\partial D_z/\partial z=0$ is satisfied. Using equation (2)-(8) and (10), we can then get,

$$\frac{\partial^2 u_r}{\partial r} + \frac{1}{r}\frac{\partial u_r}{\partial r} + \left(k^2 - \frac{1}{r^2}\right)u_r = 0 \quad (11)$$

where $k^2=\rho\omega^2/c_{11}^p$, is the wave number. The general solution of equation (11) is,

$$u_r = AJ_1(kr) + BY_1(kr) \quad (12)$$

where J_1 is the Bessel function of the first kind and first order, Y_1 is the Bessel function of the second kind and first order. *A* and *B* are constants determined by the boundary conditions. The stress-free boundary condition is that *Tr=0* at the inner and outer surface (at *r=a, b*). By using the boundary condition, weobtain,

$$\begin{vmatrix} a_{11} & a_{12} \\ a_{21} & a_{22} \end{vmatrix} \cdot \begin{vmatrix} A \\ B \end{vmatrix} = \begin{vmatrix} b_1 \\ b_2 \end{vmatrix} \cdot V \quad (13)$$

where *V* is applied voltage, and other constants except *A* and *B* are expressed as,

$$a_{11} = c_{11}^p k \cdot J_0(ka) + \left(c_{12}^p - c_{11}^p\right) \cdot J_1(ka)/a$$

$$a_{12} = c_{11}^p k \cdot Y_0(ka) + \left(c_{12}^p - c_{11}^p\right) \cdot Y_1(ka)/a$$

$$a_{21} = c_{11}^p k \cdot J_0(kb) + \left(c_{12}^p - c_{11}^p\right) \cdot J_1(kb)/b$$

$$a_{22} = c_{11}^p k \cdot Y_0(kb) + \left(c_{12}^p - c_{11}^p\right) \cdot Y_1(kb)/b$$

$$b_1 = b_2 = -e_{31}^p/d \quad (14)$$

From equation (13) and (14), constants *A* and *B* can be determined,

$$A = A_0 V, \qquad B = B_0 V \quad (15)$$

where the value of constants A_0 and B_0 is calculated from the following equation,

$$\begin{vmatrix} A_0 \\ B_0 \end{vmatrix} = \begin{vmatrix} a_{11} & a_{12} \\ a_{21} & a_{22} \end{vmatrix}^{-1} \cdot \begin{vmatrix} b_1 \\ b_2 \end{vmatrix} \quad (16)$$

To verify the approximation used in equation (10), the unknown constant *C* needs to be defined from the zero thickness stress (*Tz=0*) assumption in Kirchhoff's theory,

$$T_z = c_{13}^E \left(\frac{\partial u_r}{\partial r} + \frac{u_r}{r}\right) + \frac{c_{33}^E \partial u_z}{\partial r} + \frac{e_{33}\partial \varphi}{\partial z} = 0 \quad (17)$$

From equation (10) and (12), *w*(*r*) can be deduced,

$$\frac{\partial w}{\partial r} = \frac{1}{C}[AJ_1(kr) + BY_1(kr)]$$

$$w(r) = \int \frac{\partial w}{\partial r} dr = -\frac{1}{kC}[AJ_0(kr) + BY_0(kr)] + D \quad (18)$$

where *D* is another unknown constant from integration. Substituting u_r and u_z into equation (17),

$$T_Z = \left(c_{13}^E k + \frac{c_{33}^E}{kC}\right) \cdot [AJ_0(kr) + BY_0(kr)] + \frac{e_{33}}{d} V - c_{33}^E D = 0 \quad (19)$$

To make equation (19) valid, the components $\left(c_{13}^E k + \frac{c_{33}^E}{kC}\right)$ and $\left(\frac{e_{33}}{d} V - c_{33}^E D\right)$ need to be zero, thus the constants *C* and *D* are obtained,

$$C = -\frac{c_{33}^E}{c_{13}^E k^2}, \quad D = \frac{e_{33}}{c_{33}^E d} \cdot V \tag{20}$$

It can be seen that *C* is a frequency dependent constant. Remembering that in the approximation made in equation (10), $(Z^2/2)$ is assumed as a small value to be neglected. It is essential to check that if it is valid. Fig.3 illustrates the influence of function $Y= (Z^2/2) +C$ compared with function $Y=C$, demonstrating that the component $(Z^2/2)$ is sufficiently small to be neglected.

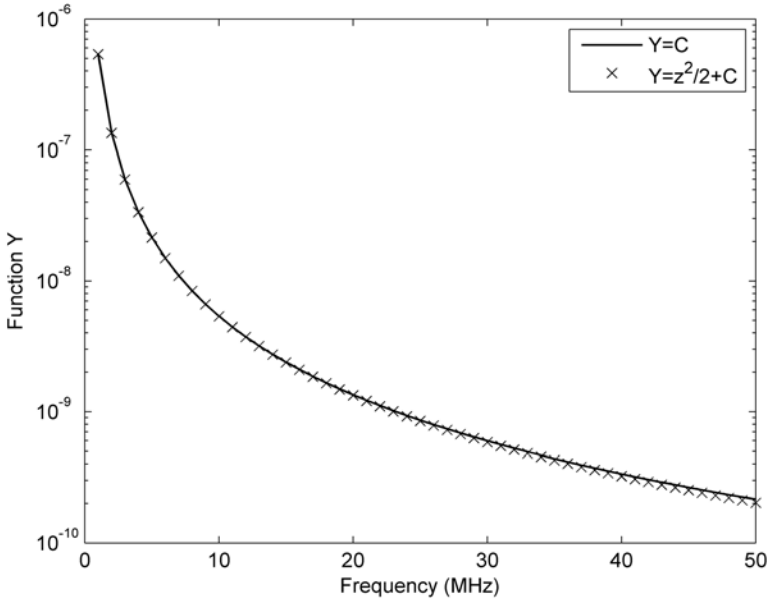

Fig. 3 Comparison of *C* and $(Z^2/2+C)$ at thickness $Z=\pm d/2$

Therefore, u_r and u_z, meeting the constraints and Kirchhoff's theory, are successfully deduced as,

$$u_z = -z \cdot \left\{\frac{c_{13}^E}{c_{33}^E} k[A_0 J_0(kr) + B_0 Y_0(kr)] + \frac{e_{33}}{c_{33}^E d}\right\} \cdot V$$

$$u_r = [A_0 J_1(kr) + B_0 Y_1(kr)] \cdot V \tag{21}$$

As far as the electric part is concerned, by using the equation below,

$$I = j\omega Q = -j\omega 2\pi \int_a^b r D_z dr \tag{22}$$

The admittance Y and impedance Z can be obtained,

$$Y = j\omega C_0 + Y_1 + Y_2, \quad Z = 1/Y \tag{23}$$

where the parameters are shown as follow, C_0 is clamped capacitance, *S* is surface area of the ring,

$$C_0 = \varepsilon_{33}^p S/d, \quad S = \pi(b^2 - a^2)$$

$$Y_1 = -j2\pi\omega \cdot e_{31}^p [bJ_1(kb) + aJ_1(ka)] \cdot A_0$$

$$Y_2 = -j2\pi\omega \cdot e_{31}^{p}[bY_1(kb) + aY_1(ka)] \cdot B_0 \quad (24)$$

III. Theoretical and FEA results

Calculation of the resonant frequency of a ring is not trivial. We can get an estimate by using the rule obtained by Lula et al [1], $f_m < f_0 < f_d$, where f_0 is the fundamental resonant frequency of ring, f_d is the resonances of a disk membrane with the same outer radius as the ring and f_m is the resonance of a thin ring whose inner radius approaches its outer radius (i.e. a very small width). f_m can be obtained by the Berlincourt model [11]. If the radius of a ring membrane needs to be about 500 µm, then the fundamental frequency f_m for the example ring can be calculated as 1MHz, while for a disk through the theory described in [9], the fundamental frequency f_d is found to be around 2MHz. According to equation (24), f_0 ranges from 1 to 2MHz. Thus for the ring as designed in Table I, we would expect a fundamental resonance of about 1.5 MHz.

Fig 4 shows the theory results of impedance from our model, compared to the FEA results from ANSYS. The correlation is very good and it can be seen that the fundamental resonance is indeed at about 1.5MHz. Table II lists the value of the resonant and anti-resonant peaks from calculation and FEA simulation. Higher R modes also show good agreement, but are not listed here.

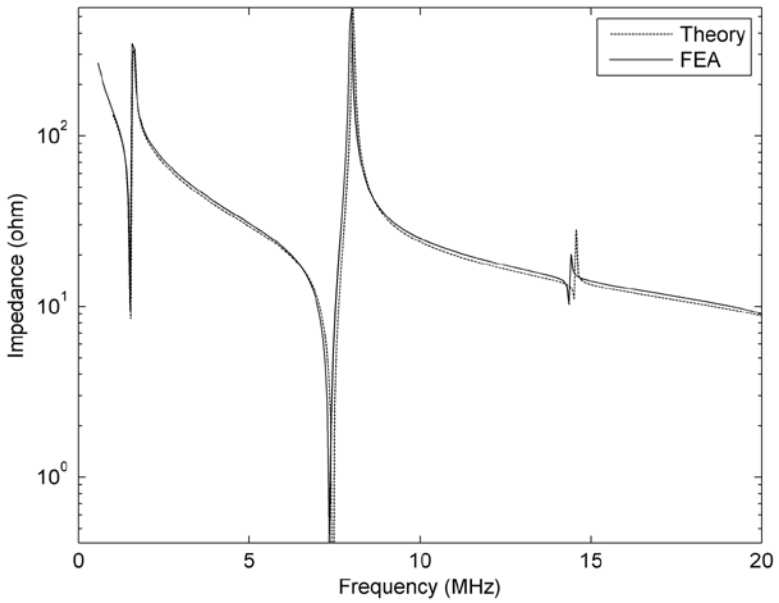

Fig. 4 The impedance from analytical theory and FEA

Table II VALUES OF RESONANT FREQUENCIES FORM THEORY AND FEA

Mode	Resonance by Computation (MHz)	Resonance by FEA (MHz)	Anti-resonance by Computation (MHz)	Anti-resonance by FEA (MHz)
1st mode	1.495	1.475	1.609	1.570
2nd mode	7.445	7.365	8.044	7.983
3rd mode	14.50	14.35	14.58	14.40

In the following figures, simulation results by FEA and computation results by the theory developed in this paper are illustrated for both u_r and u_z in the radial direction. All the displacements are for an applied voltage source of 1V, and the figures show the results for the surface of half the ring, starting from a inner radius of 250um and finishing at an outer radius of 500um. In Fig 5, theory and FEA results of displacement at the 1st R mode are given. Both of the figures show good agreement between the theory and FEA results. Likewise, Fig 7 and 8 show these displacements for the 2nd and 3rd R mode, respectively.

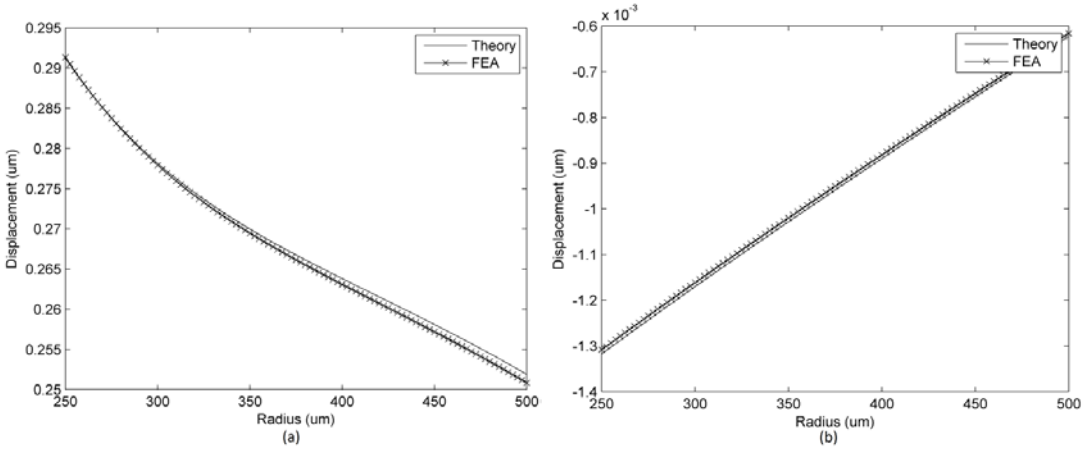

Fig. 5 Theory and FEA results of (a) u_r and (b) u_z along radial direction at 1st R mode

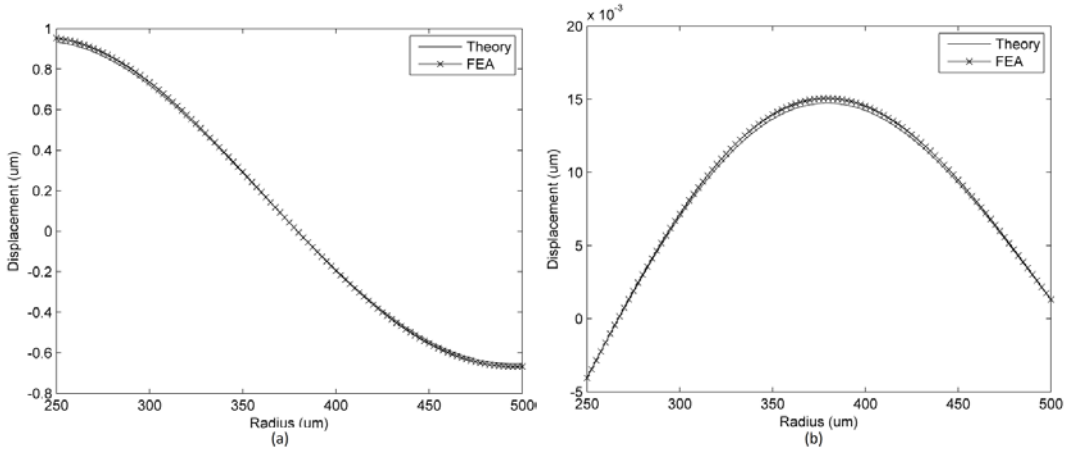

Fig. 6 Theory and FEA results of (a) u_r and (b) u_z along radial direction at 2nd R mode

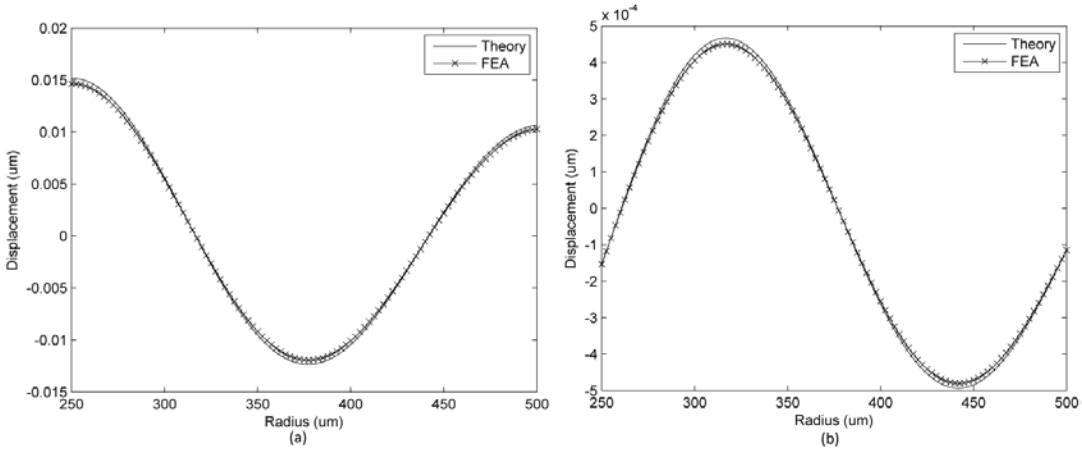

Fig. 7 Theory and FEA results of (a) u_r and (b) u_z along radial direction at 3rd R mode

Both the FEA and theory results are well matched. u_r displacement at these R modes agrees with the typical thin ring vibrations analyzed by Iula [1]. More importantly, the expected displacement u_z is shown well by the analytical model and shows a sinusoidal-shape bending vibration, especially for the high-order resonance. Fig.7b illustrates the resonant mode having nodal circles, for example, at a radial position of 0.375mm, which is generated by the coupled vibration due to R modes. More nodal circles can be found by increasing the order of resonance. At higher frequencies where the TE mode can be generated, the u_z bending obtained from the coupling of higher order R modes in this model will couple into the TE vibration.

IV. Conclusion

To conclude, a new 2-D model of a thin ring transducer has been presented, both radial and thickness displacements are expressed and shown to match the results given by FEA. This validates the new modified assumption in our analytical model to realize a coupled 2-D vibration, instead of the assumption of decoupled u_r and u_z used by previous work. This new approach shows excellent agreement with FEA solutions when considering radial modes. The proposed radial vibration is reasonable, and the bending is discovered and analyzed well by our model. At higher order modes in particular, it also shows nodal circles formed as a result of the coupling of u_r and u_z from R modes, implying that the sinusoidal-shape bending will have an impact on the TE mode in far frequency range. This effect has been associated with high order R modes, but this paper shows a possible mechanism that adds credibility to this thesis. In addition, since the assumption here is

based on coupled vibration, it is quite promising to extend this model into three dimensions and consider coupling between TE and R modes in far frequency range to investigate this point further.

Reference (only for this paper in Appendix C)

1. Iula, A., N. Lamberti, and M. Pappalardo, *A model for the theoretical characterization of thin piezoceramic rings*. Ultrasonics, Ferroelectrics and Frequency Control, IEEE Transactions on, 1996. **43**(3): p. 370-375.
2. Chi-Hung, H., M. Chien-Ching, and L. Yu-Chih, *Theoretical, numerical, and experimental investigation on resonant vibrations of piezoceramic annular disks*. Ultrasonics, Ferroelectrics and Frequency Control, IEEE Transactions on, 2005. **52**(8): p. 1204-1216.
3. Lin, S.Y., *Electro-mechanical equivalent circuit of a piezoelectric ceramic thin circular ring in radial vibration.* Sensors and Actuators a-Physical, 2007. **134**(2): p. 505-512.
4. Iula, A., N. Lamberti, and M. Pappalardo, *An approximated 3-D model of cylinder-shaped piezoceramic elements for transducer design.* Ultrasonics, Ferroelectrics and Frequency Control, IEEE Transactions on, 1998. **45**(4): p. 1056-1064.
5. Feilong, F., S. Jianzhong, and D. Jingjun, *A 2D equivalent circuit of piezoelectric ceramic ring for transducer design.* Ultrasonics, 2006. **44**: p. e723-e726.
6. Lin, S.Y., *Study on the equivalent circuit and coupled vibration for the longitudinally polarized piezoelectric ceramic hollow cylinders*. Journal of Sound and Vibration, 2004. 275(3-5): p. 859-875.
7. Lamberti, N. and M. Pappalardo, *A general approximated two-dimensional model for piezoelectric array elements*. Ultrasonics, Ferroelectrics and Frequency Control, IEEE Transactions on, 1995. **42**(2): p. 243-252.
8. Hing Leung, L., H. Jun Hui, and H.L.W. Chan, *Finite element analysis on piezoelectric ring transformer*. Ultrasonics, Ferroelectrics and Frequency Control, IEEE Transactions on, 2004. **51**(10): p. 1247-1254.
9. Meitzler, A.H., H.M. O'Bryan, Jr., and H.F. Tiersten, *Definition and Measurement of Radial Mode Coupling Factors in Piezoelectric Ceramic Materials with Large Variations in Poisson's Ratio*. Sonics and Ultrasonics, IEEE Transactions on, 1973. **20**(3): p. 233-239.
10. Percin, G. and B.T. Khuri-Yakub, *Piezoelectrically actuated flextensional micromachined ultrasound transducers*. I. Theory. Ultrasonics, Ferroelectrics and Frequency Control, IEEE Transactions on, 2002. **49**(5): p. 573-584.
11. Berlincourt, D.A., D.R. Curran, and H. Jaffe, *Piezoelectric and piezomagnetic material and their function in transducers*. Physical Acoustic, ed. W.P. Mason. Vol. Vol. 1. 1964: New York Academic.

Appendix D

Appendix D concentrates on the study of the mesh refinement study in an FEA software, ANSYS. FEA modelling of the ultrasonic transducers in this study consists of the element responses including impedance, IL (insertion loss) spectrums for an excited element; as well as the imaging performances including the pulse at focal point and the radiation pattern.

The mesh refinement study of element responses can be processed for the larger 2mm, 45MHz annular array since the applied absorbing boundary in water layer reduces the FEA element number, as discussed in Chapter 3. Two mesh sizes are selected for the FEA model: one is the coarse mesh of $\lambda/8$, while another is the fine mesh of $\lambda/20$ which is believed to show relatively accurate results. The largest and narrowest element (or 1st and 7th element) in this annular array with the two mesh sized are chosen to analyze, since the spectrum pattern may also impacted by the element width.

Their impedance spectrums are then illustrated in Figure D1, and the IL spectrums are given in Figure D2. It can be seen that very good agreement are found in both impedance and IL spectrums for the two element with coarse and finer mesh size. It implies that the coarse mesh is able to show relatively accurate element response.

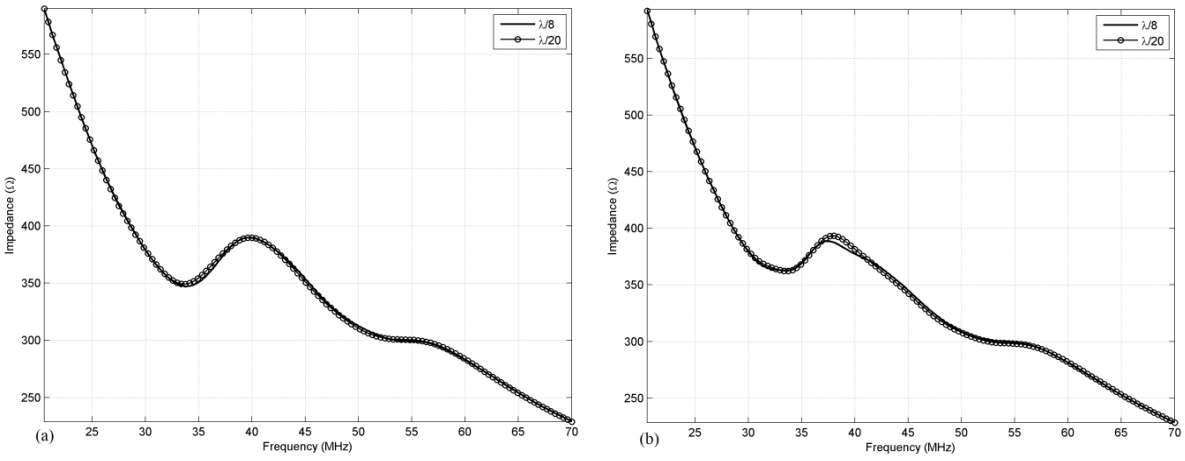

Figure D1 The impedance spectrums by the FEA models with mesh size of $\lambda/8$ and $\lambda/20$ for (a) the 1st and (b) 7th element in the 2mm annular array

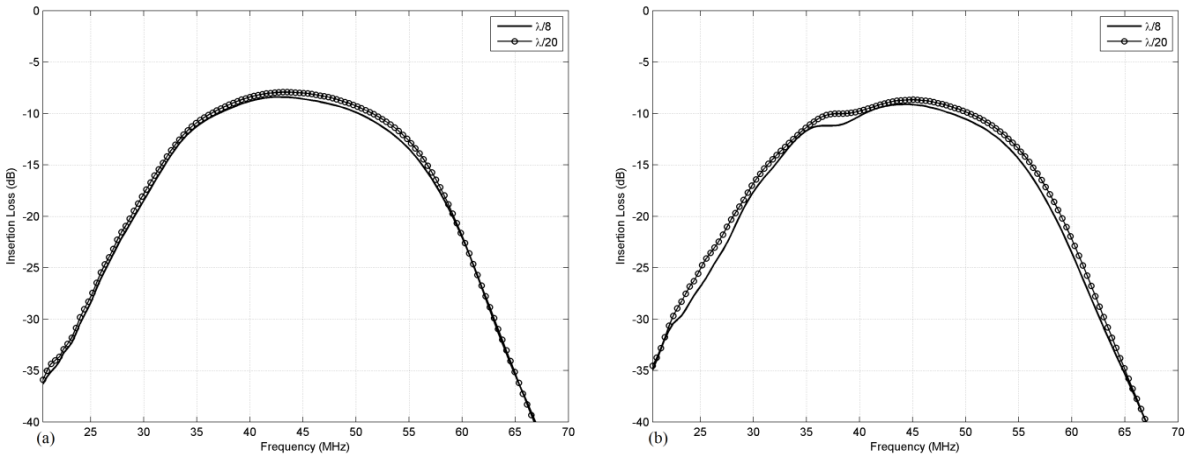

Figure D2 The IL spectrums by the FEA models with mesh size of $\lambda/8$ and $\lambda/20$ for (a) the 1st and (b) 7th element in the 2mm annular array

In terms of the radiation pattern, the mesh refinement study cannot be processed for the 2mm diameter, 45MHz, 4mm focal distance annular array, since the very large "water" layer is needed to show the radiation. When mesh size increases up to $\lambda/20$, the water layer would contains a very large number of element and makes the FEA model impossible to be computed by our computer. This is also discussed in Chapter 3.

Instead, a smaller 1mm diameter, 30MHz, 1mm focal distance annular array is used in the mesh refinement study, since the FEA model of this array could allow our computer to finish the modelling with using the fine mesh of $\lambda/20$. Figure D3 firstly shows the pressure pulses at the focal point for this smaller array with the mesh size ranging from $\lambda/8$ to $\lambda/20$. All the pressure pulses in both time and frequency domain are normalized, while the amplitude of these pulses with different mesh size are also very close to each other. Figure D4 then illustrates the radiation pattern along the focal plane, which is already displayed in Figure 3.15.

By Figure D3, it can be seen that the pulses obtained by different mesh-size FEA model are very similar to each other, especially in the frequency domain. Although some differences are found in the pulse shapes in time domain, their amplitude and bandwidth parameters are almost same. By Figure D4, the radiation patterns with different mesh size also show similar curve shapes, for example, similar beam level and the appearance of sidelobe. Therefore, it could be claimed that good agreement has been found in the imaging responses for the 1mm annular array with all the 4

different mesh size and believed to show relatively accurate results. However, the mesh study of this smaller 1mm array may not directly link to the accuracy of the FEA pattern of the larger 2mm array using coarse mesh size of λ/8, the FEA pattern for the 2mm array is still believed to show at least the trend of radiation, the detail accuracy discussion is provided in Section 3.5.2.

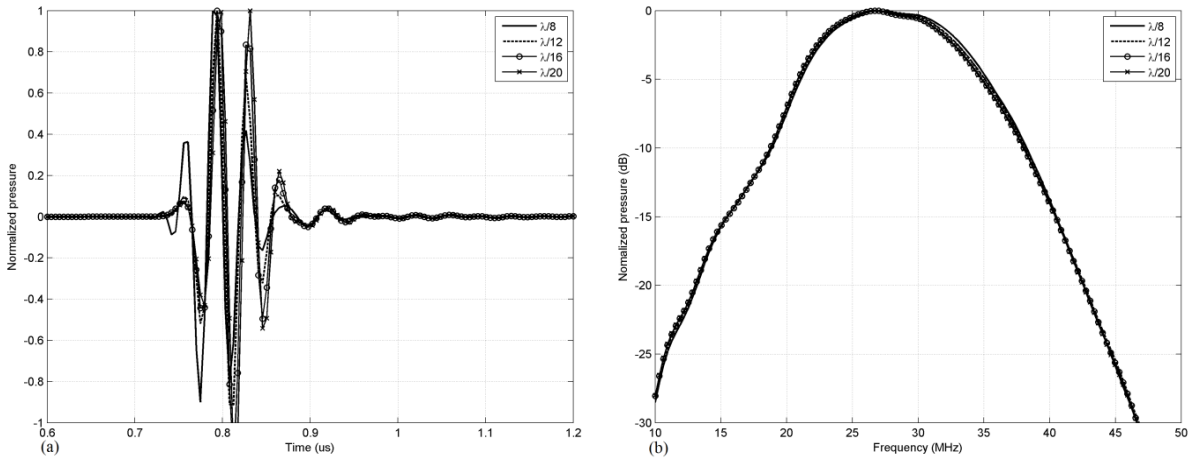

Figure D3 The pressure pulse at focal point for the smaller 1mm array with different mesh size in (a) time and (b) frequency domain

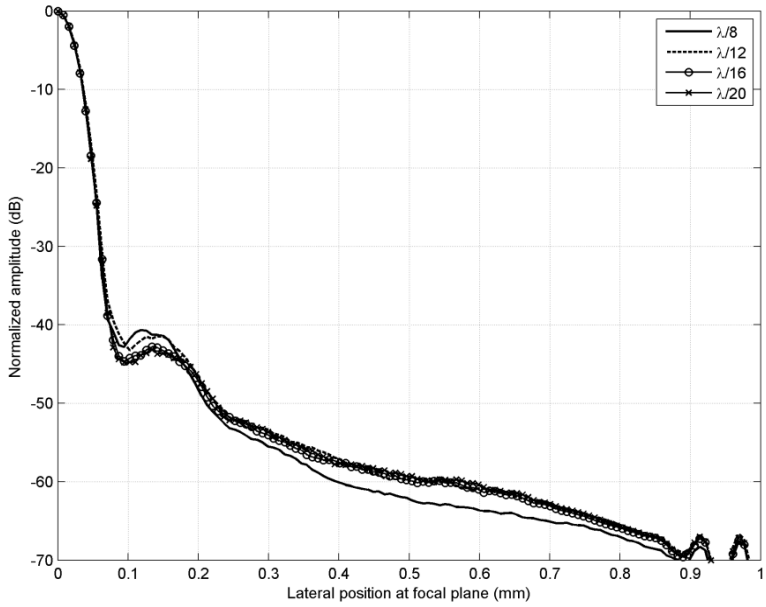

Figure D4 The radiation pattern of the 1mm annular array with using different mesh sizes

Appendix E

E.1 Algorithm to measure the band parameters in frequency domain

The band parameters that need measure are the band peak value, central frequency and fractional bandwidth for a specific band spectrum. Figure E1 shows an insertion loss (IL) spectrum for an element in an array transducer for example.

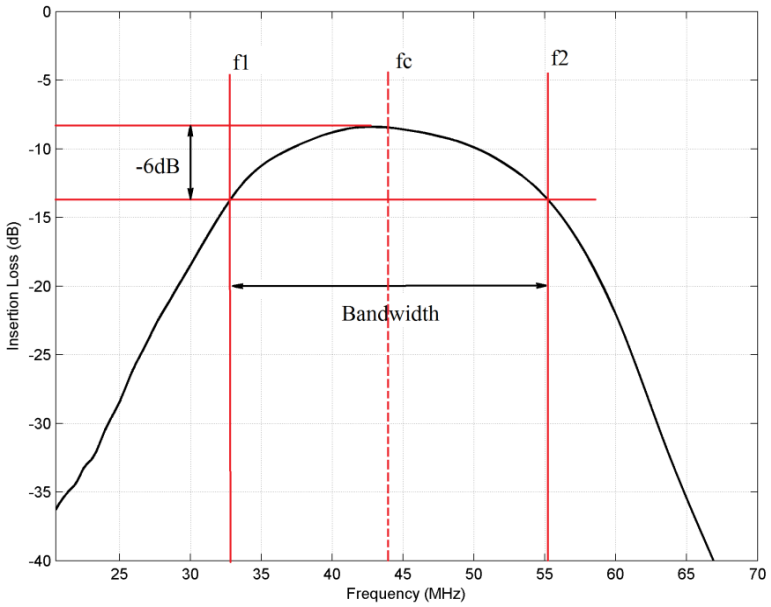

Figure E1 The diagram to show the measurement of an IL spectrum

The band peak value can be easily measured, while two cut-off frequencies f_1 and f_2 are taken as the two points -6dB lower than the peak, as displayed in the figure. Central frequency is then calculated by the average of f_1 and f_2, and the fractional bandwidth BW follows the equation expressed below,

$$BW = (f_2 - f_1)/f_c \tag{E.1}$$

E.2 Algorithm to measure the pulse parameters in time domain

The pressure pulse parameters in time domain mainly includes the pulse peak and pulse length. The pulse peak is easily to be measured, while pulse length requires the envelop detection. Figure E2(a) displays a normalized pressure pulse from a transducer as an example. An envelope detection is then applied to the pressure pulse, as illustrated in Figure E2(b). The pulse length is

then measured as the time during when the value of its envelope is -6dB down (or half) to the amplitude, as pointed out in the figure.

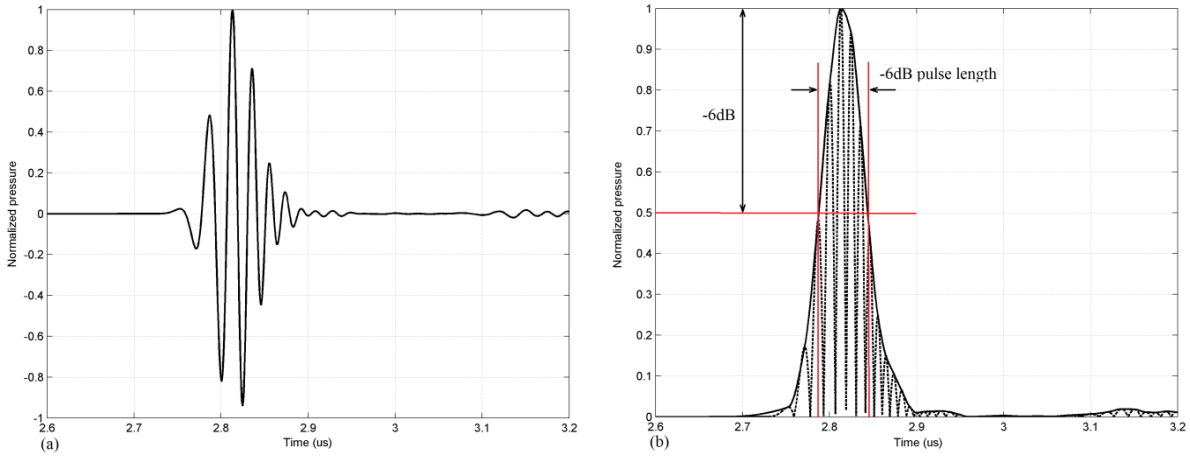

Figure E2 The diagram to show the measurement of a pulse

The Matlab code for the envelope detection function is also provided. To briefly describe, the absolute values of the original pulse are taken and then detected by the envelope function. The pulse length is thus can be measured by the envelope curve.

– Matlab code for envelope detection function

```
% Find upper and lower envelopes of a given signal
% The idea is from Envelope1.1 by Lei Wang, but here it works well when
the signal contains
% successive equal samples and also includes first and last samples of
the signal in the envelopes.
% inputs:
%   sig: vector of input signal
%   method: method of interpolation (defined as in interp1)
% outputs:
%   upperenv: upper envelope of the input signal
%   lowerenv: lower envelope of the input signal
function [upperenv lowerenv] = envelope(sig, method)
if nargin == 1
    method = 'linear';
end
upperind = find(diff(sign(diff(sig))) < 0) + 1;
lowerind = find(diff(sign(diff(sig))) > 0) + 1;
f = 1;
l = length(sig);
try
    upperind = [f upperind l];
    lowerind = [f lowerind l];
catch
    upperind = [f; upperind; l];
    lowerind = [f; lowerind; l];
```

```
end
xi = f : l;
upperenv = interp1(upperind, sig(upperind), xi, method, 'extrap');
lowerenv = interp1(lowerind, sig(lowerind), xi, method, 'extrap');
```

E.3 Algorithm of octave fitting method

Octave fitting method is always used to smooth the data with abrupt changes, and widely applied in the band smoothing in signal processing. 1/3 octave fitting is adopted here, since fitting parameter 1/3 is believed to smooth the array, but also contain the sufficient information from the original data, since a very strong smoothing could also lose the characteristics of the original band. The Matlab code of octave fitting is given as follows:

```
function [Px_oct] = oct(freq,Px,Noct)
%OCT Summary of this function goes here
%   Detailed explanation goes here
%
% Input:    freq - frequecny range
%           Px - original band data
%           Noct - octave fitting parameter (i.e 1/3 octave, Noct=1/3)
% Output:   Px_oct - data after using octave fitting
%% octave smoothing
Noct=2*Noct;
% octave center frequencies
f1=freq(1);
f2=freq(end);
i=0;
while f1 < f2
    f1=f1*10^(3/(10*Noct));
    i=i+1;
    fc(i)=f1;
end

% octave edge frequencies
for i=0:length(fc)-1
    i=i+1;
    f1=10^(3/(20*Noct))*fc(i);
    fe(i)=f1;
end

% find nearest frequency edges
for i=1:length(fe)
    fe_p=find(freq>fe(i),1,'first');
    fe_m=find(freq<fe(i),1,'last');
    fe_0=find(freq==fe(i));
    if isempty(fe_0)==0
        fe(i)=fe_0;
    else
```

```
        p=fe_p-fe(i);
        m=fe(i)-fe_m;
        if p<m
            fe(i)=fe_p;
        else
            fe(i)=fe_m;
        end
    end
end

for i=1:length(fe)-1
    Px_i=Px(fe(i):fe(i+1));
    Px_oct(i)=mean(Px_i);
end
fc=fc(2:end);
Px_oct=interp1(fc,Px_oct,freq,'cubic');
end
```

Reference

1. Biquard, P., *Paul Langevin.* Ultrasonics, 1972. **10**: p. 213-214.
2. Firestone, F.A., *The supersonic reflectoscope for interior inspection.* The Acoustical Society of America, 1946. **17**(3): p. 287-299.
3. Wild, J.J. and J.M. Reid, *Application of Echo-Ranging Techniques to the Determination of Structure of Biological Tissues.* Science, 1952. **115**(2983): p. 226-230.
4. Szabo, T.L., *Diagnostic Ultrasound Imaging: Inside Out*. 2004: Elsevier Academic Press.
5. Somer, J.C., *Electronic sector scanning for ultrasonic diagnosis.* Ultrasonics, 1968. **6**(3): p. 153-159.
6. Somer, J.C., W.A. Oosterbaan, and H.J. Freund. *Ultrasonic Tomographic Imaging of the Brain with an Electronic Sector Scanning System*. in *1973 Ultrasonics Symposium*. 1973.
7. Gururaja, T.R. and R.K. Panda. *Current status and future trends in ultrasonic transducers for medical imaging applications*. in *Applications of Ferroelectrics, 1998. ISAF 98. Proceedings of the Eleventh IEEE International Symposium on*. 1998.
8. Wells, P.N.T., *Ultrasound imaging.* Physics in Medicine and Biology, 2006. **51**(Compendex): p. R83-R98.
9. Passmann, C., et al. *In vivo ultrasound biomicroscopy*. in *Ultrasonics Symposium, 1993. Proceedings., IEEE 1993*. 1993.
10. Lockwood, G.R., et al., *Beyond 30 MHz [applications of high-frequency ultrasound imaging].* Engineering in Medicine and Biology Magazine, IEEE, 1996. **15**(6): p. 60-71.
11. Waters, K.R., et al., *On the applicability of Kramers-Kronig relations for ultrasonic attenuation obeying a frequency power law.* Journal of the Acoustical Society of America, 2000. **108**(2): p. 556-563.
12. Foster, F.S., et al., *Advances in ultrasound biomicroscopy.* Ultrasound in Medicine & Biology, 2000. **26**(1): p. 1-27.
13. Takeuchi, H., et al. *A 7.5 MHz Linear Array Ultrasonic Probe Using Modified PbTiO<inf>3</inf>Ceramics*. in *1982 Ultrasonics Symposium*. 1982.
14. Saitoh, S., et al., *A 3.7 MHz phased array probe using 0.91Pb(Zn1/3Nb2/3)O3-0.09PbTiO3.* Ultrasonics, Ferroelectrics and Frequency Control, IEEE Transactions on, 1999. **46**(2): p. 414-421.
15. Sung Min, R., et al. *A 128 channel 7.5 MHz linear array ultrasonic probe using PMN-PT single crystal*. in *Ultrasonics, 2003 IEEE Symposium on*. 2003.
16. Ramachandran, S., J.R.A. Ketterling, and Ieee. *A comparison of acoustic beam properties of a high-frequency annular and linear array*. in *IEEE Ultrasonics Symposium*. 2007. New York, NY: Ieee.
17. Shung, K.K. and M. Zippuro, *Ultrasonic transducers and arrays.* Engineering in Medicine and Biology Magazine, IEEE, 1996. **15**(6): p. 20-30.
18. Ketterling, J.A., et al. *Polyimide backed 40-MHz PVDF transducers*. in *IEEE International Ultrasonics Symposium*. 2005. Rotterdam, NETHERLANDS: Ieee.
19. Knapik, D.A., et al. *A realtime 200 MHz ultrasound B-scan imager*. in *Ultrasonics Symposium, 1997. Proceedings., 1997 IEEE*. 1997.
20. Michau, S., P. Mauchamp, and R. Dufait. *Piezocomposite 30MHz linear array for medical imaging: design challenges and performances evaluation of a 128 elements array*. in *Ultrasonics Symposium, 2004 IEEE*. 2004.
21. Inoue, T., M. Ohta, and S. Takahashi, *Design of Ultrasonic Transducers with Multiple Acoustic Matching Layers for Medical Application.* Ultrasonics, Ferroelectrics and Frequency Control, IEEE Transactions on, 1987. **34**(1): p. 8-16.

22. Wang, H.F., et al., *High frequency properties of passive materials for ultrasonic transducers.* Ieee Transactions on Ultrasonics Ferroelectrics and Frequency Control, 2001. **48**(1): p. 78-84.
23. Grewe, M.G., et al. *Acoustic properties of particle/polymer composites for transducer backing applications*. in *Ultrasonics Symposium, 1989. Proceedings., IEEE 1989*. 1989.
24. Auld, B.A., *Wave propagation and resonance in piezoelectric materials.* The Journal of the Acoustical Society of America, 1981. **70**(6): p. 1577-1585.
25. Mason, W.P., *Crystals and Their Application to Ultrasonics*. 1950, Princeton, NJ: D. Van Nostrand Co.
26. Zelenka, J., *Piezoielectric resonators and their applications*. 1986: Elsevier Science Publishers.
27. *Guide to Piezoelectric & Dielectric Ceramic - Chapter 2, Physical Basis*. Available from: http://www.morganelectroceramics.com/resources/guide-to-piezoelectric-dielectric-ceramic/.
28. Selfridge, A.R., G.S. Kino, and B.T. Khuriyakub, *Fundamental Concepts in Acoustic Transducer Array Design.* Ieee Transactions on Sonics and Ultrasonics, 1981. **28**(5): p. 399-399.
29. Onoe, M. and H.F. Tiersten, *Resonant Frequencies of Finite Piezoelectric Ceramic Vibrators with High Electromechanical Coupling.* Ultrasonics Engineering, IEEE Transactions on, 1963. **10**(1): p. 32-38.
30. Barber, J., *Plane Strain and Plane Stress*, in *Elasticity*. 2004, Springer Netherlands. p. 33-40.
31. Jaffe, H. and D.A. Berlincourt, *Piezoelectric transducer materials.* Proceedings of the IEEE, 1965. **53**(10): p. 1372-1386.
32. Berlincourt, D.A., D.R. Curran, and H. Jaffe, *Piezoelectric and piezomagnetic material and their function in transducers*. Physical Acoustic, ed. W.P. Mason. Vol. Vol. 1. 1964: New York Academic.
33. Kinsler, L.E., et al., *Fundamentals of Acoustics*. 4th Edition ed. 2000, New York: John Wiley & Sons.
34. Iula, A., N. Lamberti, and M. Pappalardo, *A model for the theoretical characterization of thin piezoceramic rings.* Ultrasonics, Ferroelectrics and Frequency Control, IEEE Transactions on, 1996. **43**(3): p. 370-375.
35. Iula, A., N. Lamberti, and M. Pappalardo, *An approximated 3-D model of cylinder-shaped piezoceramic elements for transducer design.* Ultrasonics, Ferroelectrics and Frequency Control, IEEE Transactions on, 1998. **45**(4): p. 1056-1064.
36. Feilong, F., S. Jianzhong, and D. Jingjun, *A 2D equivalent circuit of piezoelectric ceramic ring for transducer design.* Ultrasonics, 2006. **44**: p. e723-e726.
37. Lin, S.Y., *Electro-mechanical equivalent circuit of a piezoelectric ceramic thin circular ring in radial vibration.* Sensors and Actuators a-Physical, 2007. **134**(2): p. 505-512.
38. Lin, S.Y., *Study on the equivalent circuit and coupled vibration for the longitudinally polarized piezoelectric ceramic hollow cylinders.* Journal of Sound and Vibration, 2004. **275**(3-5): p. 859-875.
39. Yichen, Q., et al., *A new 2-D model of a thin annular disk using a modified assumption.* Ultrasonics, Ferroelectrics and Frequency Control, IEEE Transactions on, 2010. **57**(2): p. 421-426.
40. Smith, W.A., A. Shaulov, and B.A. Auld. *Tailoring the Properties of Composite Piezoelectric Materials for Medical Ultrasonic Transducers*. in *IEEE 1985 Ultrasonics Symposium*. 1985.

41. Shung, K., J. Cannata, and Q. Zhou, *Piezoelectric materials for high frequency medical imaging applications: A review.* Journal of Electroceramics, 2007. **19**(1): p. 141-147.
42. Snook, K.A., et al., *Design, fabrication, and evaluation of high frequency, single-element transducers incorporating different materials.* Ultrasonics, Ferroelectrics and Frequency Control, IEEE Transactions on, 2002. **49**(2): p. 169-176.
43. Foster, F.S., K.A. Harasiewicz, and M.D. Sherar, *A history of medical and biological imaging with polyvinylidene fluoride (PVDF) transducers.* Ultrasonics, Ferroelectrics and Frequency Control, IEEE Transactions on, 2000. **47**(6): p. 1363-1371.
44. Snook, K.A., T.R. Shrout, and K.K. Shung. *Development of high frequency annular arrays for medical imaging*. in *IEEE International Ultrasonics Symposium*. 2003. Honolulu, HI: Ieee.
45. Cannata, J.M., et al., *Development of a 35-MHz piezo-composite ultrasound array for medical imaging.* Ultrasonics, Ferroelectrics and Frequency Control, IEEE Transactions on, 2006. **53**(1): p. 224-236.
46. Ruibin, L., K.A. Harasiewicz, and F.S. Foster, *Interdigital pair bonding for high frequency (20-50 MHz) ultrasonic composite transducers.* Ultrasonics, Ferroelectrics and Frequency Control, IEEE Transactions on, 2001. **48**(1): p. 299-306.
47. Wenkang, Q. and C. Wenwu, *Finite element analysis of periodic and random 2-2 piezocomposite transducers with finite dimensions.* Ultrasonics, Ferroelectrics and Frequency Control, IEEE Transactions on, 1997. **44**(5): p. 1168-1171.
48. Smith, W.A. and B.A. Auld, *Modeling 1-3 composite piezoelectrics: thickness-mode oscillations.* Ultrasonics, Ferroelectrics and Frequency Control, IEEE Transactions on, 1991. **38**(1): p. 40-47.
49. Smith, W.A. *The role of piezocomposites in ultrasonic transducers*. in *Ultrasonics Symposium, 1989. Proceedings., IEEE 1989*. 1989.
50. Oakley, C.G. and M.J. Zipparo. *Single crystal piezoelectrics: a revolutionary development for transducers*. in *Ultrasonics Symposium, 2000 IEEE*. 2000.
51. Zipparo, M.J. and C.G. Oakley. *Single crystal PMN-PT and PZN-PT ultrasonic imaging arrays*. in *Applications of Ferroelectrics, 2000. ISAF 2000. Proceedings of the 2000 12th IEEE International Symposium on*. 2000.
52. Seung-Eek, P. and T.R. Shrout. *Characteristics of relaxor-based piezoelectric single crystals for ultrasonic transducers*. in *Ultrasonics Symposium, 1996. Proceedings., 1996 IEEE*. 1996.
53. Kawai, H., *The Piezoelectricity of Poly (vinylidene Fluoride).* Japanese Journal of Applied Physics, 1969. **8**: p. 975-976.
54. Brown, L.F. *Ferroelectric polymers: current and future ultrasound applications*. in *Ultrasonics Symposium, 1992. Proceedings., IEEE 1992*. 1992.
55. Brown, L.F., *Design considerations for piezoelectric polymer ultrasound transducers.* Ieee Transactions on Ultrasonics Ferroelectrics and Frequency Control, 2000. **47**(6): p. 1377-1396.
56. Goodman, J.W., *Introduction to Fourier Optics*. 3rd ed. 2004: Roberts & Company Publishers.
57. Pasquer, V., N. Dube, and A. Lamarre, *Dynamic focusing of phased arrays for non-destructive testing: Characterization and application*. Emerging Technologies in Ndt, ed. D. VanHemelrijck, A. Anastassopoulos, and T. Philippidis. 2000, Leiden: A a Balkema Publishers. 89-95.
58. Kremkau, F.W., *Diagnostic Ultrasound, Principles and Instruments*. 6th ed. 2002: W.B Saunders Company.

59. Jespersen, S.K., J.E. Wilhjelm, and H. Sillesen. *Ultrasound spatial compound scanner for improved visualization in vascular imaging*. in *Ultrasonics Symposium, 1998. Proceedings., 1998 IEEE*. 1998.
60. Foster, F.S., et al., *A new ultrasound instrument for in vivo microimaging of mice.* Ultrasound in Medicine & Biology, 2002. **28**(9): p. 1165-1172.
61. Savord, B. and R. Solomon. *Fully sampled matrix transducer for real time 3D ultrasonic imaging*. in *Ultrasonics, 2003 IEEE Symposium on*. 2003.
62. Wright, J.N. *Resolution Issues in Medical Ultrasound*. in *IEEE 1985 Ultrasonics Symposium*. 1985.
63. Foster, F.S., et al., *Principles and applications of ultrasound backscatter microscopy.* Ultrasonics, Ferroelectrics and Frequency Control, IEEE Transactions on, 1993. **40**(5): p. 608-617.
64. Shung, K.K., et al. *High frequency ultrasound: a new frontier for ultrasound*. in *2009 31/sup st/ Annual International Conference of the IEEE Engineering in Medicine and Biology Society. EMBC 2009*. 2009. Minneapolis, MN,: Ieee.
65. Turnbull, D.H., et al., *A 40-100 MHz B-scan ultrasound backscatter microscope for skin imaging.* Ultrasound in Medicine & Biology, 1995. **21**(1): p. 79-88.
66. Passmann, C. and H. Ermert, *A 100-MHz ultrasound imaging system for dermatologic and ophthalmologic diagnostics.* Ultrasonics, Ferroelectrics and Frequency Control, IEEE Transactions on, 1996. **43**(4): p. 545-552.
67. Yue, L., *Phase aberration correction using near-field signal redundancy. I. Principles [Ultrasound medical imaging].* Ultrasonics, Ferroelectrics and Frequency Control, IEEE Transactions on, 1997. **44**(2): p. 355-371.
68. Krimholtz, R., D.A. Leedom, and G.L. Matthaei, *New equivalent circuits for elementary piezoelectric transducers.* Electronics Letters, 1970. **6**(13): p. 398-399.
69. Sherrit, S., et al. *Comparison of the Mason and KLM equivalent circuits for piezoelectric resonators in the thickness mode*. in *Ultrasonics Symposium, 1999. Proceedings. 1999 IEEE*. 1999.
70. Selfridge, A.R. and S. Gehlbach. *KLM Transducer Model Implementation Using Transfer Matrices*. in *IEEE 1985 Ultrasonics Symposium*. 1985.
71. Sittig, E.K., *Transmission Parameters of Thickness-Driven Piezoelectric Transducers Arranged in Multilayer Configurations.* Sonics and Ultrasonics, IEEE Transactions on, 1967. **14**(4): p. 167-174.
72. Lockwood, G.R. and F.S. Foster, *Modeling and optimization of high-frequency ultrasound transducers.* Ultrasonics, Ferroelectrics and Frequency Control, IEEE Transactions on, 1994. **41**(2): p. 225-230.
73. Mezheritsky, A.V., *Elastic, dielectric, and piezoelectric losses in piezoceramics: how it works all together.* Ultrasonics, Ferroelectrics and Frequency Control, IEEE Transactions on, 2004. **51**(6): p. 695-707.
74. Tsurumi, T., H. Kakemoto, and S. Wada. *Dielectric, elastic and piezoelectric losses of PZT ceramics in the resonance state*. in *Applications of Ferroelectrics, 2002. ISAF 2002. Proceedings of the 13th IEEE International Symposium on*. 2002.
75. Castillo, M., P. Acevedo, and E. Moreno, *KLM model for lossy piezoelectric transducers.* Ultrasonics, 2003. **41**(8): p. 671-679.
76. Whitworth, G., *Discussion of 1-D piezoelectric transducer models with loss.* Ultrasonics, Ferroelectrics and Frequency Control, IEEE Transactions on, 2001. **48**(3): p. 844-846.

77. Tran-Huu-Hue, L.P., et al., *Comparison of several methods to characterise the high frequency behaviour of piezoelectric ceramics for transducer applications.* Ultrasonics, 2000. **38**(1-8): p. 219-223.
78. Sittig, E.K., *Definitions Relating to Conversion Losses in Piezoelectric Transducers.* Sonics and Ultrasonics, IEEE Transactions on, 1971. **18**(4): p. 231-234.
79. Harris, G.R., *Review of transient field theory for a baffled planar piston.* The Journal of the Acoustical Society of America, 1981. **70**(1): p. 10-20.
80. Hayman, A.J. and J.P. Weight, *Transmission and reception of short ultrasonic pulses by circular and square transducers.* The Journal of the Acoustical Society of America, 1979. **66**(4): p. 945-951.
81. Selfridge, A.R., G.S. Kino, and B.T. Khuri-Yakub, *A theory for the radiation pattern of a narrow-strip acoustic transducer.* Applied Physics Letters, 1980. **37**(1): p. 35-36.
82. Smith, S.W., et al., *Angular Response of Piezoelectric Elements in Phased Array Ultrasound Scanners.* Sonics and Ultrasonics, IEEE Transactions on, 1979. **26**(3): p. 185-190.
83. Stepanishen, P.R., *Transient Radiation from Pistons in an Infinite Planar Baffle.* The Journal of the Acoustical Society of America, 1971. **49**(5B): p. 1629-1638.
84. Brown, J.A., C.E.M. Demore, and G.R. Lockwood, *Design and fabrication of annular arrays for high-frequency ultrasound.* Ieee Transactions on Ultrasonics Ferroelectrics and Frequency Control, 2004. **51**(8): p. 1010-1017.
85. Kobayashi, M., et al. *Fabrication and Characterization of Thick Film Piezoelectric Ultrasonic Transducers*. in *Ultrasonics Symposium, 2006. IEEE*. 2006.
86. Dorey, R.A., et al. *Screen printed PZT thick films using composite film technology*. in *15th International Symposium on Integrated Ferroelectrics*. 2003. Colorado Springs, Colorado: Taylor & Francis Ltd.
87. Dorey, R.A. and R.W. Whatmore, *Electroceramic thick film fabrication for MEMS.* Journal of Electroceramics, 2004. **12**(1-2): p. 19-32.
88. Zipparo, M.J., K.K. Shung, and T.R. Shrout, *Piezoceramics for high-frequency (20 to 100 MHz) single-element imaging transducers.* Ieee Transactions on Ultrasonics Ferroelectrics and Frequency Control, 1997. **44**(5): p. 1038-1048.
89. Choi, W.-Y., et al., *Electrical properties of Sb-doped PZT films deposited by d.c. reactive sputtering using multi-targets.* Materials Letters, 1998. **37**(3): p. 119-127.
90. Guiffard, B., et al., *Characteristics of F doped PZT ceramics using different fluorine sources.* Materials Science and Engineering: B, 2007. **137**(1-3): p. 272-277.
91. Li, J.H., C.R. Friedrich, and R.S. Keynton, *Design and fabrication of a miniaturized, integrated, high-frequency acoustical lens-transducer system.* Journal of Micromechanics and Microengineering, 2002. **12**(3): p. 219-228.
92. Ritter, T.A., et al., *A 30-MHz piezo-composite ultrasound array for medical imaging applications.* Ultrasonics, Ferroelectrics and Frequency Control, IEEE Transactions on, 2002. **49**(2): p. 217-230.
93. Reynolds, P., J. Hyslop, and G. Hayward. *Analysis of spurious resonances in single and multi-element piezocomposite ultrasonic transducers*. in *Ultrasonics, 2003 IEEE Symposium on*. 2003.
94. Ritter, T.A., et al. *High frequency ultrasound arrays for medical imaging*. in *Ultrasonics Symposium, 2000 IEEE*. 2000.
95. Cannata, J.M., T.R. Shrout, and K.K. Shung, *A 35 MHz linear ultrasonic array for medical imaging*. Isaf 2002: Proceedings of the 13th Ieee International Symposium on Applications of Ferroelectrics, ed. G. White and T. Tsurumi. 2002, New York: Ieee. 343-346.

96. Morton, C.E. and G.R. Lockwood. *Evaluation of kerfless linear arrays*. in *Ultrasonics Symposium, 2002. Proceedings. 2002 IEEE*. 2002.
97. Da-Wei, W., et al., *Very high frequency (beyond 100 MHz) PZT kerfless linear arrays.* Ultrasonics, Ferroelectrics and Frequency Control, IEEE Transactions on, 2009. **56**(10): p. 2304-2310.
98. Demore, C.E.M., J.A. Brown, and G.R. Lockwood, *Investigation of cross talk in kerfless annular arrays for high-frequency imaging.* Ieee Transactions on Ultrasonics Ferroelectrics and Frequency Control, 2006. **53**(5): p. 1046-1056.
99. Oralkan, O., et al. *High-frequency CMUT arrays for high-resolution medical imaging*. in *Ultrasonics Symposium, 2004 IEEE*. 2004.
100. Yeh, D.T., et al. *High-resolution imaging with high-frequency 1-D linear CMUT arrays*. in *Ultrasonics Symposium, 2005 IEEE*. 2005.
101. Snook, K.A., et al., *High-frequency ultrasound annular-array imaging. Part I: Array design and fabrication.* Ieee Transactions on Ultrasonics Ferroelectrics and Frequency Control, 2006. **53**(2): p. 300-308.
102. Snook, K., T. Shrout, and K.K. Shung. *Design of a 50 MHz annular array using fine-grain lead titanate*. in *13th IEEE International Symposium on Applications of Ferroelectrics*. 2002. Nara, Japan: Ieee.
103. Wo-Hsing, C., et al. *Design and development of a 30 MHz six-channel annular array ultrasound backscatter microscope*. in *Proceedings of 2002 IEEE International Ultrasonics Symposium*. 2002. Munich, Germany: Ieee.
104. Morton, C.E. and G.R. Lockwood. *Design of a 40 MHz annular array*. in *Ultrasonics Symposium, 2001 IEEE*. 2001.
105. Brown, J.A., C.E. Morton, and G.R. Lockwood. *Fabrication and performance of 40-60 MHz annular arrays*. in *2003 IEEE Ultrasonics Symposium*. 2003. Honolulu, HI,: Ieee.
106. Gottlieb, E.J., et al., *Development of a high-frequency (> 50 MHz) copolymer annular-array, ultrasound transducer.* Ieee Transactions on Ultrasonics Ferroelectrics and Frequency Control, 2006. **53**(5): p. 1037-1045.
107. Ketterling, J.A., et al., *Design and fabrication of a 40-MHz annular array transducer.* Ultrasonics, Ferroelectrics and Frequency Control, IEEE Transactions on, 2005. **52**(4): p. 672-681.
108. Levassort, F., et al., *Modeling of highly loaded 0-3 piezoelectric composites using a matrix method.* Ultrasonics, Ferroelectrics and Frequency Control, IEEE Transactions on, 1998. **45**(6): p. 1497-1505.
109. Levassort, F., et al., *Effective electroelastic moduli of 3-3(0-3) piezocomposites.* Ultrasonics, Ferroelectrics and Frequency Control, IEEE Transactions on, 1999. **46**(4): p. 1028-1034.
110. Moser, F., L.J. Jacobs, and J. Qu, *Modeling elastic wave propagation in waveguides with the finite element method.* NDT & E International, 1999. **32**(4): p. 225-234.
111. Liu, Y., *Wave Propagation Study Using Finite Element Analysis*, in *Electrical Engineering in the Graduate College*. 2005, University of Illinois at Urbana-Champaign: Urbana, Illinois.
112. Jensen, J.A. and N.B. Svendsen, *Calculation of pressure fields from arbitrarily shaped, apodized, and excited ultrasound transducers.* Ultrasonics, Ferroelectrics and Frequency Control, IEEE Transactions on, 1992. **39**(2): p. 262-267.
113. Jensen, J.A., *A new calculation procedure for spatial impulse responses in ultrasound*. Vol. 105. 1999: ASA. 3266-3274.

114. Dorey, R.A., et al. *Fabrication and characterization of annular thickness mode piezoelectric micro ultrasonic transducers*. in *16th IEEE International Symposium on Applications of Ferroelectrics*. 2007. Nara, JAPAN: Ieee-Inst Electrical Electronics Engineers Inc.
115. Horner, M.S. and A.F. Brisken, *Ultrasonic transducer and attenuating material for use therein.* The Journal of the Acoustical Society of America, 1989. **85**(5): p. 2243-2243.
116. Moshfeghi, M., *Side-lobe suppression for ultrasonic imaging arrays.* Ultrasonics, 1987. **25**(6): p. 322-327.
117. Silverman, R.H., J.A. Ketterling, and D.J. Coleman, *High-frequency ultrasonic imaging of the anterior segment using an annular array transducer.* Ophthalmology, 2007. **114**(4): p. 816-822.
118. Cherin, E.W., et al., *Experimental characterization of fundamental and second harmonic beams for a high-frequency ultrasound transducer.* Ultrasound in Medicine & Biology, 2002. **28**(5): p. 635-646.
119. Vos, H.J., et al. *A 20-40 MHz ultrasound transducer for intravascular harmonic imaging*. in *Ultrasonics Symposium, 2004 IEEE*. 2004.
120. Silverman, R.H., et al., *High-frequency harmonic imaging of the eye*, in *Medical Imaging 2005: Ultrasonic Imaging and Signal Processing*, W.F. Walker and S.Y. Emelianov, Editors. 2005, Spie-Int Soc Optical Engineering: Bellingham. p. 16-25.
121. Cannata, J.M., et al. *Design of focused single element (50-100 MHz) transducers using lithium niobate*. in *Ultrasonics Symposium, 2000 IEEE*. 2000.
122. Cannata, J.M., et al., *Design of efficient, broadband single-element (20-80 MHz) ultrasonic transducers for medical imaging applications.* Ieee Transactions on Ultrasonics Ferroelectrics and Frequency Control, 2003. **50**(11): p. 1548-1557.